

MULTIFUNCTIONAL DIELECTRIC ELASTOMER TRANSDUCERS AS INTEGRATED AUDIO-TACTILE INTERFACES WITH SELF-SENSING CAPABILITY

Dissertation

**zur Erlangung des Grades
des Doktors der Ingenieurwissenschaften
der Naturwissenschaftlich-Technischen Fakultät
der Universität des Saarlandes**

**von
Sebastian Gratz-Kelly**

**Saarbrücken
2025**

Tag des Kolloquiums: 26.05.2025

Dekan: Prof. Dr.-Ing. Dirk Bähre

Berichterstatter: Prof. Dr.-Ing. Stefan Seelecke
Prof. Dr.-Ing. Rainer Müller

Akad. Mitarbeiter: Dr. Ing. Niklas König

Vorsitz: Prof. Dr.-Ing. Dirk Bähre

Acknowledgments

First and foremost, I would like to extend my deepest gratitude to my PhD advisor Prof. Stefan Seelecke, for giving me the possibility to work in his lab and proceed my PhD. His constant support, trust, patience, enthusiasm and guidance during my time at the lab have been invaluable contribution to me.

A special thanks goes to the whole iMSL-Team and all my co-workers and especially my student research assistants who all give lot of contributions to this thesis, many thanks go to Bettina Fasolt, Daniel Philippi, Tim Krüger, Benedikt Holz, Olivier Fritzen, Daniel Bruch and Andreas Meyer to only name a few.

I'm very grateful to Prof. Dr. Giacomo Moretti for many inspirational discussions and very helpful ideas as well as the reviewing of my publications and this dissertation. Also, I would like to thank Prof. Dr. Gianluca Rizzello and Prof. Dr. Paul Motzki for the good scientific environment and interaction at the laboratory.

Many thanks to Prof. Müller and the committee for oversee my defence and reviewing this dissertation.

Finally, I would like to thank my Family for supporting me through the years. Specially, I want to thank my mother for her effort and selfless support all my live. An inexpressible thanks that cannot be put into words goes to my lovely wife Louisa, for her support and love, and for her tireless dedication to our family.

Für den gläubigen Menschen steht Gott
am Anfang, für den Wissenschaftler
am Ende aller seiner Überlegungen.

- Max Karl Ernst Ludwig Plank (1858 -1947) -

Dedicated to my loved Family

Abstract

Dielectric elastomer transducers (DET) offer many advantages over conventional electro-mechanical drives due to their high energy efficiency, low weight and simultaneous usability as actuator and sensor. This dissertation focuses on the use of DEs as multifunctional elements, to develop fundamentally new and inventive systems for human interaction.

Through the developed advanced control of a single DET device, different structural resonance ranges of DETs are stimulated and experimentally validated. With the investigated and characterised new operating principle of DETs, multifunctional elements with tactile and simultaneous acoustic feedback, as well as input detection capabilities, are realised the first time. With this innovative principle, a lean and highly integrated audio-tactile feedback unit with self-sensing capability is developed in a systematic optimization process. This enables the extension of sensor and pure haptic systems by multifunctional interaction.

The developed elements, principles, processes and manufacturing methods are systematically described and experimentally validated. The sensor and actuator properties of the developed multifunctional systems as well as their applicability in many application areas, are identified and validated by methodical measurements and subject surveys.

In summary, innovative and systematic concepts and application-oriented solutions for DET-based user interfaces, as assistance tools and smart textile integrated composite systems, are developed.

Kurzfassung

Dielektrische Elastomere (DE) bieten durch ihre hohe Energieeffizienz, ihr geringes Gewicht und ihre gleichzeitige Verwendbarkeit als Aktor und Sensor viele Vorteile gegenüber herkömmlichen elektromechanischen Antrieben. Diese Dissertation konzentriert sich auf die Verwendung von DEs als multifunktionale Elemente, um grundlegend neue und innovative Systeme für die menschliche Interaktion zu entwickeln.

Durch die entwickelte erweiterte Ansteuerung eines einzelnen DE-Elements, werden verschiedene strukturelle Resonanzbereiche von DEs angeregt und experimentell validiert. Mit dem untersuchten und charakterisierten neuen Funktionsprinzip von DEs werden erstmals multifunktionale Elemente mit taktiler und gleichzeitiger akustischer Rückmeldung, sowie Eingabeerfassungsmöglichkeiten realisiert. Mit diesem innovativen Prinzip wird in einem systematischen Optimierungsprozess eine schlanke und hochintegrierte audio-taktile Feedback-Einheit mit Self-Sensing-Fähigkeit entwickelt. Dies ermöglicht die Erweiterung von sensorischen und rein haptischen Systemen um eine multifunktionale Interaktionsebene.

Die entwickelten Elemente, Prinzipien, Prozesse und Fertigungsmethoden werden systematisch beschrieben und experimentell validiert. Die sensorischen und aktorischen Eigenschaften der entwickelten multifunktionalen Systeme, sowie deren Anwendbarkeit in vielen Anwendungsbereichen, werden vorgestellt und durch methodische Messungen und Probandenbefragungen validiert.

Zusammenfassend werden innovative und systematische Konzepte und anwendungsorientierte Lösungen für DE-basierte Benutzerschnittstellen als Assistenzwerkzeuge und intelligente textile Verbundsysteme entwickelt.

Table of Contents

ACKNOWLEDGMENTS	I
ABSTRACT	VII
KURZFASSUNG	IX
TABLE OF CONTENTS	XI
1. INTRODUCTION	1
1.1.MOTIVATION	2
1.2.RESEARCH OBJECTIVE AND THESIS STRUCTURE	4
1.3.STATE OF THE ART.....	7
1.3.1. DIELECTRIC ELASTOMER TRANSDUCERS.....	8
1.3.2. TEXTILE INTEGRATED SENSOR AND ACTUATOR SOLUTIONS.....	10
1.3.3. HUMAN-COMPUTER ASSISTANCE TOOLS.....	12
2. FUNDAMENTALS	13
2.1.DIELECTRIC ELASTOMERS.....	13
2.1.1. ELECTROMECHANICAL WORKING PRINCIPLE	13
2.1.2. DE MANUFACTURING.....	24
2.1.3. DE CHARACTERIZATION.....	26
2.1.4. DE ELEMENT DESIGN AND STRUCTURE	29
2.2.HUMAN PERCEPTION	30
2.2.1. HUMAN ANATOMY – SENSORY NERVOUS SYSTEM	31
2.2.2. HAPTIC	31
2.2.3. ACOUSTIC.....	35
2.3.SYSTEM ARCHITECTURE DESIGN OF DET BASED USER-INTERACTION INTERFACES	37
2.3.1. DESIGN AND STRUCTURE OF USER-INTERACTION INTERFACES.....	38
2.3.2. DE BASED USER-INTERFACE DESIGN	40
3. AUDIO-TACTILE MULTI-MODE DET DEVELOPMENT	48
3.1.BASIC STRUCTURE OF THE DET FEEDBACK-ELEMENT	48
3.1.1. DET FEEDBACK-ELEMENT TOPOLOGY	48
3.1.2. SENSING STRUCTURE OF THE DET FEEDBACK-ELEMENT.....	53
3.1.3. TACTILE FEEDBACK DET.....	58
3.2.AUDIO-TACTILE FEEDBACK DET	62
3.2.1. ACOUSTIC RESPONSE DET MEMBRANE VIBRATION	64
3.2.2. AUDIO-TACTILE ELEMENT PRINCIPLE AND DEVELOPMENT.....	78
3.2.3. CONTROL AND DESIGN OF A MULTI-MODE AUDIO-TACTILE ELEMENT	81
3.2.4. EXPERIMENTAL RESULTS.....	84
3.3.COMPACT HOUSING AND CUSTOM HIGH-VOLTAGE ELECTRONIC	99
3.3.1. PROTOTYPE DESIGN	99
3.3.2. EXPERIMENTAL RESULTS.....	101
3.4.SELF-SENSING APPROACH FOR AUDIO-TACTILE ELEMENTS.....	105
3.4.1. CHARACTERIZATION OF MULTI-MODE DEA SELF-SENSING.....	110
3.4.2. EXPERIMENTAL RESULTS.....	116
3.5.TEXTILE INTEGRATED AUDIO-TACTILE ELEMENTS	122
3.5.1. DESIGN OF TEXTILE INTEGRATED AUDIO-TACTILE ELEMENTS	123
3.5.2. EXPERIMENTAL RESULTS.....	128

4. APPLICATION EXAMPLES, CONCLUSION & OUTLOOK	137
4.1.APPLICATION EXAMPLES.....	137
4.2.CONCLUSION.....	141
4.3.FUTURE DEVELOPMENT	141
REFERENCES.....	CXLIII
LIST OF APPENDICES.....	CLXIV
APPENDIX.....	CLXV
LIST OF TABLES.....	CLXXXII
LIST OF EQUATIONS.....	CLXXXIII
LIST OF FIGURES.....	CLXXXV
LIST OF ABBREVIATIONS AND ACRONYMS.....	CXCIII
LIST OF SYMBOLS	CXCIV
CURRICULUM VITAE	CXCV
PUBLICATIONS.....	CXCVI

1. Introduction

The need of communication and assistance tools for human interaction with digital components, gets more and more important. In many fields, like industry applications, help for aged and disabled people or virtual and augmented reality, as well as sports and entertainment, an intuitive and inconvenient communication tool is needed. The multifunctional elements, developed and considered in this thesis combine sensory, tactile, acoustic and self-sensing capabilities in a single element and are thus predestined for use in wearable and integrated communication elements. Especially in the industry environment, assistance tools for the human-machine interaction are important. To motivate the need of multifunctional assistance tools, their use in the industry environment is focused in the introduction. The specifications and boundary conditions also apply in a similar way to the other areas of applications mentioned.

The "digital transformation" is increasingly getting more important and being discussed in politics, business, society as well as science. The manufacturing sector is considered one of the most employment- and export-intensive industries in Germany. In 2022, just over 8 million people were employed in the 5 most important industrial sectors alone (automotive engineering, mechanical and plant engineering, chemicals, food and electrical engineering) and over 2.5 trillion euros were generated in this sector ([1], [2]).

With the fourth industrial revolution (see Figure 1.1) the tasks and demands on humans will change significantly and support systems for data processing, training and qualification will be required. The forecasts range from the loss of many jobs to strong economic growth in the industrial sector. However, the requirements in the digitalized industry will become more and more complex, so that flat, light and integrated assistance tools for worker support are needed. The world of work is already being transformed by digitization, and people must cope with many new demands. Nevertheless, "The Human remain at the centre of Industry 4.0. [and] the qualification of employees will therefore become even more important in the future" (cf. Deputy General Manager of the VDMA¹). The main vision of an "operator 4.0" is to create a symbiotic relationship between humans and automation, by integrating adaptive communication elements. This initiative aims to transform the landscape of industrial work by introducing new interaction methods that will improve the efficiency and effectiveness of human-automation interaction. The development of user interfaces, which have a significant impact on users, is a key part of this research area ([3], [4], [5], [6], [7]). The human will stay in this case in the centre of the production process, as self-organized supervisor of the production strategy and last decision-making instance ([8], [9]).

As the communication with machines and robots get more and more important, also sensing of human expression and feedback to the human is of utmost interest. Especially the use of intelligent materials with intrinsic transduction properties, like shape-memory-alloys (SMAs) or electroactive polymers (EAPs), are well suitable for wearable and flexible applications. Furthermore, EAPs

¹ Verband Deutscher Maschinen- und Anlagenbau - German Engineering Federation

and especially dielectric elastomers (DEs) are a suitable solution for textile integrated applications and user interfaces.

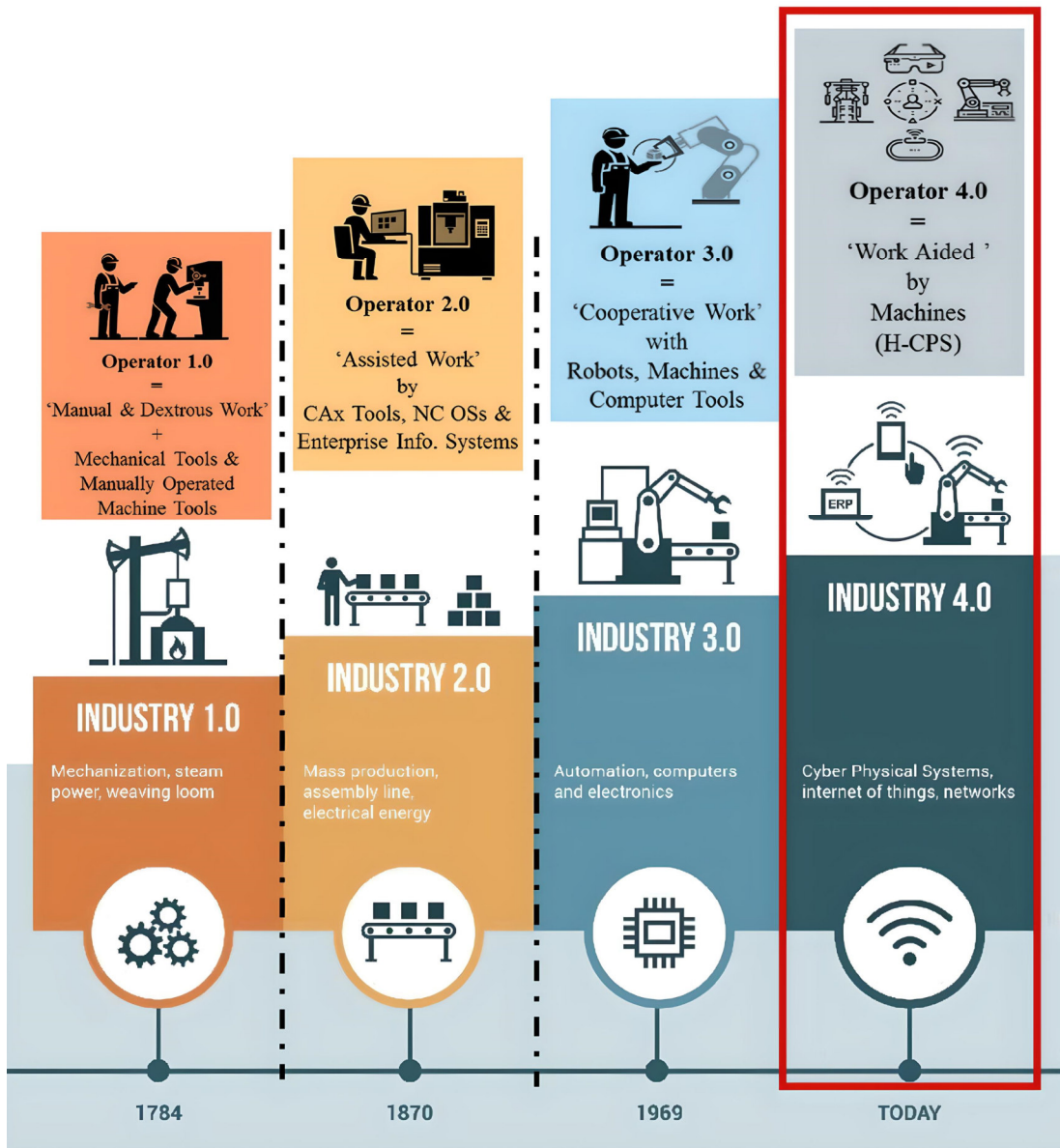


Figure 1.1: Evolution of industry production and the different operator generations from first industry level to the actual industry environment with cyber physical systems (cf. [6], [10], [11]).

Besides the industry environment many other application fields need and benefit from multifunctional integrated feedback solutions (see chapter 4.1). The development presented is particularly suitable for interaction with the user on different levels of perception. The multi-functional interaction leads to a more intuitive and efficient use of computers, robots and machinery.

1.1. Motivation

To advance digitalization in the industry 4.0 environment and increase the use of handling devices and robots in production, assistance tools for worker support are of great interest. Besides that, the digitisation through all social, economic and societal structures is strongly growing. The further development and realisation of textile-integrated and slender build interaction elements is of high interest. The requirements for these elements are similar for the different application areas.

However, the industrial sector gives quiet clear needs and is a predestined application field for assistance tools. For this reason, the industrial application area is discussed below.

The complexity and fine-tuning of individual production steps make intuitive, ergonomic, cost-efficient and flexible support for employees essential in modern industry. In view of the increasing human-machine interaction (HMI), there is a necessity for straightforward and 'lean' assistance tools, for communication with and support of the operator. Two of the four main pillars of Industry 4.0 (mobile availability, big data capability, networking, human-machine-interaction) can be improved by smart, especially textile-integrated, assistance tools. In Figure 1.2 the main pillars of the digital industry and the focus fields for assistance tools are shown. Especially the HMI is a field with a need for highly integrated and multi-mode capable light weight, energy saving actuator and sensor solutions.

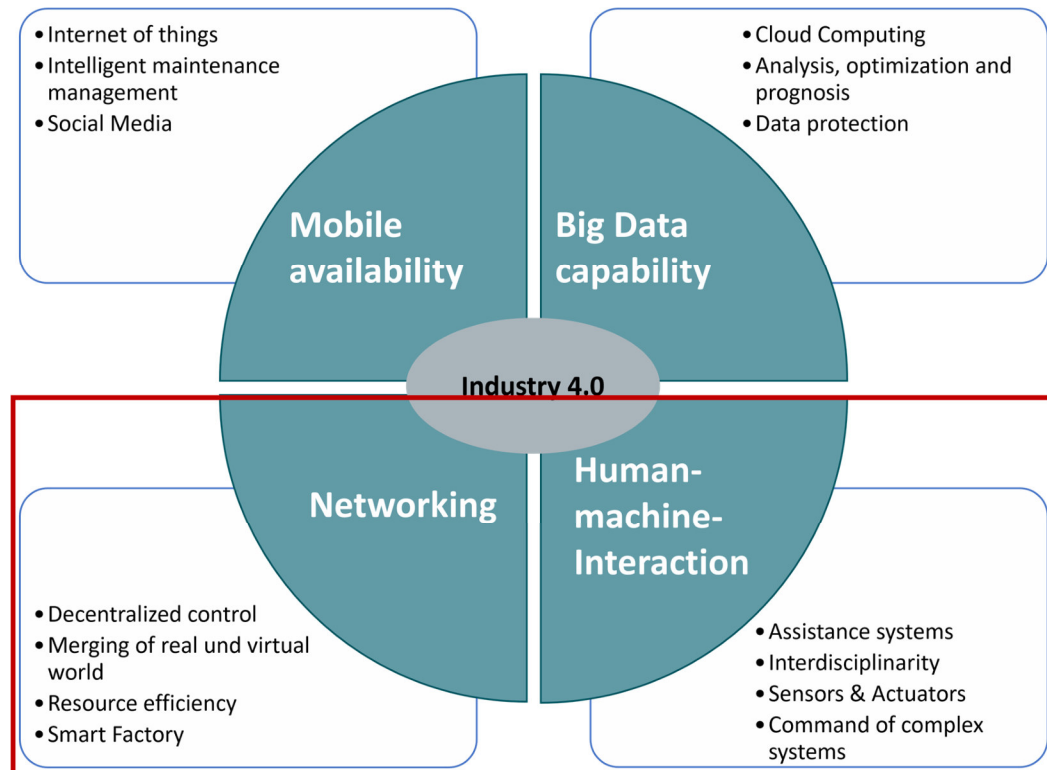


Figure 1.2: Main pillars of Industry 4.0. The developed elements are intended to improve the realization of the human-machine-interaction and the networking pillars (red marked).

Intelligent materials, and in particular dielectric elastomer transducers (DET) are, due to their properties, predestined for these applications. The ability to use DEs as sensors and actuators, even in different multi-mode and multi-frequency ranges, makes them ideal for wearable applications and intuitive feedback units. Current assistance tools have often the drawback, that they are relatively bulky, heavy and have just very specific application areas, like visualisation, safety monitoring or communication.

As already mentioned, the operator in a modern industry environment must deal with many different challenges. Mainly the communication and interaction with assets, like robots or handling devises, and the high information density, leads to a high stress level of the operator. With smart assistance tools, the operator can be supported and a lower physical and emotional burden, with higher efficiency at the same time, can be achieved (see Figure 1.3). The main goals of the

assistance tools are sensing of the operator and the direct surrounding environment, as well as the intuitive interaction with the operator via, for example, haptic or acoustic feedback. The implementation of intelligent, multifunctional assistance tools has the potential to engender further improvements. These improvements include quality and ergonomic control during the manufacturing, documentation and training during normal workflow, and intuitive communication. Beside the industry application many other application fields for the use of smart assistive tools have important impact. In Figure 1.3 two application examples are described closer (industry environment and help for elderly / disabled people), to show the main advantages of multi-functional assistance tools.

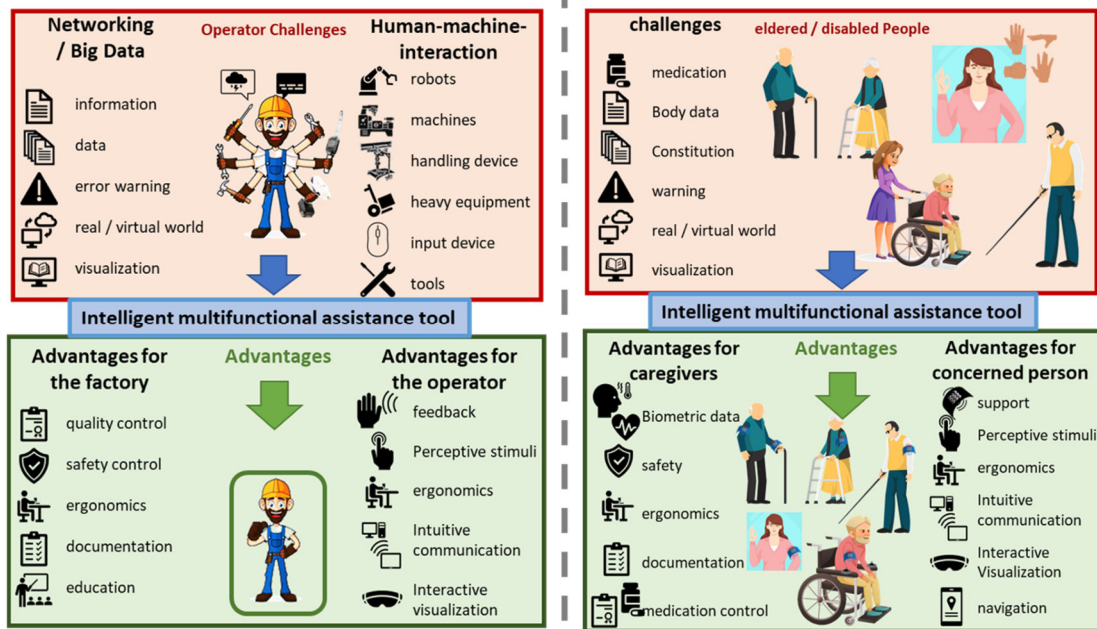


Figure 1.3: Challenges for industry operator (left) and elderly / disabled people (right) and advantages of intelligent assistance tools. With the multifunctional, audio-tactile feedback element the user can be supported by the direct interaction with the (digital) surrounding.

1.2. Research objective and thesis structure

The main goal of the present work is the development of innovative multi-functional sensor and actuator elements for user interaction. The area of recording user input, force or movement as well as tactile and acoustic feedback is of main interest. The development of flexible and textile integrable elements as well as flexible frames and electronics are important, to provide reliable and complete solutions. Based on the already known functional modes of the DET, pure sensors and low-frequency actuators are considered as state of the art in DE-based flexible wearable devices. As an extension of this state of the art applications, the primary objective is to expand the basic functionalities (e.g. sensing), to include frequency-adapted tactile and high-frequency acoustic feedback solutions. In combination with adapted control applications, all three functions can be stimulated and controlled simultaneously. This makes it possible to create a multifunctional, self-sensing capable interaction system.

Dielectric elastomers are considered in detail in many different scientific publications and papers (e.g. [12], [13], [14], [15], [16], [17], [18]). The continuous development of DEs is of scientific interest to realize alternative electro-mechanical converters for energy saving and in multi-

functional systems. Specifically, textile integration (e.g. [19], [20], [21]) and user interfaces ([19], [22], [23], [24]) are of great interest for the application of dielectric elastomers, beyond purely scientific considerations.

Motivated by the growing interest on dielectric elastomer actuator (DEA) systems, dielectric elastomer sensor (DES) systems and their combination for smart, multi-task industry-oriented applications, the development of multi-functional DET elements is the key objective. The primary aim of this thesis is to develop systems and methods to provide:

- **Multi-mode DET actuator and sensor elements:** The central point of the dissertation is the development of DET elements with multiple intrinsic functional modes, to realise small interaction units with wide sensor and actuator properties. In particular, the actuators can be controlled intelligently to cover several different operating ranges and thus, for example, simultaneously stimulate several feedback mechanisms. Additionally, the self-sensing capability of DETs is investigated and the combination with multi-mode actuation is validated, to integrate sensing and multi-mode actuation simultaneously. The researched multi-mode self-sensing working principle achieves an even higher degree of multi-feature usability of individual DE elements, with low electronic and peripheral expenditure.
- **Electronic design for multifunctional DET:** Textile integrable sensing electronics and high voltage electronics are developed and validated for the use of multifunctional DET devices. In addition, microcontrollers, communication units and batteries are integrated together, to ensure a completely self-sufficient system design.
- **Validation setup for multifunctional DE sensor and actuator elements:** Beside developing different system structures and manufacturing processes for multifunctional DETs, test setups to characterise the elements and validate their functional performance are built. The input signals for actuators are provided by different kind of digital-analog-converter (DAC) systems and output data is measured by data acquisition systems and analog-digital-converters (ADCs). The measurement setups were specially adapted to the respective geometrical and physical structures of the integrated textiles and the DET elements.
- **Textile integration of multifunctional DETs:** There are already solutions for DE sensor and partly also actuator solutions for human interaction. One task of this elaboration is to demonstrate an inherent textile integration and manufacturing process for integrated actuator-sensor elements. A manufacturing process to incorporate the textile integration process into the manufacturing process of the DEs is developed. In addition, the integration of the electronics and communication structure is also an important component dealt with in this work. With this step the investigated multifunctional DET elements can be directly integrated in textiles to develop high integrated smart-textile solutions for user feedback, based on DETs.

The thesis is structured in several under-chapters which include the following:

Chapter 2 gives an introduction into the working principle of DEs, the manufacturing, characterisation and textile integration of the DE Elements. In addition, a fundamental insight into human perception is provided, with particular reference to tactile and acoustic perception. The necessary force, deflection and sound pressure required to overcome human thresholds are outlined. Additionally, the system architecture and the design process for developing smart multi-functional

assistance tools based on DEs are shown. The communication and data processing systematic for interaction elements is described.

Chapter 3 describes the working principle of multi-functional DE based audio tactile elements. The fundamental development of this work is the realisation of simultaneous usability of different working modes of DETs. By incorporating multi-frequency excitation input signals, low-frequency and high-frequency components can be used, to simultaneously generate haptic and acoustic feedback. The intensity, frequency and shape of the two excitations can be separately adjusted. With the use of sensing and especially self-sensing capability of DEs a highly integrated multi-functional system is developed and validated with systematic measurements. Furthermore, user tests are performed to validate the usability of the system in real applications. Additionally, textile integrated prototypes are developed and validated.

Chapter 4 shows specific application examples of the developed multi-mode DE based actuators. Various assistance tool development examples, with integrated DEs, are explained for different use cases. The DEs can be used as sensors, actuators and multi-functional elements, depending on the application area and the feasibility of implementation. After showing the application examples, the thesis results are summarized and a presentation of the potential further development of the user interface based on DE elements are concluded. An outlook on further development and research topics is given.

Peer-reviewed journal articles, book chapters and patents:

			Role	IF	status
1	Title	A Multi-Mode, Multi-Frequency Dielectric Elastomer Actuator	First Author	19.9	published
	Authors	Sebastian Gratz-Kelly , Gianluca Rizzello, Marco Fontana, Stefan Seelecke, Giacomo Moretti			
	journal	Advanced functional materials, Wiley-VCH, 2022			
2	Title	A tri-modal dielectric elastomer actuator integrating linear actuation, sound generation, and self-sensing capability	First Author	4.6	published
	Authors	Sebastian Gratz-Kelly , Tim Krüger, Stefan Seelecke, Gianluca Rizzello, Giacomo Moretti			
	journal	Sensors and Actuators A: Physical, Elsevier, 2024			
3	Title	An audio-tactile interface based on dielectric elastomer actuators	First Author	4.1	published
	Authors	Sebastian Gratz-Kelly , Tim Krüger, Gianluca Rizzello, Stefan Seelecke and Giacomo Moretti			
	journal	Smart Materials and Structures, IOPscience, 2023			
4	Title	Optimized Sensor-Array based on metal sputtered dielectric elastomers for integrated user interaction	First Author	3.1	published
	Authors	Sebastian Gratz-Kelly , Mario Cerino, Daniel Philippi, Dirk Göttel, Günther Schultes, John Heppe and Paul Motzki			
	journal	Materials, MDPI, 2024			
5	Title	Gesture and force sensing based on dielectric elastomers for an intelligent glove in the digital production	First Author	1.0	published
	Authors	Sebastian Gratz-Kelly , Daniel Philippi, Betina Fasolt, Sophie Nalbach, Paul Motzki			

	journal	Measurement technology – methods, sensors, systems, and applications, De Gruyter, 2024			
6	Title	Ensemble Learning Approach for Advanced Predictive Modelling of Biometric Data and Action States with Smart Sensing	Second Author	3.4	published
	Authors	Tajbeed A. Chowdhury, Sebastian Gratz-Kelly , Eric Wagner, Paul Motzki and Martina Lehser			
	journal	IEEE Access, 2024			
7	Title	An experimental parametric analysis of the acoustic response in dielectric elastomer loudspeakers	Second Author	2.3	published
	Authors	Saverio Addario, Sebastian Gratz-Kelly , Gianluca Rizzello, David Naso, Giacomo Moretti			
	journal	Journal of Vibration and Control, Sage Journals, 2024			
8	Title	Concept studies and application development of textile integrated dielectric elastomer sensors for smart shoe technologies	Second Author	1.0	published
	Authors	Andreas Meyer, Martin Wagner, Sebastian Gratz-Kelly , Sophie Nalbach, Paul Motzki			
	journal	Measurement technology – methods, sensors, systems, and applications, De Gruyter			
9	Title	Textilbasierte Assistenzsysteme auf Basis intelligenter Materialien: Effizienzsteigerung in der Kühlmittelpumpenmontage	Author	-	under review
	Authors	Sebastian Gratz-Kelly , Paul Motzki			
	Book	Assistenzsysteme für die Produktion, Carl Hanser Verlag GmbH			
10	Title	Textilbasierte Assistenzsysteme	Author	-	under review
	Authors	Sebastian Gratz-Kelly , Tajbeed Chowdhury, Paul Motzki			
	Book	Assistenzsysteme für die Produktion, Carl Hanser Verlag GmbH			
11	Title	Audio-Tactile transducer device based on dielectric electro-active elastomers - patent	Inventor	-	published
	Authors	Giacomo Moretti, Sebastian Gratz-Kelly , Marco Fontana, Paul Motzki, Gianluca Rizzello, Stefan Seelecke			

1.3. State of the art

The basic functionalities of DETs can be divided into sensor, actuator and generator working principle. In the following, a selection of literature is shown that illustrates the applications of DEs in the sensor and actuator field. Based on these two basic functionalities of DETs, a further level of multifunctionality is developed in this thesis. The only state-of-the-art concept that provides multifunctionality for DEs is self-sensing, where simultaneous activation and sensing of the DE element is possible. An overview of the self-sensing literature is given in section 1.3.1.3.

Building on the basic DE applications, textile-integrated sensor and actuator solutions as well as feedback elements are additionally presented, as representatives of interaction elements. The focus will be on the general textile integration of sensors and actuators (1.3.2.1), the integration of DE-based elements (1.3.2.2) and specifically DE-based haptic elements and loudspeakers (1.3.1.4). In addition, human-computer interaction assistance tools are supplementary considered.

1.3.1. Dielectric elastomer transducers

1.3.1.1. Dielectric elastomer transducers as sensors

DE sensors (DES) can be used in different applications. Mainly the use as force sensors is focused in the literature, as DETs are, due to their high stretchability, directly suitable for the use as strain sensors. To develop strain sensors mainly the manufacturing process (e.g. [25], [26], [27], [28], [29]), the integration and the electronic development (e.g. [30], [31], [32]) is scientifically of interest. The single sensor working principle itself is straight forward and only of quiet low scientific interest, in contrast to more complex sensor systems (e.g. sensor arrays and multi sensor solutions).

Beside the application of stretch sensing, DEs can be used as force or pressure sensors. Due to the very low thickness of the DE film, the direct force applied to the DE membrane need to be very high to measure a realisable capacitance change. Consequently, further developments are required for the use of DETs as force sensors. In [33] the pressure inside a polymeric tube can be measured by an outer DES membrane applied to the tube. By adding a 3-dimensional structure to the DE electrode [34] shows, that a force applied to the structure can be measured by the DES. In [35] and [36] a sensor array is developed and characterised. This development enabled the recalculation of the localisation of the applied force on the DE membrane. In [37] a sensor array is realised by stacking 4 DES-layers with different geometries and measuring each overlapping capacitance to detect the pressed sensor area. In [38] a force sensor is realised by using lithium-chloride solution as electrode. ([39], [40]) developed a multi-axis compressive sensor, based on DEs and ([41], [42]) uses micro pores to realise pressure-sensitive DES. [43] instead uses a multilayer DES with a substrate, to increase the sensitivity. In [44] a 6-axis force/torque sensor is developed.

1.3.1.2. Dielectric elastomer transducers as actuators

DE actuators (DEA) are used in many different application fields. For an overview of the main fields in which DEAs are used in the literature, some publications are listed in the following. In [45] and [46] general applications of DEAs are shown and compared. One main application field for DEAs are soft-robotic use-cases. For soft-robotic applications different review papers ([47], [48], [49], [50], [51]) and many research papers are published (e.g. [52], [53], [54]). A similar application of DE actuators are artificial muscles like shown in [55] which can be also used as robotic muscles [56]. Another application field of DEA systems are high frequency actuators ([57], [58], [59]) and the controlling of vibrations at high frequency [60]. DEAs can be used for direct linear actuation ([61], [62]) as well as for more complex movements, like for three and two dimensional soft grippers ([63], [64], [65], [66], [67]), pneumatically supported grippers [65] and suction cup grippers ([68], [69]). Dielectric elastomers are particularly suitable for pumps, due to their flexible and high-frequency controllability. There are applications for micropumps ([70], [71]), fluid pumps ([72], [73]), pneumatic pumps [74] and stretchable soft pumps ([75], [76], [77]). Additionally, DEAs can be used as valves ([78], [79], [80], [81]) and for contactors ([82], [83]). A further very important application of DEAs are haptic and tactile elements and textile integrated feedback elements, some examples are shown in section 1.3.2.1 - Conventional textile integrated sensor and actuator solutions and 1.3.2.2 - EAP based textile integrated Elements.

1.3.1.3. Self-sensing applications of DETs

In the state of the art, DETs are only used multifunctionally due to the self-sensing effect. [84] proved that the functional principle of self-sensing for DEAs works. In [85] the self-sensing effect is used to realise stiffness control of dielectric elastomer actuator based soft robots. In different papers, the self-sensing is used to operate DEAs in close looped control ([86], [87], [88], [89]). The self-sensing algorithms are differentially realised, by models [90], online estimation algorithms [90], [91] or neural networks [92], [93] for example.

With the presented work a complete new multi-functionality of DEAs is developed, which is not included in recent literature. The self-sensing capability can additionally be integrated into the range of functions of the here developed DE actuators, which is presented in section 3.4.

1.3.1.4. DET based haptic and acoustic feedback

Beside specific separated sensors and actuators, general architectures of haptic elements and loudspeakers based on DETs have already been described [18]. In Figure 1.4 exemplative pictures of, in literature developed, loudspeakers and haptic feedback prototypes are shown.

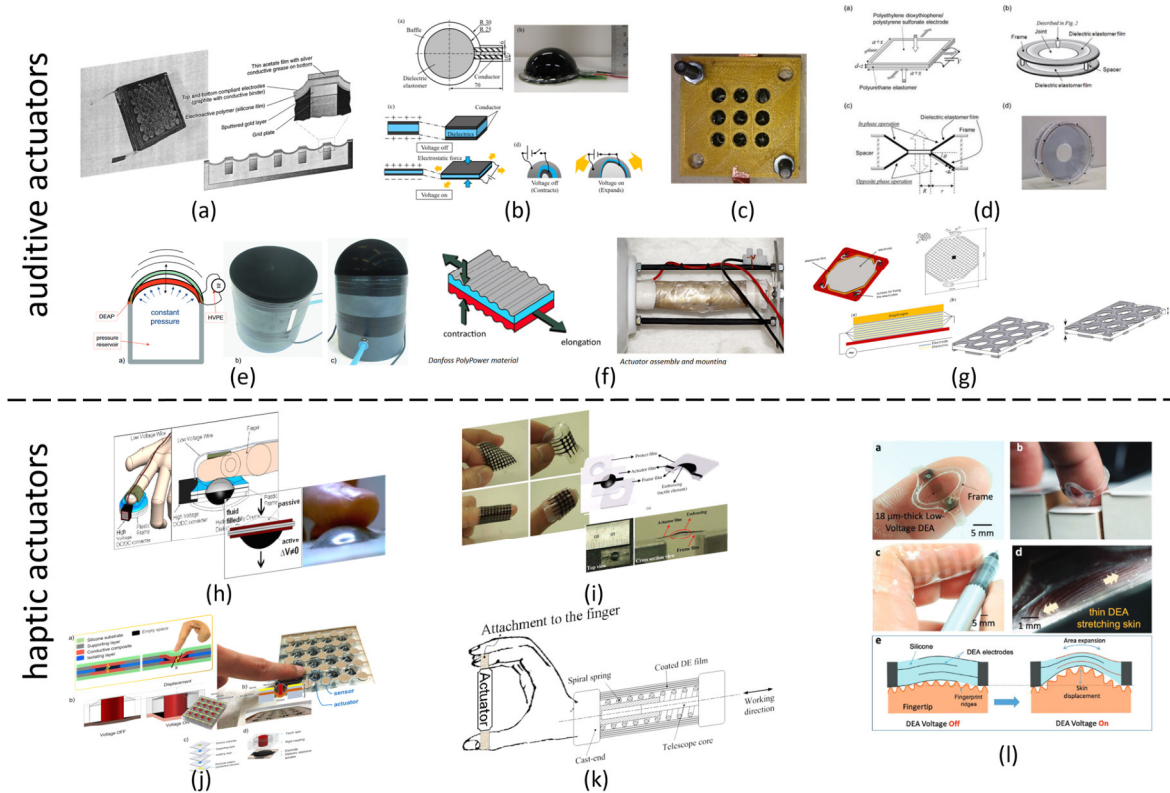


Figure 1.4: Exemplative EAP based loudspeakers and haptic transducers ((a) [94]; (b) [95]; (c) [96]; (d) [97]; (e) [98]; (f) [99]; (g) [100]; (h) [101]; (i) ([102], [103]); (j) [104]; (k) ([105], [106]); (l) [107]).

The development of DET-based loudspeaker is advanced by the SRI international (Stanford Research Institute) of the Stanford university [94], [108]. The Fraunhofer institute with the technical university Dresden developed a loudspeaker driven by a core-free rolled DEA [99]. The chair of Elektromechanische Konstruktionen of the Technical University Berlin lead by Jürgen

Maas studied the acoustic performance of buckling DEA transducers [96], [98], [109] and the chair of Mikrotechnik und Elektromechanische Systeme from Technical University of Darmstadt showed an alternative design concept of a DEA-loudspeaker and customized electronic [110]. Furthermore, [97] showed an antagonistic structure based DE loudspeaker and in [100] a flat stacked DE structure is characterised. Additionally, in [95] a hemispherical preloaded dielectric elastomer loudspeaker is developed.

In the literature, EAP based haptic and mainly tactile elements are developed by different researchers and research institutes. For example, a fluidic preloaded haptic transducer is developed by researcher from research centre E.Piaggio at the University of Pisa [101]. The Sungkyunkwan University of South Korea developed a soft actuator-based microarray and a haptic display with sensing capability ([102], [103], [104]). In [111] a piezoelectric device for tactile rendering is shown, ([105], [106]) are using rolled actuators to provide force-feedback developed by the Swiss federal laboratories for materials. The école polytechnique federal de Lausanne (EPFL) developed low voltage supplied haptic transducers, described in [107].

Several works, in the past, exploited the dynamic behaviour of DEAs (e.g., resonant behaviours) to enhance the actuation performance [112]. Among others, Shresta et al. [113], developed a transparent resonating-cavity sound absorber, whose absorption bandwidth can be tuned changing the voltage of a microperforated wall made of DEs. Linnebach et al. [114], used the mechanical resonance of a cone DEA, to maximize the continuum flow delivered by a fluidic actuator driven by the DEA and a coupled of check valves. Cao et al.[115], developed a wing mechanism capable of flapping strokes over 30° driven by a resonant double-cone DEA. At the same time, other works investigated the high-frequency continuum dynamics and modal response of DE membranes and identified potential applications in the fields of morphing optics, conveyors, and vibration control ([116], [117], [118], [119]). However, the present work represents the first attempt to concurrently exploit different eigenmodes of a same DE membrane, to produce multiple outputs, and it is the first work in which multiple actuation outputs are achieved via a single functional DE unit, which is protected by a patent [120].

1.3.2. Textile integrated sensor and actuator solutions

1.3.2.1. Conventional textile integrated sensor and actuator solutions

The general integration of smart sensors and actuators as well as smart elements is compared and described in different review papers. A range of applications is considered, including vibrotactile feedback, skin stretch or kinaesthetic feedback, artificial muscles and therapeutic compression. The elements are compared and evaluated in terms of their textile integration capabilities and working principles ([21], [121], [122]). A further important aspect for textile integrated and wearable systems are the integration of electronic and microelectronic systems into the garments [123]. Especially for sensing applications, in actual research, many further systems and technologies are included into textiles, including pressure, humidity, wetness or spectroscopy sensors ([124], [125]). A wide variety of energy harvesting and accumulation methods, as well as the use of the accumulated energy, for textile integrated functional materials, are shown in [126].

1.3.2.2. EAP based textile integrated Elements

More specifically, in literature textile-integrated and wearable EAP based sensors and actuators are presented and compared ([127], [128]). In Figure 1.5 exemplative pictures of, in literature developed, textile integrated prototypes are shown.

Different scientific institutes in the field of electro active polymers contribute to textile integrated sensor and actuator systems. A significant number of institutes have published various integrated sensor-based textiles. For instance, the Biomedical Engineering chair at the Department of Industrial Engineering, University of Florence, led by Federico Carpi, has developed biomonitoring textiles ([129], [130]). The biometrics laboratory of the Auckland bioengineering Institute led by Iain Anderson ([131], [132], [133]) showed the monitoring of human kinematics through highly stretchable strip shape DE sensors, integrated into or onto garments. The Harvard's micro robotics laboratory lead by Robert J. Wood [134] developed textile-based stretch sensors. The Kyushu Institute of Technology under Tom Shibata [135] developed integrated motion capturing. Furthermore, flexible and textile integrated actuator structures are developed and published by different institutes, like hydraulically preloaded electrostatic wearables by the soft transducers lab of the EPFL lead by Herbert Shea [23] and haptic communicators by the mentioned micro robotics laboratory of Harvard University ([19], [20]).

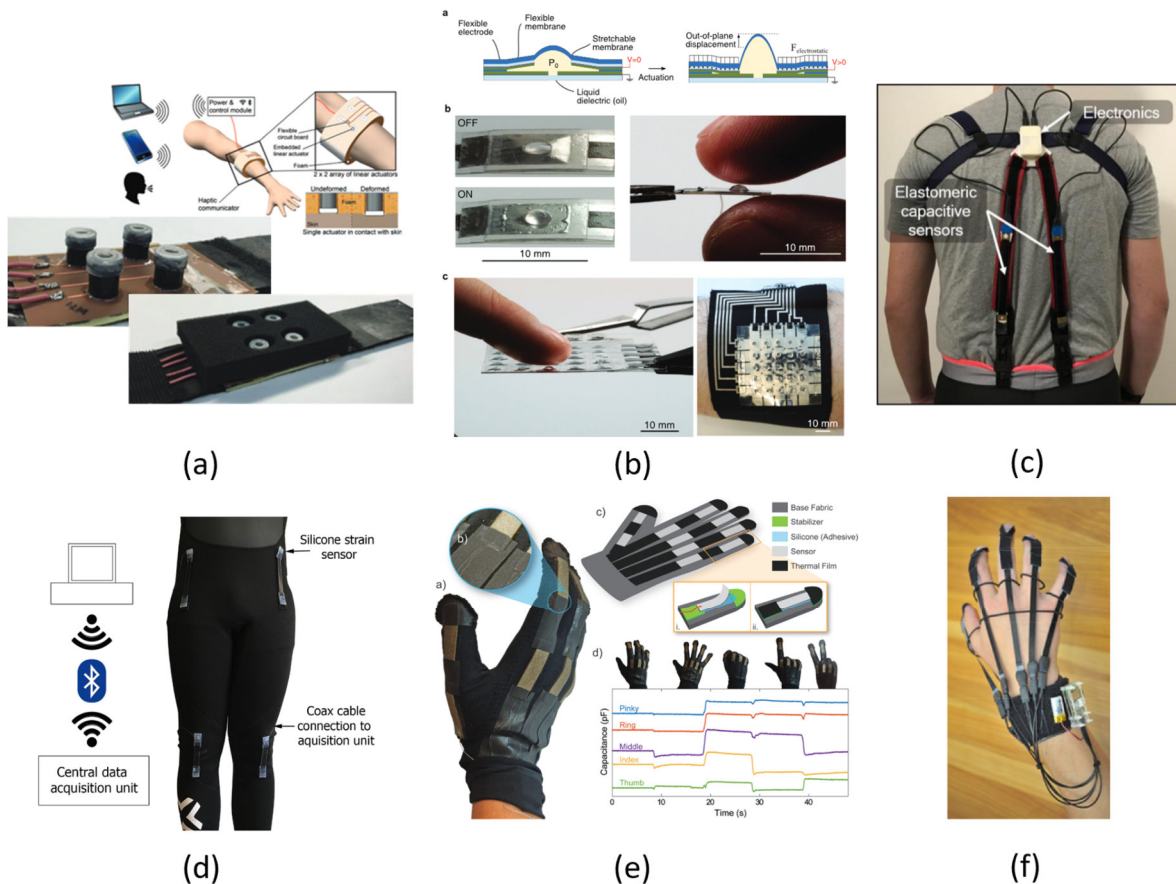


Figure 1.5: Exemplative EAP based textile integrated elements ((a) [19]; (b) [23]; (c) [129]; (d) [131]; (e) [134]; (f) [132]).

1.3.3. Human-computer assistance tools

In the literature assistance tools for many different areas, like industry and manual assembly [136], [137], [138], health care [139], [140], [141], sport and movement [142], [143], [144] as well as support for elderly people [145], [146] are under investigation.

The HMI sector has already, since almost two decades, a high impact to the science and economy [147]. One specific application area are textile integrated sensor and actuator systems. In appendix A.1 exemplative different solutions for a smart glove as one possible HMI assistance tool are shown. Only the solutions for this sub-area of human assistance tools have already over 50 products which are in a development state. This shows the high interest in that area and the potential of further development of actual solutions. It is evident that only a limited number of the solutions under consideration incorporate sensors and actuators. However, none of these solutions are characterised by a combined and integrated approach for sensor-actuator systems..

This treatise proves that DE technology enables multi-functional integrated solutions. Sensor, actuator and loudspeaker abilities are integrated in one element. The literature examples present the broad range of applications, as well as the scientific and technological interest. Many more examples, prototypes and devices can be found in the literature and may be under investigation. The examples shown serve to illustrate and clarify the most important development areas and application fields.

In comparison to all realisations here presented and further developments in current literature, the multifunctionality, which is achievable with DEAs, is a completely new investigation field. The basic developments and characteristics are shown, as well as how the multifunctional DEA elements and the required peripheral systems can be integrated into textile-based feedback and communication elements. While originating from the same background as the above-mentioned works, the presented work adds for the first time simultaneous multifunctionality of smart DE based solutions on top of user interfaces and wearable devices.

2. Fundamentals

Electro active polymers are a class of functional and intelligent materials which respond to an electrical stimulus with a large displacement. EAPs are divided in two main groups, ionic EAPs, where the motion is based on a migration of ions, and electronic EAPs, where the motion is imposed by an attraction of loads due to an electric field.

The ionic EAPs can be divided in several subgroups, ionic polymer gels (IPG), ionic polymer-metal composites (IPMC), conductive polymers (CP), carbon nanotubes (CNT) and electrorheological fluids (ERF) ([148], [149]). Electronic EAPs can be separated in ferroelectric polymers under which electrets can also be counted, electro-strictive graft elastomers, electro-strictive paper, electro-viscoelastic elastomers, liquid-crystal elastomer (LCE) materials and dielectric EAPs ([149], [150]).

The EAP technology gained high research interest with the work of Pelrine and co-workers at the end of the 20th century ([15], [16], [151], [152], [153]), even though W.C. Röntgen already described the principle over 100 years earlier ([154], [155]).

Among the electronic EAPs especially soft dielectric EAPs, also referred to as dielectric elastomers (DEs) (or dielectric elastomer transducers (DET)), show promising functional properties and can be tailored to very different sizes and shapes [156].

2.1. Dielectric Elastomers

As mentioned before DEs are a sub-group of electroactive polymers and are based on an elastic, dielectric polymer (mostly silicone, acrylic, polyurethane or natural rubber) and a compliant electrode (carbon black or metal particle in silicone for example). DEs can work at a high strain rate (up to 300 %) and have a high energy density ($>8\text{MJ}/\text{m}^3$), they are lightweight, mechanical robust, scalable and have a high electro-mechanical coupling efficiency ($>90\%$) ([157], [158]). With these advantages DEs are predestined for wearable and textile integrated applications.

2.1.1. Electromechanical working principle

By applying a voltage between the two compliant electrodes of the DE, the induced electrostatic force compresses the elastic DE membrane in the thickness direction and produces an expansion in the lateral directions. In Figure 2.1 the basic structure and working principle of a DET is shown.

DEs can perform two basic functions, namely actuation and sensing. These two functional principles can be performed with the same DE structure and simultaneously. Furthermore, due to the use of an inverse working characteristic of the DET actuator principle, energy can be generated. The high-voltage actuator signal can be used as sensing signal, enabling the actuator to self-sense (direct measurement of the DE state without using dedicated sensors) the system state.

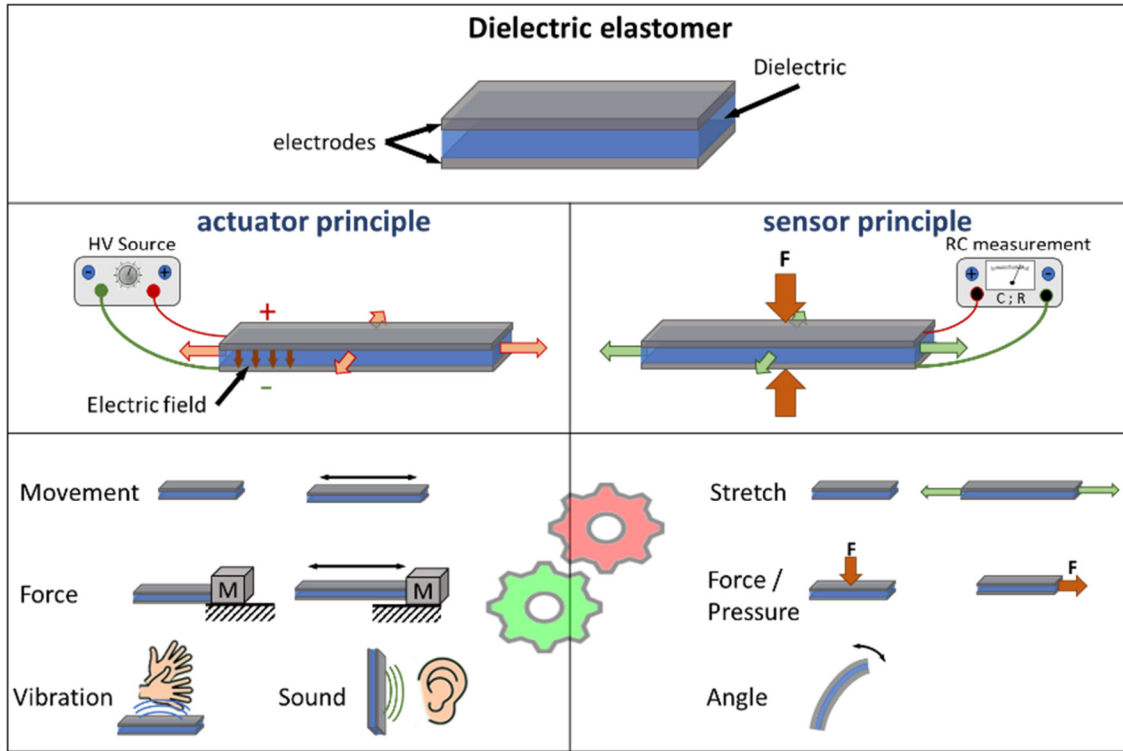


Figure 2.1: Functional principle of DEs as actuator (left) and sensor (right) with application and working fields.

2.1.1.1. Sensor

With the basic structure of the DE in Figure 2.1, by applying an external force or stretch to the DE, the thickness is reduced, and the area of the electrode is increasing. With the increasing of area and the decreasing of thickness, the capacitance C of the DE will increase:

$$C = \varepsilon_0 \cdot \varepsilon_r \cdot \frac{A}{L_z} \quad (2.1)$$

ε_0 is the void permittivity, ε_r is the elastomer relative permittivity (around 2.7 for silicone), A is the area of the electrodes and L_z is the thickness of the dielectric between the electrodes. Due to the incompressibility of the dielectric, the volume of the DE remains constant ($V_i = \lambda_x L_{x,0} \cdot \lambda_y L_{y,0} \cdot \lambda_z L_{z,0}$). For a free space uniaxial deformation in x-direction the deformation can be explained with an equal-biaxial deformation in the yz-plane, resulting in $\lambda_y = \lambda_z$ and equation 2.2 for the capacitance change

$$C(x) = \varepsilon_0 \varepsilon_r \frac{L_x \cdot L_y}{L_z} = \varepsilon_0 \varepsilon_r \cdot \frac{\lambda_y L_{y,0}}{\lambda_z L_{z,0}} \cdot \lambda_x L_{x,0} = \varepsilon_0 \varepsilon_r \frac{A_0}{L_{z,0}} \cdot \lambda_x = C_0 \cdot \lambda_x. \quad (2.2)$$

The capacitance change due to an external force with a clamped specimen can be described with equation 2.3 (for a stretch in x direction and pure-shear kinematics $\lambda_y = 1$)

$$C(x) = \varepsilon_0 \varepsilon_r \frac{L_x \cdot L_y}{L_z} = \varepsilon_0 \varepsilon_r \cdot \frac{L_{y,0}}{\lambda_z L_{z,0}} \cdot \lambda_x L_{x,0} = \varepsilon_0 \varepsilon_r \frac{A_0^2}{V_i} \cdot \lambda_x^2 = C_0 \cdot \lambda_x^2 \quad (2.3)$$

and equation 2.4 for a stretch in thickness direction z, with equal-biaxial deformation in the xy-plane ($\lambda_y = \lambda_x$)

$$C(z) = \varepsilon_0 \varepsilon_r \cdot \lambda_x L_{x,0} \lambda_y L_{y,0} \cdot \frac{1}{\lambda_z L_{z,0}} = \varepsilon_0 \varepsilon_r \frac{V_i}{L_{z,0}^2} \cdot \frac{1}{\lambda_z^2} = C_0 \cdot \frac{1}{\lambda_z^2}. \quad (2.4)$$

The capacitance for a load in x respectively z direction can be qualitative described as shown in Figure 2.2.

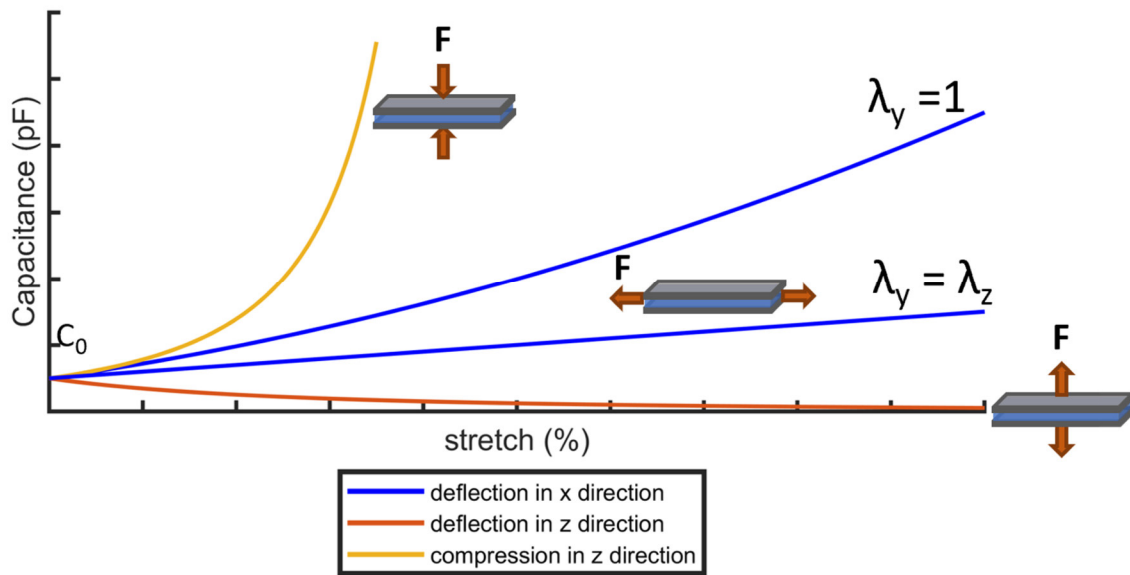


Figure 2.2: Qualitative capacitance changes due to different kind of deformation for an initial capacitance.

For the deformation in x direction the behaviour of the capacitance is influenced by the geometric assumption of the deformation of the DES (see equation 2.2 and 2.3). The relationship between stretch and capacitance depends on the deformation kinematics of the sensor, which in turns depends on the geometry (e.g. aspect ratio), constraints and loading conditions to which the sensor is subjected. Therefore, the real deformation is not linear and in a real case the capacitance change lies between the two described kinematics of pure-shear and uniaxial deformation (by assuming $\lambda_z = 1$ the capacitance would not be influenced by the deformation).

Furthermore, beside geometrical considerations the capacitance of a DE cannot be modelled just by assuming an ideal capacitive behaviour. The relatively high and deformation-dependent resistance of the compliant electrodes influences the electrical behaviour of the DET ([26], [28]). The equivalent circuit diagram of a dielectric elastomer is accordingly, in a simplified way, a capacitance in series with a resistor. The parallel membrane resistor R_p accounts for the DE conductivity of the dielectric. For silicone based DEs, with a thickness of several μm to several 100 μm and dimensions in the centimetre range, the parallel resistance is in the order of several mega ohm and can be neglected, even for relative long actuation cycle times like several seconds. In Figure 2.3 the resulting equivalent circuit of a DE sensor is shown.

The serial resistor of the DE R_s is representing the surface resistance of the flexible electrode and the contact resistance of the electrical connections. The serial resistance for the carbon black electrodes, used in this work, is in the region of several kilo Ohms (for centimetre scale DEs) depending on the geometry and the manufacturing process. The capacitance of an ideal DE can be calculated by the geometry through equation 2.1. Due to the relatively high resistance of the electrode material, a real DE cannot be adequately modelled with a simple RC circuit. The DE must be considered as a transmission line due to the high resistance, rather than as a pure parallel

connection of capacitances. A better representation of the real DE can be achieved by cascading more RC circuits in parallel [159], [160].

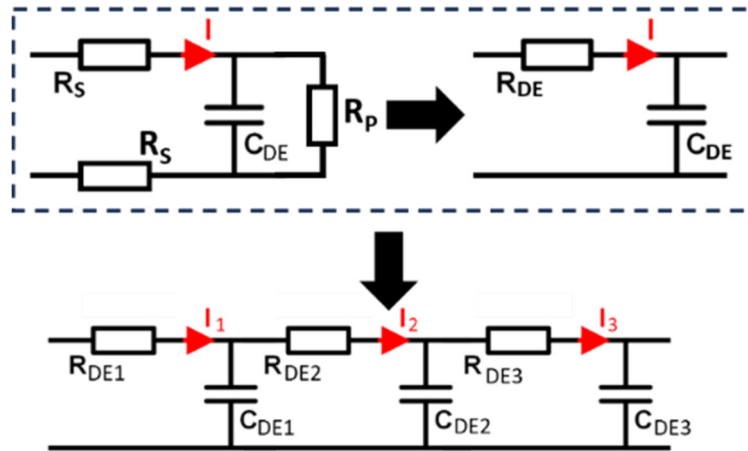


Figure 2.3: Equivalent circuit of DE sensor with a cascade of RC circuits. The parallel resistor is negligible (MOhm range); to reproduce real DEs, a cascade of several series circuits of R and C is necessary.

[159], [160] For a model of 3 RC elements like in Figure 2.3 the impedance can be calculated for symmetric model values ($R_{DE1} = R_{DE2} = R_{DE3}$ and $C_{DE1} = C_{DE2} = C_{DE3}$) with:

$$Z_{DE} = R + \frac{\frac{1}{j\omega C} \cdot \left(\frac{2R}{R + \frac{1}{j\omega C} + \frac{1}{\omega^2 C^2}} \right)}{\frac{1}{j\omega C} + \left(\frac{2R}{R + \frac{1}{j\omega C} + \frac{1}{\omega^2 C^2}} \right)} \quad (2.5)$$

With equation 2.5 it is clear that even for a relatively easy assumption for a DE model, with just 3 separation levels, the electrical behaviour of a DE is not trivial. The intricate electrical characteristics of the DE present a challenge when attempting to accurately measure its capacitance through electronic circuitry. With that in mind the measured capacitance, with normally used measurement equipment (which is accurate for an ideal capacitance), of the DE is just an approximation of a simplified DE model.

2.1.1.2. Actuator

With the same structure as described in Figure 2.1 a flexible electromechanical drive can be realized. The actuator mode functions by converting electrical energy into mechanical work. For that a high voltage (HV) is supplied to the compliant electrodes and the flexible capacitor is charged. The opposite charges of the HV and the GND electrodes attract each other and lead to a thickness reduction of the DET. Due to the incompressibility, the reduction in thickness causes an increase in the lateral direction. The maximum applicable voltage is limited by the maximum breakdown voltage of the material. For silicone the maximum field is in normal conditions around $80 - 150 \frac{V}{\mu m}$ and can be increased up to $350 \frac{V}{\mu m}$ for acrylic DEs (with tolerated maximum of $440 \frac{V}{\mu m}$) [18]. In practical applications, for silicone the maximum usable field lies at the lower band and actuators are normally used until $80 - 90 \frac{V}{\mu m}$. The force of the electro-static field between the two electrodes is depending on the applied voltage U and can be described with the mechanical energy W_m of a plate capacitor by equation 2.6:

$$W_m = F \cdot dL_z = \frac{1}{2} U^2 dC. \quad (2.6)$$

The force depends on the variation of the capacitance of the DE. By deriving equation 2.6 the force can be described with:

$$F = \frac{1}{2} U^2 \frac{dC}{dL_z} = \frac{1}{2} U^2 C_0 \cdot \frac{d}{dL_z} \frac{1}{\lambda_z^2} = \frac{1}{2} U^2 C_0 \frac{-2 \cdot L_{z,0}^2}{L_z^3}. \quad (2.7)$$

for small variations in thickness ($L_z \approx L_{z,0}$), equation 2.7 can be converted to the compressive force

$$F = -U^2 \frac{C_0}{L_{z,0}}. \quad (2.8)$$

The Maxwell-stress σ^{Max} is the compressive stress induced by the electric field E and can be described from equation 2.8 with

$$\sigma^{Max} = \frac{F}{A_0} = -U^2 \frac{\epsilon_0 \epsilon_r}{L_{z,0}^2} = -\epsilon_0 \epsilon_r \cdot E^2. \quad (2.9)$$

The induced force, and so the induced stress, are depending on the relative permittivity of the elastomer material and quadratically dependent on the applied electric field. Therefore, to increase the performance of a DEA, the maximum electric field and the permittivity of the material should be increased. For those two parameters, acrylic DEs have better properties compared to silicon (permittivity around 80 % higher and maximum electric field around 20% higher) [18]. But silicone provides much smaller mechanical losses, due the lower mechanical hysteresis, and a much better long-time performance which leads to a more reliable, stable and repeatable actuator behaviour.

With the Youngs modulus of a material (Y) the stress can be used to calculate a resulting strain ($S_{x,y,z}$). In the thickness direction the strain can be calculated from equation 2.10

$$S_z = \frac{-\epsilon_0 \epsilon_r \cdot E^2}{Y}. \quad (2.10)$$

With the Poison's ratio ν the strain in x direction can be expressed by [86]

$$S_x = \nu \frac{\epsilon_0 \epsilon_r \cdot E^2}{Y}. \quad (2.11)$$

Only the material parameters (permittivity and Youngs modulus) and the applied electric field are decisive for the free displacement of the DEA. For these parameters a qualitatively dependency from different environmental conditions and different working areas can be found in various publications ([27], [161], [162], [163], [164], [165], [166]).

With the low strain and low force provided by a single DEA actuator, a sufficient actuation is not achievable. So, it is necessary to increase either the strain or the force of the DE. There are two methods to increase the output performance of a DEA. Firstly, the actuator configuration can be modified (e.g. stacked actuators). Secondly, a biasing mechanism, which acts mechanically in parallel to the DEA, can be employed in order to reduce the initial stiffness of the DE element (see section 2.3.2.2 and A.3).

The main configurations of DEAs are either the thickness change of the dielectric (higher force but very low deformation) or the stiffness change of the actuated membrane to generate a lateral movement. This results in two main DE configurations, namely 'thickness changing' DEAs and 'membrane-stiffness changing' DEAs (Figure 2.4).

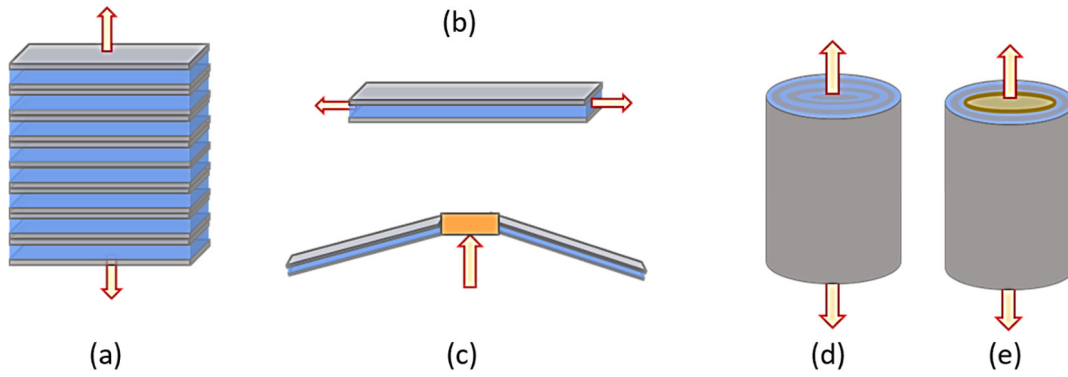


Figure 2.4: Actuator configuration principles (a) stacked actuator with thickness actuation, (b) membrane actuator in plane direction (c) membrane actuator out of plane direction (d) rolled actuator (e) tube actuator.

2.1.1.3. Loudspeaker

With the same functional principle of the DEA, the actuator (which is mainly used for haptic feedback, in the context of user interaction) can be stimulated for higher frequency responses. Since a loudspeaker is a transducer which converts electrical energy into mechanical energy, DEAs fit very well to this application. To generate an acoustic signal with a DEA system, two main principles can be used. One solution is to replace the classical drive for a conventional loudspeaker and realise it via DEAs with a corresponding biasing mechanism. The air pressure waves are in this case generated by the movement of a conventional diaphragm, which is moved by the DEA (high forces needed). The other option is to use the DE membrane itself to produce the sound. This can be done either by the well-known movement of the DE in an out-of-plane deformation. This loudspeaker principle works in a similar way as in standard loudspeakers with a diaphragm. To generate a high sound amplitude this kind of speaker works only in relatively low frequency ranges and on a relative small bandwidth. To increase the frequency and the bandwidth, the biasing element must be adapted and many DE layers are necessary.

Another principle to use the DEA directly for sound generation, elaborated in the context of this work, is to make use of structural vibrations of the DE membrane.

In literature, the preload of the membrane to generate a higher sound pressure is mainly realised by either mechanical biasing or (more often) by fluidic preloading ([94], [95], [108], [167], [168]). Using structural vibrations (rather than a pumping out-of-plane motion) for sound generation leads to several advantages. On the one hand, this allows the loudspeaker to be used in a fixed geometric configuration. So, no biasing element is necessarily needed. Another advantage of this principle is that the out-of-plane movement can be used to induce a motion or force, independent of the sound generation. This principle is explained in better detail in chapter 3.2 (Audio-tactile feedback DET). The basic functional principles of the three different loudspeaker realisations are shown in Figure 2.5.

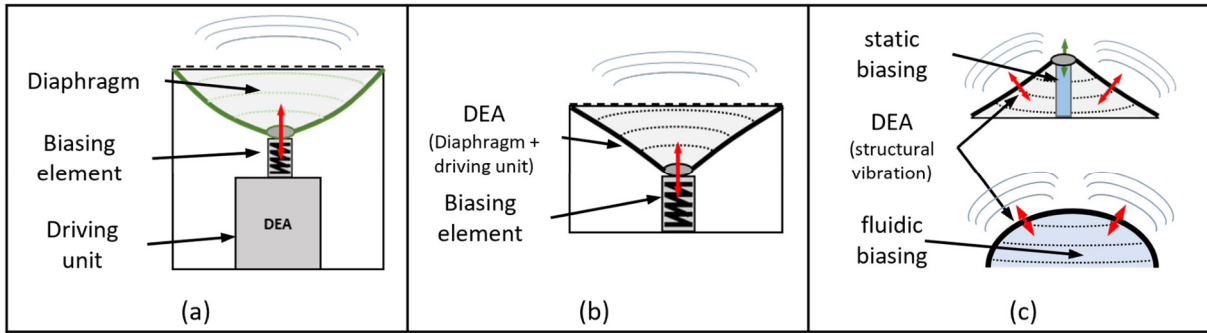


Figure 2.5: Different configurations and working principles of DEA based loudspeaker. (a) conventional loudspeaker with DEA based drive, (b) DEA membrane as driving unit and Diaphragm and (c) structural membrane vibration with mechanical or fluidic biasing.

Vibration of a stretched membrane

For the multi-functional elements described and developed in the following, mainly the structural vibrations are important. For this reason, the following section takes a slightly closer look at the vibration of membranes. For a more detailed explanation of the acoustic behaviour of loudspeakers and membrane vibrations, further literature is available on which the following elaborations are based ([169], [170], [171]).

For the prototypes developed in this thesis, the considered DEA layout is a circular out-of-plane topology, preloaded with a constant out-of-plane deformation (compare section 3.1.1 (DET feed-back-element topology)). Based on this example, the following refers to vibrations on a circular membrane, as these are of practical interest for understanding structural vibrations in the considered DET topologie. Different to traditional dynamic cone loudspeakers, where the sound is produced by a pumping motion of a rigid diaphragm, the structural mode characteristic of the DEA leads to a sound as result of membrane vibrations. A differential small part of the membrane is considered in Figure 2.6.

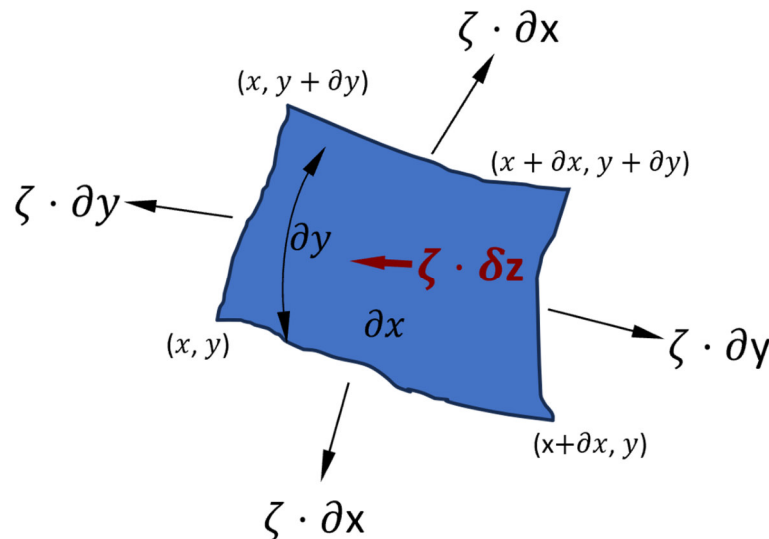


Figure 2.6: Elementary part of a vibrational membrane with acting and resulting forces (c.f. [170]).

By assuming a pre-tensioned membrane with the pretention force $\zeta \cdot dl$ and the tension ζ , the vertical force $\zeta \cdot dz$ can be calculated for a configuration like in [170] with:

$$\zeta dz = \zeta \left[dy \left(\left(\frac{\partial z}{\partial x} \right)_{x+dx} - \left(\frac{\partial z}{\partial x} \right)_x \right) + dx \left(\left(\frac{\partial z}{\partial y} \right)_{y+dy} - \left(\frac{\partial z}{\partial y} \right)_y \right) \right]. \quad (2.12)$$

With Newtons law $\zeta dz = \rho dx dy \frac{\partial^2 z}{\partial t^2}$ and the wave speed $c^2 = \frac{\zeta}{\rho}$ equation 2.12 can be written with the Laplace operator ∇^2 as

$$\nabla^2 z = \frac{1}{c^2} \frac{\partial^2 z}{\partial t^2} \quad (2.13)$$

The propriated wave equation in polar coordinates (r, θ) can be written as

$$\frac{\partial^2 z}{\partial r^2} + \frac{1}{r} \frac{\partial z}{\partial r} + \frac{1}{r^2} \frac{\partial^2 z}{\partial \theta^2} = \frac{1}{c^2} \frac{\partial^2 z}{\partial t^2} \quad (2.14)$$

With equation 2.14 and the solution $z = \psi \cdot e^{j\omega t}$ the Helmholtz equation for a circular membrane fixed at the edge in cylindrical coordinates can be formulated as follows

$$\frac{\partial^2 \psi}{\partial r^2} + \frac{1}{r} \frac{\partial \psi}{\partial r} + \frac{1}{r^2} \frac{\partial^2 \psi}{\partial \theta^2} + k^2 \psi = 0 \quad (2.15)$$

Applying the separation of variables method, the spatial variables ψ (function only of the position) can be expressed as $\psi = \Omega(r)\theta(\theta)$ and assuming θ smooth and continuous function (here a sinusoidal function) the Helmholtz equation can be recast as a Bessel equation. The substitution of ψ with the product of θ and Ω leads to an equation, which is on one side a function of r and on the other side of the equation a function of θ alone. This equation can be just solved if both functions are equal to the same constant [170]. Assuming this constant to m^2 lead to

$$\frac{\partial^2 \Omega}{\partial r^2} + \frac{1}{r} \frac{\partial \Omega}{\partial r} + \left(k^2 - \frac{m^2}{r^2} \right) \Omega = 0 \quad (2.16)$$

with the angular wavenumber $k = \frac{\omega}{c}$. Solutions of this equation are Bessel functions with order m . For finite displacement across the origin, the solution just contains Bessel functions of the first kind ($J_m(kr)$) and for physical motions, the real part of the solution is needed. With n as the number of zero crossings of the Bessel function ($J_m(kr) = 0$), we get a solution in a structure like [170], [172]:

$$\gamma_{mn}(r, \theta, t) = A_{mn} J_m(k_{mn}r) \cdot \cos(m\theta + \alpha_{mn}) \cos(\omega_{mn}t + \beta_{mn}). \quad (2.17)$$

γ_{mn} are resulting mode shape functions of the (in this case) circular membrane. The corresponding (natural) frequency f of the specific shape can be calculated with

$$f_{mn} = k_{mn} \cdot \frac{c}{2\pi} \quad (2.18)$$

In Figure 2.7 some vibrational modes of a circular membrane with number pairs (m, n) are shown, m is the number of radial nodal lines and n determines the nodal circles of the vibration schema, with associated vibration frequency expressed in terms of the fundamental frequency f_0 [170]. The vibrational modes can be measured for pre-stretched cone DEAs with a test setup presented in section 2.1.3.3, the measured vibration modes are shown in 3.2.1.

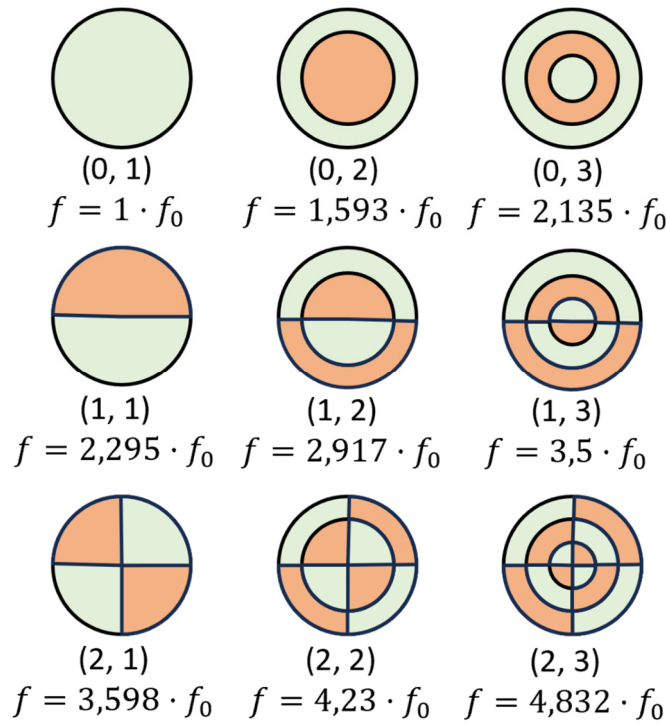


Figure 2.7: Normal modes of circular membrane with 180° out of phase vibration (red -green areas) separated by nodal lines. Frequency dependency of vibration, increasing for every nodal line (c.f. [170]).

High frequency voltage driven vibrations in DEs

A high frequency excitation of a DE membrane will result in structural membrane vibrations, comparable to the theoretical vibrations of a circular membrane in Figure 2.7. In different publications, the vibration of DE membranes were modelled [59], [173], [174], [175], [176]. In [59] Moretti et al. presented a coupled multi-domain model for COP-DEAs, with electro-mechanical interaction and the interaction with the acoustic domain. Therefore, they presented a fully-coupled model, which considered a three-dimensional membrane element like in Figure 2.8.

The basis for modelling the DEA with an axial-symmetric membrane, is the generalised Mooney-Rivlin hyper elastic model ([177], [178]) which is extended by the electrostatic energy density, induced by the DE actuator properties [176]. The fully-coupled model (Figure 2.8) combines the electro-elastic model of the DEA, with the response to the surrounding acoustic domain. With reference to a non-linear model of the COP-DE (with assumptions described in [175]), the membrane's deformation kinematics is described by finite superimposed mode shapes. The mode shapes describe approximately the deformation pattern of the membrane for different frequency ranges.

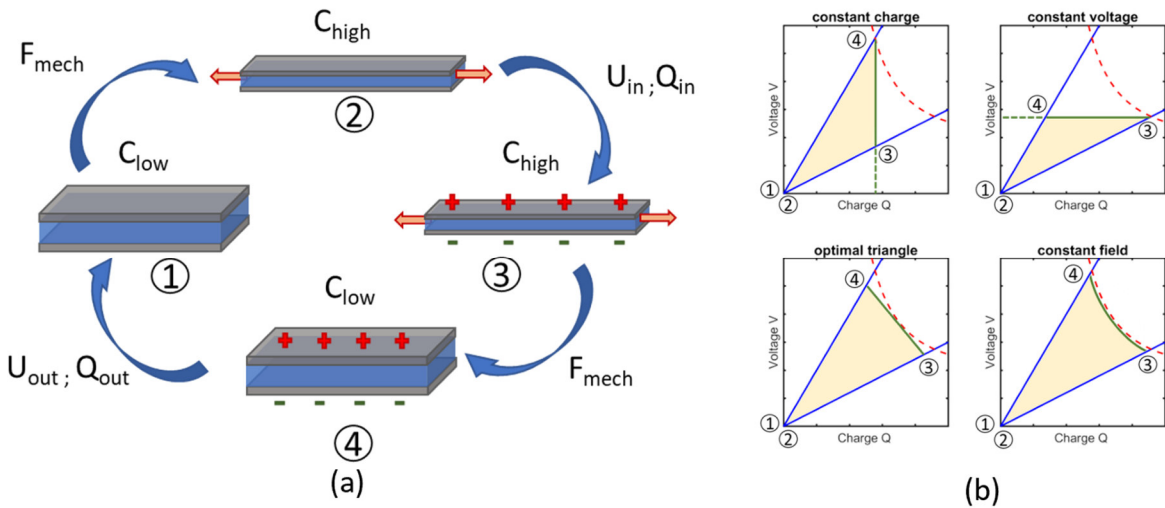


Figure 2.9: Working principle of DEG (a) energy harvesting cycle (b) different working schemes (CC, CV, OT and CE cycle).

DEGs can work in different (electrical) conditions, for the mechanical release (phase 4) of the energy harvesting cycle. Depending on the conditions (controlled voltage, charge), the transduced energy can be increased. In Figure 2.9(b) 4 main control cycles are presented. The 4 schemes are constant charge generator (CCG), constant voltage generator (CVG), optimal triangle generator (OTG) and constant electric field generator (CEG). The CEG method is the most effective approach, as it enables operation near the material's breakdown voltage, during the entire relaxation phase (Phase 4). However, its practical implementation is, due to the needed complex electrical circuit, challenging. For CCG the principle of the DEG is easy to understand. The charge stored in a capacitor is defined by (compare equation 2.6)

$$Q = C \cdot U \quad (2.20)$$

If the charge Q stays constant during the phase (3) – (4) (CCG) the voltage increases. The output voltage can be described as

$$U_{out} = \frac{C_{high}}{C_{low}} U_{in} \quad (2.21)$$

The stored energy in the capacitor E_{el} can be calculated by

$$E_{el} = \frac{1}{2} Q \cdot U. \quad (2.22)$$

For CCG conditions that leads to a generated energy (E_{gen}) of

$$E_{gen} = \frac{1}{2}(U_{out} - U_{in})Q = \frac{1}{2}\left(\frac{C_{high}}{C_{low}} U_{in} - U_{in}\right)U_{in}C_{high} = \frac{1}{2}U_{in}^2 C_{high} \left(\frac{C_{high}}{C_{low}} - 1\right). \quad (2.23)$$

For constant voltage at the relaxation phase of the DE, charge gets pumped in the reservoir and the generated energy can be calculated with:

$$E_{gen} = \frac{1}{2}(Q_{out} - Q_{in})U + E_{mech} = \frac{1}{2}\Delta QU + \Delta QU = \frac{1}{2}\Delta CU^2 \quad (2.24)$$

where E_{mech} is the mechanically induced energy.

In Figure 2.9 the generated energy is graphically shown. In all the conditions the maximum field strength of the DEG cannot be extended, that leads to a loss in convertible energy for CCG and CVG as compared to CEG. A control circuit that facilitates the interchanging of voltage and charge (e.g. controlled charging of a storage capacitor) with specific values of the storage

capacitor and the maximum input voltage, results in cycle phase 4 becoming tangential to the Q-V curve. This enhances the energy conversion efficiency in comparison to CCG and CVG, due to the expanding area of the energy plane (optimal triangle - OTG, as outlined in [179]). The highest convertible energy can be reached, if during the complete phase (3) – (4) the maximum field strength is applied to the DEG, but this needs more complex electronics.

Energy harvesting is especially interesting for wearable and textile integrated DE solutions. With this principle it is achievable to transduce the moving energy and potential energy of a human for instance to produce electrical energy (Figure 2.10).

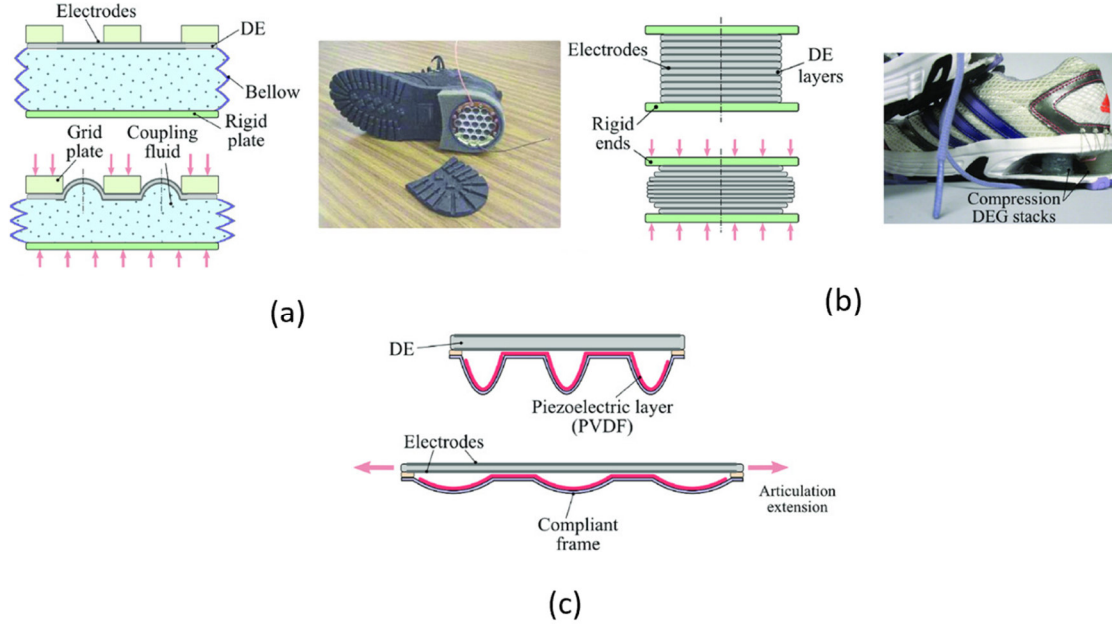


Figure 2.10: Human motion energy harvesting with DEGs for (a) shoes based on inflatable DEG [180] (b) shoes based on stacked DEGs [181] and (c) knee articulation [182] (c.f. [179]).

With this approach, it is conceivable to use the DE completely autonomously as a sensor and actuator and to provide the required energy by utilising the DEG functionality. In literature there are some examples to use DEG in wearables and mainly in Shoes, where a maximum power of around 4 W could be obtained [179]. In [180], [181], [182] different concepts of energy harvesting based on DEG in Shoes or wearables are presented and shown in Figure 2.10.

2.1.2. DE manufacturing

There are many fabrication processes available and in use to produce DEs. For carbon-based electrodes, the most common methods include pad printing, blade casting, spray or spin casting, and screen or inkjet printing ([183], [184], [185]). The manufacturing process for the DEs utilised in this elaboration is screen printing.

In all tests described in this work, the source material is Wacker Elastosil 2030 silicone film with 50 μm thickness. In Figure 2.11 the manufacturing process is shown in a schematic view.

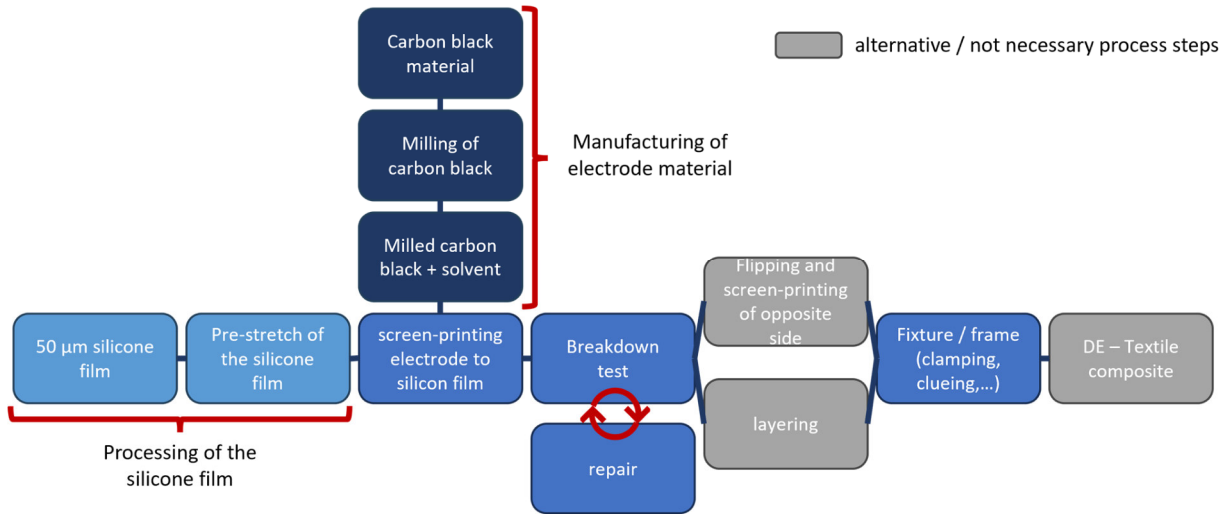


Figure 2.11: manufacturing steps for DE fabrication including electrode material and silicone film preparation, screen-printing process, breakdown test, stacking and clamping of the produced actuator.

The silicone film gets pre-stretched prior to the printing process and fixed to a metal frame. Mounted on the metal frame, the film can be handled easily and can be put in a semi-automatic screen printer (compare Figure 2.12). Through a sieve with the geometry of the desired DE, the self-made electrode mixture of polydimethylsiloxane (PDMS; (SilGel 612 by Wacker)), carbon black (Orion Printex XE2), silicon oil and solvent (e.g. VD 60) is applied to the silicone film. With the parameter of the screen printer and the material composition, the properties of the electrode (especially the resistance and hysteresis) can be adjusted [26]. After manufacturing, the electrodes are connected to an electrical conductor and the DEs can be stacked if a multi-layer layout is desired. In the case of textile-integrated elements, the assembly step can be integrated into the overall manufacturing process.

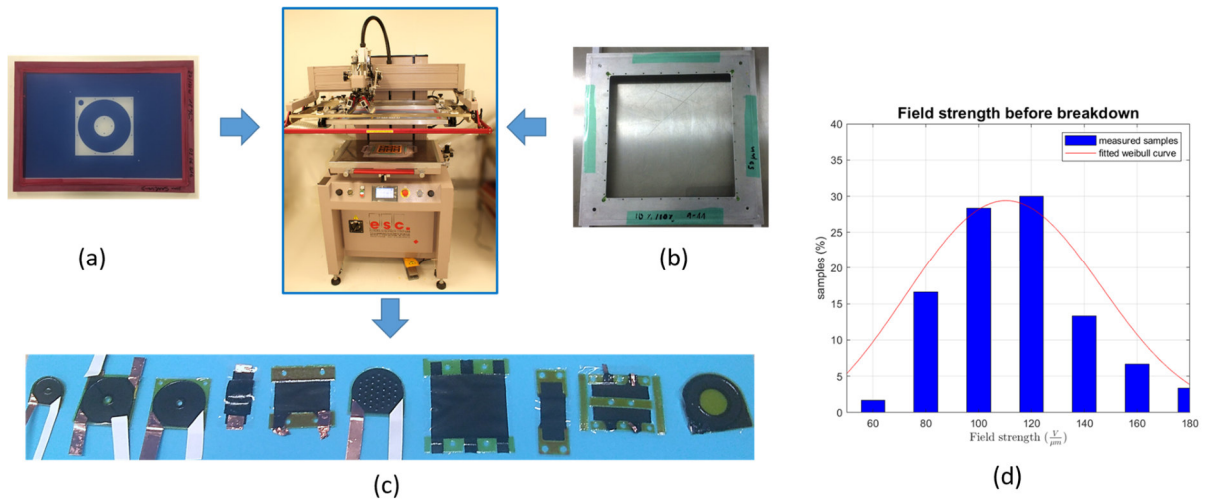


Figure 2.12: Screen printing process with (a) sieve for the DE Design (b) metal frame with silicone film and (c) examples of possible DE Designs. (d) Maximum electric field strength measurements for DEAs without pre-stretch.

A main parameter for a working DEA is the maximum breakdown field. This can be tested by applying a high voltage to the DE electrode until a breakdown of the DE appears (or until the needed working voltage is reached without breakdown). With the maximum voltage applied and

the known thickness of the DEA the electric field can be calculated. In Figure 2.12(d) the measured maximum electric fields for DEA samples without pre-stretch are shown. The maximum breakdown voltage for the silicone material is given with 80 – 100 V/ μm from the manufacturer (Wacker Chemie AG). The measurements in Figure 2.12(d) show that some samples even hold a higher field strength and that the medium value is approx. 110 V/ μm . To be sure that the actuators work for many cycles and under different environmental conditions, the given field strength of 80 V/ μm should not be overcome. The yield of the manufactured DE actuators can be increased with a repairing process (see Figure 2.11) described in [186].

2.1.3. DE characterization

During the design process of a DE system, the characterization of the system (e.g. DE force, biasing, mass, vibration behaviour, capacitance, resistance) is necessary. The physical behaviour of the DE system must be measured, to validate the system output performance. For sensor, actuator and loudspeaker applications different measurement units can be used. Figure 2.13 shows all needed components for the different characterisation methods of DETs.

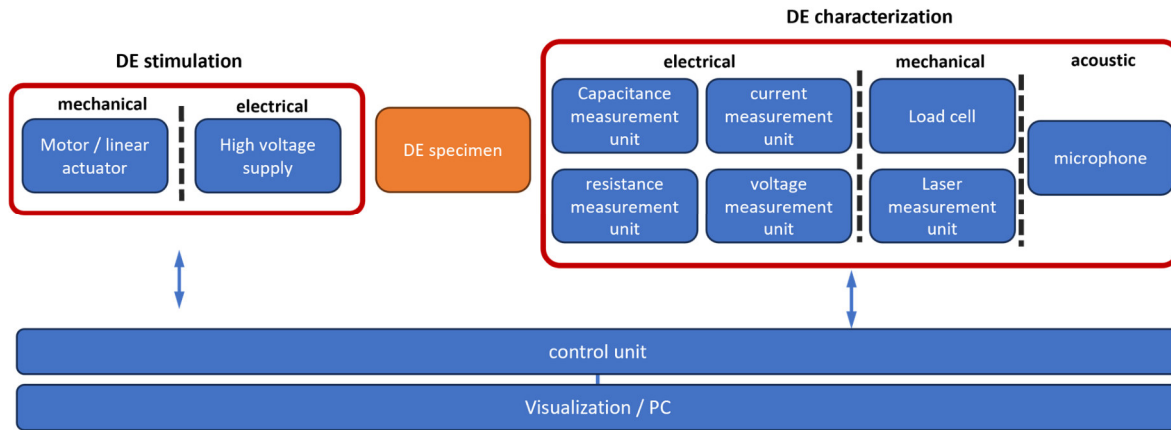


Figure 2.13: components for a DE characterisation setup. With elements for the control of the system, the mechanical or electrical stimulation of the DE specimen and validation/measurement units.

2.1.3.1. Sensors

For sensory applications, the most important value to measure is the capacitance of the DE. In a test environment a LCR meter is used, to measure the change in capacitance during movement. The mechanical impression is done by a linear motor, and the force is measured by a loadcell. With this configuration, force-, linear- and bending sensors can be characterised. Beside the capacitance, the resistance of the electrodes of the DE has a high impact to the system performance and can be measured with the LCR meter. The displacement of the specimen is measured by a laser measuring unit. In Figure 2.14 the used measuring setup for characterising DES is shown.

The integrated DES system can be validated by applying the desired external load (e.g. stretch, pressure/force or angle of the element) and measuring the capacitance change with the LCR meter or a specific designed sensing electronic.

The electrical behaviour of the DE must be characterised, to design a sensor system and develop a specific sensing electronic. The DE is not an ideal capacitor, because of the geometrically distributed electrode and the relatively high resistance, and cannot be modelled as a simple ideal capacitor. Figure 2.14(b) shows an equivalent circuit rendering the electrical behaviour of a DES with cascaded RC elements (compare Figure 2.3).

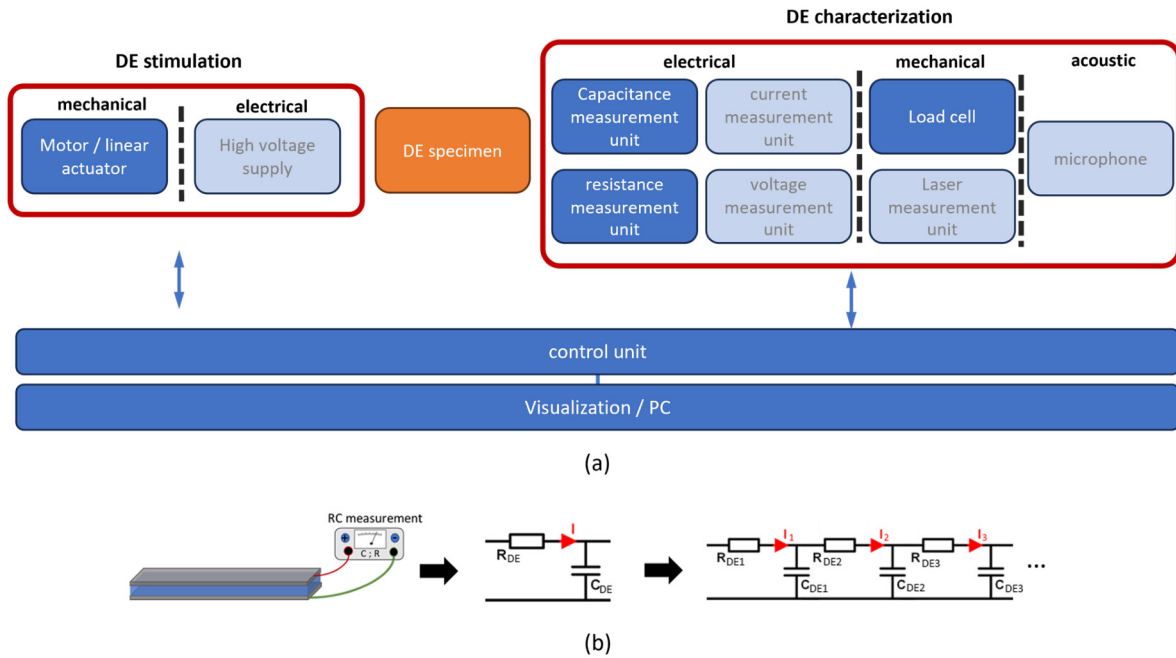


Figure 2.14: (a) components for DES characterisation and (b) capacitance and resistance measurement of a real DES and assumed simplified electrical model.

2.1.3.2. Actuators

For the characterisation of the mechanical behaviour of the DE within electrical actuation, a similar setup as for the sensor characterisation is used (Figure 2.15). In order to design a DEA, it is necessary to consider the force-displacement characteristic, particularly in the context of stimulation through the application of different voltages. For that stimulation a high voltage power supply is required.

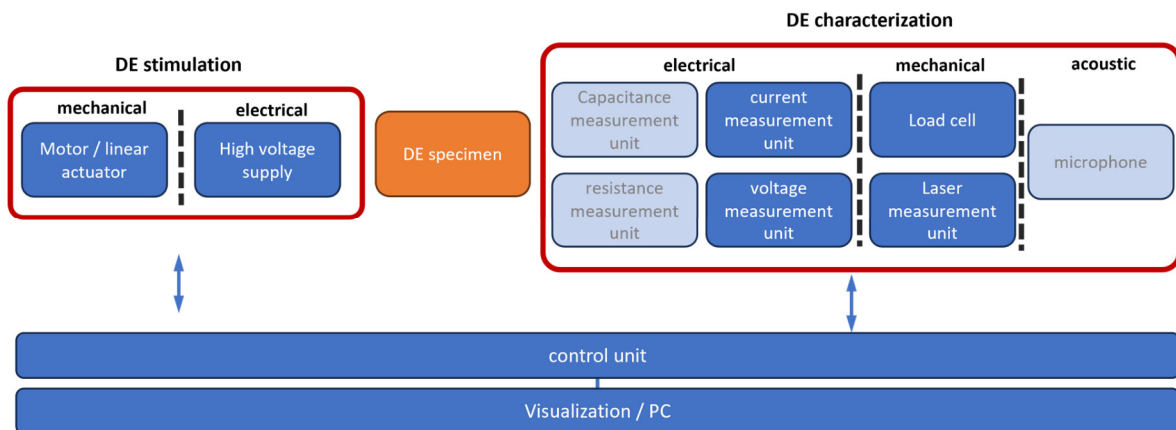


Figure 2.15 components for DEA characterisation.

The characterisation can be achieved with constant voltage (CV) measurements. These studies are performed by applying the excitation voltage (normally 0 V and maximum allowed voltage) to the electrodes, where the linear motor is moving from zero position to a maximum strain position and back. This measurement can be repeated with a higher number of cycles, to quantify if the force changes with different cycles. CV measurements are performed for the complete DEA

system, to see the influence of a biasing element to the system behaviour. With the force displacement characteristic of the DE and the biasing element respectively, the system behaviour can be validated, and the maximum performance of the system is achievable, by adjusting the biasing element (see also chapter 2.1.4).

Another characterisation parameter is the blocking force, which is measured under constant position test (CPT) conditions. During that measurement the stretch of the DE is kept constant, and the voltage varies cyclically from 0 V to the maximal voltage. With this configuration, the force output of the DE at a fixed position and the dynamic performed for the complete DEA setup (with biasing element) can be measured. In Figure 2.15 the needed components for the DEA characterisation are shown. With the corresponding setup, complete DE elements, with biasing and housing, can be characterised, whereby the DEA behaviour is validated.

2.1.3.3. Loudspeaker

For the sound quality and intensity characterisation and the validation of vibration behaviour of the DE, a specific setup is utilised. To characterize the moving and vibrational behaviour of DEAs for higher frequencies, a 3D laser-doppler vibrometer is used (Polytec PSV-500 3D). The vibrometer measures the doppler shift of a Laser, with the relation between the stationary system and the moving system, the velocity of the measured point can be determined. With a shift of the focus point, a 1-dimensional scan can be performed. In the current configuration, a 3D scanner is utilised, comprising three individual 1-dimensional scanners that collectively facilitate the capture of a 3D motion image. With this setup the complex movement of a DEA, during higher frequency actuation, can be recorded. Figure 2.16(a) shows the needed components for acoustic characterisation of a DE based loudspeaker.

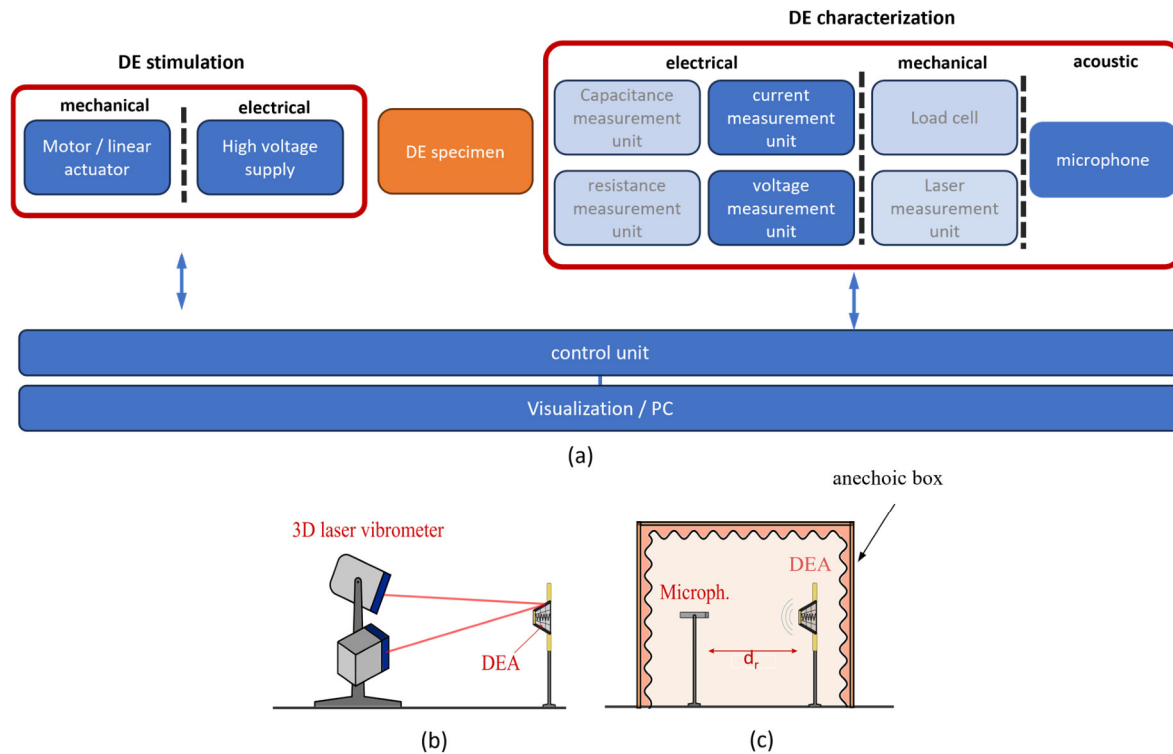


Figure 2.16: High frequency measurement setup for DE characterisation with (a) components of a loudspeaker test rig (b) 3D laser vibrometer for membrane movement measurements (c) anechoic box for acoustic measurements.

In Figure 2.16(b) a schematic drawing of the 3 D laser vibrometer and the DEA specimen is shown. To measure the sound, directly produced by the DEA, an anechoic chamber is used (compare Figure 2.16(c)). On one hand the chamber illuminates acoustic waves from the surrounding, which could interfere with the microphone measurement, on the other hand the reflections of the acoustic waves are reduced. A microphone, which measures the sound/air pressure, is placed at a certain distance of the DEA. If the DE is driven with specific higher frequency input signals (e.g. a chirp signal), the SPL of the microphone can be assigned to the respective frequency, and a frequency spectrum is calculated.

2.1.4. DE Element design and structure

To develop a proper working DE system, it is essential to consider both the properties of the DE element itself and those of the periphery. In the case of sensors, the critical mechanical and electrical properties are the resistance of the electrode and the electrical connection. The resistor is mainly dependent on the manufacturing process and the material properties of the electrode. The contact consists of two components. Firstly, it is important to establish a low-resistance electrical connection, in order to reduce the contact resistance. This in turn has a direct effect on the capacitance measurement of the DES. Secondly, sufficient mechanical contact must be ensured to enable the required coupling of the sensor to the measuring environment. In Figure 2.17 the main components for a DES element are shown.

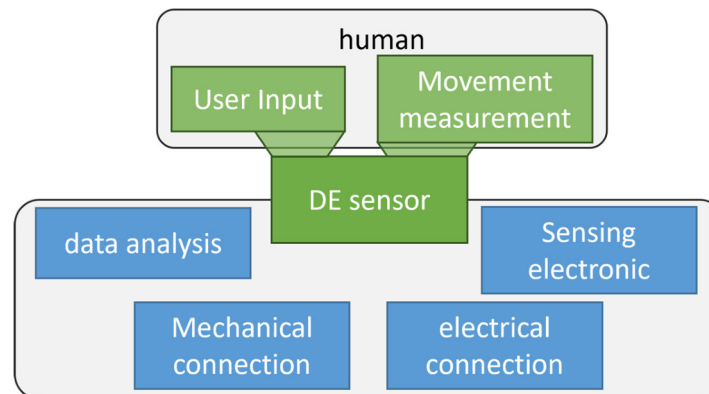


Figure 2.17: DE sensor element with peripheral elements. The human interaction is sensed by the DES with a suitable sensing electronic and measurement-based data analysis. The electrical and mechanical connection represent the interconnecting level between the DES and the surrounding system structure.

For membrane actuator structures the main design and developing part is the biasing mechanism and the layering of different DEA membranes. With the layering of DE membranes, the output force of the DEA system can be linear enhanced. To realise a layered DEA, a stacking process for the single elements is needed. Also, the electrical and mechanical connection must be specially designed for stacking. The mechanical connection of the single DE layers is mostly done by either glueing of the single elements, screen printing stiff reinforcements around the electrode (e.g. epoxy) for connection during the DE fabrication or using clamps (e.g. plastic frames). It is essential for the optimization of the system, to combine DEAs with a proper designed biasing mechanism. Additionally, adapted high-voltage electronics and control electronics are part of the overall structure of the actuator system. In Figure 2.18 the main components for a DEA feedback element are shown.

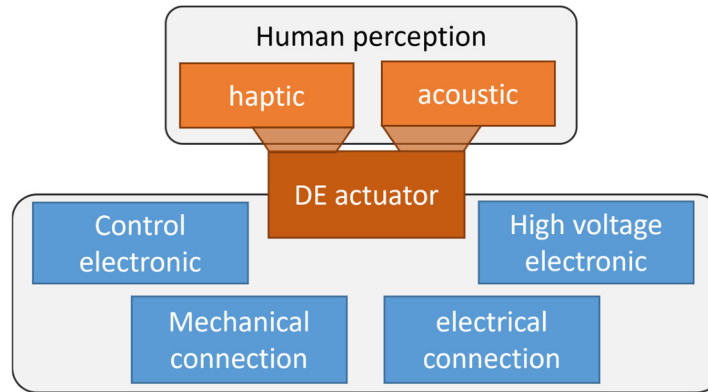


Figure 2.18 DE actuator element with peripheral elements. The DEA, combined with a suitable high voltage and control electronic, provides tactile and acoustic feedback to the user. The electrical and mechanical connection represent the interconnecting level between the DEA and the surrounding system structure.

2.2. Human perception

The human nervous system transmits stimuli from sensory receptors to the brain and spinal cord and sends impulses back to the rest of the body. The two main parts of the nervous system are the central nervous system (CNS) and the peripheral nervous system (PNS). The nervous system controls the ability to move, breath, adjust heartbeat and perceive sense, as much more. In Figure 2.19 the structure of the nervous system is shown, which also includes the afferent and the efferent division.

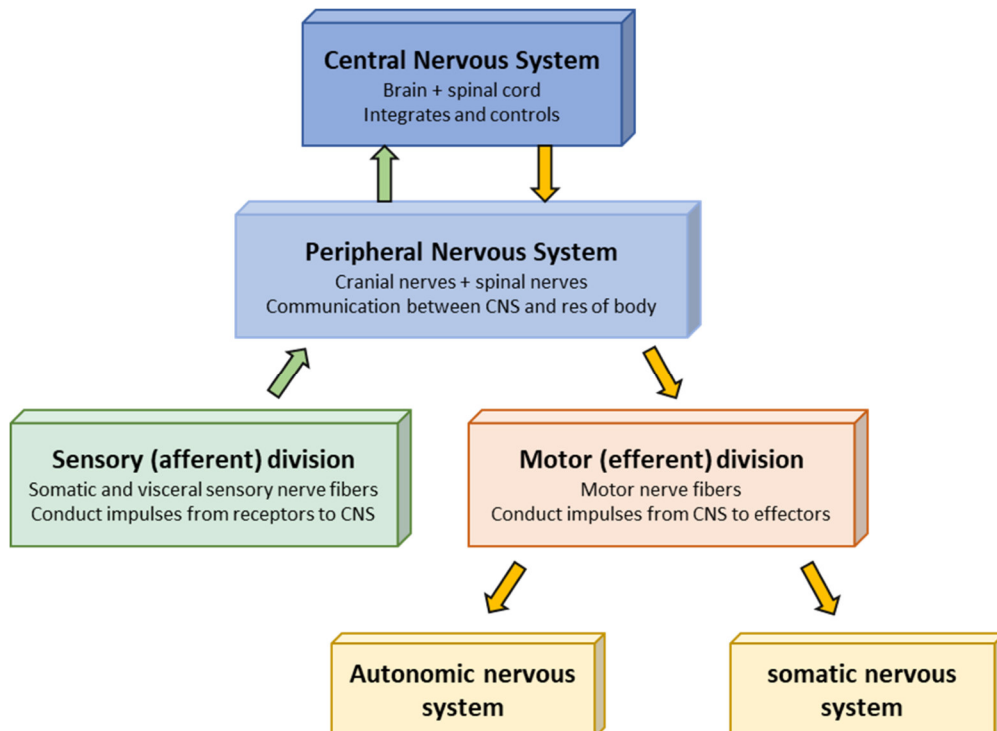


Figure 2.19: Structural organisation of the nervous system (c.f. [187]).

The efferent division controls the autonomic (not consciously directed) and the somatic (consciously directed) nervous system. The autonomic nervous system is further divided into the sympathetic (increasing activity e.g. heart rate and blood pressure) and the parasympathetic (decreasing activity and relaxation of muscles) division.

For the human perception the sensory division, which includes somatic (information from skin, muscles bones & joints) and visceral (internal information from organs) nerve fibres and transfers the impulses from the receptors to the PNS and from there to the CNS, is important [187].

2.2.1. Human anatomy – sensory nervous system

The sensory nervous system can sense external inputs via different kind of extero-receptors [188], which are olfactory sensory neurons (smell), gustatory receptors (taste), photoreceptor cells (vision), hair cells (auditory system and vestibular system), thermoreceptors (temperature) and mechanoreceptors which are responsible for force, pressure or fibrillation sensation on the skin. In Figure 2.20 the structure of the CNS and PNS as well as the neuron structure is shown (mainly consists of: cell body (soma), dendrites, axons and synapses).

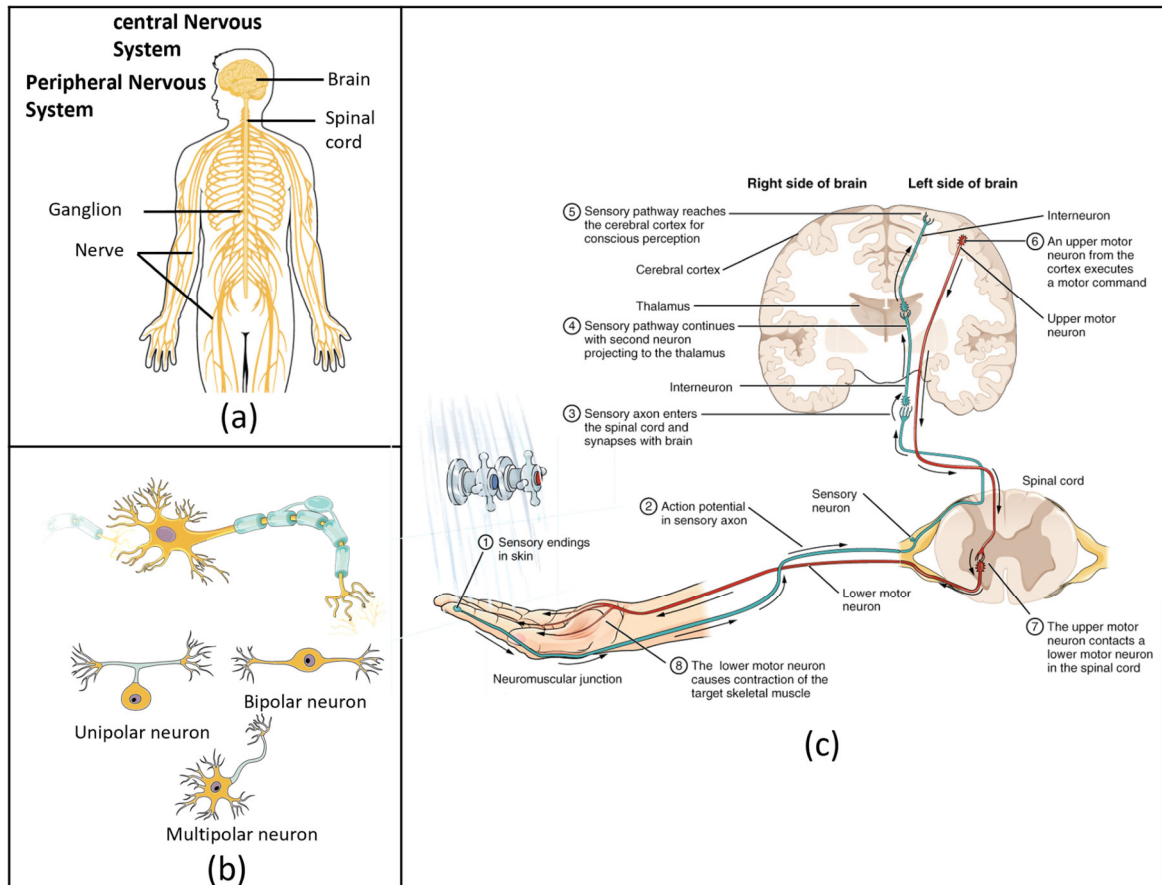


Figure 2.20: (a) The nervous system of the human body as well as (b) the structure of neurons and (c) the process of precepting a sensory stimulus [189].

2.2.2. Haptic

The haptic perception of the human works according to the same principle as shown in the previous section. Haptics comes from the Latin hapticé (meaning “science of touch”) and originally from the Greek haptesthai (meaning “to touch”) and was originally a medical synonym for tactile. Tactile is original form the Latin verb tangere (meaning: “to touch”). By the 20th century the two words become more separated and developed in a more psychological sense [190], [191].

Physiologically, haptic feeling is an overall term for the sensation of the skin and limbs, which includes heat sensation, pain sensation, tactile perception and kinesthetics. As shown in Figure 2.21, the human senses can be divided in mechanical, radiation and chemical group. For a mechanical haptic device, the tactile and the kinesthetic feedback are important.

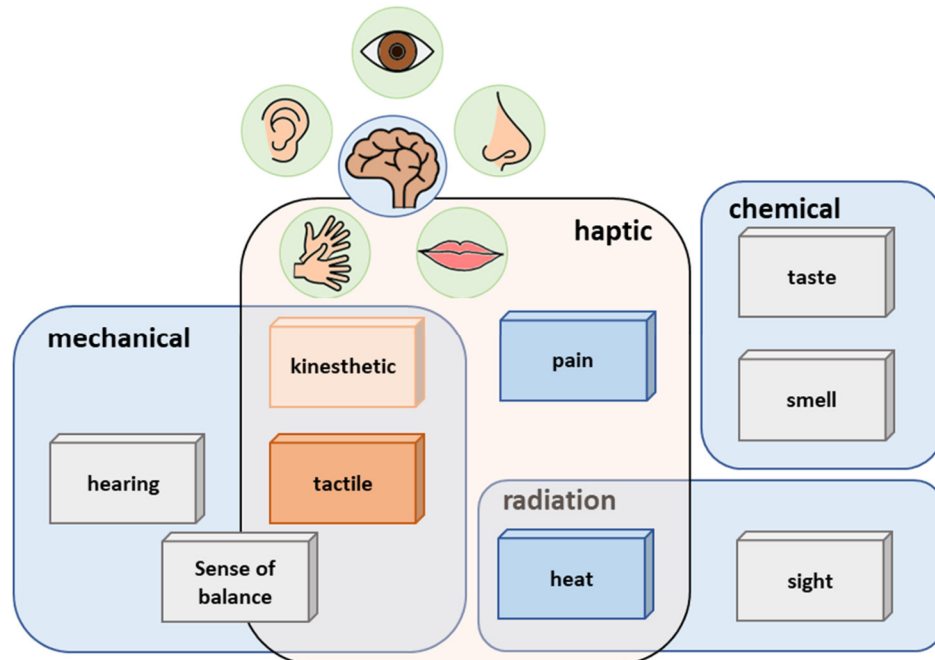


Figure 2.21: The human sense, including mechanical, chemical, radiation and haptic sensing, and the haptic sub-group (c.f.[192]). The haptic sub-group contains tactile, kinesthetics, heat and pain feeling. The sense of balance is located in the ear and represents a hybrid form of haptic and hearing sense.

The neurons for haptic feeling are in different parts of the skin located and responsible for different areas of sensation. The Pacinian corpuscle is responsible for vibrotactile feedback, stimulated by DEs for instance. In Figure 2.22 the cells are classified according to their position, response rate, receptor density and detection rate. The kinesthetic perception is the ability to measure force and position in the 3D space. This is realised by cells in the joints, muscles and tendons (cf. Figure 2.22).

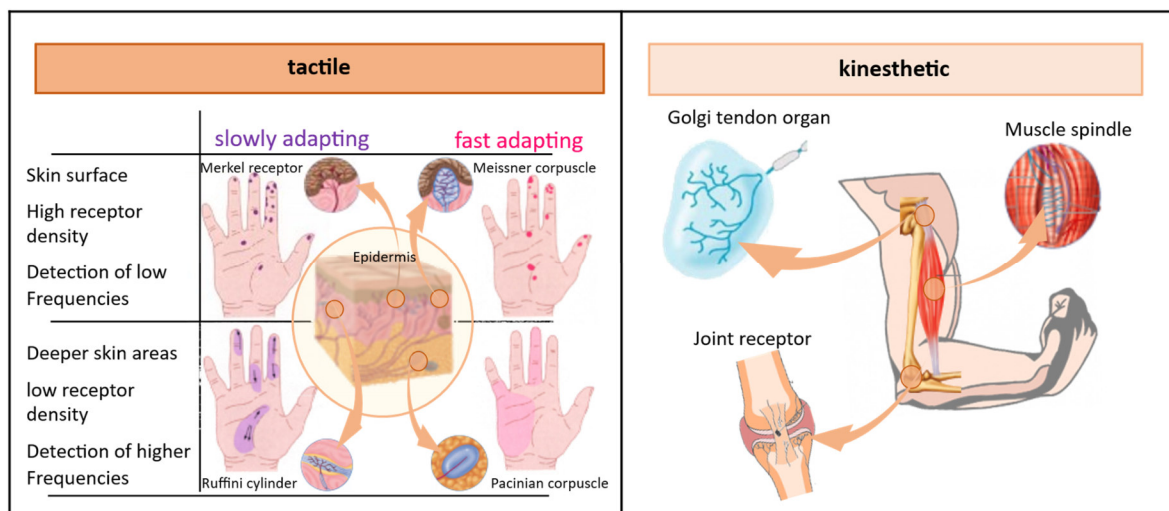


Figure 2.22: Principle of the tactile and kinesthetic perception (c.f. [193], [194], [195], [196], [197]).

To develop a feedback system that targets the tactile receptors and elicits effective perception, it is necessary to determine the sensitivity threshold of the cells. For this purpose, several user-based perceptual studies in the field of experimental psychology have been carried out, which show the just-noticeable difference (JND) and the absolute perceptual threshold (AT) of the human skin. The AT describes for example the lowest amount of force that a human can detect at a specific skin area, the JND is the smallest necessary difference of two impulses to detect them separately. The JND and the AT are in the same order of magnitude and have roughly the same course. In Figure 2.23 the JND for the force perception and for deflection perception of the human skin is presented. The threshold is very dependent on the skin area (due to stiffness of the skin and the density of perception cells) and the conduct of the studies, therefore, the courses are only indicative of quality. For example, the resulted thresholds from Hatzfeld and Werthschützky [198] are about 20 dB higher than from Isar et. al. [199].

For the design of the DEA mainly the highest values of the force and the displacement, which the actuator needs to produce, are necessary. These minimum perception values are proportional to the JND. The JND is also used for other perceptions, like sound and heat or brightness. The perception in the most of these cases is not linear with the intensity of the stimuli but logarithmically. For this purpose the perception-strength (P) of the human related to the stimulus-strength (S), is described by the weber-fechner-law of the human sensation as

$$P = a \cdot \log\left(\frac{S}{S_0}\right) \quad (2.25)$$

where a is a constant depending on the explicit stimulus and sense, and S_0 is the stimulation threshold which refers to the lowest noticeable stimulation [195], [200], [201]. The JND is due to the behaviour described in equation 2.25 normally presented in decibel (dB).

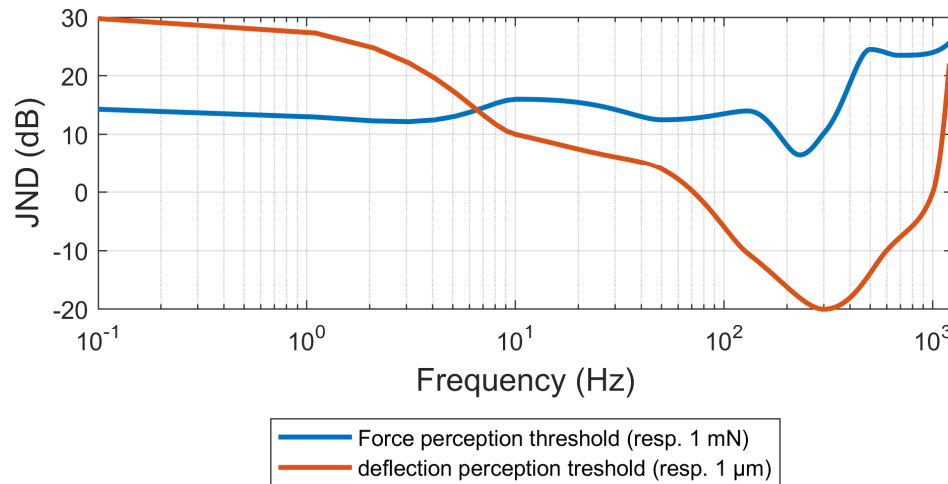


Figure 2.23: Just noticeable difference for force and deflection of human skin (c.f.[198], [199], [202], [203], [204]).

Besides the intensity of the stimulus, the spatial resolution of the stimulus is also dependent on the mechanoreceptor density. A distinction must be made between simultaneous and successive spatial thresholds. In Figure 2.24 are the respective space thresholds of the parts of the human body established, the successive threshold is about a quarter of the simultaneous threshold [205], [206]. That leads to a much higher actuator density, in the case of timely variant stimuli.

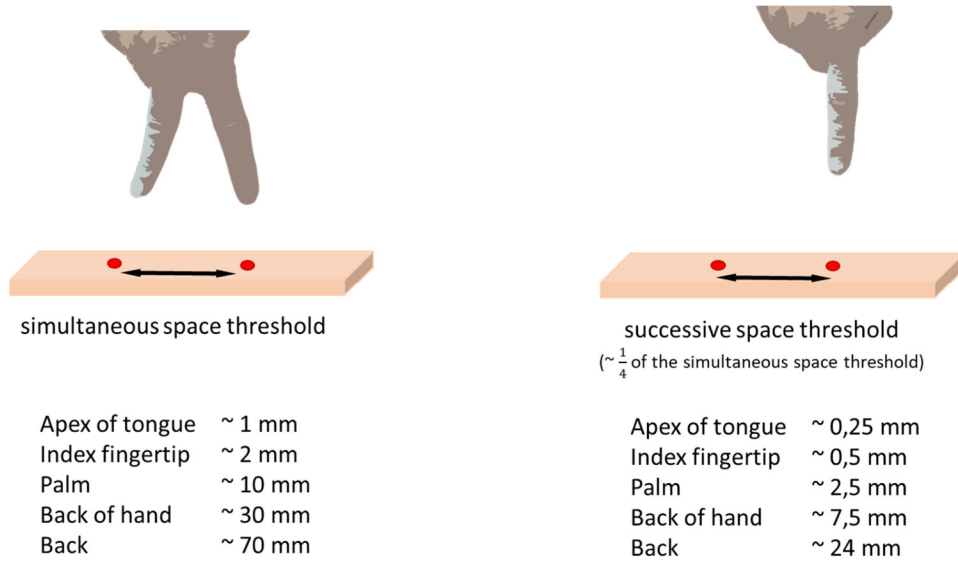


Figure 2.24: Simultaneous and successive special thresholds of different parts of the human Body(c.f.[205], [206]).

For the feedback to the user and for the development of textile integrated actuators, which are completely or partially in contact with the human skin, the mechanical behaviour of the skin is interesting. The mechanical impedance \overline{Z}_m can be described as a mechanical structural resistance against applied vibrations. \overline{Z}_m can be validated by the applied force \overline{F} to the structure, divided by the velocity \overline{v}

$$\overline{Z}_m = \frac{\overline{F}}{\overline{v}} = \frac{F}{v} \cdot e^{j\varphi} \quad (2.26)$$

where φ is the reciprocal phase between the force and the velocity. The Impedance is not only dependent on the force and the velocity but also on the phase between them. The qualitative progression of the frequency dependent Impedance is shown in Figure 2.25.

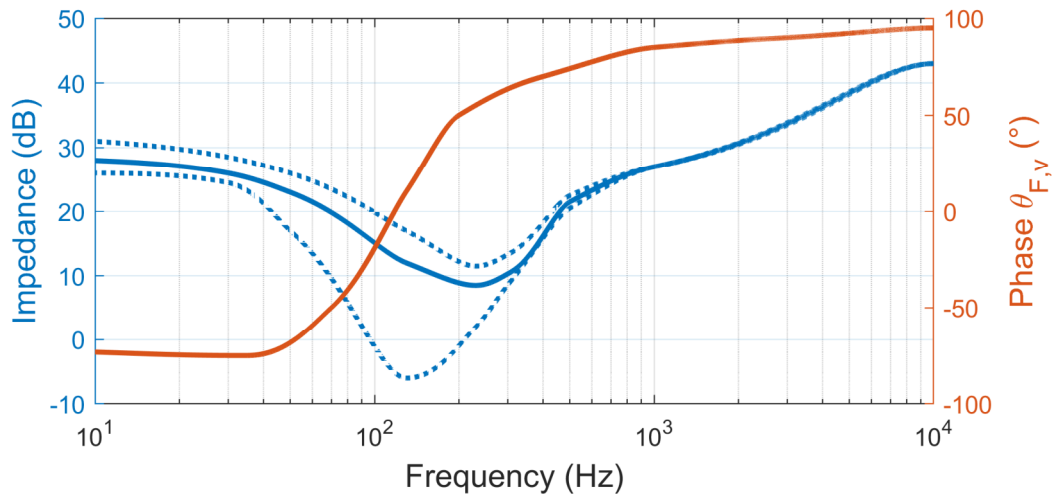


Figure 2.25: Qualitative progression of the Impedance and phase of the mechanical Impedance (c.f. [202], [207]).

The descriptive mechanical system of the human skin can be modelled by separate lumped elements, like a spring, damper and a mass. The frequency behaviour of the three elements is shown in Figure 2.26. In a simple case, the mechanical model can be realized by interconnecting the three elements. By choosing different values for the mechanical material constants of the model, the

behaviour of the skin at different areas can be modelled (see [202]). In [207] A. Kern shows a more complex mechanical model of the human skin, which is adapted to the behaviour of the skin evaluated by various measurements.

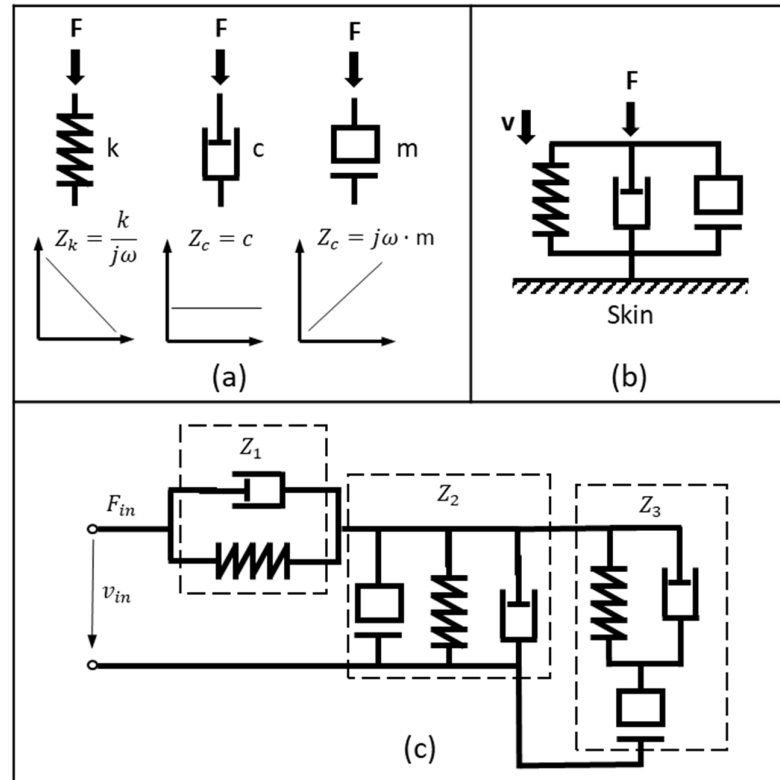


Figure 2.26: Single mechanical elements (a) and simple model for the human skin (b). As well as a more complex model of the human skin (c) ([202], [207]).

2.2.3. Acoustic

The acoustic sense of the human converts sound waves in neuronal signals, the PNS sends the signal directly to the CNS and to the auditory cortex of the brain. The ear itself has 3 main parts the outer ear (auricle and external auditory canal), the middle ear (eardrum and tympanic cavity) and the inner ear (cochlea and organ of balance). In Figure 2.27 the structure of the auditory system is shown. The sound waves reach the outer ear and get forwarded to the tympanic membrane which starts to vibrate. The vibration passes on to the middle and inner ear and the cochlea, where the stimuli get recorded by the cochlear nerve and send to the CPS [194], [195], [208].

The auditory perception is not linear with the sound pressure P_s but rather follows a logarithmic scale and can be described according to equation 2.25. The sound pressure level (SPL) is the pressure level of a sound measured in dB. The SPL of a perception is thus presented in dB which can be calculated by the equation:

$$SPL = 20 \cdot \log \left(\frac{P_s}{S_0} \right) \quad (2.27)$$

S_0 is the absolute threshold (AT) of the human ear and its normally set to 20 μPa at 1 kHz.

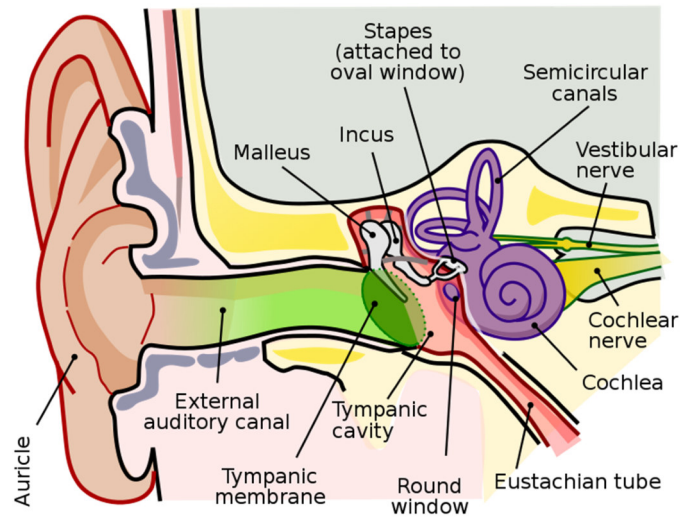


Figure 2.27: Anatomy of the ear and the auditory meatus, including outer, middle and inner ear [208].

The psychoacoustic measuring unit for loudness is phone (reference to a sinusoidal signal with 1 kHz). In Figure 2.28 the SPL and the sound Intensity is shown, for different precepted loudness.

The lowest curve refers to the absolute human threshold and the upper lime refers to the pain threshold. The human ear is specially in the region from around 400 Hz to 6000 Hz very sensitive. In this region the human can hear softer sounds then the most other animals (even if they are normally able to here higher and lower frequencies) which can be explained by the importance for human speech in this frequency range [210].

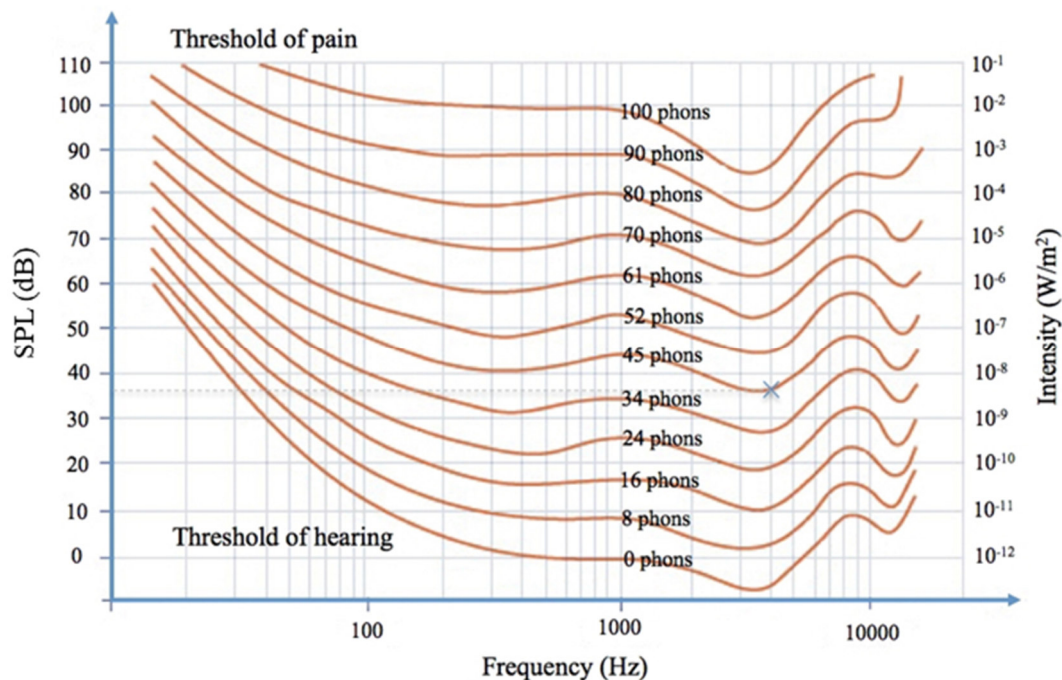


Figure 2.28: Normal loudness contours for sound pressure level and Intensity (pure tones) ([209], [210]). Phons lines refer to equally loud perceived loudness by the human hearing.

[210]The JND for acoustic perception can mainly be divided into two parts, the distinguishability for loudness and for the tone high (frequency). There are also some studies for noise and sharpness of the acoustic signal, but they are comparable to the other two groups ([209], [211], [212]).

The sensitivity peak in the region of 3.5 kHz is explainable due to a tube resonance of the auditor channel (compare Figure 2.27). The JND for the loudness also depends on the SPL itself, so for example if the loudness is in a low level region a change need to be higher to be detected compared to higher SPL (e.g. for 80 dB SPL a change of 0.5 dB can be detected but for 40 dB the change of loudness needs to be already around 1.5 dB) [210]. In Figure 2.29 the JND for different bias SPL at specific frequencies (Figure 2.29(a)) and the JND over the signal frequency (Figure 2.29(b)) are shown.

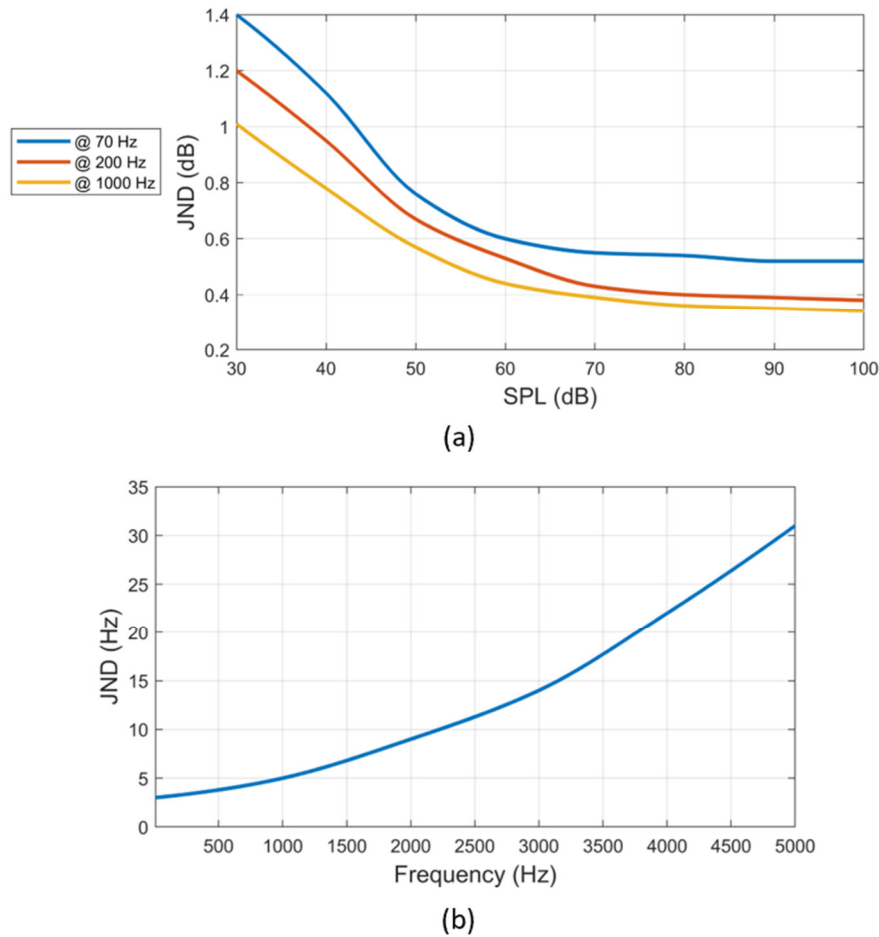


Figure 2.29: SPL JND of the human hearing for different frequencies depending on the initial SPL and the frequency JND, depending on the initial frequency ([213], [214]).

2.3. System architecture design of DET based user-interaction interfaces

With the aims described in Chapter 1.1 and 1.2, the primary objective is the development of assistance tools, based on complete new and inventive combined features, which makes the human-machine-interaction and human-computer-interaction more intuitive and natural, without bulky and heavy equipment. Intelligent materials and in particular DETs are used, because of their outstanding properties for wearable applications and multi-functionality.

2.3.1. Design and structure of user-interaction interfaces

The user interface (UI) which connects the human, such as an industrial operator, with a diverse interaction structure, must be intuitive, efficient, interactive and user friendly. To guarantee an effective interaction, the interface should provide on the one hand a reliable and inconspicuous user input measuring and on the other hand be able to generate an intuitive, understandable feedback. The user interface transfers the sensed user input to the underlying digital system structure and enables an interaction with the user, by stimulating specific perceptive receptors of the user. In Figure 2.30 a schematic of the UI role for human-machine interaction is shown. The user movement, gesture, or input is measured via sensing elements and validated in the interaction structure.

The multi-functional DE elements presented here, sense mainly the user input in the form of a button or an interactive textile-based surface. Additionally, touchpads or for example smart cloths could be also realised (e.g. smart glove [215]). The interaction structure can calculate and provide feedback, depending on internal system states or in a response to environmental and the user input conditions, directly to the human.

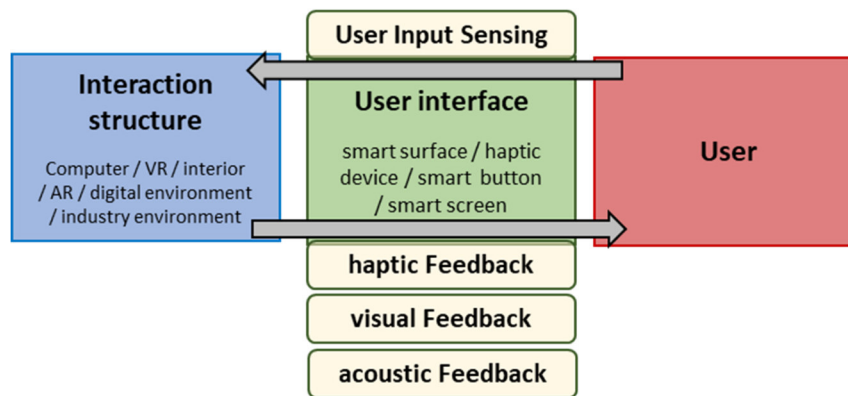


Figure 2.30: Assistance tool as user interface for HMI. The user interface transfers the sensed user input to the underlying digital structure and enables an interaction with the user by stimulating specific perceptive receptors of the user.

The assistance tool is an important element of a cyber-physical system (CPS), as shown in Figure 2.31. The CPS integrates the communication capabilities and processing power of new generation electronics, facilitating improved integration of heterogeneous devices and systems. It combines this with modern visualisation, sensing and actuation elements to generate an architecture for human-virtual reality systems and for Internet of Things (IoT) applications.

Using an interactive assistance tool, the tasks of the three connection points of the CPS-triangle (Figure 2.31) between human and physical components and virtual components can be fulfilled. In different publications, generated in the framework of this research, sensory and multi-functional assistance and interaction systems are shown in the context of textile integrated and user communication, respectively sensing devices ([215], [216]).

There are many fields of application for integrated sensor and actuator elements, to realise human-machine interaction (see also section 4.1). The broad spectrum of potential applications spans industrial production, automotive interiors, leisure, office environments, virtual reality (VR) and augmented reality (AR), and gaming. Furthermore, important application fields are medicine and support for handicapped and aged people as well as sport and comfort.

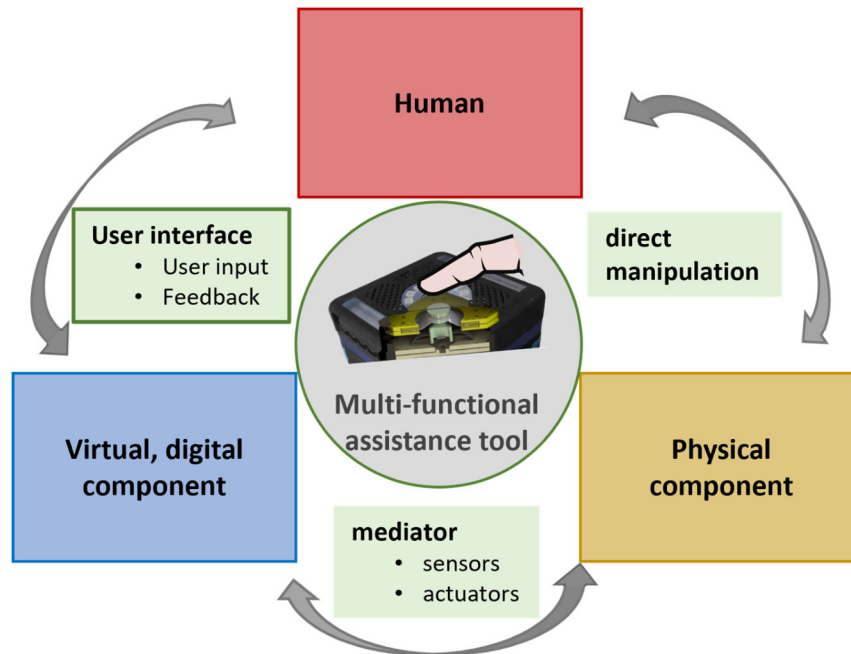


Figure 2.31: Assistance tool as a main element of a cyber-physical system (CPS) cf.[8]. A multi-functional assistance tool can be used as direct interaction with the virtual world (VR applications) or as interaction with real physical components (AR applications). The sensing capability of the assistance tool can additionally be used for the sensing of the environment (physical component) and connect the virtual component with the physical component.

The realisation of the interaction and user interface can vary depending on the application. In any case, the solution must meet the requirements of the application and the user, while providing natural and unobtrusive interaction. Besides cameras, infrared sensors and environmental sensors as well as strain sensors, often IMUs (inertial measurement unit) are used to track the human movement. IMUs and strain sensors can partly be integrated into textiles but are normally not specially designed for the integration and connection and the power lines are often not very suitable for human interaction applications.

Textile integrated solutions are particularly suitable, to ensure a natural and direct as well as efficient interaction with the user. Furthermore, the electronics, to realise the sensing and the actuation signal computation and data processing, must fit to the application and enable an inherent textile integrated and portability suitable design. To realise integrated multi-functional elements the whole system and the production of the DE-based element need to be understood and adapted to the specific needs. Additionally, the system structure must be customized to realise the effective use and combine single features of the elements.

The main object of vision for the present work are multifunctional systems, which should show the main features of an above-described intelligent assistance tools. The smart-material based elements should include, on the one hand, the ability to sense user input and, on the other hand, the ability to provide haptic and/or acoustic feedback to the user in a highly integrated manner.

In Figure 2.32 the components of a user interface, combined with parts of the computer system are shown. The input of the user is measured with sensors and transferred via a communication and evaluation unit to the computer system. With the logic and control unit, adapted outputs like a certain perceptive feedback or visualisation elements are controlled.

To develop ‘good’ interaction interfaces – which are easy to learn and easy to use – different kind of hard and software components are needed. The design of the user interface and the manner in which users interact with computerized systems, vary according to the specific system application. The user interface is the part of the computer system which the user uses to undertake some tasks or achieve some goals. The computer system itself is a combination of hard- and software components that receive input from and communicate output to a user, to support the performance of a task (see Figure 2.30). Although the UI is the part of the computer system that enables interaction and serves as a bridge between the system and the user. For the user the interface often builds the complete system, so the user’s view of the system is often limited and based on the experience with the user interface itself [217]. Intuitive interaction with the user is important, both for the acceptance of the entire physical system and the computer system, as well as for the holistic user experience.

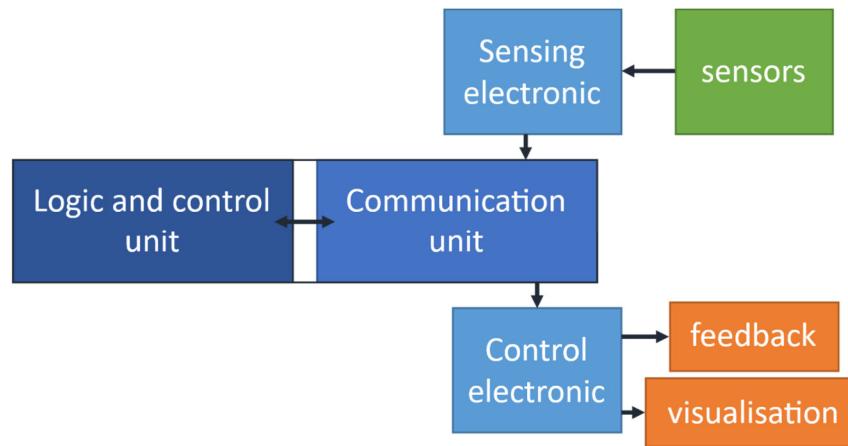


Figure 2.32: Structure and components of interaction interfaces. The sensor combined with a certain sensing electronics is used to measure the user input. A communication unit manages the interaction to the surrounding periphery and the internal electronics (sensing and control electronics). The control electronic drives the output elements for the interaction with the user.

2.3.2. DE based User-Interface Design

User interfaces which are based on dielectric elastomers have the same structure. One main advantage of DEs is the, already described, possibility to use them as sensor and actuator at the same time and within one single functional element. In Figure 2.33 the adapted scheme for the UI, realised with DETs is shown. The DE is used as a sensor, with a specific designed measurement electronics and an actuator, with corresponding control and high voltage electronics, is used as feedback unit. The other parts of the CPS remain the same as for general interaction interfaces.

The individual components are discussed in more detail in the following sections. Furthermore, concepts for textile integration of the components are considered.

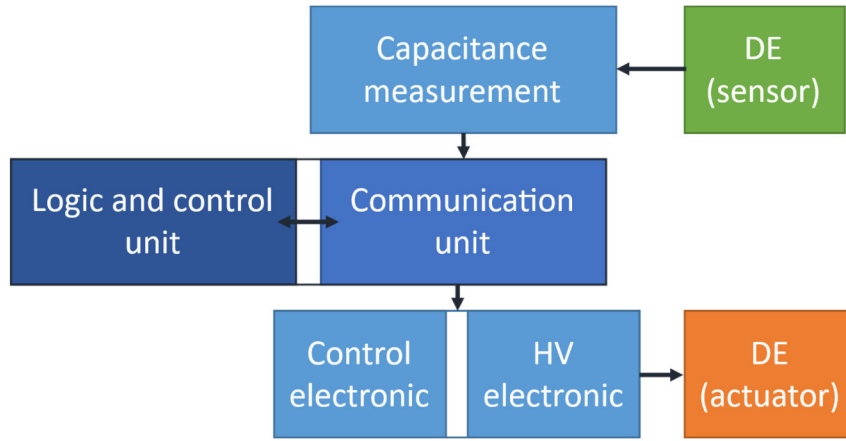


Figure 2.33 Structure components of DE-based interaction interfaces. The DE sensor combined with certain sensing electronics (capacitance measurement) is used to measure the user input. A communication unit manages the interaction to the surrounding periphery and the internal electronics (sensing and control electronics). The control electronic drives the high volt power amplifier to control the DE actuator for the interaction with the user. One DE element can fulfil both works of the DE (sensing and actuation).

2.3.2.1. Sensor design

To measure the input of the user, sensors to measure especially the flexion and extension of the joints and forces applied to an object are needed. Furthermore, sensors to measure even more complex movements or also vital signals (mainly blood pressure, heart frequency, breathing frequency and body temperature) can be realised to present the human being in a holistic image (c.f. [218]).

For the most important UI tasks, relatively simple sensing concepts are usually sufficient. In the following, concepts for position sensing and force sensing are shown as examples. The DE element must fulfil some requirements like resistance to environmental influences; mechanical stability; insensitivity to moisture, heat, and dirt; reproducibility; high resolution; low force-displacement hysteresis; adaptable sensor deflection.

Position sensing

To measure the body position of a user or to measure the state of an input element (e.g. the state of the presented smart button) the capacitance change of the DES can be used. The measured stretch of the DE can be recalculated to determine the position, angle or state of a sensing element. In Figure 2.34 three examples of sensing element topologies are shown, which can be used for user interaction sensing. One example is a strip in plane (SIP) DES, mainly used for lateral stretch sensing. In the context of textile-integrated applications, the SIP-DE geometry finds primary utilization as an angle-measuring sensor to measure the user's joint angle. For textile integrated sensors specifically, angular joint sensors are important to measure the human movement directly.

In Figure 2.34(c) a COP topology, to measure the user's touch intensity in a user interface, is used. Depending on the system structure (e.g. pre-stretch element) the deformation dependent capacitance behaviour can be influenced, to adapt to a specific task or to the actual operator.

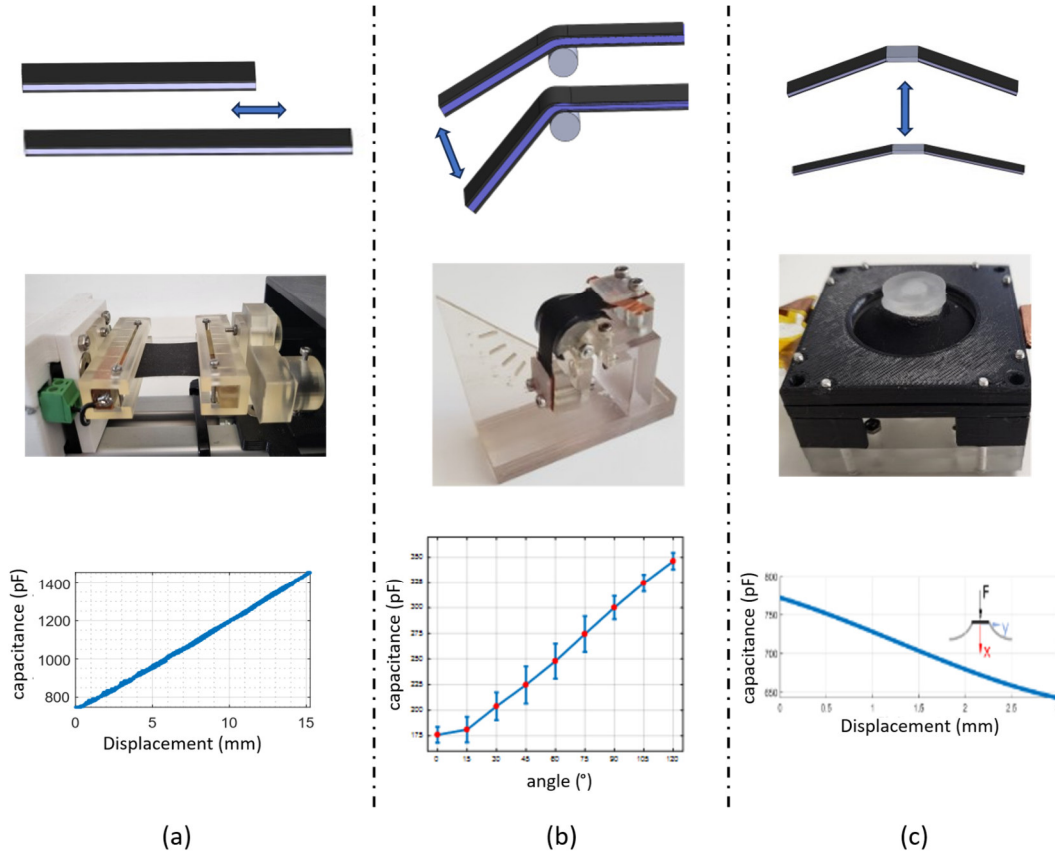


Figure 2.34: Examples of DE sensing elements for (a) strip in plane (SIP) stretch sensing (b) joint angle measurement and (c) user input measurement with circular out of plane (COP) DE.

Force sensing

For many applications, in addition to position measuring, also the force applied by a user is very important. Especially for the interaction with objects, tools or other people, the force is an important parameter to validate the intention of a human, concerning the intuitive handling and interaction. In [219] different use cases for force sensing in the field of human interaction are shown. The examples are mainly focused on industrial applications, but different other fields like medicine and gaming can also be improved by human force sensing.

As discussed in section 2.1.1.1, a capacitance change in the dielectric elastomer can be caused by a change in thickness or by a change of the electrode area. Both phenomena can be exploited for force sensing purpose. To effectively measure forces in a practically useful range, the DE must be combined with an element which transforms the external force into a stretch applied to the DE. In [219] different realisations of force sensing elements are shown, where the different methods result in very different hysteresis properties.

In [215] a concept of structured electrode for force sensing DES is examined more closely in the context of textile-based assistance tools. In Figure 2.35, the capacitance for different geometries and pre-stretches of the DE membrane is displayed. Presented are the mean values of 3 measurements for the used geometries.

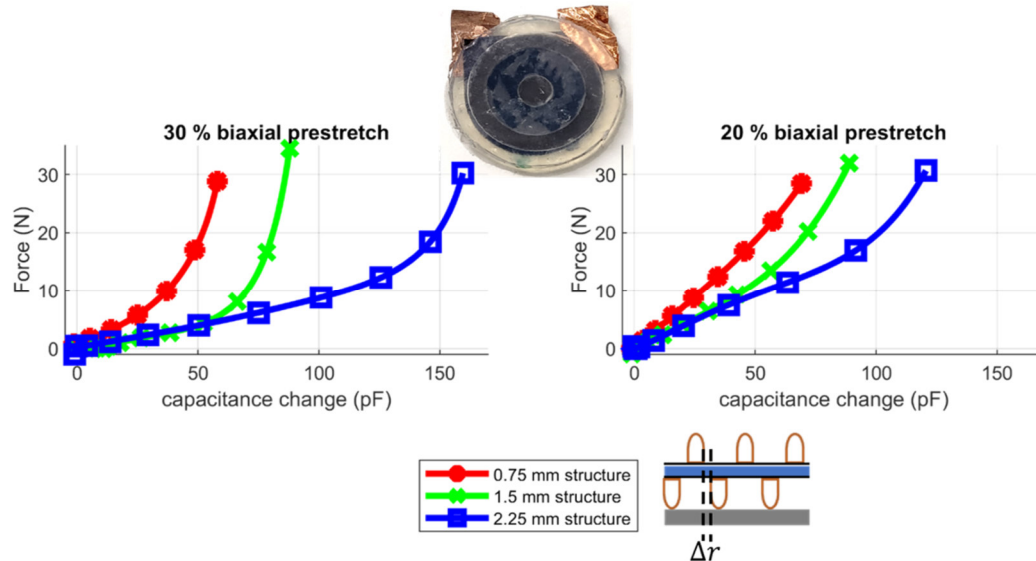


Figure 2.35: Influence of the structure geometry and pre-stretch of the DE membrane to the capacitance-force performance. (a) 30 % biaxial pre-stretch and (b) 20 % biaxial pre-stretch of the membrane. The different structure values characterize the distance Δr between the intersection structures on opposite side of the DE [215].

The measurable force is higher for higher pretensions of the silicone membrane and increase when the gap of the intersection silicone structures becomes narrower. One main characteristic for the later sensor system is the beforementioned hysteresis appearing in the force-displacement characteristics, which causes delays and inaccuracies in the force reading. [219] Moreover, by using patterned electrodes the direction of the force respectively the pressed area can be determined. Therefore, in the test setup a plunger, moved by a linear motor, presses just on one element of a four-segmented DE sensor. All four segments of the sensor are read out and simultaneously the applied force is recorded with a load cell.

In Figure 2.36(a and b), the deformation profile of the motor and the resulting force measured with the load cell is illustrated. For the one segment, which is directly deformed, the force-displacement and displacement-capacitance curves are shown.

In Figure 2.36(c) the capacitance changes of different sensors, with different geometries and pre-stretch of the DE membrane are compared. The capacitance variation is shown in a boxplot with median (middle line in the box) and lower and higher quartile.

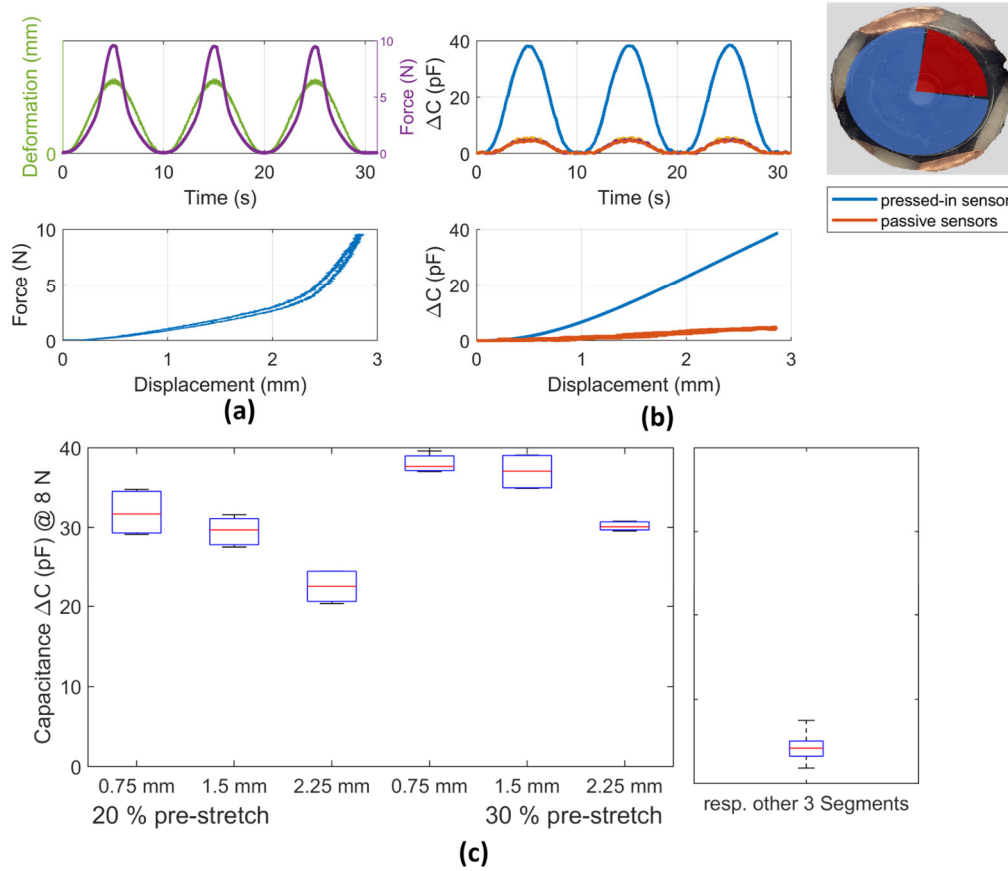


Figure 2.36: Measured deformation of one segment of the force sensor with (a) force and deformation of the pressed sensor segment and (b) capacitance change for the pressed segment and comparison with the capacitance change of the three other segments. (c) capacitance variation for different geometries and pre-stretch of the silicone foil for different sensors [215].

Textile integration

To develop user friendly and intuitive usable user interfaces, the textile integration of the single components is an important factor. The process for the textile integration should be done during the normal manufacturing process of the DE itself. In Figure 2.37 the manufacturing process, including electrical connectors and textile integration is shown.

In the process, electrical connectors are glued to the DE electrode with a conductive glue. The DE is directly glued onto the textile, with a gluing layer applied with the same screen-printing process used to apply the electrode onto the silicone. By the shown manufacturing processes, an integrated DE-textile composite, with layering of more DEs and electrical connectors can be produced during the DE manufacturing process. Furthermore, the DE stack can be directly applied onto a textile. In that case, the textile (reference composition used: 80 % polyamide, 20 % elastane; 210 g/sqm) first gets pre-laminated with an adhesive layer and then the stacked DE element is bonded to the textile. During the manufacturing it is feasible to integrate electrical connections and electrical boards on the silicone film. By using flexible printed circuit boards (PCBs) and conductive adhesive connections, a compact interconnected system (DE + connectors + PCB + textile) can be produced. With the flexible connection the mechanical stress in the electrical contact can be reduced. The DE element's low thickness (50–70 μm per layer) allows for seamless integration with the textile to create a highly compact composite. [215].

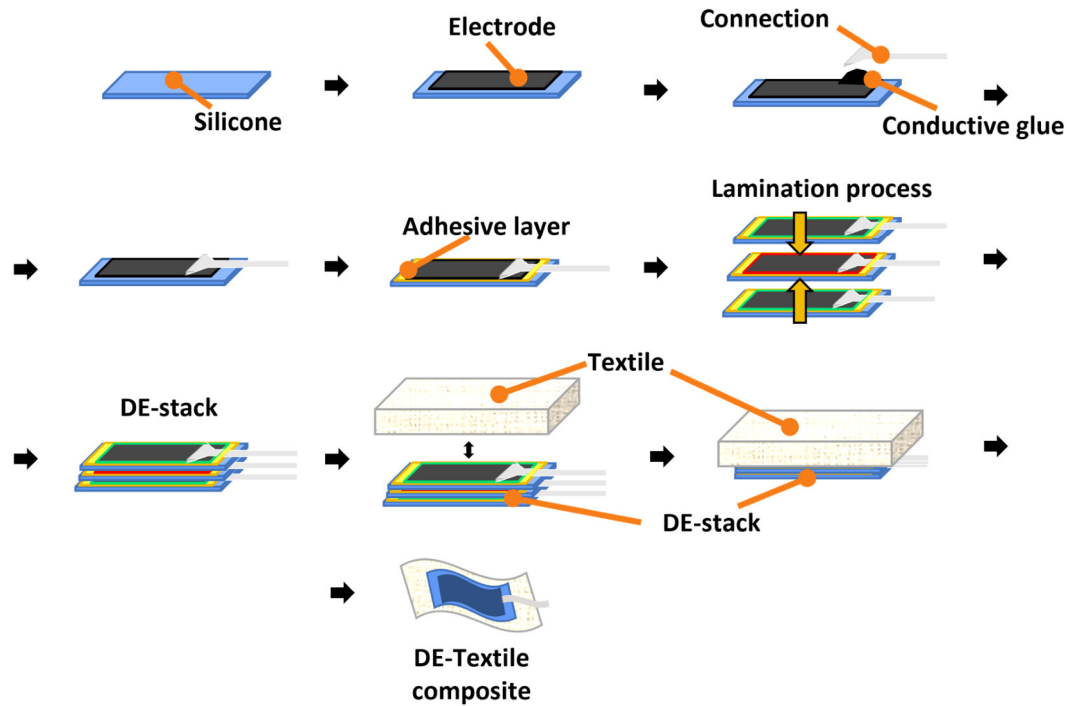


Figure 2.37: manufacturing process of the DE sensing element including DE manufacturing, electrical connection, lamination process, textile integration and mechanical connection [215].

2.3.2.2. Actuator design

To generate a movement or a force, the electromechanical transducer effect of DEs, as described in section 2.1.1.2, can be used. With the realisation of a textile integrated DEA, direct perceptive feedback can be generated. Compared to Figure 2.30 in section 2.3.1, with DEAs it is possible to generate tactile feedback with a wide frequency range and additionally acoustic feedback to a user, so two main parts of the feedback loop can be given by the DE technology.

To generate a reasonable actuation with a DEA it is important to compensate the inherent stiffness of the material and apply a high voltage accordingly. The stiffness reduction can be achieved with a biasing force system, which can be specifically adapted to the DE material stiffness. The most important biasing mechanisms are mass, stiff pre-stretch element (hard stop), linear spring, magnet and negative rate bias spring (NBS). In appendix A.3 the different actuator design concepts are shown, and the force output of the system is described.

Textile integration

To integrate tactile actuators into textiles various factors must be considered. One aspect is simply the fixation to the textile. This can be achieved in various ways. A similar way as for the DES is glueing of the DE element onto the textile (see Figure 2.38). To enable a force transmission to the skin and hold the pre stretch of the DE a stiffer frame is necessary. For example, silicone can be used as material for the frame. The silicone frame can thus fulfil several tasks. The frame can be used as glueing and connection element, hold the pre stretch of the DE and transmit the force to the skin, protect the skin from the HV and additionally hold the electrical connections. In Figure 2.38, a sample structure of a textile integrated DEA element is shown. Depending on the actuator

principle and force direction, further elements for pre-stretch or force transmission are needed. However, simple implementations with silicone parts only, are possible.

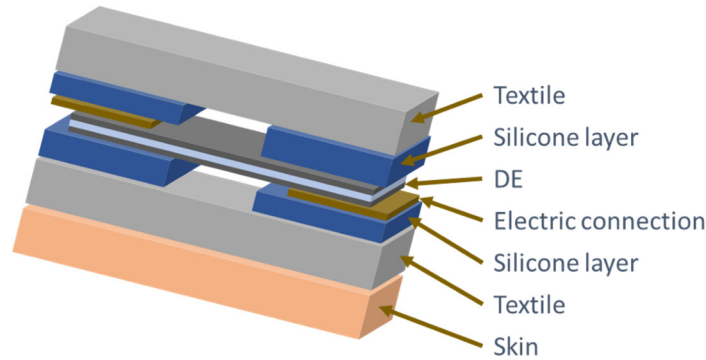


Figure 2.38: Textile integrated DE element with silicone frame. The DEA is encapsulated between two silicone layers and connected to the textile.

In Figure 2.39 the process from the DE production to the system integration of the whole actuator is shown accordingly. In a similar way as shown in Figure 2.37, the DE manufacturing process and the textile integration of the DEA element can be realized in one process chain. For the actuator integration a few more points and parts must be considered, like the shielding of the human skin from the high voltage, the high voltage connections and the pre-stretching of the DE element. Therefore, additional to the procedure in Figure 2.37 a protection layer is added between textile and DEA element and a pre-stretch element is integrated.

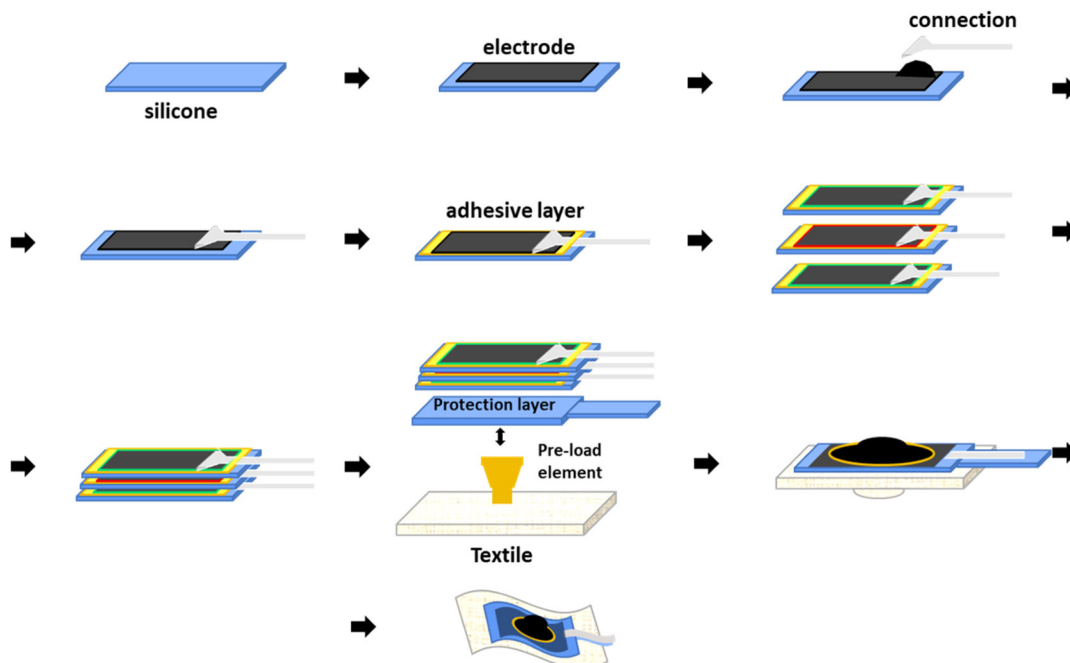


Figure 2.39: Textile integration and connection of DE actuator elements from single DE manufacturing to system integration of the whole actuator.

In the simplest way the pre-stretch element is just a fixed size spacer and, to increase the performance, a pre-load element (biasing) like those described in A.3 can be integrated. The integration of the pre-load element makes the process and the design of the textile (pre-tensioning; geometry) much more complex, compared with the sensor integration. For the use of DEAs, in most cases more layers are needed, which makes the whole construction stiffer and thus more difficult to

integrate. The showed procedure for one single element can also be used for more elements and for example arrays of DEA actuators and sensors.

2.3.2.3. Communication electronic design

Beside the specific sensing and high voltage electronics, an electronic for interfacing and controlling the single electronics is necessary. For example, the control electronic can communicate with external computers or visualisation electronics. The electronic receives and validates on the one side the sensing values from the sensing electronic and controls correspondingly, based on implemented scenarios, the high voltage electronic. Furthermore, the communication electronic can be integrated in a more complex scenario, for example industrial environment, to control the DEA accordingly. In [220], for example, the multifunctional DEA is combined with a neuronal network based human sensing algorithm (heat detection) to expand the DE sensing. In Addition, an intelligent calculation for the output signal and a closed loop control based on the sensing values can be realised

In Figure 2.40 an example of a communication board is shown. Beside the capacitance measurement electronics, a main microcontroller is integrated to execute the control logics, handle the communication, read the sensor data and calculate a certain control signal for an external high voltage electronic (see Figure 3.10). Further operations like for example models, based on artificial intelligent (AI) algorithms (e.g. human digital twin), additional sensors and control algorithms can be implemented on the communication unit.

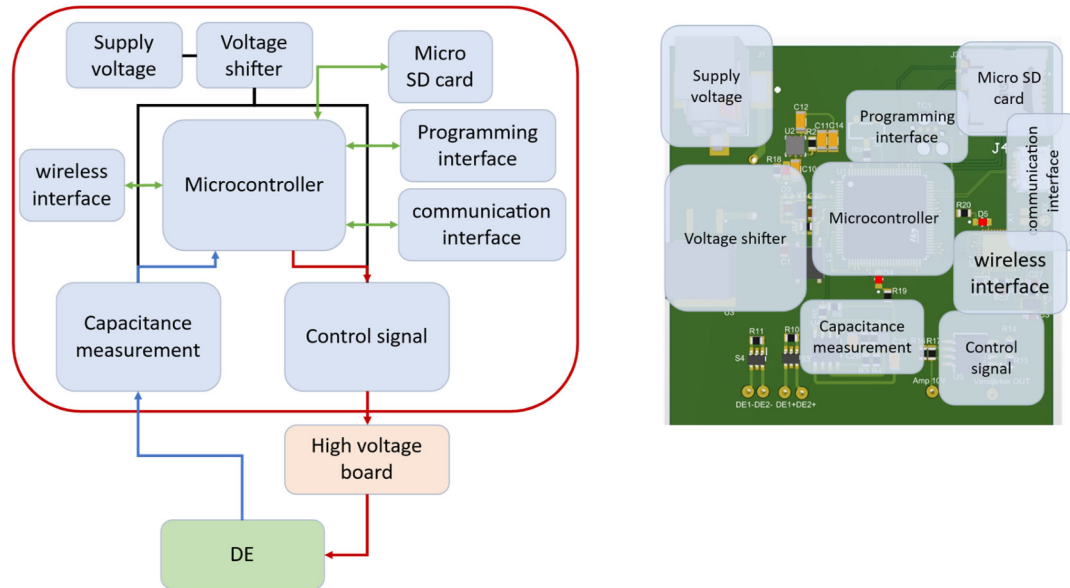


Figure 2.40: Example for a communication main board for user interaction [221].

3. Audio-tactile multi-mode DET development

The main focus of the presented thesis is the development of multifunctional elements, based on dielectric elastomers. The single features of DETs like actuation, sensing and sound generation, described above, can be excited and controlled independently and simultaneously using a single active DE element. This expansion of the standard capabilities of DEs, including integrated self-sensing and textile integration for wearable devices, are investigated in this section. Firstly, the basic topology of the developed multifunctional DET elements and afterwards the developed sensing structure of the DET elements is described. Based on the basic DET structure additionally the tactile feedback capability of the DET elements is shown.

For the validation of the complete new invented multi-functional audio-tactile feedback actuator in a second sub-chapter (section 3.2), based on the basic DET topology the combined audio-tactile feedback capability is systematically developed and experimentally approved. Therefore, the structural vibrations dynamic of DEA membranes is presented, examined and validated by parameter studies. Afterwards, the construction and development of a multi-functional audio-tactile feedback interface is theoretically and with systematic measurements described. In further sub-chapters, the performance with a custom high-voltage electronic is validated (section 3.3), the extension with self-sensing capabilities (section 3.4) is developed and the textile integration of the multi-functional device is realised (section 3.5). All the presented concepts are supported with measurements and characterisations and partly tested with user experiments under real conditions.

3.1. Basic structure of the DET feedback-element

3.1.1. DET feedback-element topology

The considered topology of the DET is a cone DEA ([222], [223]) (compare Figure 2.34(c) and Figure 3.1), which consists of an initially-flat active polymeric membrane mounted, with a certain pre-stretch, on a holding frame with diameter d_o . The central portion of the membrane (with diameter d_i) is attached to a rigid output disc to perform as end-effector. The active membrane is made of a stack of DE layers, including compliant electrodes with alternated polarity (Figure 3.1). Increasing the number of layers allows increasing the actuator's blocking force. In the mounting equilibrium configuration, the membrane is deformed out-of-plane, in a conical fashion, by means of a biasing spring that provides the end-effector with an axial force.

When a voltage difference v is statically applied on the electrodes, Coulomb forces between opposite-sign charges generate an electrostatic stress σ_{Max} , called the Maxwell stress, which acts on the electrodes' plane (along the principal deformation directions) and is proportional to the squared electric field over the dielectric of the DE [224] (see chapter 2.1.1 equation 2.9). This electrostatic pressure is responsible for voltage-driven deformations of the DE membrane [17].

The interface can be used as an active push-button, in which axial movements of the end-effector generated by users' touches can be detected, by means of the sensing layer, and used to trigger vibrotactile and acoustic stimulations by means of the actuation layers.

The device design consisting of 3 actuation layers and a single sensing layer. The sensing layer is used for application-oriented prototype measurements in section 3.2.3 and 3.2.4. For the principle measurements in section 3.2.2, a 3-layer actuator without extra sensing layer is used. In

section 3.3 instead of the sensing layer the self-sensing capability of the DET is integrated, to realise the function of the sensing layer.

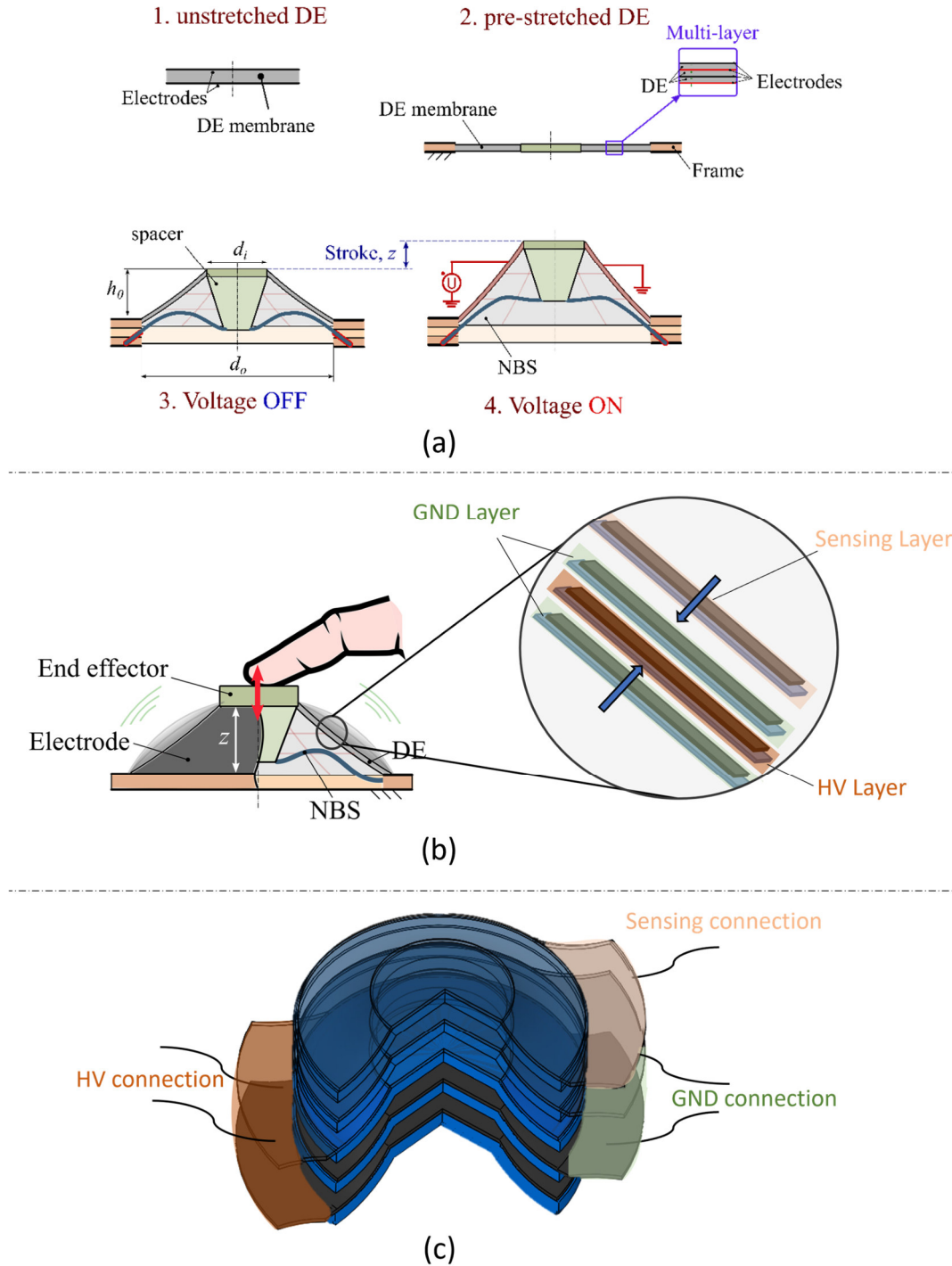


Figure 3.1: Cone DEA setup (a) flat pre-stretched and biased mounting configuration with NBS with and without voltage (b) construction of HV and sensing layer and (c) connection to the single DE Layers (c.f. [216], [225]).

The structure of the DE layering and the connection is shown in Figure 3.1(b). The system has two electrodes connected to ground (GND), two electrodes connected to HV, and (in the extended version) an additional positive electrode for sensing. The actuation and sensing layers share a

common ground. The connections (tracks) between the deformable electrodes and the circuit wires feature the layout shown in Figure 3.1(c). The developed prototype consists of cone DEAs with an outer diameter d_o of 30 mm and an inner diameter d_i of 15 mm. The single silicone layers of the DE (3 actuation and 1 sensing layer) are 50 μm thick. HV and GND tracks run on diametrically opposite sides of the electrodes, whereas the positive sensing electrode track overlaps with the GND track. Thanks to this structure, the sensing electronic can be installed on the GND side and connected to the same GND as the HV electronic, to reduce the required number of GND electrodes.

Applying a low frequency (LF) voltage waveform, results in a linear movement of the end-effector along the device axis. A nonlinear negative stiffness biasing element (NBS) [226] is used as pre-loading element (see section 2.3.2.2), consisting of a metallic buckled beam. In the presence of high frequency (HF) voltage excitations, the motion of the end-effector becomes negligible, as a result of the low-pass dynamics of the device. However, the DE is still able to generate sound by means of the voltage-driven transverse structural vibrations of the membrane surface (Figure 3.2).

Exciting the actuation layers with a multi-chromatic voltage, allows concurrently producing a linear LF actuation and generate sound. In the application, multi-mode actuation is used to provide users with vibrotactile feedback (LF actuation), acoustic feedback (HF actuation) or combinations of the two.

When subject to a time-varying voltage $v(t)$, the cone DEA response changes depending on the frequency content of the excitation voltage. At low-frequency, the DEA shows the same pistonic out-of-plane deformation pattern (i.e., axial displacement of the end-effector) as in the static case, hence behaving as a linear actuator. At high driving frequencies, the motion of the end-effector becomes negligible (low-pass filter behavior), that is, the DEA loses its ability to provide a linear stroke. But the DEA membrane can still generate sound, as a result of the membrane's structural vibrations, that is, it behaves as a loudspeaker.

These different behaviors over different frequency ranges depend on the DEA's dynamics, which follow different deformation patterns (the deformation modes) based on the frequency of the electrical excitation. A set of deformation modes (including the low-frequency pumping mode and the higher-frequency structural modes) are qualitatively depicted in Figure 3.2(a). In contrast to the low-frequency pumping mode, at high frequency the membrane exhibits a sequence of mode shapes, hereafter called structural modes, similar to those observed on flat annular tensioned membranes with fixed rims (see section 2.1.1.3 and [227]). The end-effector motion is negligible for structural modes, since its mass is much larger than the membrane inertia [228]. We denote (m, n) a generic structural mode with m circumferential nodes and $n + 1$ radial nodes (including the central node and the fixed outer rim). Axial-symmetrical modes have no circumferential nodes, that is, they are of type $(0, n)$ (compare section 2.1.3.3).

The ranges where the cone DEA exhibits either an out-of-plane “pumping” motion (linear actuation behavior) or structural vibrations (loudspeaker behavior) depend on the systems dimensions, the relative masses of the membrane and the rigid end-effector disc, the stresses (elastic + electrostatic) acting on the membrane, and the elasto-acoustic interactions (i.e., the air pressure load on the membrane caused by the membrane vibrations [168]).

Based on the frequency response of the DEA hereby it is shown that sound generation is ascribable to the structural modes, with negligible contribution from the pumping mode. Reciprocally, the axial motion of the end-effector filters out high-frequency voltage components present in the

excitation. A broad gap exists between the frequency range where the DEA shows a pumping motion and the range where structural modes are excited. Taking advantage of this feature enables to concurrently use the DEA as a linear actuator and a loudspeaker (Figure 3.2(b)), by separately exciting its deformation modes (the pumping mode and the structural modes) via multi-chromatic input voltage excitation.

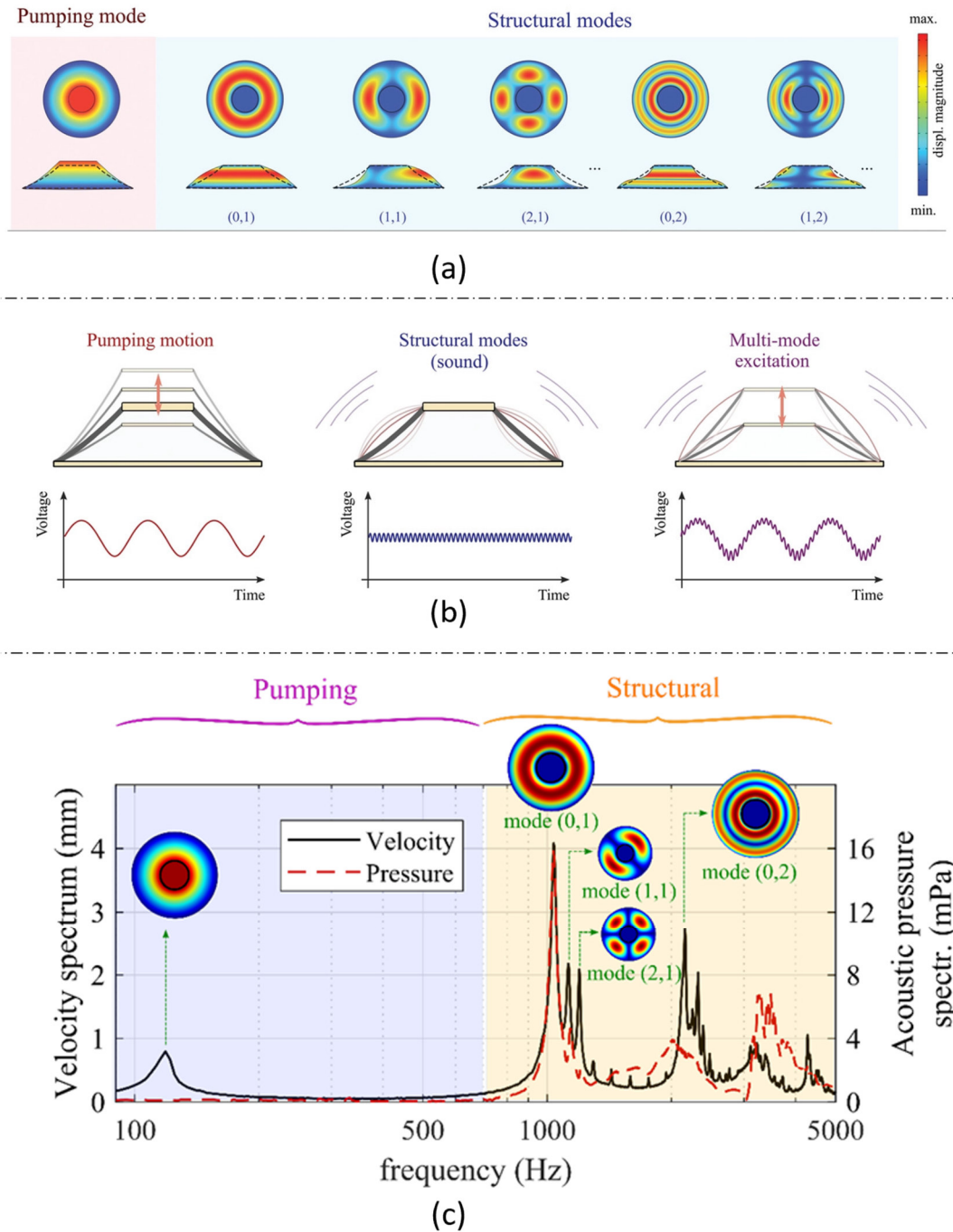


Figure 3.2: Working principle of the audio-tactile element with (a) deformation modes of the DEA (b) motion of the DEA element for LF input, HF input and combined input voltages and (c) spectral of average axial velocity and the resulting acoustic pressure (c.f. [225]).

The vibratory and acoustic response of the DEA can be stimulated using a time-varying voltage $v(t)$, in the following form,

$$v(t) = \sqrt{U_0 + U_1 \cdot \check{v}(t)}, \text{ with } U_0 = V_b^2, U_1 = 2V_b V_k \quad (3.1)$$

where V_b is a constant bias voltage, V_a is a constant excitation amplitude, and $\check{v}(t)$ is an excitation waveform with unit amplitude. The form of $v(t)$ in equation 3.1 is chosen based on the analysed linearized response of the system. Because the DEA responds to the square of the applied voltage (see equation 2.9), a voltage in the form given by equation 3.1 guarantees that the Maxwell stress variations are proportional to $\check{v}(t)$, in spite of the quadratic nonlinearity [110]. The quadratic nonlinearity result in distortions which can be explained by assuming a sinusoidal input voltage $v_{in} = \hat{v}_{in} \cdot \sin(\omega t)$, and the quadratic dependency of the thickness change (compare equation 2.10) can be described with the use of addition theorems of trigonometric function as

$$\Delta L_z \sim v_{in}^2 = \frac{1}{2} \hat{v}_{in}^2 + \frac{1}{2} \hat{v}_{in}^2 \cdot \cos(2\omega t). \quad (3.2)$$

where the deformation in the z direction ΔL_z is proportional to the square of the applied voltage. By using a bias voltage (to enable symmetrical signal shapes) the input signal has an additional term

$$\begin{aligned} \Delta L_z &\sim (v_{bias} + \hat{v}_{in} \cdot \sin(\omega t))^2 \\ &= v_{bias}^2 + \frac{1}{2} \hat{v}_{in}^2 + 2 \cdot v_{bias} \cdot \hat{v}_{in} \sin(\omega t) + \frac{1}{2} \hat{v}_{in}^2 \cdot \cos(2\omega t). \end{aligned} \quad (3.3)$$

using equation 3.1 leads to a linear behaviour of the movement and conclusion of the sound output, by assuming equation 3.3 [110]. The cosine argument with the doubled frequency is in this assumption the only disturbance of the signal. Notice that, if $V_k \ll V_b$ (\hat{v}_{in}^2 is neglectable in equation 3.3), then $v(t) \cong V_b + V_k \check{v}(t)$, that is, V_k roughly represents the amplitude of the time-varying component. For high biasing voltages and low high frequency amplitudes the disturbance is relatively low.

Concurrently the spectra of the average velocity on the DEA surface (DE membrane + end-effector) and the acoustic response are measured (Figure 3.2(c)), setting $\check{v}(t)$ equal to a periodic chirp [119], [228].

The velocity spectrum (solid line in Figure 3.2(c)), measured with the laser Doppler vibrometer described before, presents a series of peaks corresponding to the different mode shapes of the DEA. The abscissa of the peaks roughly represents the natural frequencies of the associated modes. In the range below 600–700 Hz, the velocity spectrum has a single isolated peak in correspondence of the natural frequency of the pumping mode (119 Hz). At higher frequencies, the spectrum presents a set of peaks with high modal density, associated to the membrane structural modes (see Figure 3.2(a)). The first structural mode, namely (0,1), has a natural frequency of 1038 Hz. In the range under investigation (below 5000 Hz), the maximum average velocity is reached in correspondence of the axial symmetrical modes (pumping, (0, 1), (0, 2)). Although the DEA has an axial symmetrical shape, peaks corresponding to the non-symmetrical modes, for example, (1, 1), (2, 1), are also present. These are excited as a consequence of inhomogeneities in the layers thickness or higher order effects (e.g., aerodynamic loads or gradients in the voltage distribution due to the electrodes resistivity and the electrodes' connections to the circuit [229]).

Because of the large inertia of the end-effector (compared to the membrane mass), the natural frequency of the pumping mode is much lower than the natural frequencies of the structural modes, the end-effector displacement practically falls to zero in the range where the structural modes are excited. The acoustic pressure spectrum (dashed line in Figure 3.2(c)) shows that the

DEA generates sound in the mid/upper-mid regions of the audible band. In particular, no acoustic output is generated in the range below 700 Hz, that is, sound is only generated as a result of the structural modes (with the passband of mode (0,1) representing the cut-in frequency for sound generation), with negligible contribution from the pumping motion.

This observation is confirmed by comparing the sound pressure level (SPL) generated by the DEA in free and blocking conditions (compare Figure 3.26), with the end-effector free to move or locked in a fixed position respectively. The SPL generated by the free DEA at a given bias voltage V_b is close to that measured in blocking conditions with the DEA subject to the same out-of-plane displacement as that measured in free conditions at that same bias voltage. Sensible differences (>2 dB) between the free and the constrained cases are only present over specific frequency ranges (e.g., 2300–3000 Hz) and they are ascribable to mounting misalignments in the blocking case, which affect the stress distribution over the DE.

The acoustic response is not uniform in the considered frequency range, as a result of the system's modal dynamics. The DEA generates a maximum SPL of 88 dB with bias voltage $V_b = 2$ kV, and 77 dB with $V_b = 1$ kV. This is achieved in correspondence of the natural frequency of structural mode (0,1). Compared to the other structural modes, mode (0,1) generates a sharper peak in the acoustic frequency response, because it features unidirectional (single-lobe) deformations of the DEA, which cause unidirectional alternated compression/expansion of the surrounding air. Increasing the bias voltage causes an increase in the SPL because of the reduction in stress generated by the electric field (Equation 2.9), which causes the membrane vibration amplitude to increase. The decrease in stress due to the voltage also causes the peaks in the acoustic frequency response to shift toward left with increasing V_b .

3.1.2. Sensing structure of the DET feedback-element

To demonstrate the functional principle of the DET in the sensory configuration (feedback modes not stimulated), the described DEA configuration is first measured and validated in the sensory operating mode. The DEA (installed inside the housing described in section 3.2.3) is deformed from its initial equilibrium position towards the flat configuration by means of a linear motor (Aerotech ANT-25LA) connected to a load cell (5 N; ME-Meßsysteme KD34s) on a custom-built tensile tester. Tensile cycles are performed at a frequency of 1 Hz. The force-stroke characteristic shows that the elastic force is on the order of 1.5 N when the DEA end-effector is pushed 3 mm towards the flat configuration. The hysteretic behaviour in the response is due to the DE material's viscoelasticity. During the tensile test, the capacitance of the DE sensing layer was measured with an LCR meter (Rohde & Schwarz Hameg HM 8118). The resulting capacitance profile (averaged values at different strokes) is shown in Figure 3.3 (bottom).

In the considered deformation range, the sensing layer's capacitance varies by approximately 100 pF. Figure 3.3 (top) shows the quasi-static passive force-stroke response of the DEA (with no applied voltage), corresponding to the force feedback perceived by users upon pushing on the interface (in the plot, displacement equal to zero corresponds to the pre-loaded equilibrium position of the DEA with NBS). With the presented principle on top of the pushing force, tactile feedback and auditive feedback is superimposed.

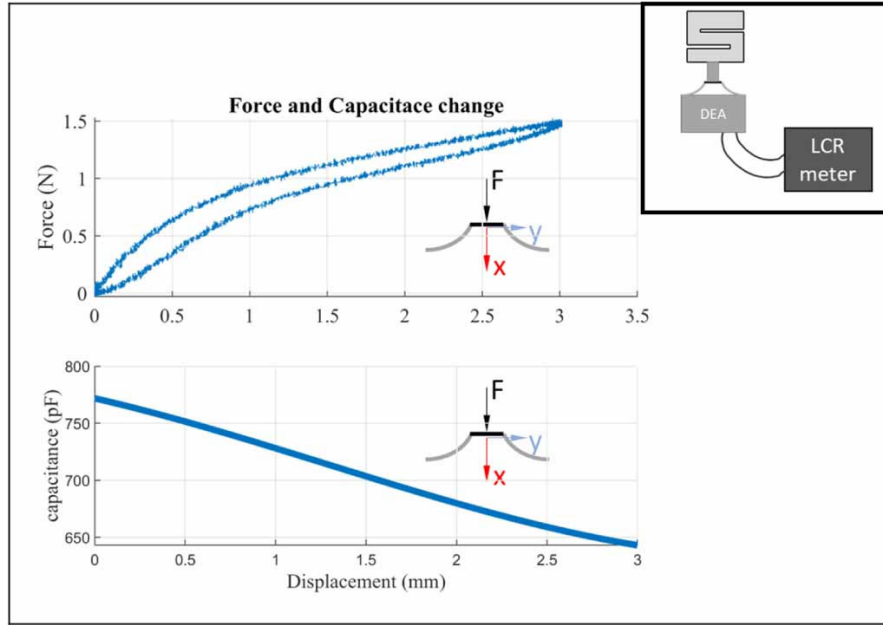


Figure 3.3: Force and capacitance measurement depending on the end-effector deformation ([216]).

Sensing electronic

To use the sensing capability of DEs a sensing electronic is needed. As shown in 2.1.1.1 the DE has a more complex electrical structure than an ideal capacitor. Due to the stretch of the electrode and the relatively high resistance ($>$ several kilo Ohm for typical centimetre-scale devices) the measurement of the capacitance is influenced by the resistance change. As opposed to the capacitance, the resistance has a not monotonic change over the stretch [29] and depends on several external factors like temperature and humidity. This behaviour on one side makes the evaluation of the deformation-related change in capacitance more difficult, but on the other hand, enables the recording of other system variables by using more complex evaluation methods.

The sensing electronic used for this work and in ([215], [216]), performs a measurement of the cyclic charging- and discharging- time as explained in more detail in the following. In Figure 3.4 the function of the sensing principle is displayed and explained.

The capacitor (e.g. the DE sensor) is cyclically charged up to voltage U_{\max} and discharged down to voltage U_{\min} (with $U_{\min} < U_{\max} < U_{\text{supp}}$), and the duration of the resulting cycle, $t_r = t_c + t_d$, given by the sum of the charging and discharging times (t_c, t_d respectively), is measured. By varying the geometry of the DE, the capacitance of the DE changes and the resulting time for a full charge-discharge cycle also changes.

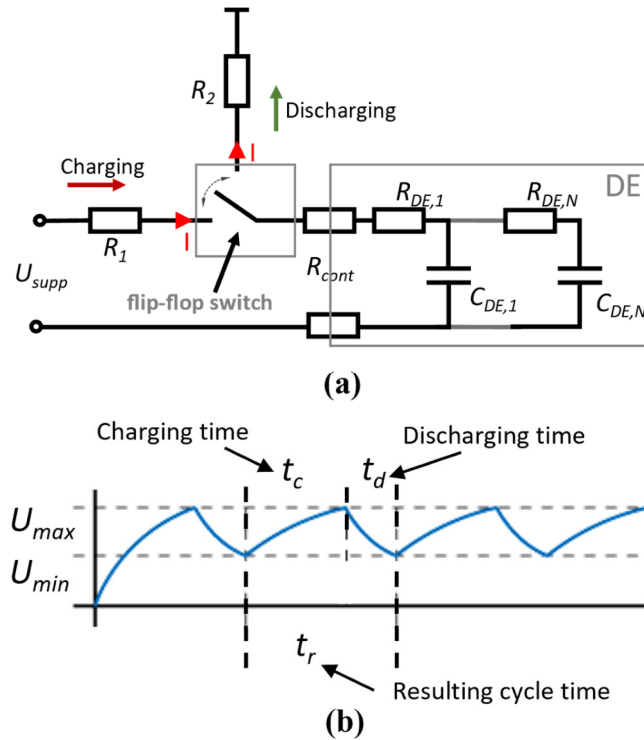


Figure 3.4: Functional principle of the used DE sensing electronic (a) equivalent circuit of the capacitance measurement, (b) charging and discharging time diagram. ([216]).

The current $I(t)$ flowing in the circuit and the DE during the charging transient is

$$I(t) = \frac{U_{supp} - U_{min}}{R_1} \cdot e^{-\frac{t}{R_1 \cdot C_{DE}}} \quad (3.4)$$

where t is the time, and the voltage on the DE at $t = 0$ is U_{min} and the initial current is $I(t) = (U_{supp} - U_{min})/R_1$ where U_{supp} is the operating voltage of the circuit. The charging time is calculated by setting

$$I(t_c) = \frac{U_{supp} - U_{max}}{R_1} \quad (3.5)$$

corresponding to a condition where the voltage on the DE sensing layer is U_{max} , which leads to:

$$t_c = R_1 C_{DE} \ln \left(\frac{U_{supp} - U_{min}}{U_{supp} - U_{max}} \right). \quad (3.6)$$

Similarly, the discharging time, during which the DE voltage is decreased from U_{max} to U_{min} through resistor R_2 is

$$t_d = R_2 C_{DE} \ln \left(\frac{U_{max}}{U_{min}} \right). \quad (3.7)$$

The total cycle time is thus proportional to C_{DE} :

$$t_r = \left[R_1 \ln \left(\frac{U_{supp} - U_{min}}{U_{supp} - U_{max}} \right) + R_2 \ln \left(\frac{U_{max}}{U_{min}} \right) \right] C_{DE}. \quad (3.8)$$

While in practice more complicated relationships between t_r and C_{DE} might apply (owing, e.g., to the DE's compliant electrodes resistance), a monotonic relationship between cycle time and capacitance is expected to hold, which can be identified upon calibration.

The DE sensing is combined with electronics that produce an output that is inversely proportional to the cycle time t_r . Integrated logics recognize how much the sensor is deformed and can recalculate the deformation out of the capacitance change.

Realisation of DE sensing electronic

The sensing electronic can be used to measure the user specific movement and the interaction of the user in DE user-interfaces applications. Furthermore, for example thresholds can be integrated to quantify the user input intensity (see [216] and section 3.2.4).

In Figure 3.5 a realisation of the measurement electronic and a corresponding logic on a flexible printed circuit board (flex PCB) is shown.

Beside the explained measurement unit, a microcontroller to measure the output frequency of the charging and discharging stage and recalculate the capacitance is included, as well as power supply, wireless communication and programming interfaces are included. Additionally, many different sensors or sensor elements can be measured by using multiplexers for example (see [35], [230], [231]).

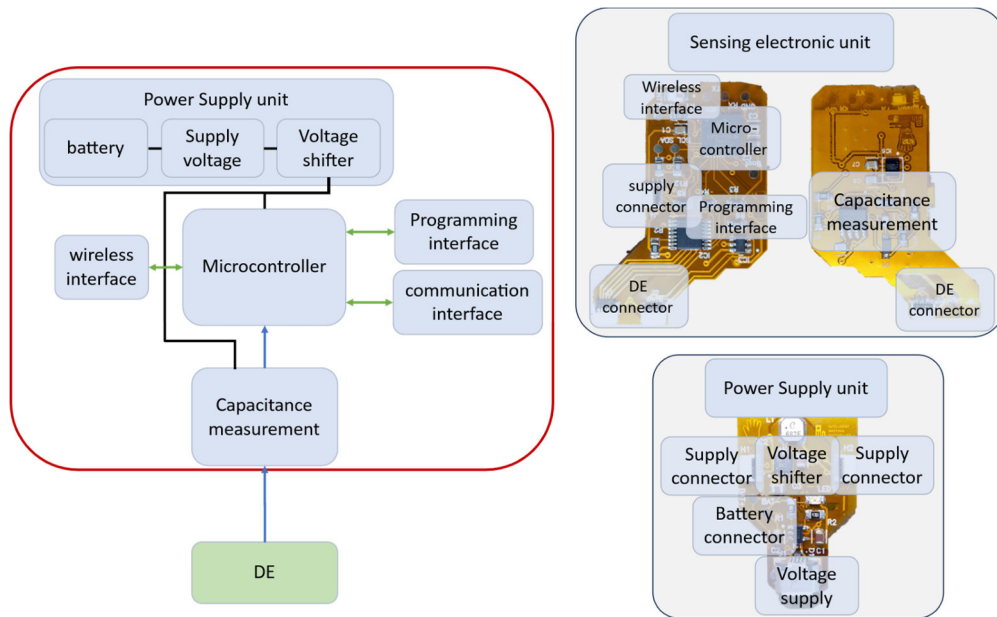


Figure 3.5: Measurement and logic electronic to measure the deformation of a DE on a flexible printed circuit board (flex PCB) [221].

An assessment of the sensing capability of the user interface (DE sensing layer + sensing electronics/logics) is performed, by evaluating its ability to detect and count sequences of user touches (with different intensities and frequencies).

Figure 3.6 shows the sensor output signal (which has the dimension of a frequency, and is inversely proportional to the charging-discharging time of the sensing circuit in Figure 3.4) in response to a sequence of touches impressed on the unit by two different users (left and right column). Each plot reports two sequences of deformations impressed by a same user (red and blue lines). The sensing logics were executed on the microprocessor using three different threshold values in parallel, which were used to count the number of touches. The logics count one touch each time the sensing signal crosses the threshold while decreasing.

Sensing characteristic

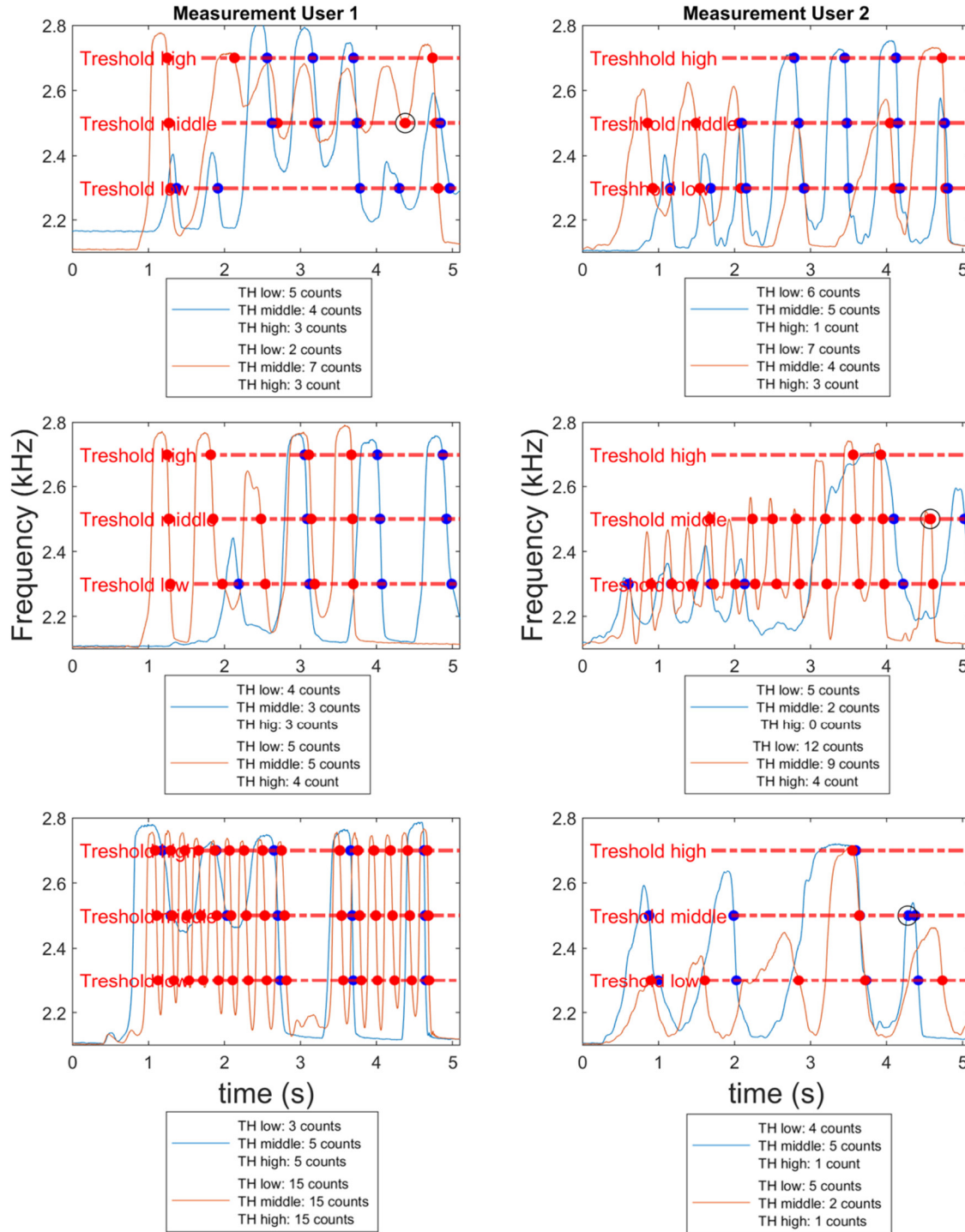


Figure 3.6: Sensing tests with users. Pushing the button changes the capacitance and allows measuring the number of times the interface has been pushed. Counts of the number of touches performed by the sensing algorithm for each threshold are represented with red and blue dots, and wrong/double counts are represented with black markers ([216]).

The results show that the sensing layer and electronics produce a smooth output signal, which in turns allows obtaining an accurate count of the number of crossings of the threshold values.

Different thresholds consistently lead to the detection of a different number of touches: the lowest value of the threshold allows detecting touches of small intensity, but it does not allow distinguishing among consecutive touches unless the user completely releases the end-effector (letting it go back to the initial position) in between consecutive touches. The highest threshold, in turn, allows recognising consecutive touches even when the user does not release the end-effector completely, provided that each touch has sufficient intensity. Wrong counts (in which a wrong estimate of the number of touches was provided, even with the maximum/minimum intensity of the touch lying within the selected thresholds) only happened in a few cases, during which the peak values of the sensing signal felt close to/in correspondence of the threshold values.

For the sake of the tests described in section 3.2.4.3, the threshold are set to the intermediate value among those shown in Figure 3.6 and set a second threshold close to that to prevent wrong counts.

Textile integration

To realise wearable multifunctional user interfaces, besides the DE element itself the electronic needs to be integrated into textiles. A variety of integration options for electronics exist. The electronics, used in the presented applications, is glued onto the textile during or after the DES manufacturing process (see section 2.3.2.1 (Textile integration)). A silicon frame enables flexibility and protects the electronic from environmental influences (Figure 3.7).

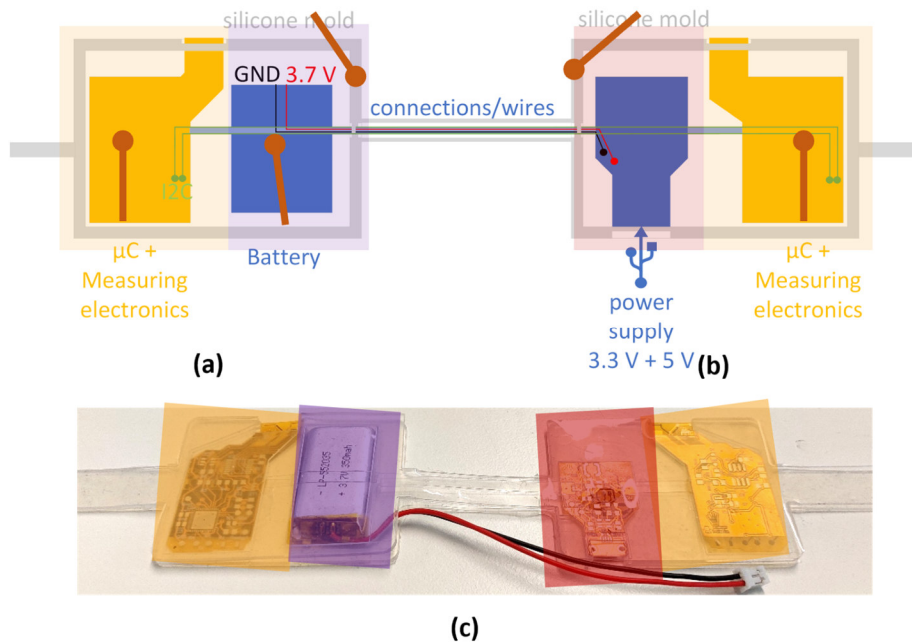


Figure 3.7: Electronics assembly with silicone holder, battery, voltage supply and programming unit and sensing electronic. (a) measurement unit with battery element, (b) power supply and second measurement unit and (c) picture of assembled electronics with silicone holder. ([215] c.f. [231]).

3.1.3. Tactile feedback DET

To generate vibrotactile feedback units based on DETs, the output force and displacement of the unit needs to be higher than the JND (see section 2.2.2, Figure 2.23). To achieve this goal the stiffness of the DE needs to be adapted to the skin, which can be achieved by a negative bias spring (NBS) or another pre tensioning element (compare DE actuator design appendix A.3). Another option is to directly bias the DE element with the human skin. Due to a high variety of the

mechanical skin impedance, depending on the body part, the actuator output can vary with the application. An additional method to pre-tensioning the DEA is the direct use of the textile, where the DE element is integrated in. This new approach is investigated and considered in more detail in section 3.5.

In Figure 3.8 blocking forces for different feedback concepts at different working points over the working frequency are shown. In addition to their different output force, the various concepts have other key distinguishing features such as the application of force (transverse or longitudinal to the skin), size, integration capability in textiles and adaptability.

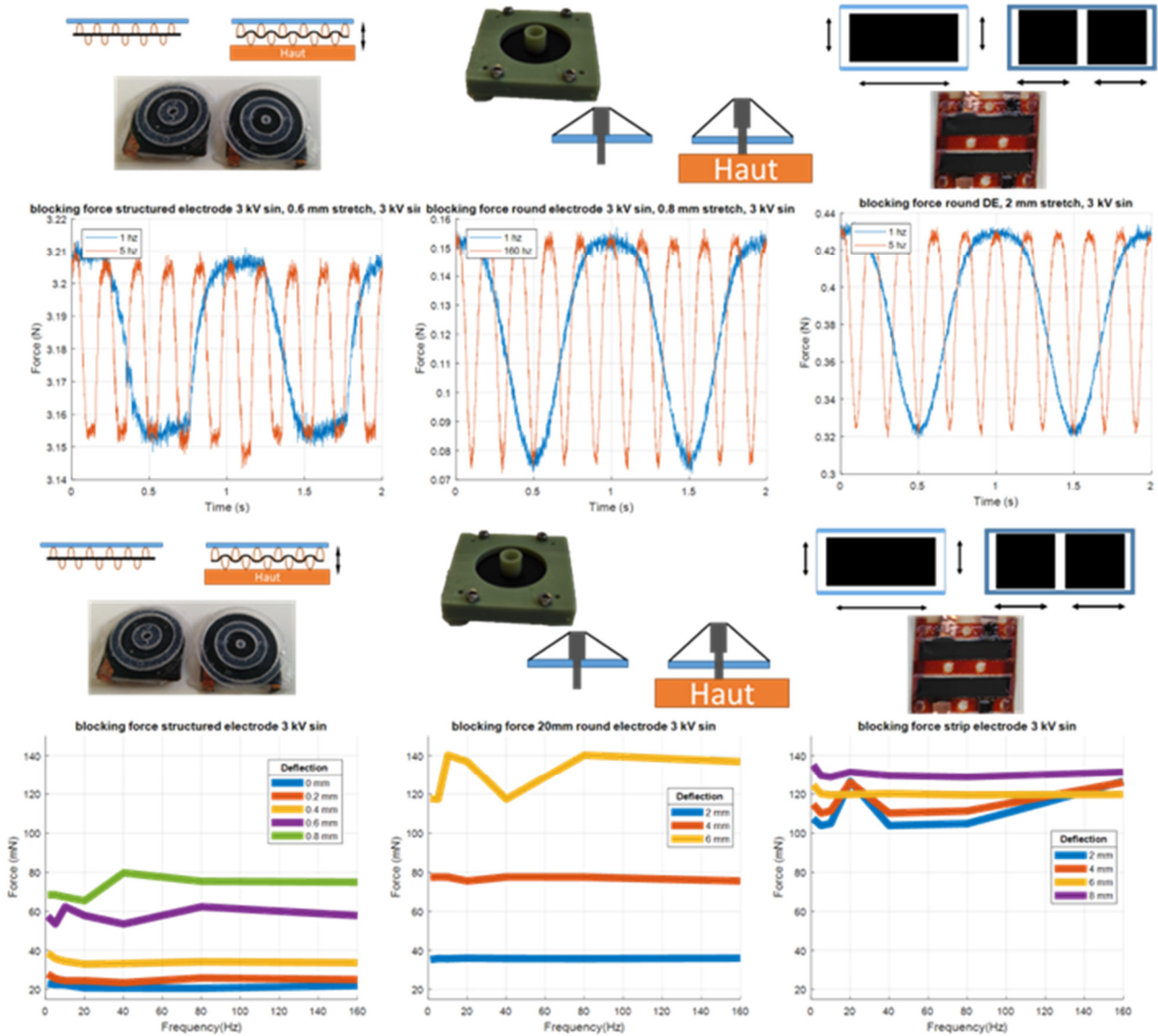


Figure 3.8: Output force of different DEA feedback element topologies, validated with various system conditions (bias voltage, input signal, frequencies and DE pre-stretch).

For the control of DE based tactile elements a voltage range of 0 – 3 kV is normally considered, the frequency range for the vibrotactile feedback is below approx. 350 Hz. The wide frequency range and the flexible control signal (e.g. sin, rect, peaks) are advantages of DE based elements. The considered frequency range corresponds to a low frequency control input signal in equation

3.1. To increase the force output of the feedback element more DEA layers can be stacked on each other.

The in Figure 3.8 considered topologies are exemplary to show the potentials of DEA based tactile elements. For the development and system characterisation in the following the DEA topology described in 3.1.1 is considered.

High voltage actuation electronic

To drive the DE with HV, a controlled amplifier is necessary. To generate the HV, different circuit realizations are considered. With a controlling input-voltage the output-voltage in kilovolt range can be controlled. In Figure 3.9 different realisations are shown.

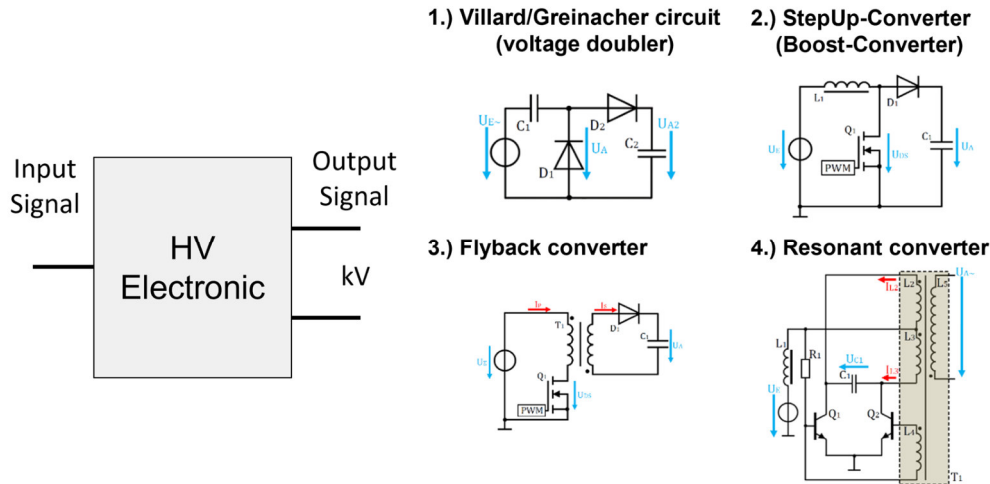


Figure 3.9: High voltage circuit principles and different realisations.

The different realisations can be combined to increase the performance of the HV electronic. To control the output voltage for a capacitive load, additionally to the loading phase, the charge needs to be discharged from the load again. To achieve such a controlled HV output a discharging stage is necessary. The discharging stage can be realised with switchable resistors, to adjust the discharging current. In different publications ([31], [32], [232]) the HV circuit structure as described in Figure 3.10 is developed and described. At the higher component level, the circuit consists of a resonant converter and a rectifier, which can be also a voltage doubler. In addition, a discharging stage is integrated.

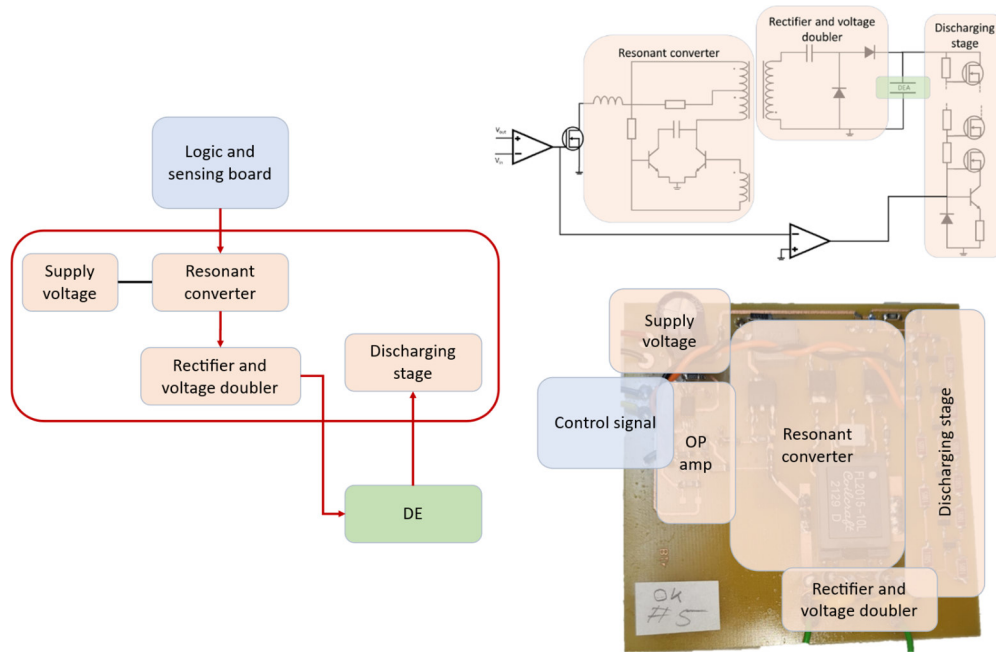


Figure 3.10: Realised HV circuit with resonant converter, rectifier and discharging stage ([221]; c.f. [31], [32]).

Textile integration of the HV electronic

The textile integration of HV electronics has additional challenges compared to the sensing electronics (compare section 3.1.2). However, the principle structure of textile integration is the same as for the sensing electronic (compare Figure 3.7). Important for the high voltage electronic is that the user and the environment are always safely separated from the potentially high voltage signals. In Figure 3.11, to separate the high voltage electronic, a shielding with silicone on both sides of the board is integrated.

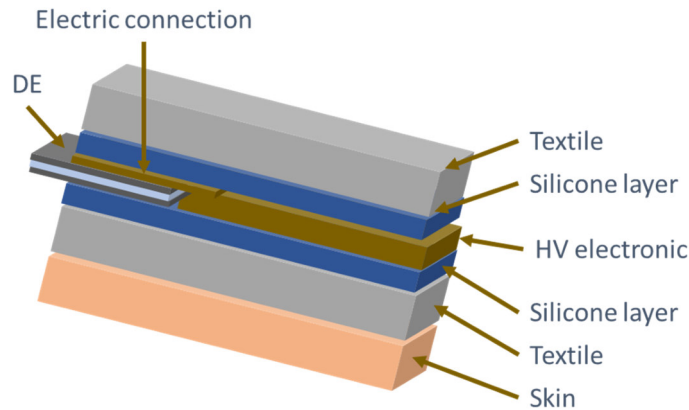


Figure 3.11: Textile integration principle of high voltage electronics.

Since the current driving the DEA and the capacitance of the DEA itself are very low (maximum current output of used HV electronic 10 mA and DEA capacitance ~ 1 nF (for small layer number and DE in the centimetre range)), the potential harm that can provoke to users is negligible. Compared to the safety limits recommended for DEA applications (20 mA continuous DC and > 100 nF) [233], the used high voltage is quite harmless. However, a silicone shielding, needed to

prevent any discomfort due to electrical arching, can additionally be used as fixture of the electronic onto the textile-composite.

3.2. Audio-tactile feedback DET

This section is based on the published papers:

S. Gratz-Kelly, G. Rizzello, M. Fontana, S. Seelecke, and G. Moretti (2022), “A Multi-Mode, Multi-Frequency Dielectric Elastomer Actuator”, *Advanced Functional Material*, Vol. 32, Issue 34, doi: 10.1002/adfm.202201889.

and

S. Gratz-Kelly, T. Krüger, G. Rizzello, S. Seelecke and G. Moretti (2023), “An audio-tactile interface based on dielectric elastomer actuators”, *Smart Materials and Structures*, Vol. 32, Nr. 3, doi: 10.1088/1361-665X/acb6da

A relative unexplored ground, on which DEs might mark a real breakthrough, is that of multi-functionality. This is the combination of multiple independent functions, normally implemented via separate transducers, into a single unit, with the aim of pushing a system’s bounds in terms of lightweight and compactness. Attempts to achieve multi-functionality via DEAs have mostly gone in the direction of self-sensing, which consists in determining a DEA’s force/stroke based on measurement of its electrical state, with no need for external mechanical sensors [84], [88], [234]. This is typically achieved superposing a high-frequency small-amplitude component, on top of the actuation driving voltage, and using the resulting measured current to infer information on the DEA state [88], [235].

In this thesis a principle to develop multi-function DE devices that can concurrently accomplish audible sound generation and linear actuation is developed. The in section 2.3.2.2 described known reference topology of an out-of-plane cone DEA [222], [235] is used (section 3.1.1). Optical measurements of voltage-driven deformations are used to show that the frequency response of the DEA system features two clearly distinct and resolved working ranges: a lower-frequency (LF) range where the actuator features a pumping-like linear motion, associated to the displacement of a massive rigid moving frame attached the DE membrane; and a higher-frequency (HF) range where no motion of the suspended rigid frame occurs, but where higher-order structural modes of the DEA membrane are excited [116], [228]. With acoustic measurements it can be shown that no sensible acoustic pressure is produced, within the passband of the pumping mode, and sound generation is only achieved as a consequence of the HF structural mode excitation [167], [236]. Based on these different dynamic behaviors at different frequencies the concurrently production of a linear motion and generate sound is possible. This is achieved by exciting the DEA with a single multi-chromatic voltage input, including a LF high-amplitude component (responsible for linear actuation) and a HF low-amplitude component (responsible for sound generation) which can be programmed independently. With this setting, a centimetre-scale DEA can concurrently achieve a linear stroke in the millimetre range and sound generation with level over 60 dB at a distance of 0.35 m from the speaker. Dually, blocking the axial motion of the DEA, the membrane can generate voltage-driven blocking force variations in the order of several hundred mN, while still producing sound with a similar pressure level as in the free case.

To practically prove the ability of the DEA to concurrently serve multiple purposes (linear actuation and sound generation) in different operating conditions, different proof-of-concept tests are performed. Including validation that the DEA can reproduce complex audio signals, with level of 60–70 dB, while at the same time producing an axial movement or lifting a load of 20 g (roughly, 200 times the DE membrane mass). Additionally, it can be shown that different sensing methods can be used to provide the DEA with the additional ability to recognize deformations impressed by external loads or user interaction. The methods include electric current measurements, specific additional sensing layer which can be used to measure the deformation with the in section 3.1.2 described capacitance sensing method and direct self-sensing methods during the performed actuation. The subsequent section 3.3 will provide a detailed exposition of the self-sensing performance to develop a tri-mode DEA, which has been designed using the twofold mode previously delineated. . In particular, the DEA can be used to sense the deformations impressed by a user and provide a vibrotactile stimulus combined with superposed sound feedback. Despite their simplicity, these case studies demonstrate that DEA multi-functionality might be used in the future to develop compact lightweight multi-modal interfaces, capable of collocated audio-tactile feedback [24], [237], [238], [239], or buttons with programmable audio and tactile click feedback [240], [241].

The multi-frequency, multi-mode principle proposed here leverages and takes advantage of some general features of DEAs, such as surface-distributed actuation which allows exciting different deformation modes of the same membrane via a single input. Compared to other multi-functional membrane actuators based on polymeric transducers (e.g., ferroelectric and electrostrictive polymers [240]), DEs exhibit a relatively low elastic modulus (on the order of 10^{-1} – 100 MPa, as opposed for example, to 103 MPa of PVDF-based ferroelectric polymers), and can achieve larger stretches (>100%, as opposed to typical maximum values close to 10% for ferroelectric or conducting polymers [242]). This combination of features allows them to undergo large actuation strains (here used to produce linear actuation) while simultaneously being subject to small-amplitude vibrations (leading to sound generation). The specific cone DEA layout considered here (section 3.1.1) further allows obtaining a convenient frequency response (characterized by clearly distinct regions where the DE membrane either features a pumping motion or structural vibrations) for multi-mode operation. Although the cone DEA layout has been largely used in the past separately as a linear actuator in the low-frequency range ([88], [243]) or a loudspeaker, ([97], [228]), this is the first work that proves that the two operation modes can be exploited at the same time. In contrast to other DE loudspeakers, which in most cases rely on a pneumatically-biased bubble-like DEA membrane (compare section 2.1.3.3) ([167], [168], [244]), here the use of a large suspended mass (the moving rigid frame) allows creating a large frequency gap between the band where the DEA provides linear actuation, and the region where structural modes with high modal density are excited and generate sound. In contrast to traditional coil-based loudspeakers with rigid cone diaphragm, the LF pumping motion here does not contribute to generating audible sound in the bass range [169], but produces a usable force/displacement output instead. These features allow producing independent linear actuation and sound generation at the same time by concurrent excitation of different vibration regimes. Audio-tactile interfaces aim to add an acoustic function layer on top of vibrotactile stimulation, so as to convey complex actuation patterns or interaction modes (e.g., the clicking feedback of buttons) in a virtual manner [245]. State-of-the-art solutions for audio-tactile interfaces typically require two separate actuation units for vibration

and acoustic feedback, such as vibration motors and electrodynamic speakers [246]. These units are usually made with stiff and bulky components, and they might be difficult to install close to one another. This would offer limited levels of co-location of the haptic and acoustic stimuli and limited potential for rendering realistic localized scenes [247]. The State-of-the-art solutions for DE based interfaces and tactile, as well as acoustic transducers are presented in section 1.3.

The sensing of deformation can be either performed by using the DEA layers (e.g. current measurement) or can be realised due to an incorporation of a dedicated sensing layer in the active stack. The extra sensing layer allows performing advanced sensing tasks (e.g., distinguishing rapid sequences of user-prescribed deformations) and improves the system reliability. In the concept proposed here, the sensing layer is operated with low voltages, potentially leading to a significant improvement in lifetime. The incorporation of the sensing layer (with its own elastic stiffness) comes at the cost of a moderate reduction in the strain of the active DE stack. But the sensing layer allows maintaining a simple and compact layout for the active DE interface with high sensing capability.

3.2.1. Acoustic response DET membrane vibration

This section is based on the published paper:

S. Addario, S. Gratz-Kelly, G. Rizzello, D. Naso, G. Moretti (2024), “An experimental parametric analysis of the acoustic response in Dielectric Elastomer Loudspeakers”, Journal of Vibration and Control.

In this chapter the structural vibrations and the corresponding sound output of the DEA membrane are characterised and the described theory is validated with parametric measurements. Therefore, different DEA geometries (diameter, thickness and inner to outer diameter ratio) are manufactured and validated under different boundary conditions (stretch, mechanical and electrical operation point, applied voltage).

As already described in section 2.1.1, DEAs can be used as actuators which, in the case of user interaction applications, can be used to provide haptic feedback to users. Furthermore, as shown in section 2.1.1.3, DEAs can also be used as loudspeakers. The different concepts for DE based loudspeakers are explained in section 2.1.1.3. For wearable applications mainly the membrane vibration is predestined for acoustic feedback. In ([59], [174], [248]) the basic concept and simulation of a DEA membrane vibration-based loudspeaker are described.

3.2.1.1. Characterisation of structural acoustic response

The basic mathematical derivation of structural membrane vibrations (mainly for circular based structures) is shown in section 2.1.1.3. In this chapter the basic mathematical derivation is concretized and compared with models published in the literature ([59], [174], [175]) and real measurements.

With using equation 2.19 the structural frequencies can be calculated analytically. From equation 2.19, by linearisation of the DE membrane dynamics, the resulting modal formulation is given by ([59], [175])

$$\mathbf{M}_\alpha \ddot{\alpha} + \mathbf{D}_\alpha \dot{\alpha} + \mathbf{K}_\alpha \alpha = h_\alpha(\alpha) U^2 \quad (3.9)$$

with K_α as stiffness matrix. The displacement of a target point X on the DE surface $u(X)$ can be expressed as a linear combination of shape functions $m_k(X)$

$$u(X) = \sum_{k=1}^r \alpha_k m_k(X) \quad (3.10)$$

As observed in [59], the mass M_α is made of two contributions: one due to the membrane inertia and one due to the added acoustic mass, which is non-negligible for thin lightweight membranes vibrating in air [248], considering orthogonal modes, M_α and K_α are diagonal. It is therefore appropriate to define the natural frequency f_k of the k -th mode as a function of the above-mentioned mass contributions, with the following formulation [174]:

$$f_k = \frac{1}{2\pi} \sqrt{\frac{k_k}{m_k^d + m_k^a}} = \frac{1}{2\pi} \sqrt{\frac{k_k}{m_k^d(1 + r_m)}} = \frac{\bar{f}_k}{\sqrt{1 + r_m}} \quad (3.11)$$

where k_k is the lumped modal stiffness of the DE (associated to mode k), m_k^d is the modal mass due to the DE inertia and m_k^a is the modal air mass contribution [174]. The ratio r_m can be calculated based on a reference configuration r_m^{ref} (DE diameter d_0^{ref} and thickness $L_{z,0}^{ref}$). By considering m_k^d to be proportional to $d_0^2 L_{z,0}$ and m_k^a proportional to d_0^3 the ratio $r_m = \frac{m_k^a}{m_k^d}$ is resulting proportional to $\frac{d_0}{L_{z,0}}$ (e.g. equation 7.5.15 in [170]). The ratio r_m can be expressed based on the reference configuration with

$$r_m = \frac{d_0}{d_0^{ref}} \frac{L_{z,0}^{ref}}{L_{z,0}} r_m^{ref} \text{ with } r_m^{ref} = \left(\frac{\bar{f}_k^{ref}}{f_k^{ref}} \right)^2 - 1 \quad (3.12)$$

f_k^{ref} represents the value of f_k in the reference configuration.

In Figure 3.12 the topology of a reference DE loudspeaker (compare Figure 3.1) as well as the working configuration is shown. Furthermore in Figure 3.12(b) two examples of vibration-modes of the DE membrane (radial symmetric) are depicted.

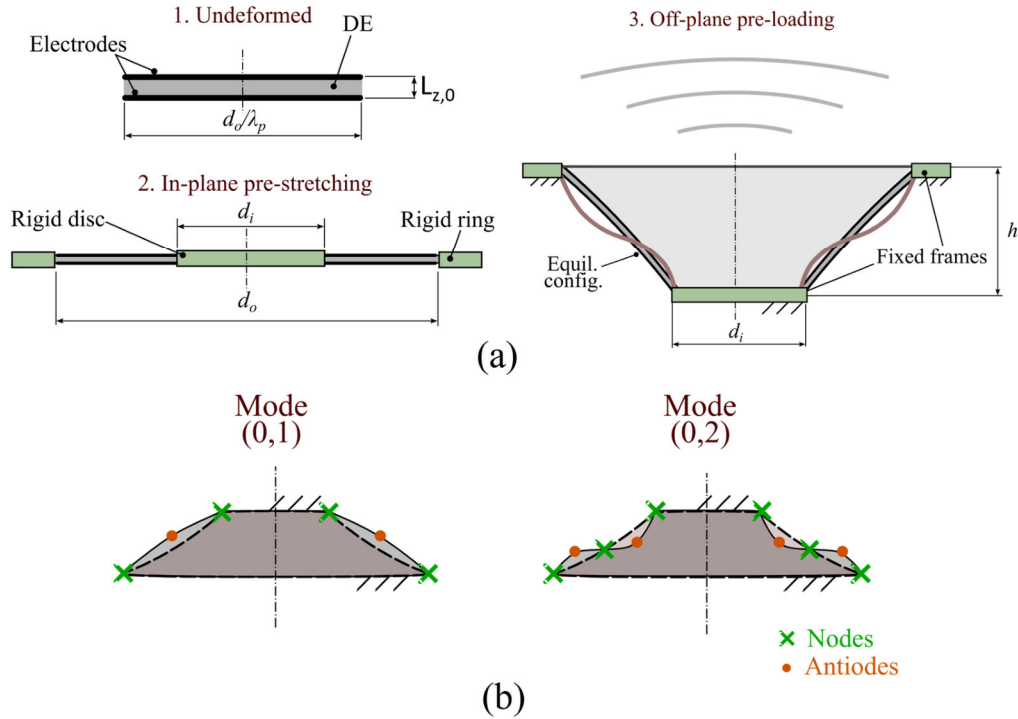


Figure 3.12: (a) Layout of a COP DE loudspeaker with initial in plane pre-stretching and out of plane working configuration and (b) exemplative vibration modes of the DE membrane (c.f. [249]).

In [59] a multi-domain model of the COP-DEA is presented in a way, that the electro-mechanical interaction and the interaction between acoustic domain and the structure of the DE membrane is covered. Moretti et. al. showed in their work that with a fully coupled model, with the structure shown in Figure 3.13, the vibrational modes and the generated sound of a loudspeaker with a topology like in Figure 3.12 can be modelled. The electro-mechanical and acoustic coupled model Figure 3.13 (a) takes the square of the applied voltage v (compare equation 3.1) and calculates the motion profile of the membrane surface (compare equation 3.9) with respect to the modal coordinate α . The subsequent acoustic model calculates the acoustic pressure p at a target point in space. With a linear parameter-varying model (LPV) and the splitting in fast and slow DE dynamic, the non-linear model (equation 3.9) can be reduced.

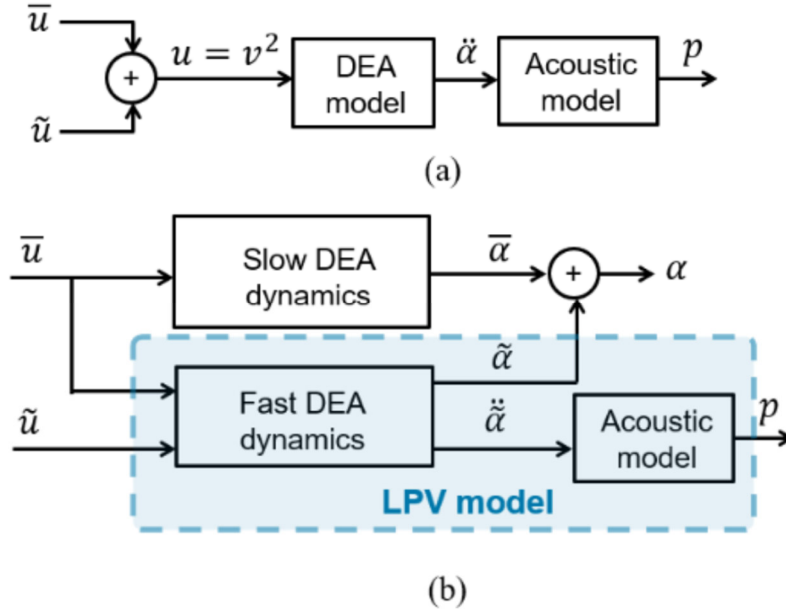


Figure 3.13: Block-diagram structure of the (a) electro-mechanical and acoustic coupled model and (b) the splitting in a slow and fast DE dynamic to realise a LPV model [175].

With the 3D Doppler laser vibrometer PSV-500 3D by Polytec, described in 2.1.1.3, the vibrations of the membrane can be measured. The three heads of the vibrometer allow to measure the velocity components of a target point. With the setup shown in Figure 3.14(b) the vibration of different points on the membrane can be validated and the vibration intensity can be calculated. With different excitation frequencies the vibration modes of the membrane changes, and different structural deformations appear (Figure 3.14(c)).

The model of the DEA loudspeaker bases on a lumped parameter model [250] with an extension of the model for the effect of the acoustic loads on the structural dynamics of the DEA membrane. The in section 2.1.3.3 already described model (Figure 2.8) can be divided in a fast (structural vibration) and slow (macroscopic movement) DEA dynamic model, which allows a model reduction from a ‘fully-non-linear’ electro-elasto-acoustic model to LPV [175].

With the model described in [175] the measured velocity spectra can be simulated with a finite-element-method (FEM) model. The fully-coupled model is able to predict the natural frequencies of the DEA for different scenarios accurately. For different parameters like the voltage, the mechanical biasing as well as the geometry of the DEA, the model can be used to predict the

frequency dependent velocity of the loudspeaker [59]. The coupled model provides a more consistent estimation of the natural frequencies that a pure structural model of the DEA.

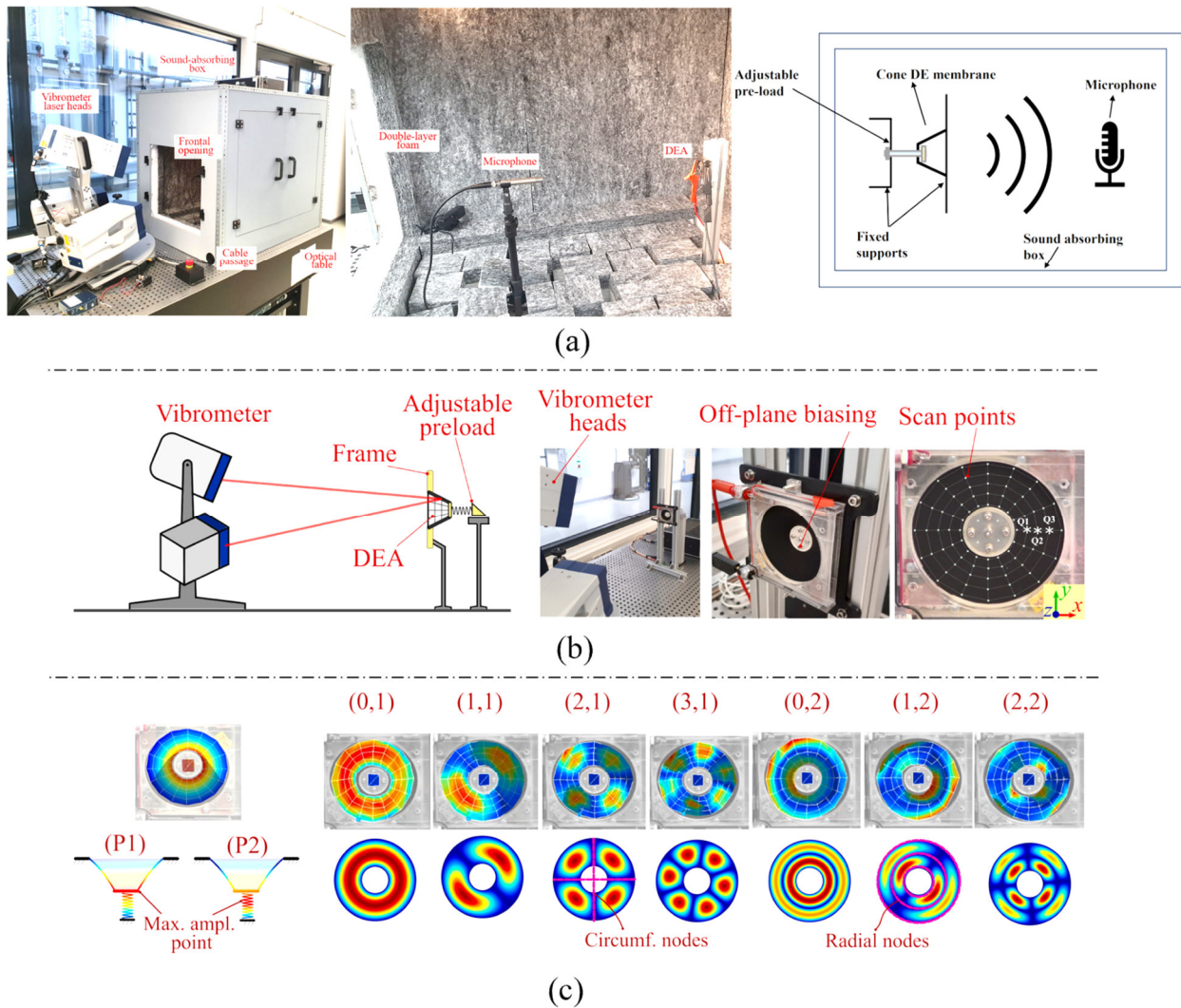


Figure 3.14: (a) Test setup with anechoic sound absorbing chamber for sound measurements (b) schematic and photo of the experimental test bench and distribution of the measurement point. (c) experimental contour plots of the DEA membrane velocity distribution and mode nomenclature (c.f. [59])

In Figure 3.15 the experimental measurements of the membrane velocity and the output SPL are compared with the prediction of the FEM model. The measurement- samples have a 100 μm thick silicone film and an outer diameter of 70 mm with an initial biaxial pre-stretch of 20 % and a an out of plane deformation of approximately 15 mm. The membrane aspect ration $\eta_d = \frac{d_i}{d_o}$ of the two samples is different (0.5 (G1) and 0.34 (G2)) ([59], [174]).

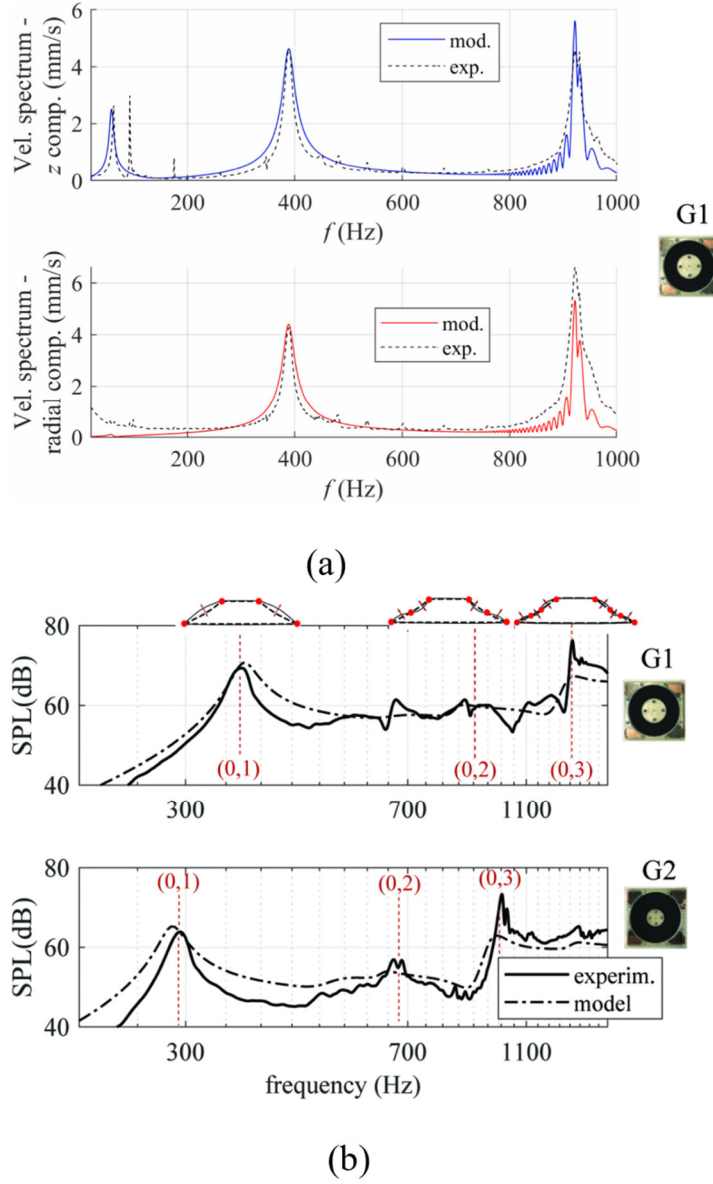


Figure 3.15: Comparison of model (solid lines) and experimental (dashed lines) of the (a) average velocity spectra and (b) SPL of the COP DE membrane. (c.f. [59], [174]).

3.2.1.2. Parameter influence on the acoustic response

With parametric studies of the thickness and the diameter of the DEA membrane as well as the biasing voltage and mechanical biasing of the DEA element, the functionalities and parameter dependencies of structural-vibration based DEA loudspeakers can be shown.

The eigenfrequencies (natural frequency) of membranes vibrating in vacuum scale proportionally to the inverse of the diameter and are independent of the membrane thickness [170]. The eigenfrequency \bar{f}_k for a generic choice of the thickness and diameter of the membrane related to the reference geometry \bar{f}_k^{ref} can therefore be written as

$$\bar{f}_k = \frac{d_0^{ref}}{d_0} \cdot \bar{f}_k^{ref}. \quad (3.13)$$

The natural frequency for the k -th mode-response of the DE can be approximately explicitly expressed by assuming equations 3.11 to 3.13 with

$$f_k = \frac{d_0^{ref}}{d_0} \frac{\bar{f}_k^{ref}}{\sqrt{1 + \frac{d_0}{d_0^{ref}} \frac{L_{z,0}^{ref}}{L_{z,0}} \left[\left(\frac{\bar{f}_k^{ref}}{f_k^{ref}} \right)^2 - 1 \right]}}}. \quad (3.14)$$

Equation (3.14) highlights scaling trends for f_k . Although the DE's eigenfrequencies in a reference configuration might be not immediately available (especially the vacuum natural frequency \bar{f}_k), equation (3.14) still provides relevant insight into the trends associated to the system dimensions. Among others, the equation shows that, as the DE thickness increases, the natural frequency in air asymptotically approaches that in vacuum, as the effect of the acoustic added mass becomes progressively smaller than the DE inertia.

Influence of the membrane thickness

The influence of the membrane thickness on the eigenfrequencies of the acoustic output of the DE can be estimated with equation 3.11. In [174] the frequency behaviour of the DEA for different values of the membrane thickness are shown based on a FE model. With the model the SPL of the membrane is calculated. The frequency and maxima of the SPL increases for higher thickness of the membrane, due to the reduced influence of the air mass (m_k^a). Equation 3.14 shows that, as the DE thickness increases, the natural frequency in air asymptotically approaches that in vacuum, as the effect of the acoustic added mass becomes progressively smaller than the DE inertia.

To validate the model and the influence of the membrane thickness, DEAs with different thickness are measured with the same test rig setup like in Figure 3.14. For the measurement a DE diaphragm, that has a diameter of 30 mm, a fixed out-of-plane deformation ($h = 0.25 \cdot d_0$) and the applied bias voltage of 1 kV, is considered. The effect of thickness scaling, which is achieved by varying the number of layers of the dielectric material (each 50 μm thick), is analysed. A series of experiments was performed to test the consistency of the simulative results [174].

As shown in Figure 3.16(a), the intensity of the first peak sound pressure level (SPL) increases with the membrane thickness. This effect is most pronounced at low frequencies, whereas at high frequencies the diaphragm proves to be less sensitive to aero-acoustic loads. Since the passband of the pumping-mode is low in the frequency range, the acoustic response is mainly determined by the structural mode. The phenomenon of each first peak is attributable to the structural vibration modes of the diaphragm, which consist of a radial movement and a simultaneous axial movement of the diaphragm itself.

An important aspect for the measurement uncertainty is the assembly of the membrane and the consequent alignment of this in the setup, used to conduct the test. In the shown plots at low frequencies the peaks are more pronounced and recognisable, while at high frequencies the trends are much less clear. The observed phenomenon may be attributed to the presence of errors in the assembly of the different membranes, misalignment, or constraint issues. The dashed red curve in Figure 3.16(b) comes from a three-point fitting, starting from the equation 3.21.

Figure 3.16 shows how an increase in thickness simultaneously corresponds to an increase in the frequency of the first resonance peak (natural frequency of the first mode (0,1)) until asymptotically reaching the vacuum resonance frequency of the system.

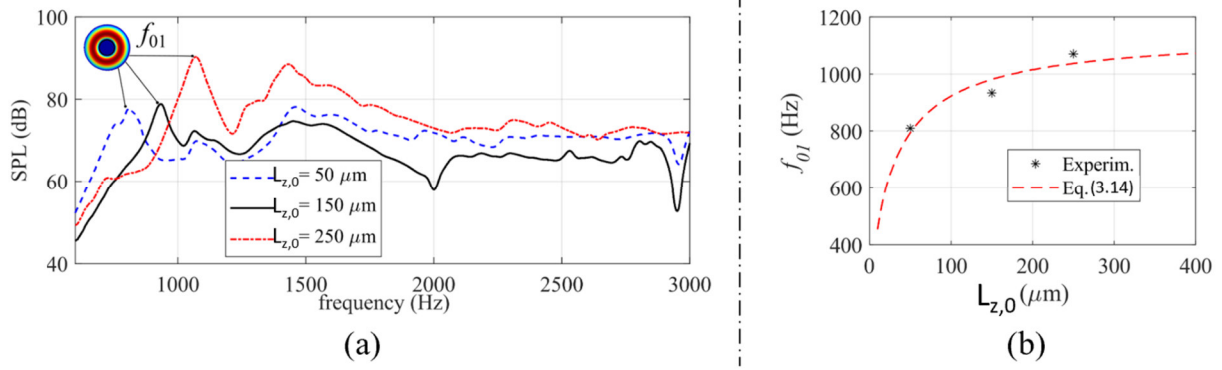


Figure 3.16: (a) measured SPL as a function of the frequency, for different membrane thicknesses; (b) natural frequency of the first mode (0,1) as a function of the initial thickness. Data are relative to a DEA with $L_{z,0} = 30 \text{ mm}$ subject to bias voltage of 1 kV and out-of-plane pre-deformation $h = 0.25 \cdot d_0$ (c.f. [249]).

Influence of the membrane diameter

The scaling of the radial dimensions of the DE influences the frequency behavior of the DEA system. By fixing the boundary conditions of the DE constant (same thickness and applied voltage, proportional out-of-plane deformation $h = \alpha_h \cdot d_0$ and inner diameter $d_i = \alpha_h \cdot d_0$), the frequency of the first mode for different diameter can be calculated with equation 3.14 and is proportional to $d_0^{\frac{2}{3}}$.

The study measurements for validation concerning the variation of SPL as the diameter varies is conducted, while holding constant membrane thickness values ($L_{z,0} = 150 \mu\text{m}$), applied voltage (1 kV) and pre-deformation ($h = 0.25 \cdot d_0$). Figure 3.17(a) shows the first resonance peak of each membrane, and from this trend the corresponding sound pressure scales sub-linearly with the membrane diameter.

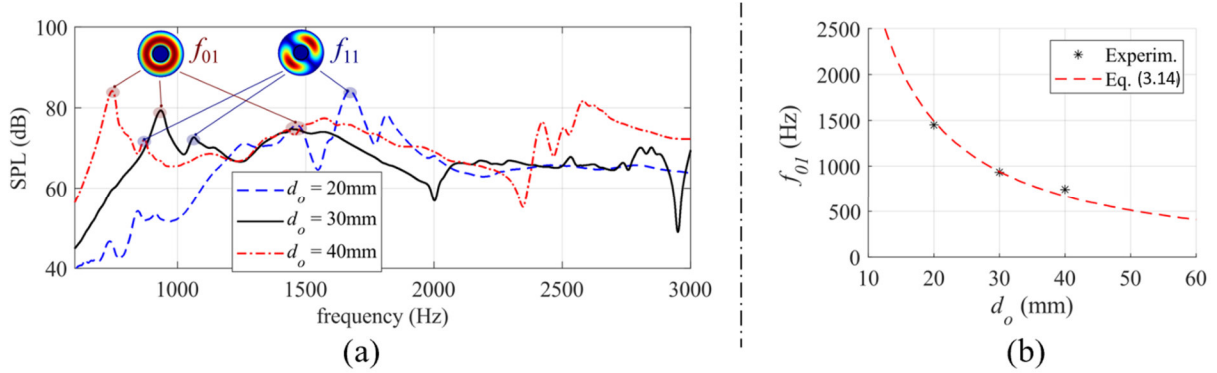


Figure 3.17: (a) measured SPL as a function of the frequency, for different membrane diameters; (b) natural frequency of the first mode (0,1) as a function of the diameter d_0 . Data are relative to DEA with $L_{z,0} = 150 \mu\text{m}$ (3 layers) subject to bias voltage of 1 kV and out-of-plane pre-deformation $h = 0.25 \cdot d_0$.

The modification of the diameter is associated with a change in the acoustic level. However, of greater significance is the alteration in the frequency range within which resonances occur, thereby influencing the operational range of the speaker. The trend of the eigenfrequency of mode (0,1) is shown in Figure 3.17(b) as a function of the membrane diameter and it thus follows, that the experimental results actually trace the curve calculated from equation 3.14. The red dashed curve in Figure 3.17(b) is plotted for the same parameters for Figure 3.16(b).

Influence of the aspect ratio

Besides the outer diameter of the DEA also the inner diameter has an influence on the behavior. In general, the mechanical characteristic and influence of the inner and outer diameter of a COP-DEA can be predicted. With simple equations the force and stroke of the COP-DE can be calculated [251], [252]. The average radial stretch $\bar{\lambda}$ of the DE membrane is determined with

$$\bar{\lambda} = \frac{\sqrt{h^2 + (d_o - d_i)^2}}{(d_o - d_i)} = \frac{\sqrt{h^2 + (1 - \eta_d)^2}}{(1 - \eta_d)} \quad (3.15)$$

where $\eta_d = \frac{d_i}{d_o}$ is the membrane aspect ratio. The stress in the membrane σ can be calculated depending on the force on the DE end-effector F_{DE} and the cross-sectional area of the membrane A_{CS}

$$\sigma = \frac{F_{DE} \sqrt{h^2 + (1 - \eta_d)^2}}{h A_{CS}} \quad (3.16)$$

The thickness of the membrane during deflection $L_{z,d}$ is determined by the surface area of a truncated cone with the assumption of incompressibility of the material with

$$L_{z,d} = L_{z,0} \cdot \frac{(1 - \eta_d)}{\sqrt{h^2 + (1 - \eta_d)^2}} \quad (3.17)$$

This leads to the cross-sectional area of the membrane A_{CS} dependent on the respective DE diameter $d \in [d_i, d_o]$

$$A_{CS} = \pi \cdot d \cdot L_{z,d} = L_{z,0} \cdot \frac{\pi \cdot d \cdot (1 - \eta_d)}{\sqrt{h^2 + (1 - \eta_d)^2}}. \quad (3.18)$$

Inserting equation 3.18 into 3.16 results and substituting 3.15 in the following for the membrane stress at the diameter d

$$\sigma = \frac{F_{DE} (h^2 + (1 - \eta_d)^2)}{L_{z,0} \cdot h^2 \pi \cdot d \cdot (1 - \eta_d)} = \frac{F_{DE} (1 - \eta_d) \cdot \bar{\lambda}^2}{L_{z,0} \cdot h \cdot \pi \cdot d}. \quad (3.19)$$

It can be concluded that the membrane stress (which influences the SPL and the eigenfrequency of the DEA loudspeaker) increases with the stretch of the membrane and is dependent on the aspect ratio η_d .

In Figure 3.18 the mechanical performance for different aspect ratios of the DEA is shown ([252]). The blocking force and stress are dependent on the ratio of inner and outer diameter and on the electrode ring diameter [252]. The frequency response of the membrane shifts toward higher frequencies with increasing stress in the membrane and thus by increasing η_d . Also, the peak value of the SPL increases with η_d which can be explained by the higher electric field applied to the membrane [174].

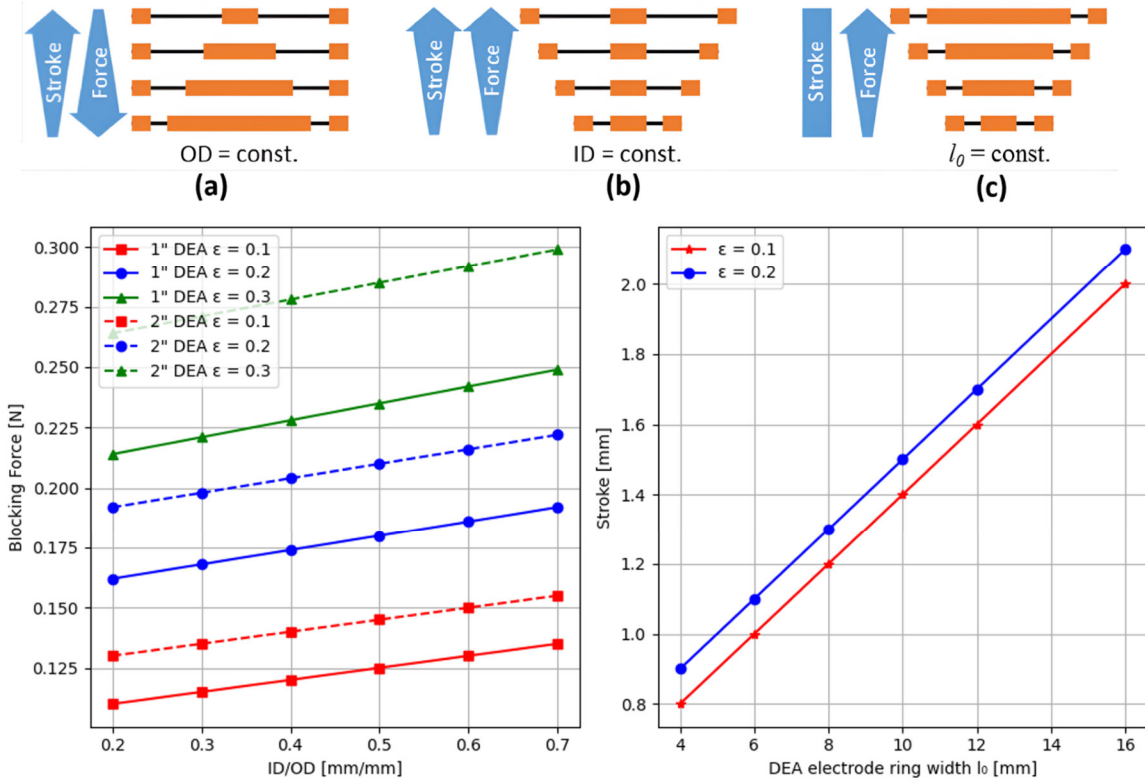


Figure 3.18: Resulting performance of a COP-DE depending on the inner and outer diameter ((a), (b), (c)) with (d) blocking force and (e) stroke (c.f. [252]). The geometries of the six different test specimens used in [252] are : 1'' small (ID: 8.6 mm; OD: 21 mm); 1'' medium (ID: 11.4 mm; OD: 21 mm); 1'' small (ID: 13.5 mm; OD: 21 mm); 2'' small (ID: 8.6 mm; OD: 41.9 mm); 2'' medium (ID: 20.1 mm; OD: 41.9 mm); 2'' small (ID: 26.8 mm; OD: 41.9 mm) ([251]).

By assuming the out-of-plane deformation h to be constant, the resulting electric field in the membrane changes with the aspect ratio η_d . In Figure 3.19(a) the SPL over the frequency for different η_d , shown in [174], is displayed. The dashed lines show the behaviour for a linear compensation of the resulting electric field [174]. In Figure 3.19(b) the eigenfrequency for different η_d is plotted and compared with the analytical calculation of equation 3.11.

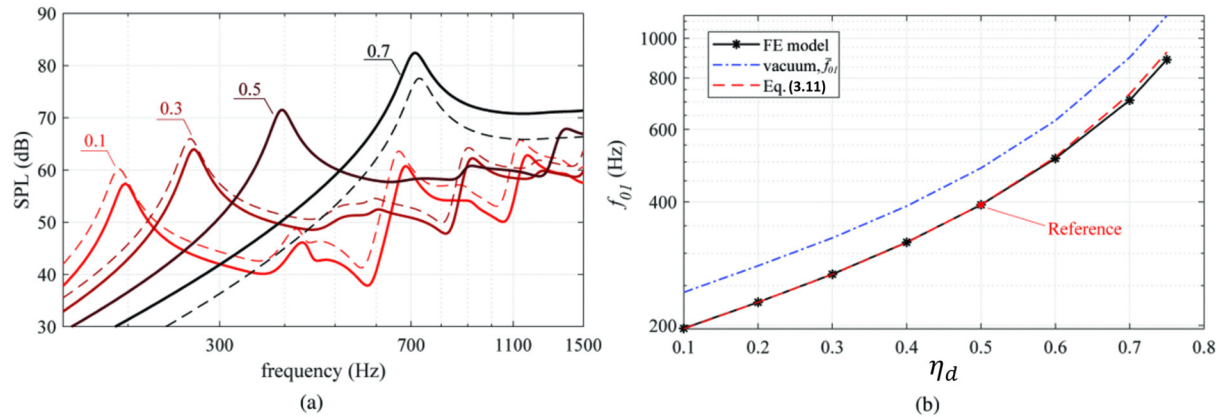


Figure 3.19: (a) SPL as a function of the frequency response of the DE membrane for different values of η_d and (b) function of the eigenfrequency of mode (0,1) as function of η_d (c.f. [174]).

Influence of electrical and mechanical biasing

The effect of the biasing voltage and applied mechanical preload to a DE membrane are investigated in this section. The analysis is carried out keeping diameter ($d_o = 30$ mm) and thickness ($t_o = 150$ μ m) unchanged. In the shown plots (Figure 3.20(a) and (b)) it is the macroscopic trends can be noted, because they are obtained from the same membrane (changing the operating conditions).

The minor discrepancies in aspect ratio that arise due to variations in assembly or dimensional tolerances are circumvented by concurrent production of the samples within the same process. This is accomplished by employing a singular screen-printing screen to facilitate the printing of diverse configurations. The results in Figure 3.20(a) (upper and lower figures) are related to a pre-loaded (2 different configurations: $h/d_o = 25\%$ and $h/d_o = 33\%$) DE membrane subjected to different bias voltages between 1.0 kV and 2.5 kV.

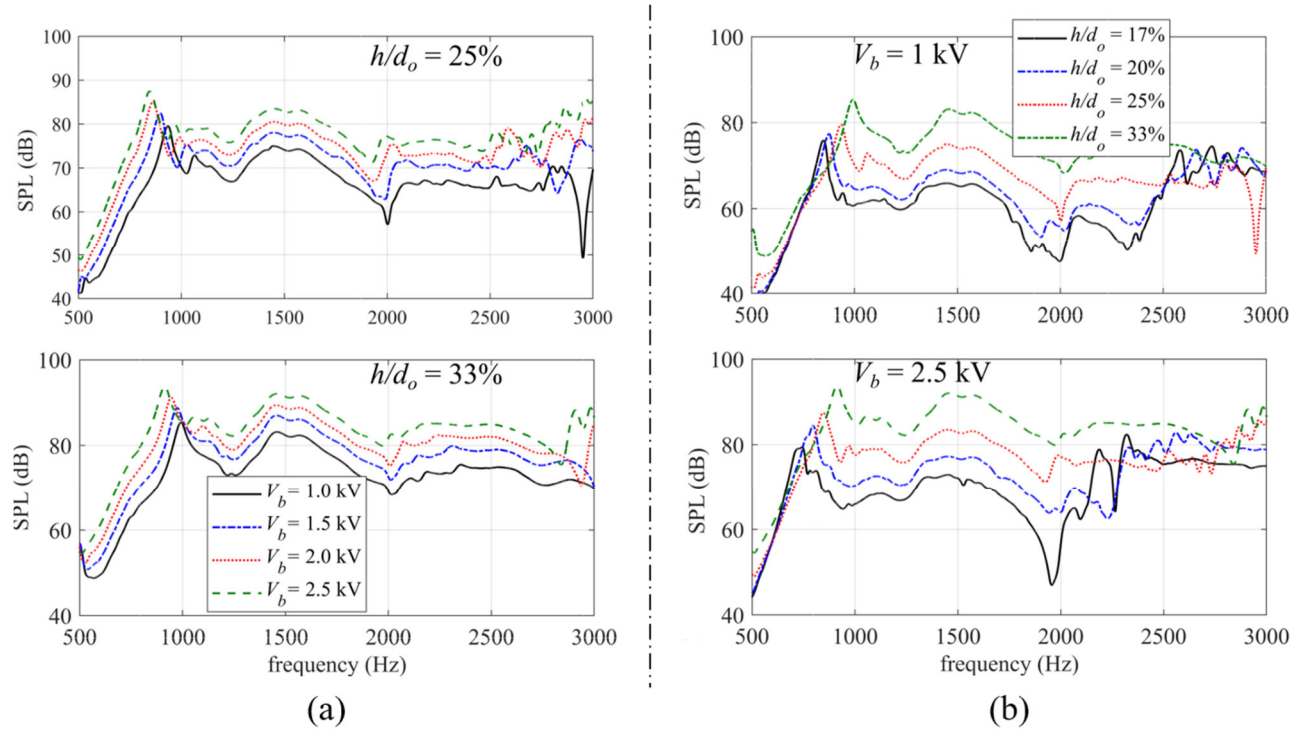


Figure 3.20: SPL as a function of the frequency response for a DEA with $d_o = 30$ mm and $t_o = 150$ μ m subject (a) to constant out-of-plane deformation (top: $h/d_o = 25\%$, bottom: $h/d_o = 33\%$) and different bias voltages; and (b) constant bias voltage (top: $V_b = 1.0$ kV, bottom: $V_b = 2.5$ kV) and different mechanical pre-loads.

The increase in bias voltage generates a decrease in the stress acting on the membrane (due to Maxwell stress) and leads to a reduction in the natural frequencies of the different modes. Furthermore, Figure 3.20(a) shows how the SPL, generated by the membrane, increases as the applied voltage increases. The Figure 3.20(b) (upper and lower figures) shows a comparison of the frequency-SPL trend characterised by different values of applied preloads (d_o/h), keeping the biasing voltage constant. Increasing the d_o/h ratio causes a visible increase in the natural frequency relative to the mode (0.1), because of the increased stress induced on the membrane. In addition, the SPL value is raised over the entire frequency spectrum considered. It can be noticed that the

difference between the natural frequencies that the membrane presents is more pronounced the higher the voltage to which it is subjected and, consequently, the electrical stresses is.

In Figure 3.21 the natural frequency is extrapolated as a function of out-of-plane deformation and applied voltage. The underlined yellow area is the function within which the natural frequency varies. The highest point is almost 992.6Hz (with $V_b = 1$ kV) and the lowest 744Hz (with $V_b = 2.5$ kV), ensuring a natural frequency modulation range of more than 30% when considering the two minimum and maximum peaks.

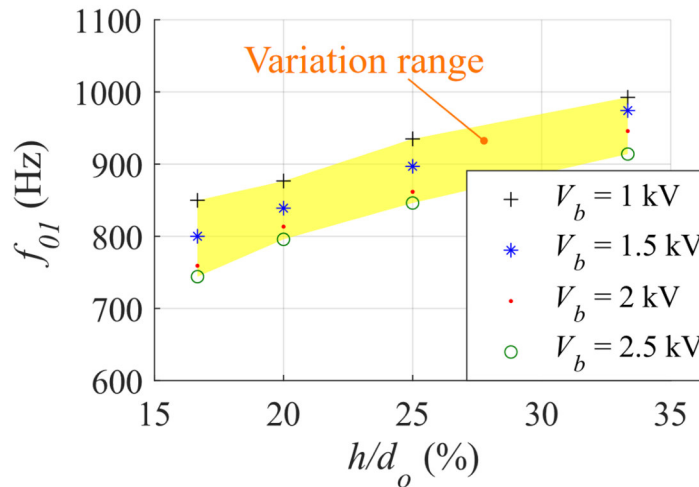


Figure 3.21: Range of variation of natural frequency of the first mode (0,1) for a DEA with $d_o = 30$ mm and $t_0 = 150$ μ m subject to different out-of-plane pre-loads and bias voltages.

Influence of electrode material

A further influencing aspect to the membrane vibration is the electrode material. The electrode highly contributes to the mass of the DE membrane (approx. 33 %, for a 1:1 mass mixture of the electrode (silicone / carbon black) and a (double-sided) electrode of 10 μ m each with a 50 μ m silicone film; The densities are assumed to be 1.2 g/cm³ for silicone and 1.8 g/cm³ for carbon black) and to the thickness of the membrane, which in turn influences the vibration behavior of the membrane. For the manufacturing process, shortly described in section 2.1.2, carbon-black based electrodes with a thickness of roughly 10 μ m are used. To compare the influence of the electrode material a newly developed method for manufacture the DE membrane with sputtered metal electrodes is used ([253], [254]). For the manufacturing the same silicone material (Elastosil 2030 with a thickness of approx. 50 μ m) is used and biaxially pre-stretched (37.5 %) during the manufacturing process. The pre-loaded silicone film is fixed to a metal frame and then coated in a 45x45x45 cm³ vacuum chamber with 10 nm nickel and chrome. The exact manufacturing process and influence of the materials to the performance are described in [254]. In a further step the electrode can be shaped by an ultra-short pulse laser, like shown in [253]. With that manufacturing process it is possible to build metal-electrode DEAs with the same shape than for the conventional process, but with lower thickness and higher conductivity. In the application and for the measurements, the sample can be stretched up to the pre-stretch configuration during the manufacturing process while retaining its full functionality. For higher strain, the metal electrode can be damaged, and the mechanical resistance increases significantly. In Figure 3.22 the mechanical behavior of the two different electrode materials are shown.

The absolute hysteresis of both materials are comparable. Due to the wrinkles which appear at the sputtered electrode the mechanical force is much lower than for the carbon black electrodes.

Due to the manufacturing process the sputtered metal electrode DEAs have no pre-stretch in the flat position (configuration of no out-of-plane deformation). This leads to a very low pre-load of the membrane for small out-of-plane deformations.

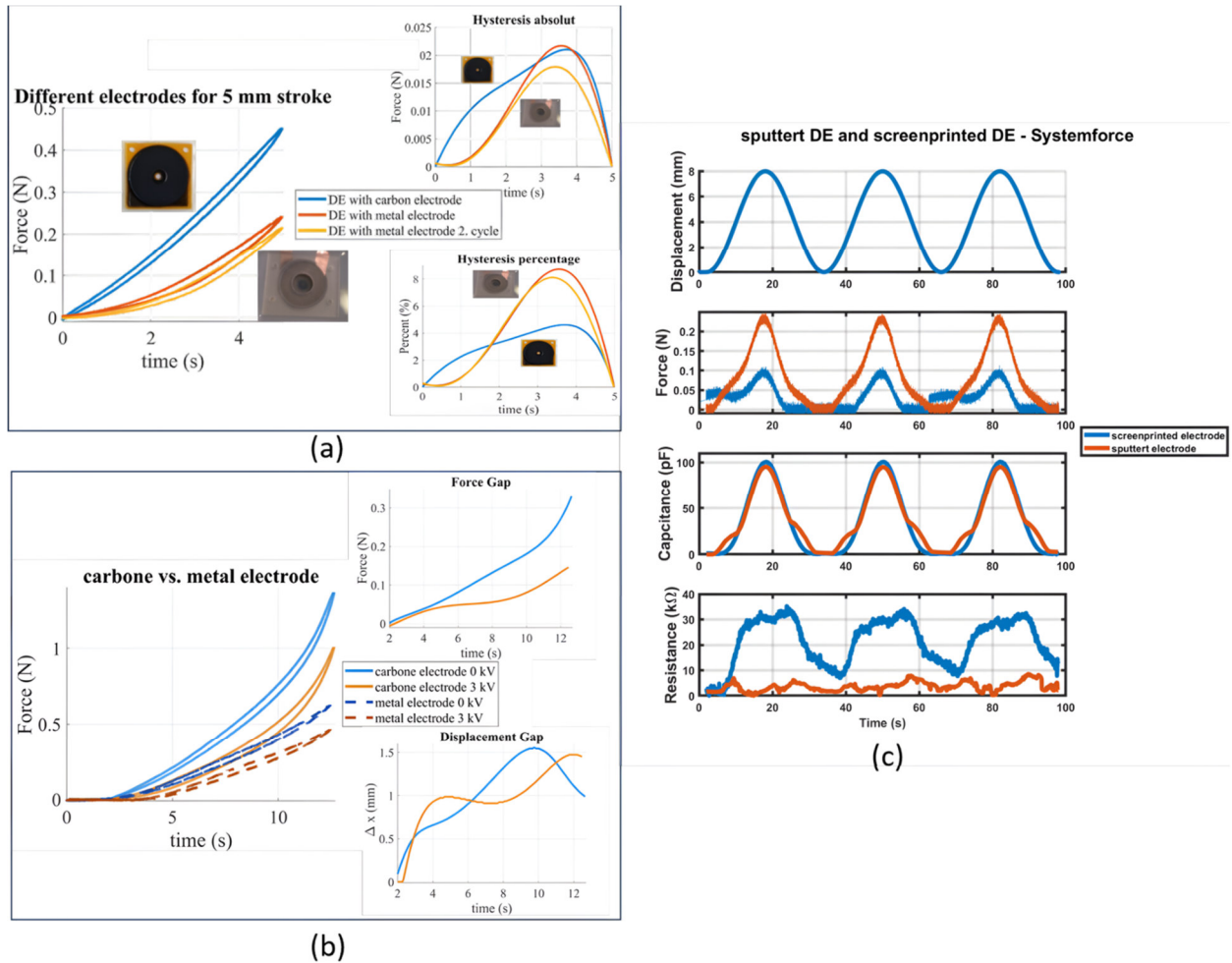


Figure 3.22: Comparison of the, (a) mechanical DE behaviour and hysteresis, (b) electro-mechanical behavior and output performance, and (c) the system behavior (DE + NBS) for sputtered metal electrodes and screen-printed carbon black electrode.

In Figure 3.23 the SPL of the metal electrode DEA for different out-of-plane deformations and for different biasing voltages is shown. The overall behavior, except for low deformations, is comparable to the carbon black electrode membrane.

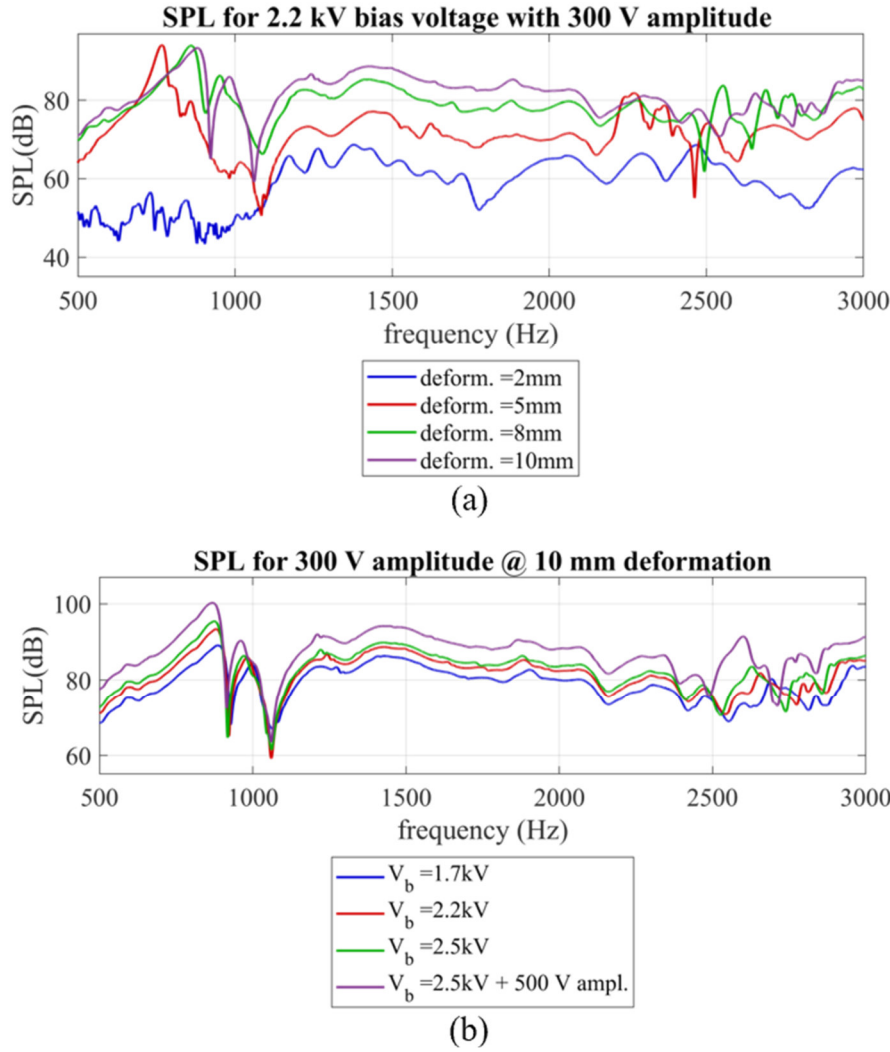


Figure 3.23: SPL of sputtered metal electrode membrane for (a) different out-of-plane deformations and (b) different bias voltage.

For the direct comparison, measurements with the same geometry and layer number of sputtered and screen-printed electrodes are performed. The comparison is done for the same reference deformation (5mm) and the same membrane stretch for both electrode types, compared to the reference configuration. In Figure 3.24 the SPL for the different configurations with two different bias voltages are presented.

The stretch of the carbon black electrode in the 5 mm configuration is $\lambda=1.73$ which leads to a deformation of 10.58 mm out-of-plane deformation for the metal electrode to have the same membrane stretch. Due to the different pre-stretch in the initially flat configuration, it is not realizable to perform the exact same measurements for both specimens. This leads to measurements with deviating boundary conditions for the different DEAs. For example, the resulting deformed shape and the circumferential stretch for both configurations are not the same. The configurations utilized are intended to be an approximation of comparable DEA measurements.

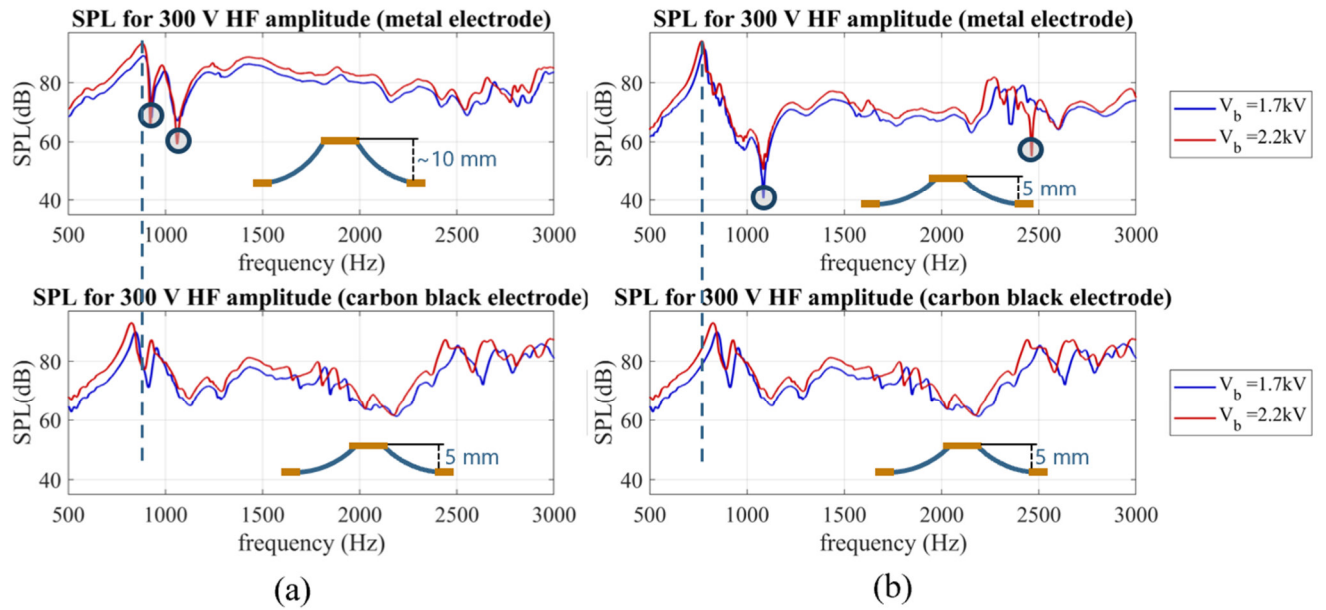


Figure 3.24: SPL comparison for sputtered and screen-printed electrode with (a) same membrane stretch and (b) same deformation.

Figure 3.25 shows the direct comparison of the SPL for the two electrode materials. The output performance is in the same range and the frequency peaks change as expected.

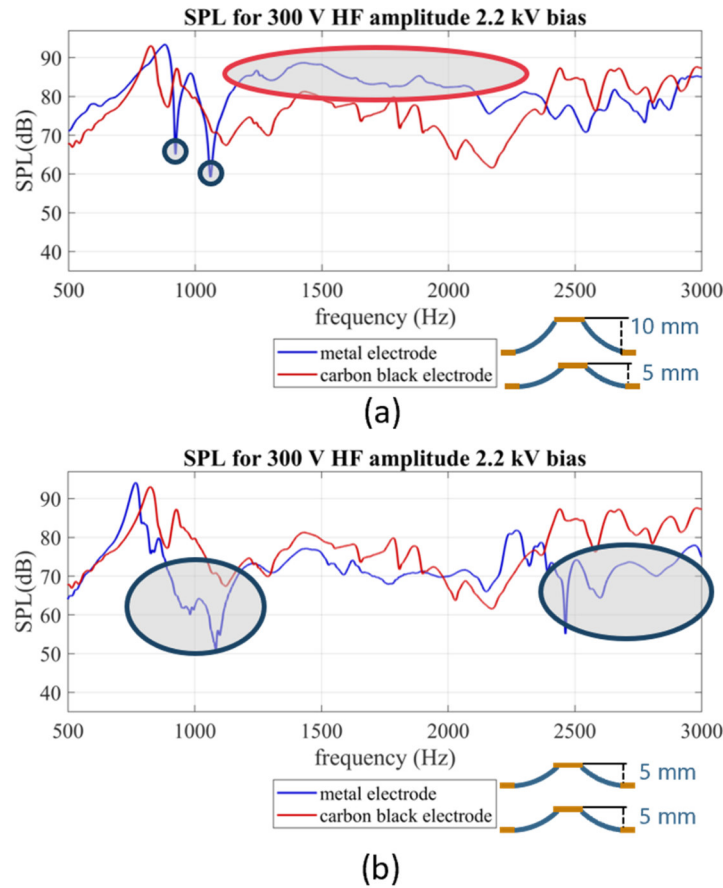


Figure 3.25: Direct SPL comparison for sputtered and screen-printed electrode with (a) same membrane stretch and (b) same deformation.

One significant difference is the (in Figure 3.25 marked) low peaks at around 900 and 1100 Hz of the sputtered electrode. The peaks are broad for 5 mm deformation and very steep for higher deformations. One explanation for this behavior is the wrinkle structure of the membrane which can lead to absorptions of the membrane transversal vibration by change of the wrinkle structure.

3.2.2. Audio-tactile element principle and development

By exciting the DEA prototype, with a multichromatic input (Figure 3.2(b)), given by the sum of a bias, an LF term, and an HF term, it is possible to concurrently produce a stroke (linear actuator working mode) and generate sound (loudspeaker working mode). This is achieved by driving the actuator with an input excitation that is the combination of a signal with LF fundamental frequency and large amplitude (responsible for the pumping mode excitation), and a HF low-amplitude signal (responsible for the excitation of structural modes, corresponding to transversal vibrations of the DE membrane):

$$v(t) = \sqrt{U_0 + U_1 \bar{v}(t) + U_2 \cdot \check{v}(t)}, \quad (3.20)$$

with $U_0 = \frac{V_{max}^2 + V_{min}^2}{2}$, $U_1 = \frac{V_{max}^2 - V_{min}^2}{2}$, $U_2 = 2V_{max}V_k$, $V_k \ll V_{max}$

where $\bar{v}(t)$ and $\check{v}(t)$ are signals ranging between -1 and +1 that vary in time on different time scales; $\bar{v}(t)$ has fundamental frequency in the LF range (e.g., 10^0 - 10^2 Hz), $\check{v}(t)$ has most of its spectral content in the range $5 \cdot 10^2$ - $5 \cdot 10^3$ Hz; V_{max} and V_{min} are the maximum/minimum voltages to which the DEA is subject when $\check{v} = 0$, while V_k is a measure of the amplitude of the HF voltage component, since

$$v(t) \approx V_{max} + V_k \check{v}(t) \quad (3.21)$$

in the time intervals where $\bar{v}(t) \approx 1$.

The LF component of the excitation (i.e., $U_1 \bar{v}(t)$) is responsible for the generation of a linear stroke of the end-effector. The HF component (i.e., $U_2 \cdot \check{v}(t)$) is responsible for sound generation.

The time-series of the end-effector stroke and the SPL are shown in Figure 3.26 for a case with $f_L = 3$ Hz (with $\bar{v}(t)$ equal to a sine and a trapezoid pulse respectively) and sinusoidal HF excitation with $f_H = 1108$ Hz (i.e., a $C_6^\#$). The DEA is able to concurrently generate a stroke on the order of 0.8 mm and a SPL on the order of 60–70 dB. Because the frequency range in which the DEA shows a pumping behaviour does not present overlaps with the range where structural modes are excited (Figure 3.2), the displacement z of the end-effector entirely filters out the HF component of the excitation.

A slow drift in the end-effector position is only visible in the case of trapezoid LF excitation, but that is a result of the DE material viscosity. In contrast to that, an LF modulation (with the same frequency as the LF excitation) is present in the SPL. In particular, the sound intensity is higher when $\bar{v}(t)$ is maximum. This happens because the DEA stiffness associated to the structural modes varies with the applied voltage: increasing $\bar{v}(t)$ (and, hence, v) causes the stress on the DE membrane to decrease and leads to higher-amplitude structural vibrations (see also Figure 3.2) and higher SPL. Technically, the LF variation in the DEA stiffness causes a beat in the DEA response, with a resulting acoustic output that holds spurious components (including, e.g., $f_H \pm f_L$) in addition to the fundamental (compare appendix A.2).

The distortion can be mitigated by introducing an LF compensation in the amplitude of the HF component in phase opposition with $\bar{v}(t)$. This was done by replacing V_k , in equation 3.20, with

a time-varying amplitude $v_\kappa(t)$, which is maximum when $\bar{v}(t)$ is minimum, and vice versa, namely:

$$v_\kappa(t) = [\kappa - (\kappa - 1)\bar{v}(t)]V_\kappa \quad (3.22)$$

where κ is a constant coefficient such that $\kappa \geq 1$. In the case of a 3 Hz LF sinusoidal excitation with a superposed 1108 Hz HF excitation (Figure 3.26a), using $\kappa = 2$ (i.e., v_κ varying in a range $V_\kappa \leq v_\kappa \leq 3V_\kappa$) provides a more uniform trend in SPL (red dashed line) compared to the base case (black solid line), with maximum fluctuations on the order of 4 dB.

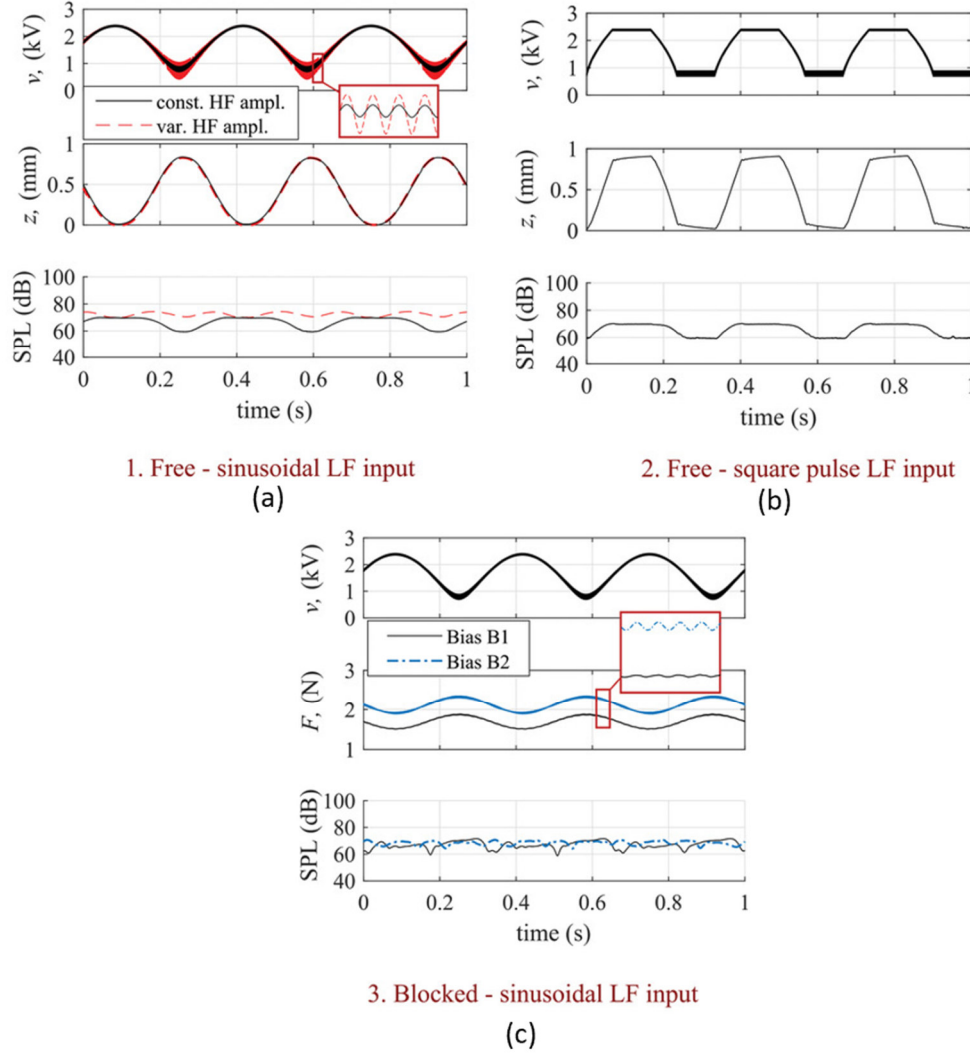


Figure 3.26: Response of the DEA to a multi-chromatic input voltage (a) sinusoidal and (b) square wave LF input voltage with a high frequency pitch (constant amplitude black and variable amplitude red). (c) axial force and SPL in two different blocking conditions ([225]).

The simple compensation strategy in equation and the corresponding results in Figure 3.26(a) have the aim of highlighting margins and directions for equalizing the DEA sound output in the presence of a superposed linear actuation. Simple equalization strategies might be built using the heuristics in equation for example, by identifying a map of values of κ that aims to obtain constant-level sound in the presence of different combinations of voltage bias, amplitude and HF excitation frequency. It is however worth remarking that the simple method proposed in equation does not keep into account the complexity of the system nonlinear response (i.e., the fact that

the sound pressure is a complex function of the DEA state) (see section 3.4.2). For this reason, a more promising approach, and a direction for follow-up works, might be to build dynamic filters based on a model of the system. Compared to the simple logics in equation , this might allow removing spurious harmonics from the sound output even in the presence of complex broadband multi-frequency excitations.

In blocking conditions (i.e., when the end-effector is locked), the DEA is able to produce sound with a level on the same order as that measured in free conditions at the same levels of voltage/deformation (Figure 3.26(c)). The SPL time trends differ from those in free conditions, as they are highly sensitive to misalignments and lateral loads in the blocking configuration. The reaction force generated by the blocked end-effector, which is proportional to v^2 , contains both LF and HF components, with the latter showing a significantly smaller amplitude (on the order of 10 times) than the LF component, as a result of the small amplitude of the HF excitation. The maximum force variation (namely, the blocking force) produced by the DEA between the maximum and minimum voltage is 0.5 N.

Figure 3.27 presents a summary of the multi-mode response of the DEA, subject to multi-frequency inputs, in terms of SPL (variation range) and force/stroke (variation over a period).

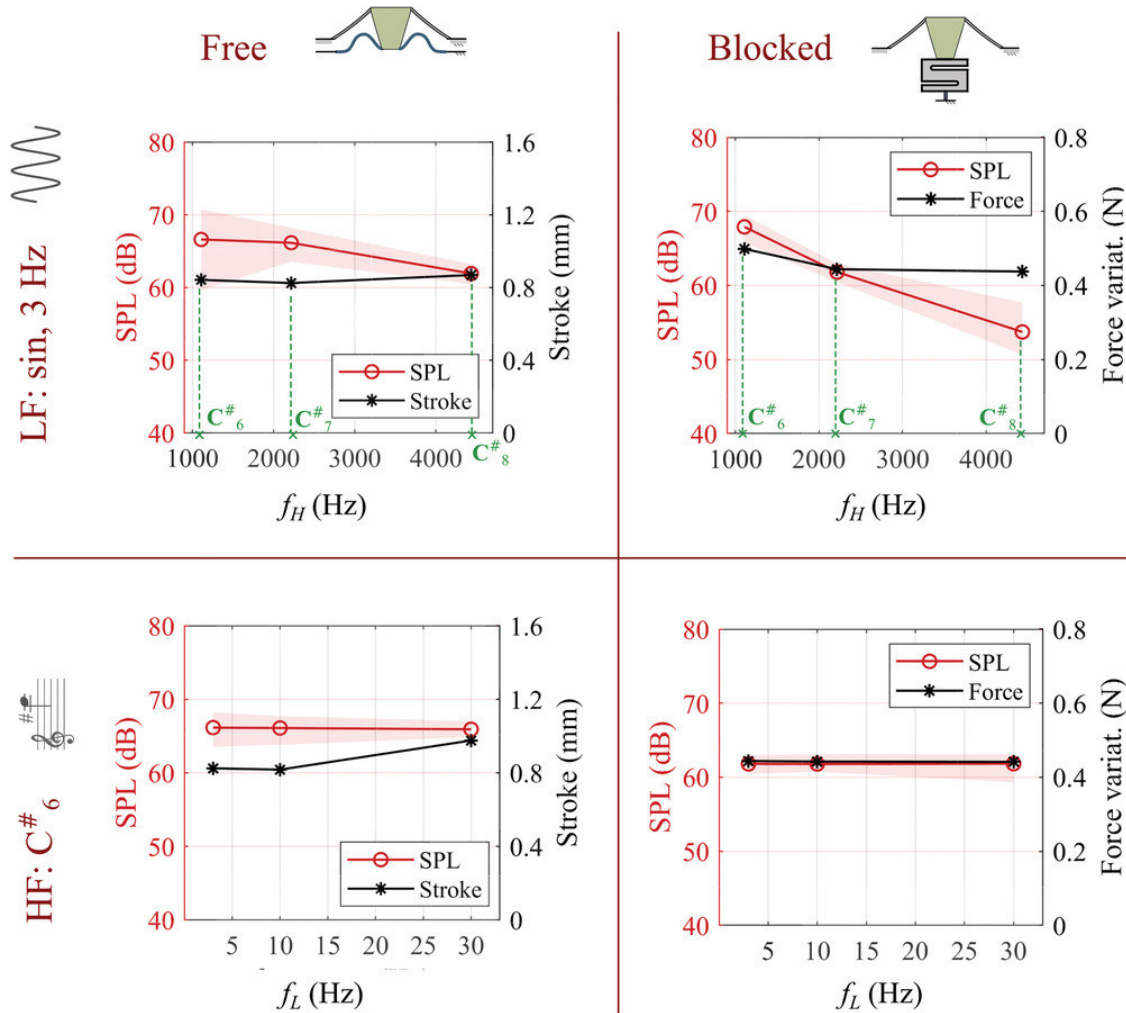


Figure 3.27: SPL and stroke/force variation for multi chromatic input voltage ($V_{\max}=2.4\text{kV}$, $V_{\min}=0.8\text{ kV}$ and $V_a=0.1\text{ kV}$). The left column show free displacement test, right column blocking force test and upper row refers to constant LF sinusoidal excitation, while the lower row refers to a HF signal with 1180 Hz ($C_6^\#$) ([225]).

For a given LF excitation (top row), changing the pitch f_H of the HF excitation ($C_6^\#$ to $C_8^\#$) does not cause significant modifications in the DEA free stroke or blocking force.

Here the lowest considered pitch ($C_6^\#$) gives the largest SPL, as this frequency is the closest to the (0,1) spectral peak (see Figure 3.2). Varying the frequency f_L of the LF excitation for a given HF pitch (bottom row), the SPL and its variation range in time stay nearly constant. The blocking force is constant with the frequency, whereas the stroke is larger at the highest frequency ($f_L = 30$ Hz), which is closer to the natural frequency of the pumping mode (see Figure 3.2). The SPL is on the same order in free and blocking conditions, even though differences can be observed, especially in correspondence of the highest frequencies pitches ($C_8^\#$). As observed before, this is due to lateral misalignments introduced in the DE membrane in blocking conditions. This has a big impact on the DEA acoustic response at higher frequencies and are reflected by local differences in the sound spectra in Figure 3.2.

The sound pressure changes depend on the out of plane deformation of the DEA. In Figure 3.28 is the SPL for different configurations of the DEA shown (without housing). Two out-of-plane positions of the end-effector are adjusted while for each position the end-effector can either freely move or is hold fix under blocking conditions. The SPL over the frequency is just affected very slightly. With a higher out-of-plane deformation of the DEA the SPL increases. The SPL responses shown in Figure 3.28 can be explained using already developed multi-physics models (see section 2.1.1.3, section 3.2.1, the appendix A.4 and [248]).

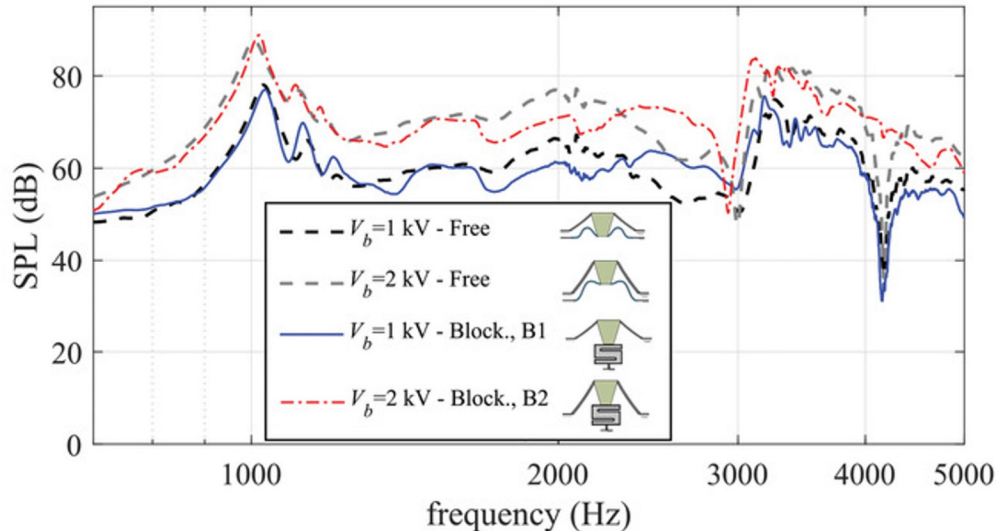


Figure 3.28: Sound pressure level at 0.35 m in front of the DEA (input: voltage sweep with amplitude $V_a = 100$ V and different bias levels). Two scenarios are considered: free and blocked end-effector. In each blocking test, the out-of-plane displacement of the DEA is set equal to the value measured at the same bias voltage in free conditions ([225]).

3.2.3. Control and Design of a multi-mode audio-tactile element

To realise user-interfaces, using the before invented multi-functional DET response capability, the control of the electrical stimulation is important. The in section 2.3.2, Figure 2.33, shown component-structure of a DET based user interaction element can be designed more efficient. This objective can be achieved by integrating touch and sound feedback into a single component, in conjunction with the incorporation of an additional special sensing layer positioned on top of the

layers for movement stimulation (compare Figure 3.1). In Figure 3.29 the resulting component structure is depicted [169].

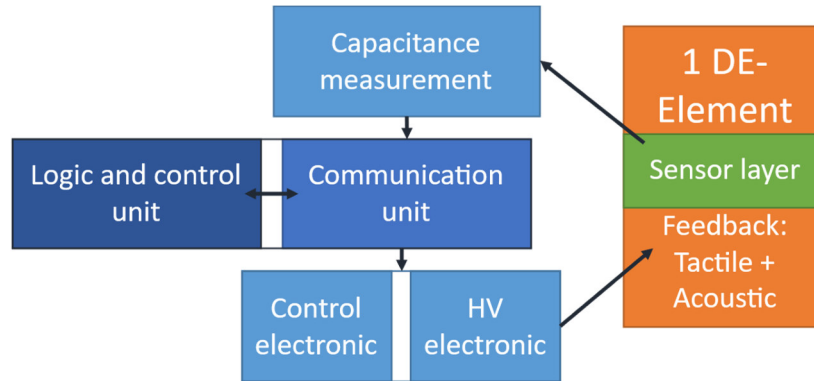


Figure 3.29: Structure components of DE-based interaction interfaces based on multi-functional DEA. The tactile and auditive feedback can be simultaneously realised with one DEA membrane, the sensing is integrated in an additionally sensing layer, stacked to the actuation layers.

For the audio-tactile element a COP-DEA prototype with the parameters described before (section 3.1.1) is used. The DE layers have a radial pre-stretch of 20% in the planar mounting configuration. The NBS features a design similar to that described in A.3 with an angled buckled beam and consists of a stack of two layers of 50 μm spring steel, cut using a cab XENO 1 Laser. The out-of-plane equilibrium displacement of the end-effector with respect to the membrane base plane is 5.25 mm.

The assembly of the DEA, the NBS, the clamping system, and the connections is installed into a 3D-printed housing (Figure 3.30). The latter is used to prevent a direct contact between the user and the DE membrane surface (for safety reasons and to guarantee the structural integrity of the DE), while also serving as an acoustic enclosure for the DE membrane which prevents acoustic short circuits between the back and the front faces of the membrane [169]. The top cover of the housing holds a printed grid, to allow sound waves to leave the box. A plastic spacer is installed on top of the DE's end-effector and connected to a circular layer of acoustic fabric (akustikstoff.com; item No.: eb150100), whose perimeter is connected (with no pre-strain) to a circular aperture in the housing. In the equilibrium configuration, the textile layer is flat. Pushing on the acoustic textile causes a downward deformation of both the textile layer and the DE. The spacer between the DE and the textile surface has the aim to create a significant distance (on the order of 10 mm) between the user's finger and the point where HV is applied. The mass of the axially moving parts (NBS, disc, spacer, screw) is 8 g, whereas the mass of the DE membrane is below 0.1 g.

An exploded view of the Setup is shown in Figure 3.30. After preparation, the 4 DE layers are clamped together via 3 D printed clamps, from where the electrical connections to the electrode are led outside. The NBS is also clamped and connected with a 3D printed spacer to the DE. Adjustment of the working out-of-plane equilibrium position of the membrane is performed by regulating the spacing between the DE and the NBS through a screw. Wiring of the prototype box is done with 4 mm jack plugs that can be directly connected to the HV power supply and the sensing electronics.

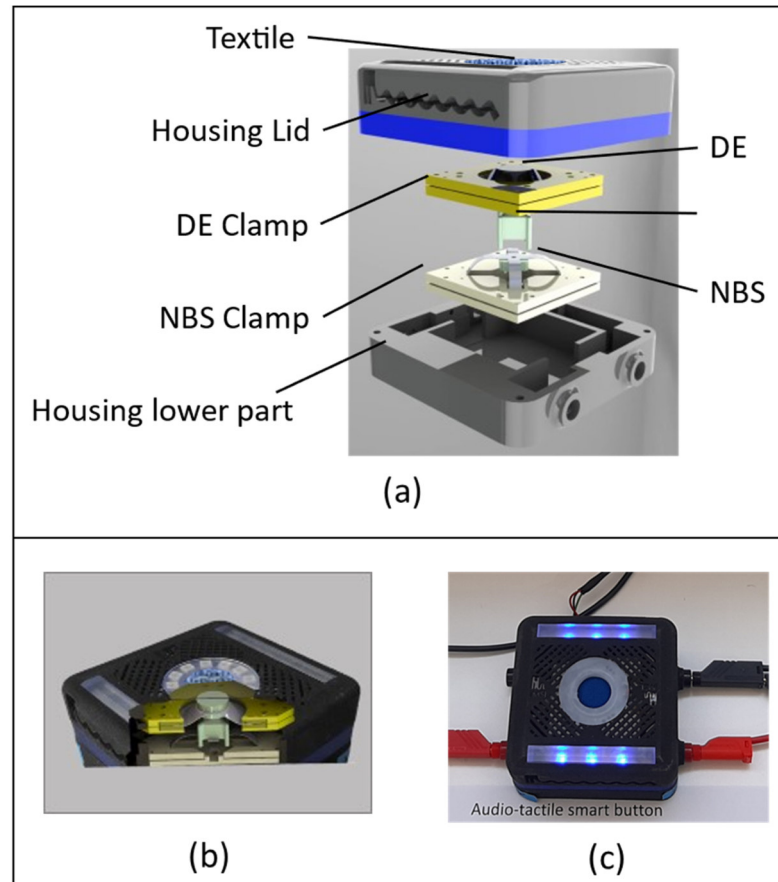


Figure 3.30: Housing of the DEA interface. (a) exploded view and (b) cut side view of the device and (c) top view with cables connected ([216]).

The logics and electronic architecture of the prototype is shown in Figure 3.31. The audio-tactile interface (DE membrane with mounting case, as shown in Figure 3.30) is the core element of the system. The sensing electronics used to detect users' touches feature a custom circuit design (section 3.1.2). A microcontroller (STM32 H743ZI2) is used to read the capacitance sensor electronic, provide a driving waveform to the HV amplifier, execute the logics, and drive built-in ancillary systems (LEDs). Driving voltage waveforms (v in equation 3.20) are generated by the microcontroller and delivered to a power amplifier by means of an integrated digital-to-analog converter (DAC). The sampling frequency of the DAC depends on the clock frequency of the system, which requires the value of the signal output be recalculated for every resulting timestep of the DAC output.

A commercial programable HV amplifier HA51U-3P5 by hivolt.de GmbH & Co. KG with 3000 V maximum voltage and 10 mA maximum current is used as the power supply, and a custom amplifier board is included, in order to fit the maximum output voltage of the microcontroller (3.3 V) to the maximum input voltage of the amplifier (10 V). Since the actuation layers have a capacitance of around 1 nF and the maximum current of the amplifier is 10 mA with maximum voltage of 3 kV, the audio-tactile interface is within the safety limits (20 mA continuous DC current and >100 nF) recommended for DEA applications [233]. Nevertheless, the housing is provided with redundant measurements (distances from HV connections, housing's hard walls) to prevent contact between user, membrane, and HV tracks.

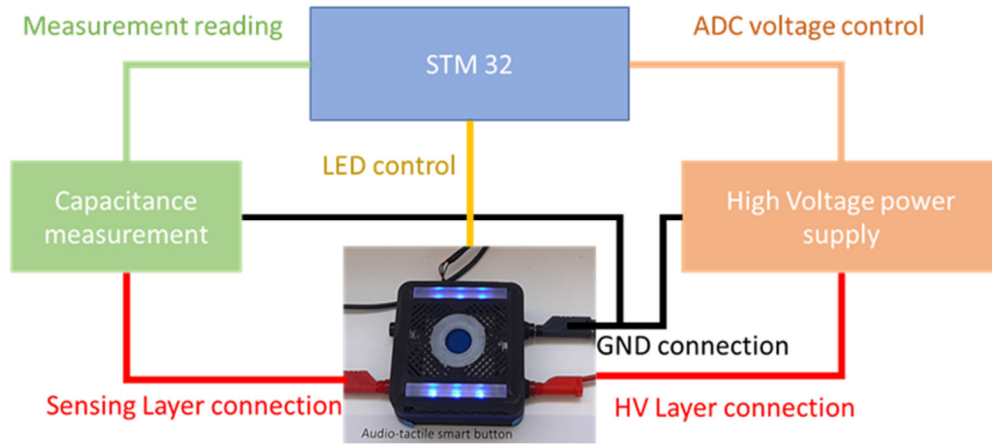


Figure 3.31: Subcomponents of the DEA interface including sensing electronic, microcontroller, HV electronic and multi-functional DET interface with housing ([216]).

3.2.4. Experimental results

With the aim of proving the DEA's ability to combine linear actuation and sound generation and to characterize the user interface, different measurements and case studies are presented, which demonstrate the actuator's multi-functionality in complex working scenarios. Each of the following case studies contributes in proving that the multi-mode principle introduced in Section 3.2.2 (where simple archetypal multi-frequency excitation inputs are considered) can be extended to advanced scenarios, where the DEA is subject to complex excitation signals or complex boundary conditions.

Firstly, measurements of the linear stroke/force at the end-effector in the presence of LF excitations, to quantify the DEA's ability to convey vibrotactile stimulations, and the acoustic response to HF excitations, are made. Then the sensing performance in terms of the device ability to recognise user touches with different frequencies and intensities is investigated. Finally, user tests that prove that the interface can provide perceivable and recognizable feedback are presented. It can be shown that the DEA is able to provide combined audio-tactile feedback through a series of multi-frequency excitation profiles.

To measure the different modes of the DE, namely linear movement of the end-effector and sound generation by the structural vibration of the DE membrane, a combined measurement setup, with the elements shown in Figure 3.32, is used.

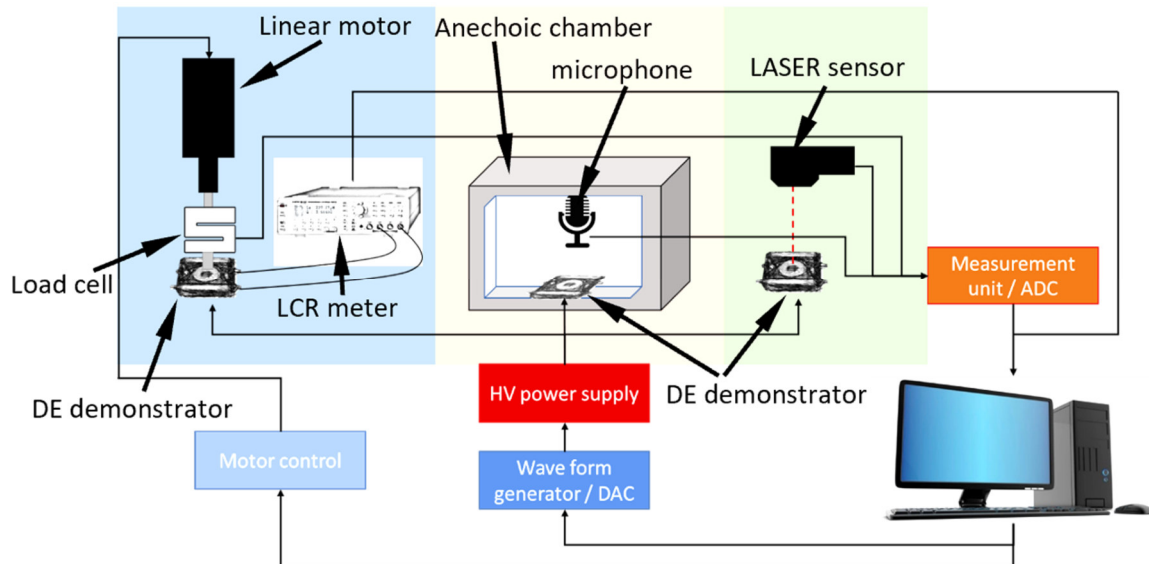


Figure 3.32: Test setup for multi-mode measurements with force-, sound- and displacement measurement units (c.f. [216]).

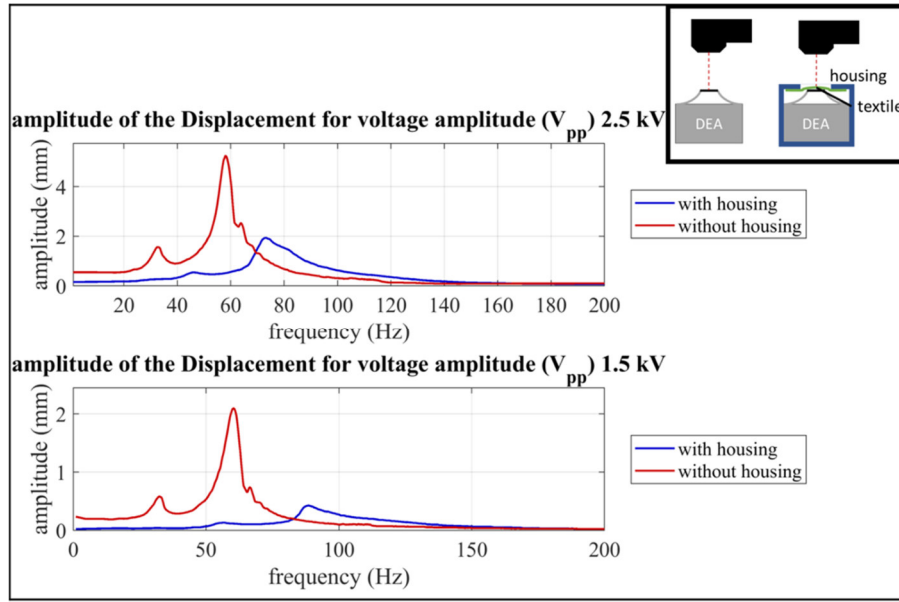
3.2.4.1. Audio-tactile Measurements

With the aim of characterising the device performance as linear actuator, the DEA free displacement and blocking force in a frequency range on the order of $0\text{--}10^2$ Hz is measured.

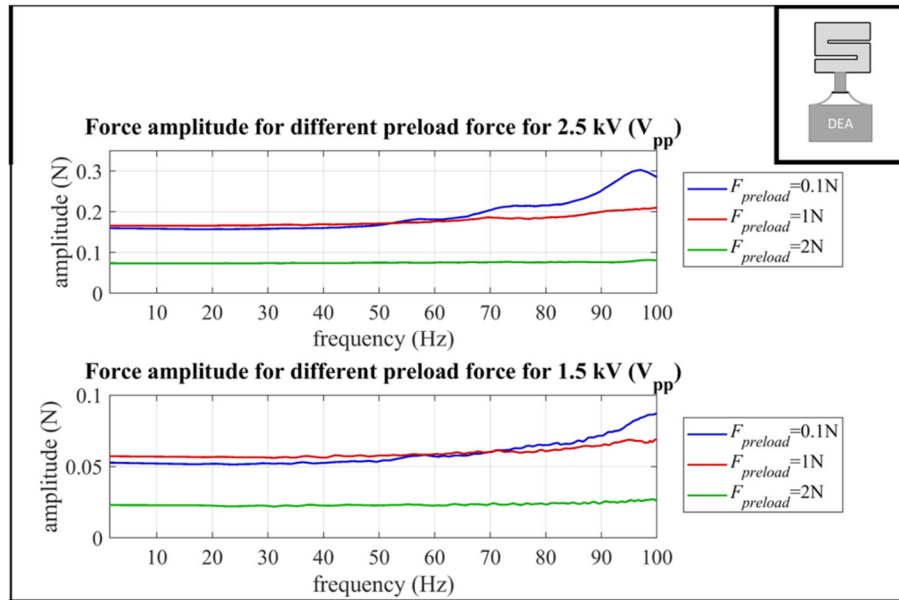
Free displacement tests were performed by applying a voltage sweep on the DEA and measuring the resulting end-effector displacement with a micro-epsilon optoNCD11402 laser sensor. Measurements were performed on the DEA assembly alone (without housing) and on the assembled system (with housing). Results in Figure 3.33(a) show the device response to a signal with peak-to-peak amplitude between 0 and 2.5 kV (top) or 1.5 kV (bottom) respectively.

As expected, the displacement is significantly reduced for lower excitation amplitudes (owing to the quadratic dependence of the Maxwell stress on the voltage). At low frequencies, the displacement of the assembled interface is lower than that of the free DEA. This is a consequence of the stiffness of the textile layer mounted on top of the DEA's end-effector, which is initially slack but gets stretched when the DEA moves out-of-plane. In static conditions, the displacement of the free DEA is of 0.47 mm (at 2.5 kV peak-to-peak excitation), whereas the initial out-of-plane bias displacement of the assembled unit is roughly 5.25 mm. The highest peak in the free displacement response corresponds to the natural frequency of the pumping motion of the end-effector (against the DE and the end effector stiffness), whereas secondary peaks owe to the DEA nonlinear response. Because of the additional stiffness of the acoustic textile, the pumping motion has higher natural frequency and lower amplitude in the assembled version of the prototype. The displacement of the DE with acoustic textile in static conditions is 0.18 mm (at 2.5 kV peak-to-peak excitation).

The blocking force produced by the device in the LF range is measured using a loadcell ME-Meßsysteme KD40s ± 5 N, connected via a rigid spacer to the DEA end-effector. Different measurements are performed by changing the axial distance between the load cell assembly and the DEA holding frame, so as to impress different pre-loads on the load cell



(a)



(b)

Figure 3.33: LF free displacement measurement with and without housing (a); Blocking force for different preload positions (b) ([216]).

Figure 3.33(b) shows that the amplitude of the generated force is constant over the considered frequency bandwidth (deviations from a flat trend in the final portion of the range are ascribable to mechanical resonances introduced by the load cell and are not representative of the actual device response). The output force is nearly constant in a relatively broad band of pre-loads (0.1–1 N), causing a modest axial movement of the end-effector (<1 mm, see Figure 3.3(top)). Further increasing the pre-load (2 N) causes a significant downwards motion of the end-effector, with a consequent reduction in the output force (as the membrane approaches the flat mechanically singular configuration).

The maximum force and displacements generated by the DEA, shown in Figure 3.3, are well above known thresholds for human perception [255] (i.e. 10–100 mN, 10–100 μm ; section 2.2.2).

The SPL produced in different operating conditions and at various locations is measured, by installing the DEA in the custom-built sound absorbing box using calibrated microphone RODE NT-USB placed at a distance of 0.3 m from the device. Acoustic measurements were performed with the device (including housing) installed on a support frame (with the device axis parallel to the horizontal plane), that allows varying the relative angle between device and microphone. The device was driven with HF voltage sweeps for different bias voltages (in the range 1.5-2.5 kV) and amplitudes (100-300 V, i.e., much lower than the bias voltage). An overview of the SPL response of the device is shown Figure 3.34. The device produces low or no acoustic output in the range below ~ 800 Hz. The SPL response shows a peak in the neighbourhood of 1 kHz. This corresponds to the natural frequency of the first structural vibration mode of the DE membrane (characterised by little or no motion of the end effector, and a bubble-like deformation of the membrane lateral surface - Figure 3.2). This can be regarded as a “cut-in frequency” for the device acoustic response, i.e., the device is able to steadily provide acoustic outputs above 70 dB at frequencies higher than the natural frequency of the first structural mode (except for some anti-resonance over narrow frequency ranges). This frequency range is well above the passband of the pumping motion used to generate tactile stimulations (see Figure 3.3 left), and above typical perception thresholds for human fingers [255]. As a result, exciting the DEA in this HF range is expected to produce no sensible tactile stimulation.

By increasing the bias voltage and/or the HF excitation amplitude, the sound pressure level increases accordingly. In particular, increasing the bias voltage, the elastic stresses on the membrane decrease (due to Maxwell stress), and the peaks in the SPL shift toward lower frequencies (compare Figure 3.28).

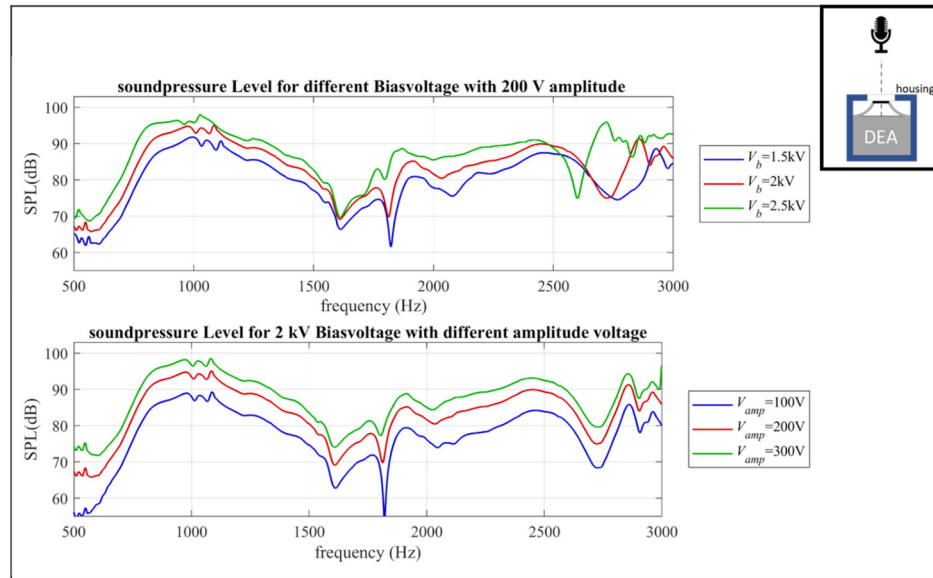
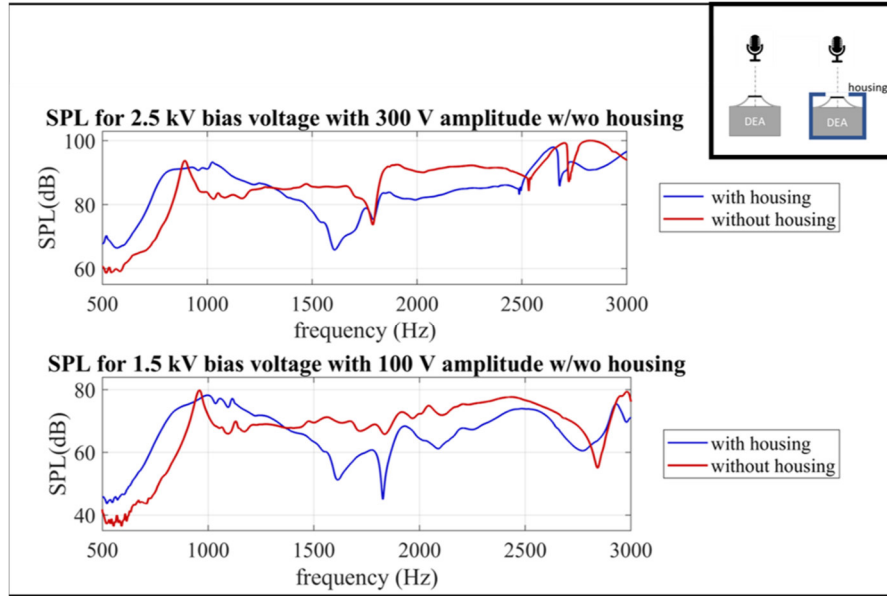


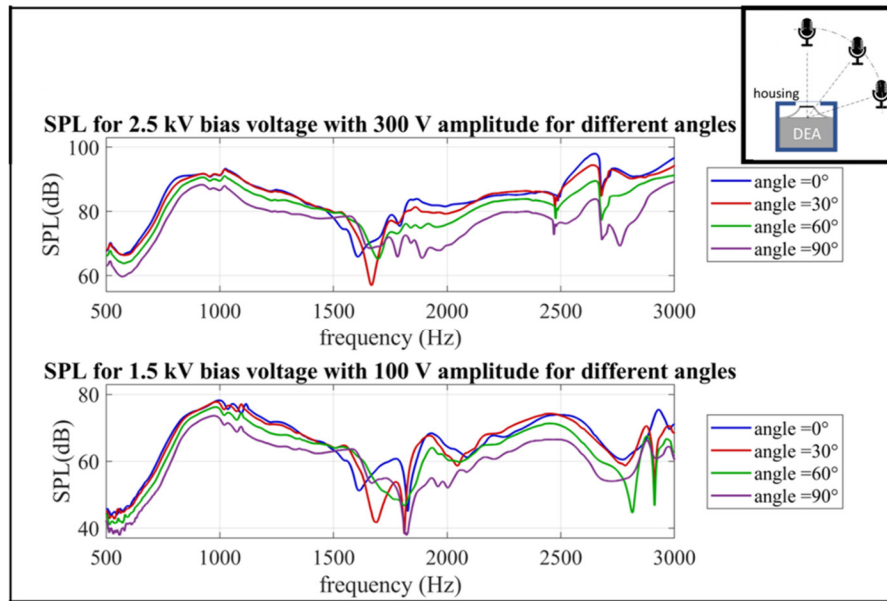
Figure 3.34: SPL of the prototype (with housing) for different control input signals ([216]).

To assess the influence of the housing on the acoustic response of the interface, the SPL produced by the assembled device, with that of the sole COP-DEA installed outside of its enclosure (Figure 3.35(a)), is compared. The SPL response of the free COP-DEA (without housing) differs from that of the assembled system in that

- a) The assembled interface features higher SPL at low frequencies, and similar (or lower) level in the HF range;
- b) The response of the free DEA shows a clear prominent peak in correspondence of the (cut-in) natural frequency of the first structural mode, as opposed to a flatter resonance response for the assembled unit;
- c) The abscissa (natural frequency) of the first resonance peak is lower for the free DEA. [173]



(a)



(b)

Figure 3.35: Influence of the housing on the SPL (left); and directivity analysis of the SPL for different angular positions of the microphone (right) ([216]).

These differences are due to the geometry of the housing, that creates a nearly closed volume of air underneath the DE, located between the DEA bottom face and the internal walls of the enclosure. The housing structure behaves as an enclosure for the DEA membrane, preventing acoustic

short circuits between the top and the bottom faces of the vibrating membrane, hence increasing the SPL generated in the LF range. Increases in the natural frequency of the structural mode are consistent with additional stiffness contributions due to the compressibility of the enclosed air volumes (see appendix A.5). Loss of SPL at higher frequencies are due to shadowing effects caused by the top wall of the housing.

A study of the device directivity was eventually carried out. The speaker off-axis response is measured, by rotating the device with respect to the microphone (Figure 3.35(b)). The SPL decreases with the angle, experimenting a reduction of up to 10 dB at 90°. This result is in accordance with simulation studies presented in [173], which proved that COP-DEA speakers have directional response, characterised by shadow regions at 90° radiation angles.

Additional force, displacement and sound measurements with different conditions are shown in the Appendix (A.7).

3.2.4.2. Proof of concept Tests

With the aim of providing a proof of the DEA's ability to combine linear actuation and sound generation, hereby four exemplative case studies are presented, which demonstrate the actuator's multi-functionality in complex working scenarios. Each of the following case studies contributes to proving that the multi-mode principle introduced in Section 3.2.2 can be extended to advanced scenarios, where the DEA is subject to complex excitation signals or complex boundary conditions. In particular,

- a) The linear actuation can be produced in combination with complex acoustic signals, by concurrently using the DEA as a speaker (that uses structural vibrations to play a tune) and a metronome (which produces a pumping motion in sync with the tune's beat).
- b) The same scenario as above (complex acoustic signals reproduction + linear actuation) can also be achieved when the DEA is subjected to a large external force (e.g., a weight applied on its end-effector, on the same order as the blocking force measured in Figure 3.27 and Figure 3.3, that contrasts its linear actuation).
- c) Additionally, to combined multi-frequency actuation, the DE membrane can incorporate a sensing function. For example, crossing voltage and current measurements allows the DEA to recognize a touch applied by a user on the end-effector and respond with a combined vibrotactile and acoustic stimulation.
- d) By adding the specific sensing layer (compare Figure 3.1) and putting the prototype into a housing combined with a microcontroller and a structure described in Figure 3.31 a complete self-standing audio-tactile interface with different modes (closer described in section 3.2.4.3) can be developed

For all presented proof-of-concepts, quantitative figures of merit are reported in the following. Whereas further structured applications of the presented principle might be developed in the future, the simple tests reported here show that a single DE active unit can concurrently accomplish complex linear actuation, sound generation, and sensing tasks. At the same time, the presented results provide indications for future application directions, including multi-modal collocated audio-tactile interfaces, [237] or virtual programmable buttons. [241].

Time-beating loudspeaker: The DEA can simultaneously work as a loudspeaker and a metronome, beating the tempo of the tune that it is reproducing through the axial movement of the end-effector (Figure 3.36(a)).

This has been achieved by supplying the DEA with an input, v^2 , which is the sum of a low amplitude HF component rendering the music track and a higher amplitude ($V_{\min} = 0.8$ kV, $V_{\max} = 2.4$ kV) LF square wave term with a fundamental frequency equal to the beat of the tune (here, 134 BPM). The amplitude of the HF component has been modulated over time as described in equation , using $V_{\kappa} = 0.2$ kV and $\kappa = 2.5$. In the initial/final phases, the DEA reproduces a clicking sound synchronized with the pumping movement (beat) of the end-effector. Following that, the DEA plays music while the upward movement of the end-effector concurrently marks the pulses of the measure. Plots in Figure 3.36(a) are relative to a portion of the experiment. The music line in the plot only shows the melodic line, whereas in the test the DEA played both melody and accompaniment. The stroke of the DEA end-effector on the beats is of 0.8 mm, whereas the average SPL during sound reproduction is 62 dB. Similar to the results discussed in section 3.2.2 the end-effector movement is unaffected by the HF excitation. In contrast with pure tones, which are affected by a recognizable beat distortion caused by the superposed LF actuation (Figure 3.26), in this case the multichromatic nature of the reproduced tune masks such distortions to the listener's ear.

Sound generation under load: Although in the previous case study the DEA is free from external applied loads (other than the forces due to the DE elasticity and the NBS), DEA is able to generate sound and linear actuation even under the effect of an applied load. A mass of 20 g (i.e., comparable with the blocking force discussed in Figure 3.27) is applied on the end-effector, and by applying an audio signal (song track) onto the DE (Figure 3.36(b)) the demonstrator plays music. The peak amplitude of the acoustic signal is on the order of 0.4 kV, and it is thus not sufficient to produce any axial motion of the end-effector, regardless of the waveform bandwidth. By applying a step variation (between $V_{\min} = 0.8$ to $V_{\max} = 2.6$ kV) on the bias voltage, the DEA can lift the mass while concurrently playing the music piece. Figure 3.36(b) compares the time-series of the end-effector displacement and the generated sound pressure for the two cases of free and loaded DEA (without and with loading mass respectively), in the presence of a same input signal (piece-wise constant bias + soundtrack).

The end-effector stroke is 1.2 mm in the free case and 1.8 mm in the loaded case (Figure 3.36(c)). In fact, when a mass is applied on the device, the initial value of the DEA's out-of-plane equilibrium displacement h_0 is lower, hence making a larger stroke available for the end-effector upon voltage application. The end-effector displacement is free from HF components due to the audio track, even though an underdamped oscillation is visible in the case with applied mass (oval inset). This is due to the free oscillation of the DEA + mass system, which has a natural frequency of 22 Hz (as opposed to 119 Hz of the free DEA). Figure 3.36(d) shows the trend of the SPL in the two cases with and without load. The SPL in the two cases is comparable, hence confirming that sound generation is loosely affected by constraints on the end-effector axial displacement. The SPL in the loaded case is, however, generally lower than that in free conditions. This is partly due to the fact that the out-of-plane deformation of the cone DEA is lower because of the applied mass, and partly due to shading effects due to the 20-g-mass body (aligned with the DEA axis).

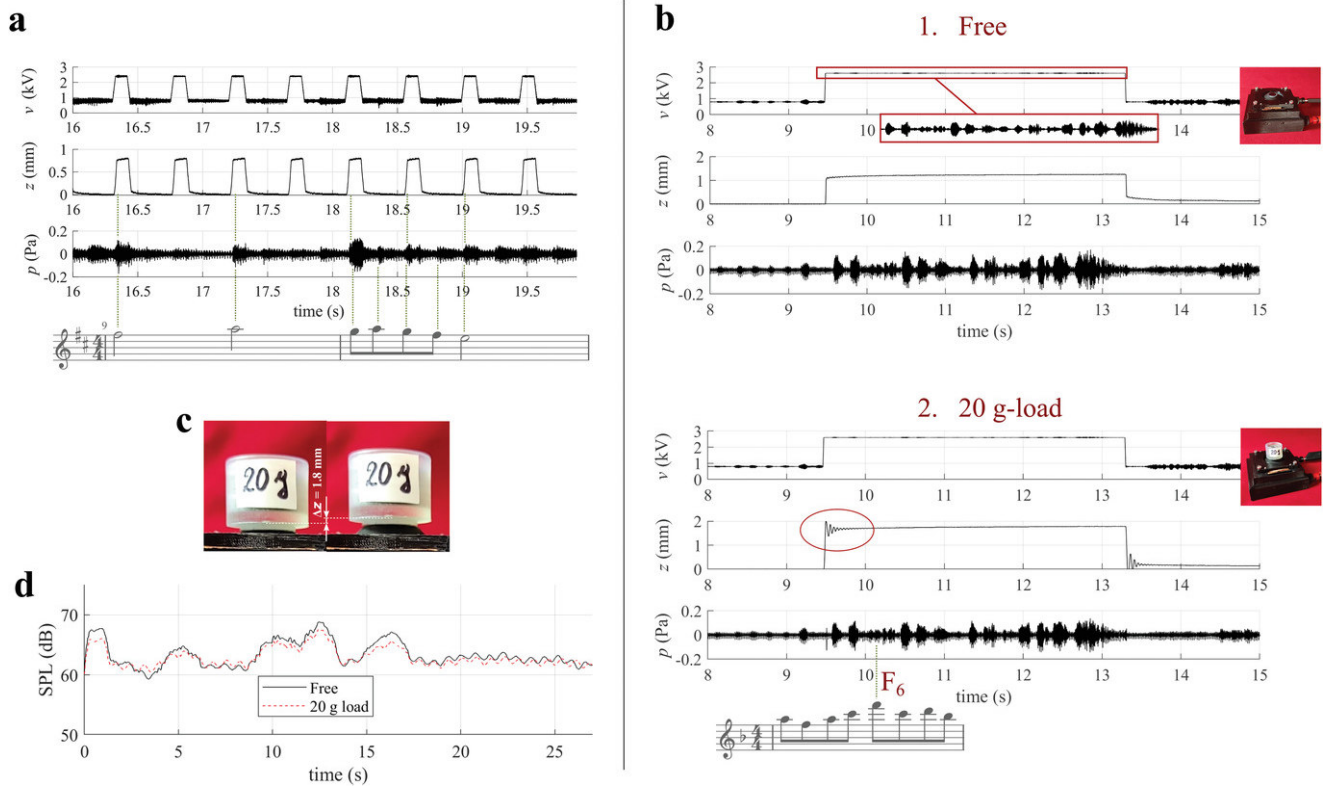


Figure 3.36: a) Time-beating loudspeaker. The plot shows an excerpt (two bars) of the timeseries of the applied voltage, the axial stroke, and the acoustic pressure. The DEA is driven with an input which is the sum of a high-frequency component responsible for the tune reproduction, and a low frequency component, causing the DEA end-effector to move upward in sync with the beats of the tune's tempo. b–d) DEA playing a tune under load. b) Excerpt of a time-series of voltage, stroke and acoustic pressure for the free DEA (top) and in the presence of a 20 g mass applied on the DEA's end-effector. c) Increasing the voltage from $V_{min} = 0.8$ kV to $V_{max} = 2.6$ kV causes the DEA to lift up the mass by 1.8 mm, while the tune is hitting the top notes. d) Time-trend of the SPL (moving-average) for the two cases with free and loaded DEA ([225]).

Audio-tactile button: To show that the DE interface can concurrently produce multiple outputs (namely, LF tactile stimulation and HF acoustic outputs), the device is driven with different voltage inputs, in the form given by equation 3.20, characterised by different combinations of LF and HF components. Measuring the output current allows inferring information on the DEA state and using it as a sensor, hence providing the system with a further functional layer, in addition to LF and acoustic actuation. In contrast to the extra sensing layer and electronic the current measurement allows only rough estimation of the deformation, like detecting a threshold for example. When a bias voltage is applied to the DEA, a sudden change in device configuration (and therefore capacitance), such as a touch, generates a current peak that can be used to trigger a response. In section 3.3 a specific self-sensing algorithm, which uses the measured voltage and current signal, is utilised to perform much higher accuracy in the deformation sensing. In the presented measurements the DEA is employed as an audio-tactile button, able to sense a compression applied by a user on the end-effector and respond with an acoustic and a vibrotactile stimulus (Figure 3.37).

Upon recognizing the user's touch via current measurements, the button executes a pre-defined routine, consisting of: 1) a clicking sound, generated via a HF sinusoidal excitation with exponentially decreasing amplitude; and 2) a combined LF square wave excitation and a pulsated HF

excitation (sine wave with exponentially decreasing amplitude), applied in correspondence of the phases in which the LF component is maximum. The latter produces a combined vibrotactile and acoustic feedback. Because the human vibrotactile range lies below 1000 Hz [236], tactile stimulation here is entirely due to the LF component of the excitation, whereas the HF component only contributes sound feedback. Note also that the DEA blocking force (see, e.g., Figure 3.33) is largely above (roughly, one order of magnitude) the finger's perceptual threshold [255], that is, the DEA generates a clearly perceivable stimulus.

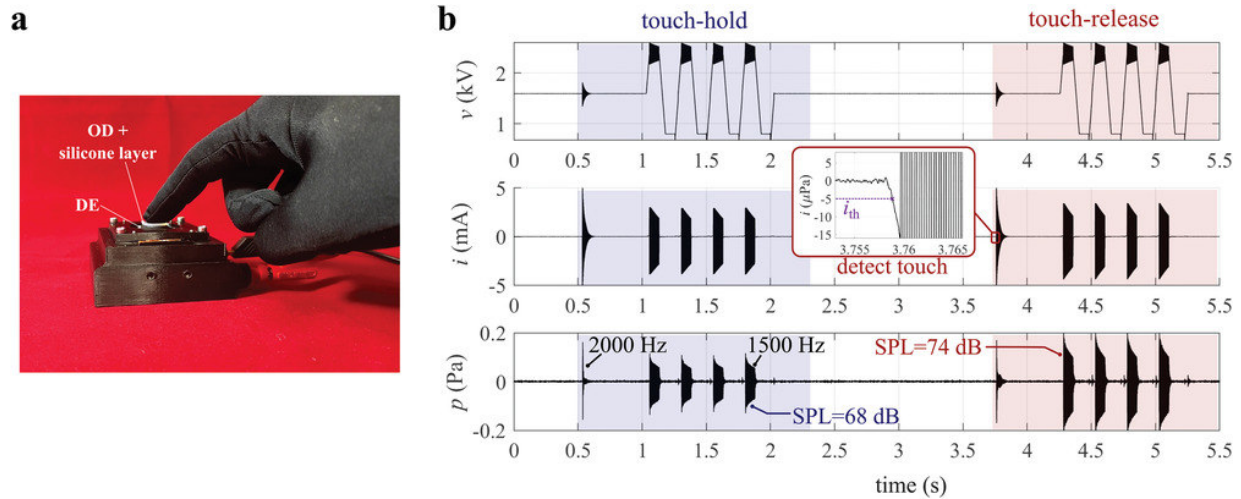


Figure 3.37: Audio-tactile DEA interface. a) Picture of a user pushing the DEA OD, hence triggering an audio-tactile response. b) A constant voltage of 1.6 kV is initially applied on the DEA. Pushing the interface with a finger causes a peak in the current. When the current surpasses a fixed threshold, the DEA responds with a complex feedback consisting of: a click sound (2 kHz frequency, with exponentially decreasing amplitude), followed by a low-frequency (4 Hz) axial motion of the end-effector and a superposed pulsated sound (1.5 kHz with exponentially decreasing amplitude). In the plots, the DEA repeats its routine twice: in the first iteration, the user pushes the DEA to trigger it and keeps it pressed all through the routine; in the second iteration, the user pushes the DEA and then removes the finger ([225]).

Although, during operation, the users are constraining the axial pumping motion of the DEA end-effector through their finger, sound is still generated as a result of the DEA higher-order structural modes. Keeping a pressure applied on the end-effector upon touch results in SPLs of 68 dB (Figure 3.37(b) left), whereas releasing the end-effector after the touch results in a level of 74 dB (Figure 3.37(b) right). The difference between the two cases is due to the difference in the DEA bias axial deformation (the DEA is pushed downward when a touch is applied) and acoustic shielding due the user's hand (which partly covers the sound pattern toward the microphone).

Compared to conventional combined audio-tactile interfaces, which make use of separate transducers and devices for sound generation and vibrotactile stimulation ([239], [256]). The DEA audio-tactile button requires a single active DE element to produce both outputs, in addition to generating the tactile and the acoustic stimuli in a perfectly co-located manner. In the future, this might represent an interesting paradigm for the development of advanced rendering interfaces capable of optimally combining acoustic and tactile stimulation [245], [257].

Sensing audio tactile button (with housing): As an extension of the previously presented concept, a prototype with an extra sensing layer (compare Figure 3.1) and housing (Figure 3.30) is presented below. by using a microcontroller, the structure described below can be operated completely autonomously. In Figure 3.38 the device output in response to 3 different excitation waveforms: 1) a waveform which solely consists of a LF square waveform, meant to provide users with

a variable-frequency vibrotactile stimulation (top row); 2) a waveform which only includes HF harmonics, resulting in the execution of a jingle with no tactile stimulation (bottom row); and 3) a composite LF + HF signal, providing the user with a simple audio-tactile multi-sensory stimulation (central row), is presented.

The signals provided for the measurements in Figure 3.38 can be calculated by using equation 3.20 with the following parameters. The tactile LF excitation waveform (top row) consists in a square wave signal \bar{v} with swept frequency (rising from 1 to 90 Hz and then decreasing back to 1 Hz) and amplitude between $V_{min}=200$ V and $V_{max}=2100$ V (with no HF superposed signal, $V_k=0$). The purely HF excitation signal (bottom row) is a waveform \check{v} with bias voltage $V_{max}=V_{min}=2300$ V and amplitude $V_k=300$ V, rendering a soundtrack. The composite audio-tactile excitation waveform (middle row) is a LF square wave \bar{v} (fundamental frequency 2 Hz, duty cycle 50%, $V_{max}=2500$ V; $V_{min}=700$ V) with a superposed 850 Hz HF pure pitch \check{v} , with slowly varying amplitude, which changes synchronously with \bar{v} : $V_k=220$ V when \bar{v} is maximum, and $V_k=66$ V when \bar{v} is minimum. The resulting output sound is a syren alarm, whose beat is synchronised with the tactile stimulation. In addition to those discussed in Figure 3.38, other multi-chromatic excitation waveforms were coded on the DE button prototype. The different additional working modes are described in the Appendix (A.6).

Blocking tests of the device are performed, in which the force produced by the interface against a load cell, mounted against the device end-effector with a pre-load of 1 N (in the same fashion as Figure 3.33 right) is measured. Free displacement tests in which the end-effector displacement is validated with a laser (Figure 3.33 left). The plots in Figure 3.38 show the timeseries of the excitation voltage, the force produced in blocking conditions, the free displacement and SPL generated in free displacement conditions.

The interface consistently produces outputs with forces on the order of 0.2-0.4 N, free displacements of 0.1-0.2 mm and acoustic pressure outputs of up to 1 Pa amplitude (roughly 90 dB). It can be noted that in the purely tactile working mode (no HF component, $V_k=0$) an acoustic output is also produced in addition to the LF force and displacement outputs. The intensity of this phenomenon is comparatively diminished in relation to that observed in the other two cases, wherein sound is generated by a high-frequency small-amplitude excitation. The observed intensity can be attributed to the presence of higher-order harmonics in the driving signal component \bar{v} , as well as structural vibrations in the moving parts, such as the metallic NBS, which are induced by the steep rising/falling times of the square excitation waveform. For the purely acoustic mode (bottom row), very small vibrational feedback (displacement and force variation) is measurable, as the excitation frequency is well above the resonance frequency of the pumping motion. Such residual axial movements/forces fall above the perceivable threshold for human tactile sensitivity [258]. The combined audio-tactile excitation scenario (middle row) consistently produces LF force variations close to 0.5 N and acoustic pressure with peak amplitude over 0.5 Pa.

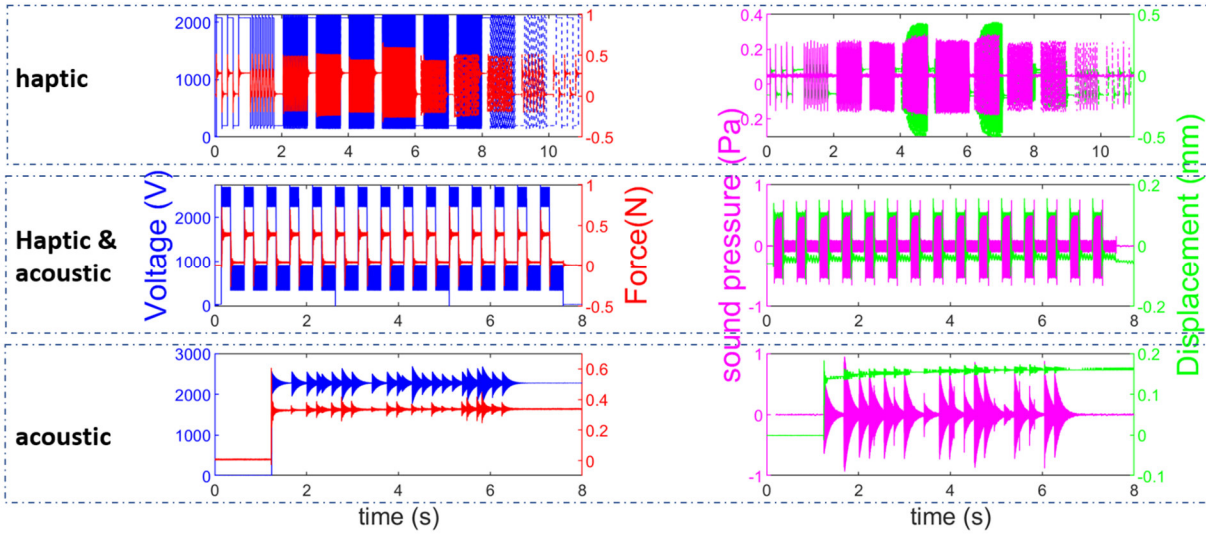


Figure 3.38: Feedback characteristic (blocking force, free displacement, SPL in free motion condition) of the DE interface subject to three different voltage excitation waveforms. Top: LF excitation signal (rendering a tactile stimulation); Middle: composite LF+HF waveform (producing a combined audio-tactile stimulation). Bottom: HF excitation (soundtrack) ([216]).

To improve the sensing capability and performance, an additional sensing layer is added (see Figure 3.1). In the presented application, capacitance measurements are analysed to detect touches, impressed by a user on the DE interface (which result in a decrease in z and, hence, on the capacitance C_{DE}). The DE sensing layer is combined with electronics (see section 3.1.2) that produce an output that is inversely proportional to the cycle time t_p . Integrated logics recognize whether (and how often) the sensor output surpasses a certain threshold (indicating the achievement of a certain minimum displacement), hence allowing to detect and count separate touches performed by the user (compare Figure 3.6).

3.2.4.3. User tests

A combined sensing and multi-sensory actuation capability can be realized by programming the DE interface in a way that it produces different outputs (namely, the 3 waveforms discussed in Figure 3.38) in response to different users' inputs (number of touches (Figure 3.6)), that are detected using the logics discussed. Each output is triggered by pushing the interface end-effector a different number of times: the sensing logic recognises the number of touches impressed by the user and produces a different vibro-tactile routine accordingly.

To show the performance of the resulting integrated demonstrator, two different types of user tests (with 14 volunteer subjects) are carried out.

In a first test, the subjects are asked to push the button a prescribed number of times, so as to trigger a response, and keep their index finger on the interface end-effector during the successive execution of the feedback routine. For each of the routines described in Figure 3.38, users are then asked to rate the intensity of the tactile and acoustic feedback of the device on a scale from 0 (weak) to 10 (strong). Sensing was automatically tested by recording the actual number of touches detected by the interface in response to the intended number of user's touches (for which a success rate of 100% was achieved).

A boxplot with median, 25th and 75th percentiles, and the most extreme data points for the rating of the users perceived intensity (determined using the `iqr` command in Matlab) are shown in Figure 3.39. Ratings assigned by users demonstrate that the interface produces an appreciable level of

tactile and acoustic feedback. Excitation with a LF variable-frequency signal, with $\bar{v}=0$ (same waveform as in Figure 3.38-top), was also reported to produce a sensible level of acoustic feedback (left column in Figure 3.39).

As already mentioned with reference to Figure 3.38, this is due to high-amplitude higher-order harmonics in the excitation (that consists in a sequence of square pulses) and vibrations of the spring and the housing. In the purely acoustic working mode (where the sole HF excitation \bar{v} is applied), users consistently reported no or very low levels of haptic feedback, possibly due to an illusory perception of motion triggered by the acoustic feedback (right column in Figure 3.39). In the case of a composite audio-tactile actuation (with low frequency tactile stimulation at 2 Hz, and high-frequency sound feedback at 850 Hz), both stimuli (tactile and acoustic) were reported to be clearly perceptible (central column in Figure 3.39). Vibrotactile intensity has been reported to be higher in the first case (tactile stimulation alone), because of the larger applied frequencies (90 Hz), to which human tactile perception is more sensitive. The two additional signals of the user tests (5 signals together) are described in appendix A.6.

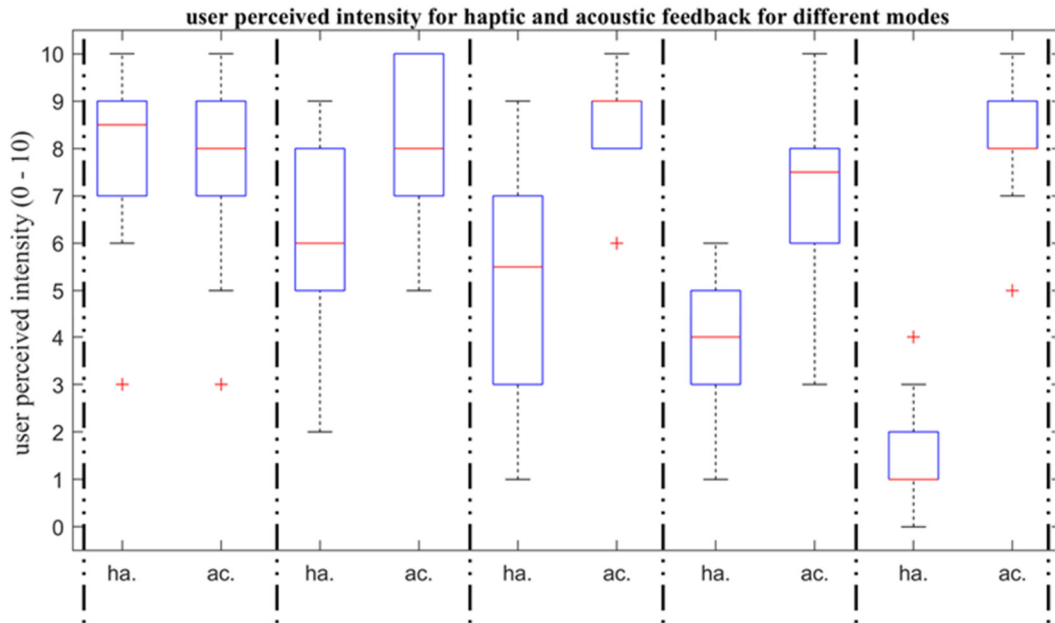


Figure 3.39: Test subjects' rating of the tactile and acoustic output intensity for three different applied excitation signals (Left: LF tactile only; Middle: LF+HF audio-tactile; Right: HF acoustic only, as defined in Figure 3.38). Red central lines indicate median values, top and bottom edges of the blue box indicate 25th and 75th percentiles, black error bars indicate the maxima and minima data point and the red '+' marker indicates outliers (when present). Data were processed using the iqr command in Matlab. Labels ha. and ac. on the horizontal axis denote "haptic" and "acoustic" feedback respectively (c.f [216]).

A second set of tests is performed with the aim of evaluating the local assignability of the output (vibrotactile, acoustic, or combined) by a user, who interacts with different replicas of the DE user interface and, hence, highlight perception advantages of a co-located audio-tactile interfaces. For this purpose, two identical prototypes (DEA + NBS + housing) are built. The two units are located on a same workbench at variable relative distances, and users are asked to place their index fingers on the end effectors of the two interfaces (Figure 3.40). The two devices are then excited with different (but synchronous) combinations of inputs, built starting from the composite voltage excitation waveform presented in Figure 3.38-middle. The signal is divided into two components

(LF and HF), that can be used to separately excite the two units. Each device can be excited with: HF frequency signal (resulting in an acoustic output); LF signal (resulting in a tactile stimulation); a combined multi-frequency signal (audio-tactile feedback), same as in Figure 3.38-middle; no signal. A correction factor is applied on the amplitudes of the HF signal in the different scenarios, to ensure that the measured sound output has the same intensity in both cases where it is executed alone (acoustic output only) or in combination with a LF signal (audio-tactile output).



Figure 3.40: User test setup for local assignability tests with two units. User position and different locations of the demonstrators ([216]).

Users are presented 8 different repetitions (some of which are executed twice), in which the two devices are excited with different combinations of inputs. They are then asked to recognise what type of output is being produced by each of the units (purely haptic, purely acoustic, audio-tactile, no output) every time. The eight permutations of applied inputs are shown in Figure 3.41.

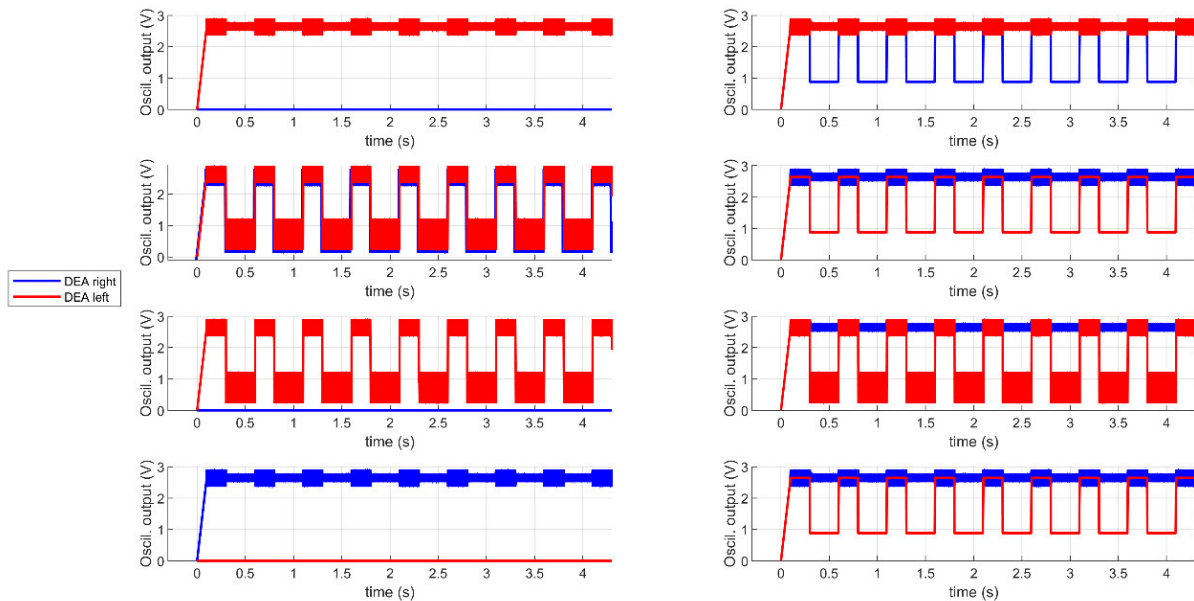


Figure 3.41: Permutations of excitation signals applied on the two DEAs for user tests ([216]).

The first repetition (row 1, column 1) corresponds to a case in which the device on the right user side produces no output and the device on the left produces a purely acoustic output; in the second repetition (row 1 column 2), the left DEA produces a purely acoustic output while the right DEA produces a purely tactile output, etc. All 8 permutations are repeated (in a random order) at 3 distances between the devices (10, 20 and 30 cm), the case with minimum distance (10 cm) corresponding to a scenario in which the sides of the two devices nearly touch one another. Results from the tests are processed and reported in Figure 3.42 in the form of confusion matrices, which count the number of times a user perceived a certain type of stimulus (haptic, acoustic, no stimulus) on the correct side (left, right): different matrices correspond to tests with different distances between the two DEA button units.

Entries in each matrix correspond to cumulated values for the left and right unit. Elements on the rows represent the actual stimulus supplied to the user (e.g., *non_l* means that no feedback was applied on the left device, *haptic_r* means that the stimulus applied on the right unit had an haptic component, etc.); elements on the columns represent the feedback reported by the user (e.g., *non_l* means that the user perceived no feedback on the left finger, *haptic_r* means that the user perceived a feedback containing a tactile component on the right side, etc.) The elements on the diagonal correspond to correct associations between the supplied stimulus and the stimulus reported by the user. Different signals combinations (among those in Figure 3.41) produce a different number of entries in the matrix, because of the composite nature of the signals (which, in general, contain tactile and acoustic components). Details on how the matrices have been populated starting from the users' answers are reported in the Appendix (A.8). The percentages associated to the different rows express how often a given stimulus was correctly classified by the users. Conversely, the percentages associated to the columns express how often a given answer provided by users corresponded to the actual supplied stimulus.

Despite the complex nature of the task (note indeed that users were asked to concurrently identify stimuli received by two units at the same time), the average percentage of correct assignments (diagonal elements) is significantly higher than that of misinterpreted inputs. As expected, this holds especially true in cases where the two devices are located at a greater distance, rendering the collocation task easier for the user. Most common confusion scenarios are related to the assignment of a sound source (left vs right), with results that consistently improve as the distance among units is increased. In particular, in the scenarios where a vibrotactile feedback and an acoustic feedback are applied on different units (e.g., top right case in Figure 3.41), users tend to wrongly assign the location of the acoustic stimulus with higher probability (i.e., they locate the sound source on the same side as that of the tactile stimulation). This is a natural result of cross-modal associations between sound and tactile perceptions, reported by specialistic perception studies [258], [259], [260].

Despite the abovementioned effects, the presented results prove that users are generally able to correctly collocate different (or composite) stimuli in space. This offers an even stronger motivation in favour of the co-located feedback generation approach pursued by the presented DET button interface. Being able to provide co-located vibrotactile and acoustic feedback (with both stimuli generated at a same spatial location), the proposed DE user interface might find applications in VR for multi-sensory rendering of localized scenes.

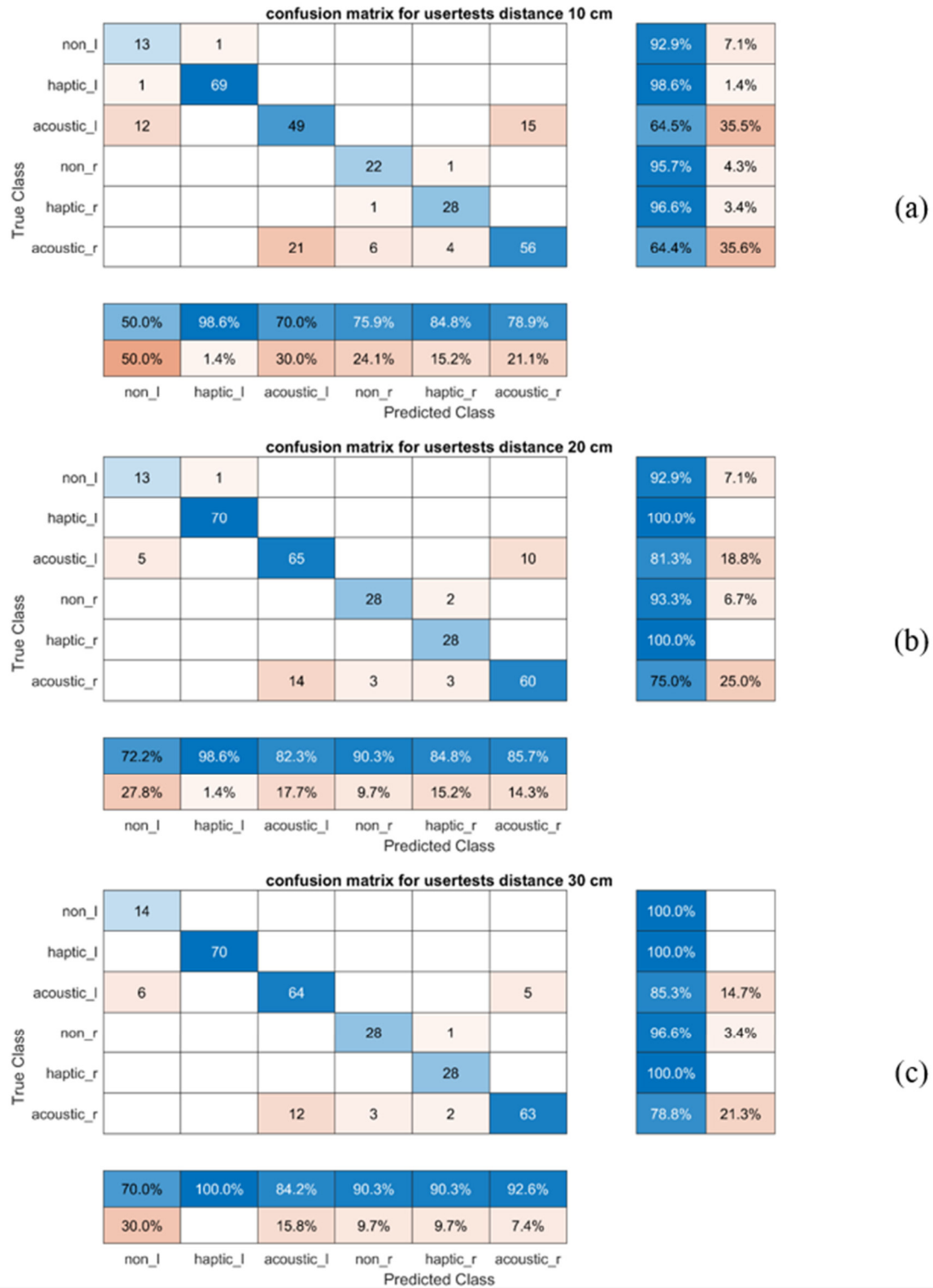


Figure 3.42: Confusion matrix for the user tests with 2 replicas of the DEA button, located at a distance of 10 cm (a), 20 cm (b) and 30 cm (c) from one another. The matrix elements correspond to different types of stimuli (haptic, acoustic, no stimulus), elements on the rows stand for the actual feedback generated by the units, whereas elements on the columns represent stimuli perceived by the users. Elements on the diagonal denote a correct association between supplied stimulus and user's answer. Entries in the matrix correspond to the number of times a certain combination was reported by users. Percentages on the different rows quantify how often a given stimulus was correctly identified by the user. Percentages on the columns indicate how often a certain feedback category reported by users matched the actual applied stimulus ([216]).

3.3. Compact housing and custom high-voltage electronic

This section is based on the published conference paper:

S. Gratz-Kelly, B. Holz, T. Krüger, S. Seelecke, G. Rizzello, P. Motzki, G. Moretti (2023), “An integrated Audio-tactile Interface based on DE Actuators for User Interaction”, Proc. Of ASME, SMASIS2023, 111228.

To realise a completely integrated multi-functional device, beside the core development of the DEA technology, the complete system setup and the electronics (described in section 2.3 - System architecture design of DET based user-interaction interfaces) need to be integrated in a compact unit.

3.3.1. Prototype design

As opposed to the commercial sensing and HV electronics shown in Figure 3.31, in this section a custom made logic and sensing electronic, and a HV electronics are presented, as described in section 3.1.2 and 3.1.3. In Figure 3.43 the signal shapes of the HV electronics and the control schematic for the HV electronic are shown. The prototype described here can be seen as a further development and a step towards higher integration of the previously presented prototype. In section 3.3.2 the presented custom made electronic is tested and the performance is compared with the used commercial High voltage electronic. For all other experimental results and system characterisations the higher quality commercial HV electronic is used since the performance of the multi-functional DEA element itself is at the focus.

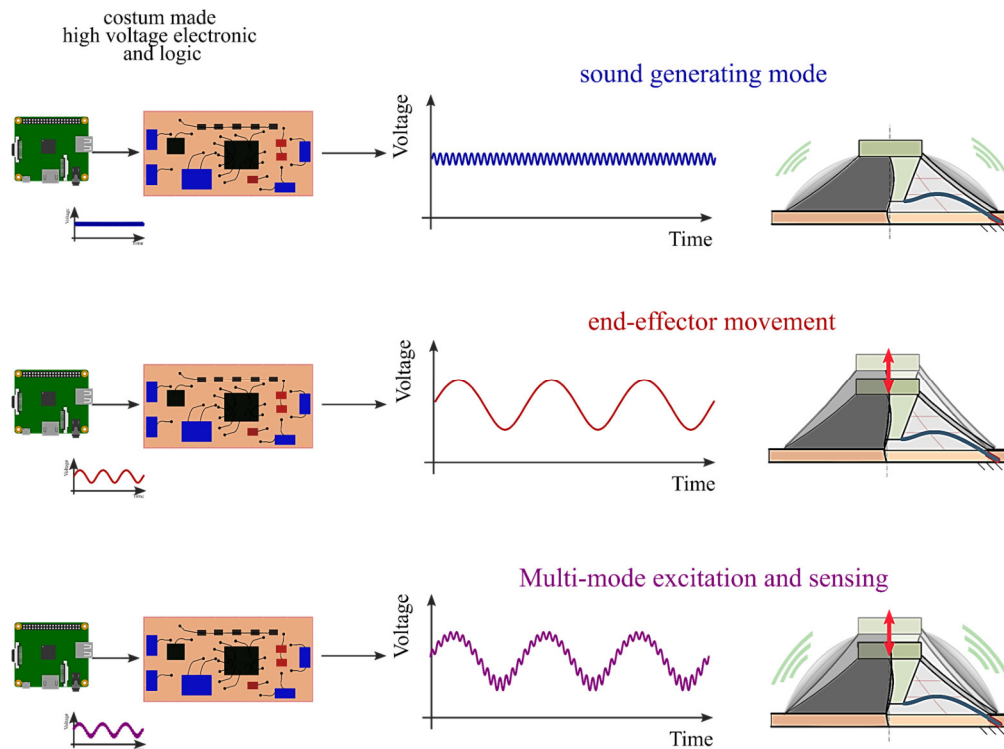


Figure 3.43: Controlled Working modes of the DEA system and corresponding high voltage signals generated by the custom made electronic [221].

For the custom electronics the DEA is installed into a 3D printed housing in a similar way then before. In Figure 3.44, the structure of the custom electronics is shown. All the components are integrated into one housing and need just a 12 V power supply to power all electronics, by means of a 5.5 mm coaxial plug. The logic section includes a wireless local area network (WLAN) connection that grants the opportunity to communicate with the setup wireless (e.g., with a smartphone App).

The electronics are split into two boards. One of them contains both logic and sensing circuits (compare Figure 3.5), and a second one is used to supply HV to the actuation layers of the COP-DEA (compare Figure 3.10).

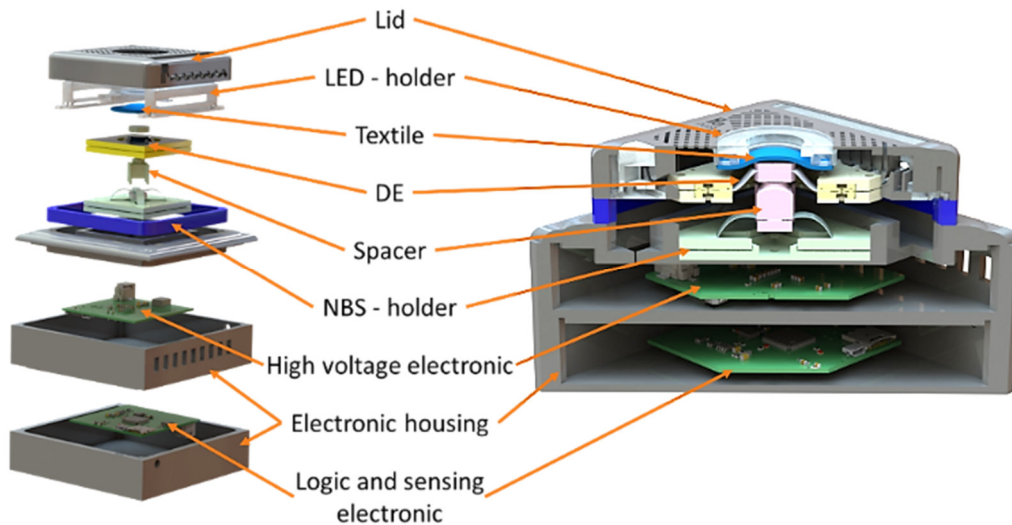


Figure 3.44: Housing and setup of the multi-mode DEA device, including housing, DEA-element, NBS and electronics [221].

The logic and sensing board consists of a stm32 microcontroller and a capacitance measurement circuit based on a charging-discharging time measurement (section 3.1.2 and [216]). In addition to the main functional boards, other interfaces, include programming and communication interfaces and power supply, are integrated. To grant fast access to large amounts of data (e.g., audio tracks), a slot for a micro-SD card is included.

The deformation sensing of the DE, for example due to user pushing, is measured with a custom designed sensing electronic (see section 3.1.2). The electronic measures the capacitance change of the additional sensing layer (see Figure 3.1(c)) which is related to the deformation of the DE. The capacitance measurement unit is based on a charging and discharging time measurement, where the DE is loaded and unloaded to a certain voltage and the time (respectively the frequency) of the cycling can be recalculated to the capacitance of the DE.

The sensing-logic board produces actuation-signals on-demand, based on the readings of the sensing unit. The microcontroller recognizes the users' inputs (i.e., a touch applied on the end effector) by processing the sensing unit measurements and produces an analog output with maximum amplitude of 3.3 V (rendering a vibrotactile and/or acoustic feedback), that is fed as input into the HV amplifier. In the most general case, the output signal of the microcontroller might contain harmonics up to several kHz frequency. To avoid saturating the current at the microcontroller's analog output, an operational amplifier is connected between the controller output and the HV amplifier input. The whole sensing-logic unit is implemented on a board of approx. 65 x 65 mm, which is installed directly into the mechanical casing of the interface. All components

and the interaction between them and the HV board including a physical component diagram with the board is shown in section 3.1.2; Figure 3.5.

The HV amplifier magnifies the analog output of the microcontroller with a gain of 1000, up to a maximum voltage of 3000 V. The HV amplifier is designed to achieve inexpensive manufacturing and small dimensions to drive the commercialization of DEs and is therefore particularly suitable for portable stand-alone systems [32].

The presented circuit (Figure 3.10) consists of a resonant converter with three coils (primary, secondary and feedback coil). A capacitor in parallel to the primary winding is included to generate a LC resonant circuit with fixed resonance frequency. The feedback winding triggers two transistors to keep the circuit operating in resonance (see section 3.1.3). The complexity of the circuit is relatively low, and it needs a low number of components. Thanks to the resonant working principle, the power consumption is very low. The resonant converter outputs an AC voltage, which is rectified before application to the DEA. Most resonant converters are only used up to maximum 2 kV output. To generate a sufficient output for the DE, a Greinacher circuit (voltage doubler) is used to increase the voltage. The Greinacher circuit can be used as rectifier and voltage doubler at the same time [32].

To drive the DEA with high frequency it is important also to discharge the electrodes with sufficiently quick dynamics. The discharging is realized with high impedance resistors which are shortcut via HV MOSFET transistors. If the desired voltage is lower than the voltage supplied on the DE, the transistors are switched on, and the DE gets unloaded until the comparator is negative. In section 3.1.3; Figure 3.10, the principle structure of the HV electronic with relevant components are shown.

3.3.2. Experimental results

To characterize the performance of the prototype with custom HV electronics, as described in section 3.2.3 and 3.1.3, measurements with the developed HV electronics and with a conventional available HV amplifier (HA51U-3P5 by hivolt.de GmbH & Co. KG with 3000 V maximum voltage and 10 mA maximum current) are performed. The commercial HV electronics is heavier, larger and has a cost on the order of several thousand euros, compared to the presented electronic which is much smaller lightweight and costs below 100 €. Owing to the different target and architectural complexity of the two systems, it can be expected that the performance of the commercial electronics represents an upper bound to the performance of the custom HV amplifier. On the other hand, in order to bring portable and integrated DE-based interfaces to the market, the step towards low-cost and small high-voltage electronics is a must, even though it might come at the cost of a moderate loss in performance.

Measurements with a LF signal with high amplitude are performed. In Figure 3.45, the out-of-plane movement of the end-effector for a sinusoidal sweep with different amplitudes up to 180 Hz, measured with a laser displacement sensor (epsilon optoNCD11402) is shown. The displacements obtained with the custom electronics are slightly higher, because the actual gain of the circuit is slightly higher than the nominal value of 1000 (c.f. [221]).

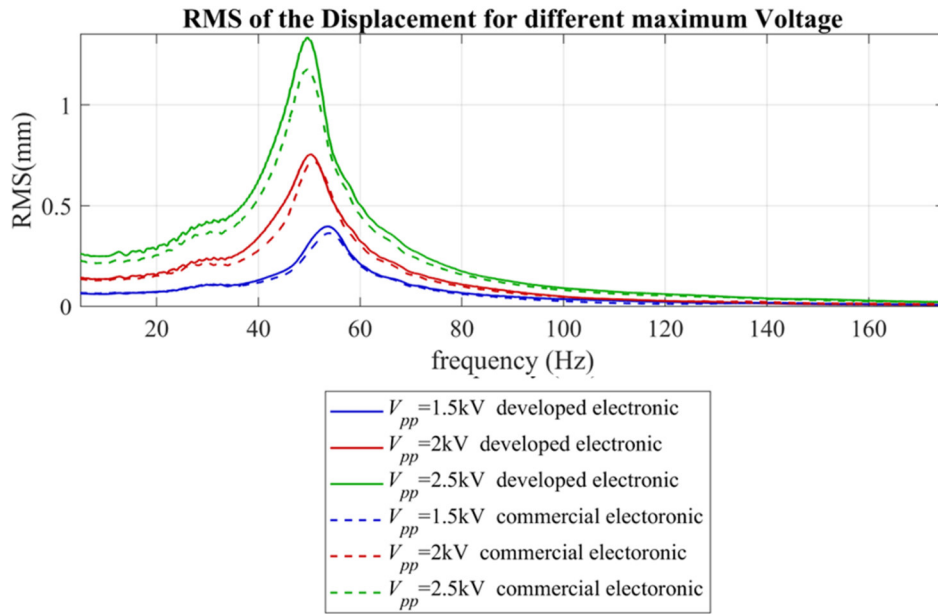


Figure 3.45: Displacement of the end-effector for different voltage amplitudes [221].

In Figure 3.46 the timeseries of sound pressure (in response to a chirp voltage input) of the commercial HV electronic compared to the developed electronic is shown. The sound pressure is measured with a microphone M210 by Microtech Gefell, located at a distance of 30 cm from the DEA, with conditioning module M33. The conventional electronic can generate higher sound pressure at the highest frequencies, but the frequency response of the system is not altered by the used electronic. The lower sound pressure of the developed electronic can be explained by the lower rated current and the poorer performance of the resonant circuit at high frequencies (especially for what concerns the discharging phase). The performance of the two electronics (in terms of sound pressure output) is comparable at lower frequencies, with the custom electronics providing slightly larger pressure output in the range below 600 Hz, because of the slight error in the nominal gain of the electronics (c.f [221]).

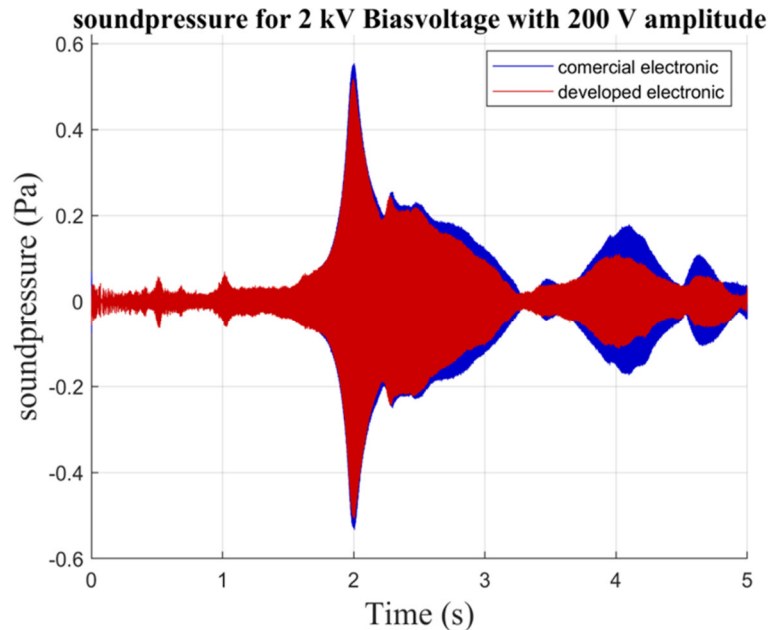


Figure 3.46: Measured acoustic pressure for sinusoidal-sweep (0 – 2 kHz) with a bias voltage of 1.5 kV and amplitude of 100 V [221].

The SPL of the device (DEA + custom electronics) for different HF amplitudes and biasing voltages is characterised, as shown in Figure 3.47 (top). The maximum measured SPL is nearly 90 dB at around 1 kHz, which represents the first natural frequency of the structural vibrations of the DEA membrane (compare with Figure 3.28 and Figure 3.35 - section 3.2).

As expected, the SPL increases with higher biasing and higher amplitude. Additionally, in Figure 3.47 (bottom) the SPL for the developed and the commercial electronic are compared. Again, at higher frequencies the commercial electronic generates higher SPL (c.f. [221]).

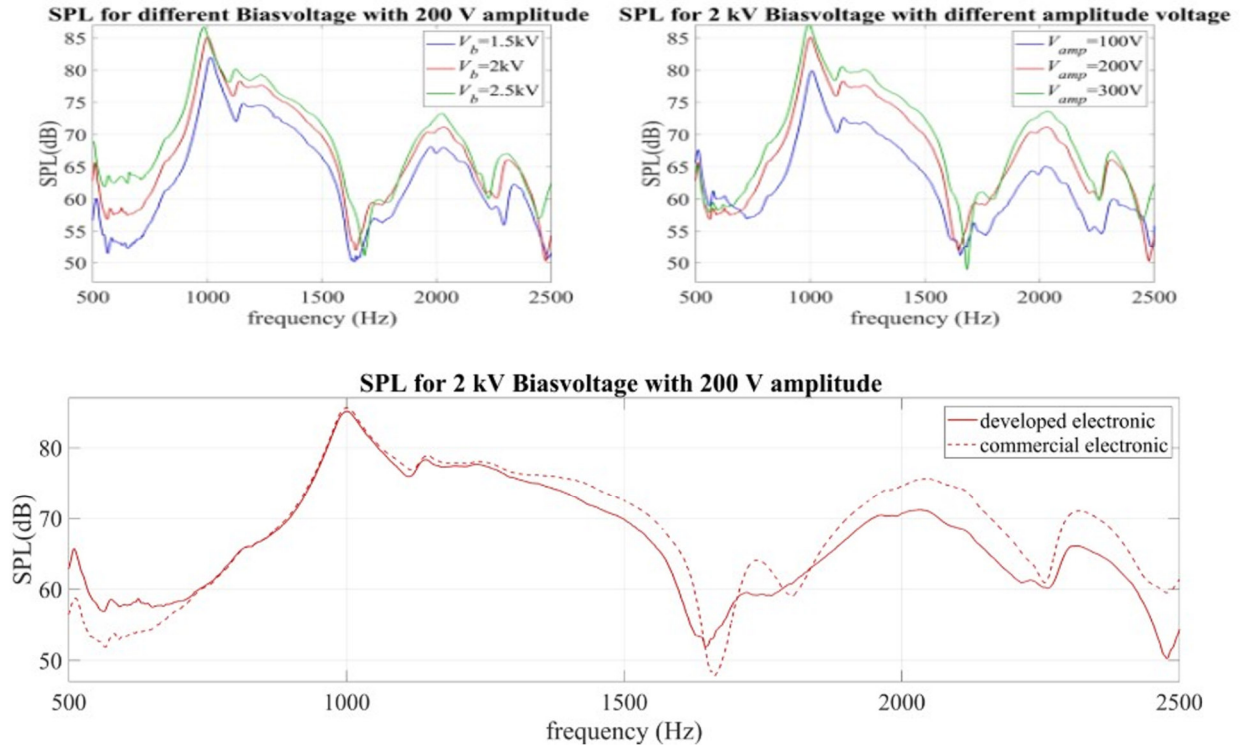


Figure 3.47: SPL of the DEA with custom for different input signals of the HV source (top). Comparison of the SPL performance of the DEA with custom and commercial HV amplifiers (bottom) [221].

To compare the signal quality of the two electronics, the total harmonic distortion (THD) is calculated. In Figure 3.48, the THD for both electronics (relative to a test with bias of 2 kV and amplitude of 300 V) is shown. The distortion factor measured with the commercial electronics can mainly be attributed to the DEA, while the additional distortions achieved with the customised circuit board can be attributed to the circuit behaviour.

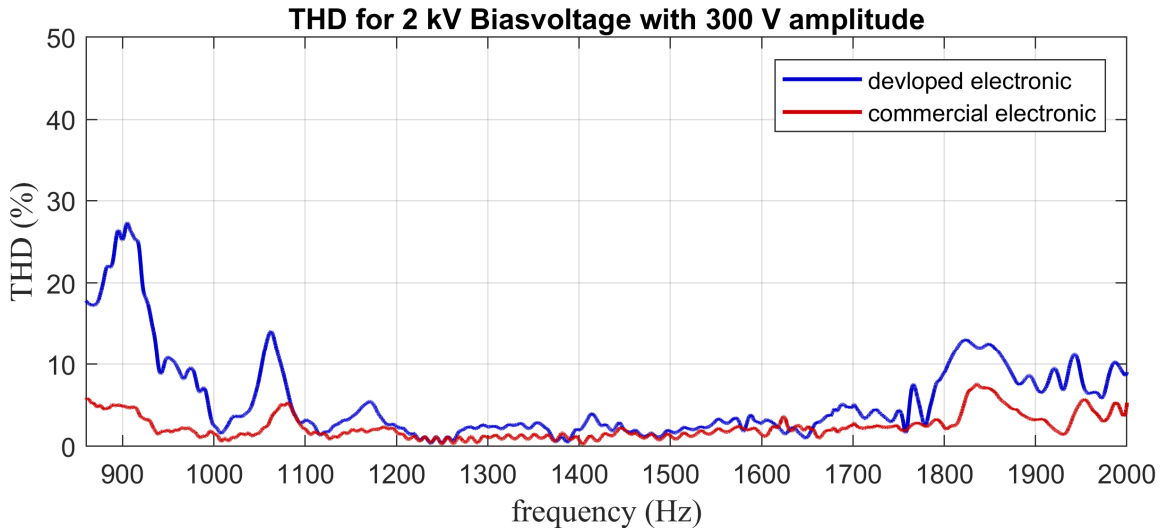


Figure 3.48 Total harmonic distortion (THD) of the sinusoidal sound signal compared with commercial electronic [221].

The signal of the developed electronic has more distortion at low and higher frequencies. The THD of the developed electronic is in the worst case around 20% (absolute) higher than the commercial electronic. In the region 1100-1700 Hz, the THD of the custom board is approximately the same as that of the commercial amplifier and the distortion can be thus assumed entirely due to the nonlinear DEA response (c.f. [221]).

In Figure 3.49, the prototype is tested with multi-chromatic signals including a LF and a HF component. The applied voltage consists of a sinusoidally varying LF signal (5 Hz) with two different superposed HF signals (middle: sinusoidal HF signal 950 Hz: and bottom: soundtrack). The sound pressure shows a beat distortion due to LF modulation (as already observed in Figure 3.26), which should be compensated for through suitable controls, whereas the displacement of the end-effector is smoothly varying, unaffected by the HF signal.

These results show that a multifunctional control of the DEA can be realized with the developed HV electronic. Even if the performance and the sound quality is lower than that obtained with a commercial amplifier, these electronics might represent a promising option for wearable or low-cost stand-alone applications, due to their compact size, lightweight and low cost (c.f. [221]).

The other measurements presented in this thesis were made with higher accuracy and better quality HV electronic (like the one used for the comparison in this section). Even though the developed electronic can control the DEA in a comparable manner, the sound quality of the acoustic output is lower and could have an impact to the more general observed and investigated features of the DEA element. Also, for the performed user-tests (section 3.2.4.3) a commercial electronic is used, even if it turns out that the tactile feel and performance of the developed electronics in particular is no worse than that of commercially available electronics.

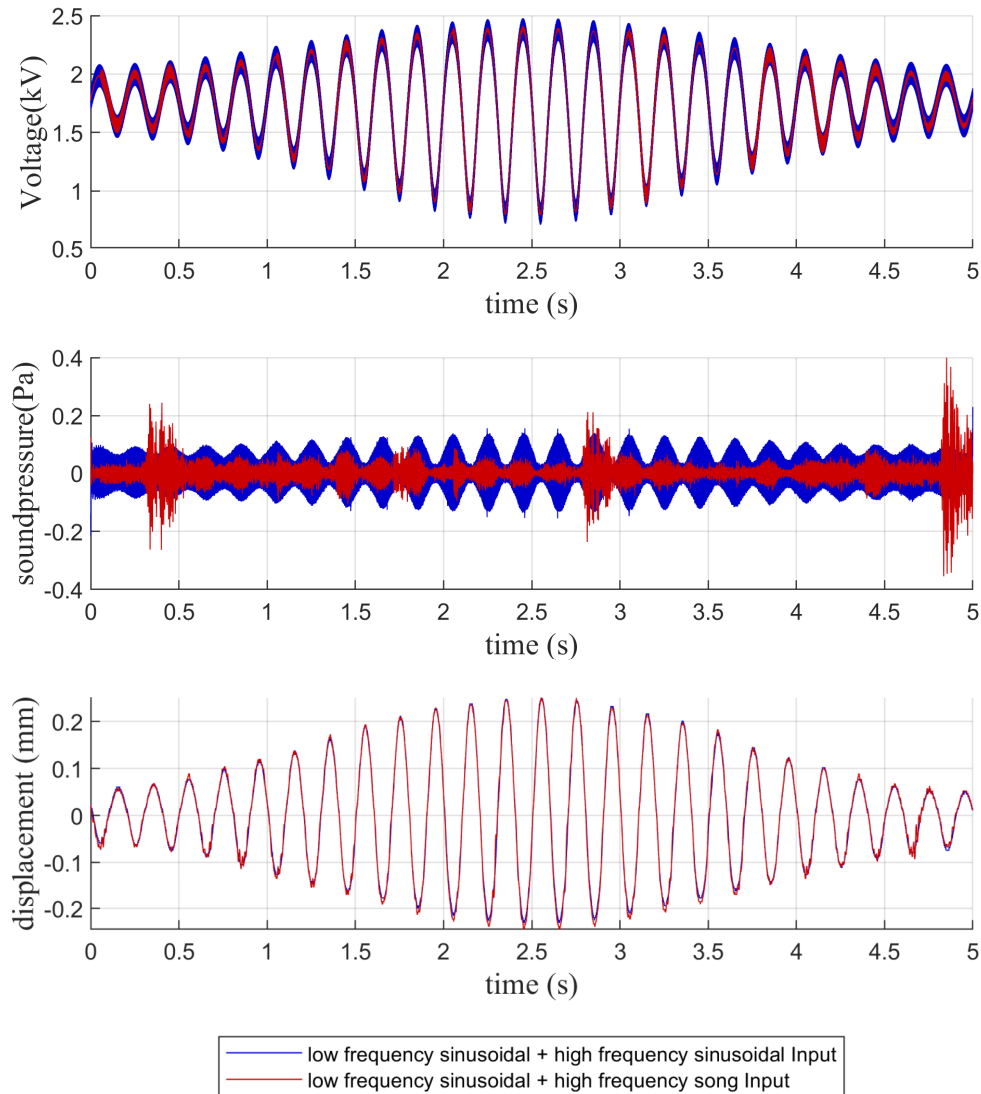


Figure 3.49: Multimode LF and HF combined working mode of the DEA. With Input voltage (LF sin + HF sin and LF sin+ HF song), measured sound pressure and displacement of the end-effector [221].

3.4. Self-sensing approach for audio-tactile elements

This section is based on the published paper:

S. Gratz-Kelly, T. Krüger, S. Seelecke, G. Rizzello, G. Moretti (2024), “A tri-modal dielectric elastomer actuator integrating linear actuation, sound generation, and self-sensing capabilities”, *Sensors and Actuators: A. Physical*, Vol. 372, Issue 115332, doi: 10.1016/j.sna.2024.115332.

An additional functional capability can be added on top of the described multi-mode actuation capability by means of self-sensing. By adding this function, the additional sensor layer can be made redundant without compromising the detection performance of the system. With that

advancement, besides the scientific interest of the topic, the performance of the whole system can be improved. Figure 3.50 shows the structure of the DET based user interaction interface (compare Figure 2.33).

The extra sensing layer, used for the smart sensing audio tactile button in section 3.2.4.3, is very susceptible to noise when used with HV actuated layers. For this reason, simultaneous sensing and actuation of the DEA prototype is not feasible and the features must be performed one after the other (in time). With the use of self-sensing, simultaneous deformation sensing of the DEA during actuation is realized. The additional sensing layer also increases the stiffness and hysteresis of the system, which leads to a reduction in actuation performance.

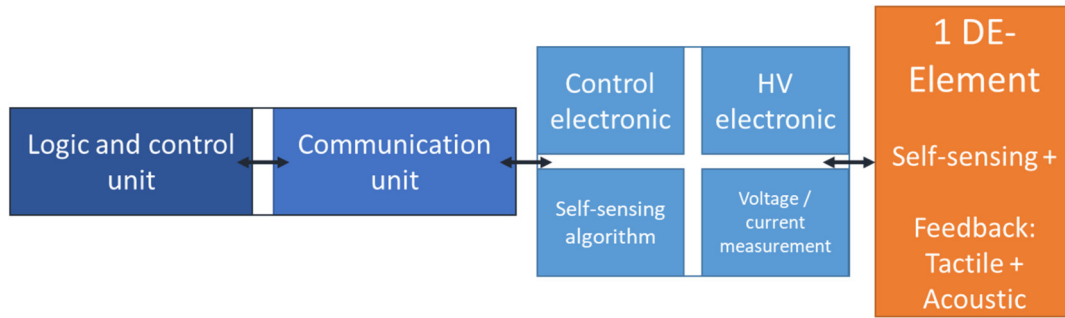


Figure 3.50: Structure components of DE-based interaction interfaces with multi-functional DEA combined with self-sensing.

Different self-sensing paradigms can be implemented, leveraging the COP-DEA dynamic response. On the one hand, when the device operates in the HF region producing an acoustic output, the HF actuation signal component can be directly used for self-sensing mode without any further physical or structural additions (e.g., dedicated capacitive sensing layers) or dedicated superposed sensing signals (which increase the maximum voltage to which the DEA is subject).

On the other hand, if no acoustic output is requested, self-sensing can still be performed by injecting a dedicated small-amplitude sensing signal (superposed to the LF driving signal, if present) with spectral content in an intermediate mid-frequency (MF) region where neither linear actuation and acoustic feedback are produced (Figure 3.51). Although, in this case, the driving voltage still has the form given by equation 3.20 (with \tilde{v} representing the MF sensing signal), the choice of the sensing signal \tilde{v} frequency prevents (or strongly limits) sound generation.

In both cases, self-sensing algorithms are implemented using measurements of the DEA applied voltage and current (which is dominated by HF/MF components of the driving signal), which in turn can be used to reconstruct LF variations in the DEA capacitance, which are correlated to variations in the stroke z .

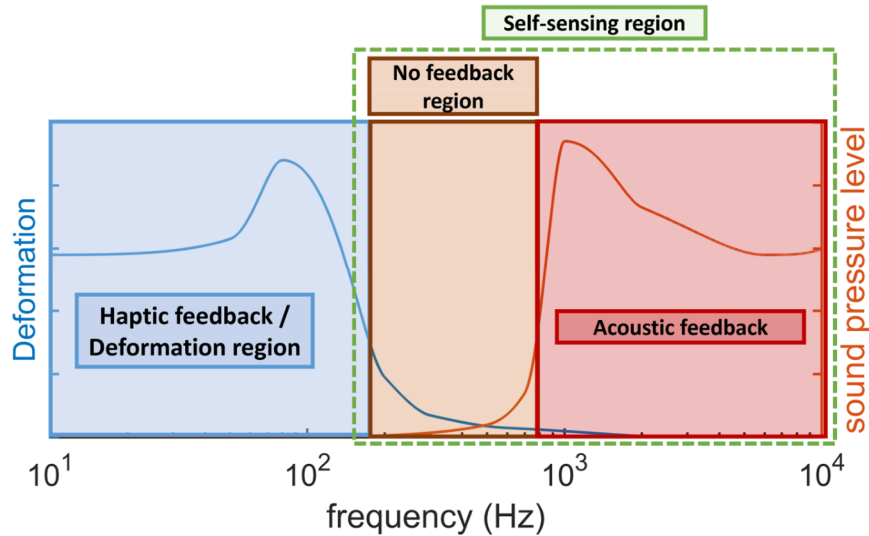


Figure 3.51: Working regions of the audio-tactile DEA. With LF linear movement region, MF no feedback region and HF acoustic feedback region. Self-sensing region can be used for MF and HF regions and partially LF region. The plot is qualitative: frequency ranges shown on the frequency axis are an approximate indication that holds for centimetre-scale DEAs with features/material properties discussed ([261]).

A DEA can be described as a cascade RC circuit with the contact resistor, electrode resistor and leakage resistor in parallel to the dielectric of the DE. A very simplified model is just a simple RC circuit like the one shown in Figure 3.52. Compared to the circuit explained in section 2.1.1.1 (Figure 2.3) the leakage resistor is not included here, because the resistance is very high and has only a relevant contribution for very small frequencies. As proposed in [262], the series resistor of a DEA has a non-linear and hysteretic behaviour which makes it difficult to be used for displacement estimation. The capacitance-displacement behaviour, on the other hand, is monotonic and has only very low hysteresis. For this reason, the capacitance is the most suitable variable for displacement estimation of DEAs.

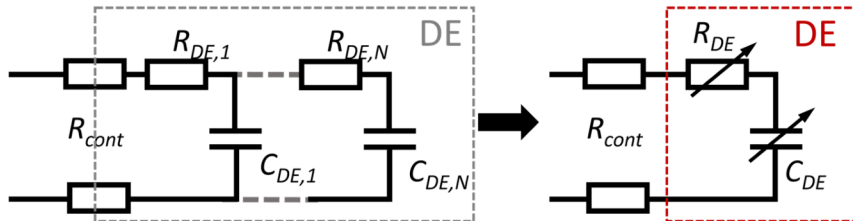


Figure 3.52: DE equivalent circuit for self-sensing model by reducing the RC cascade to a simplified single RC element to roughly represent the DEA electrically (c.f. Figure 3.4).

To sense the deformation of the DEA a HF signal is superimposed to the normal driving signal. With that the current can be magnified to increase the accuracy of the sensing. The DE movement induced by the HF signal is, due to the low pass characteristics of the system, very low compared to the movement induced by the LF HV signal, leading to a minor or no influence on the system behavior. The described algorithm was proposed by Rizzelo et al. [235], [262].

The circuit can be described by a state-space representation of the electrical model. The series resistor and the capacitance are represented as functions of the deformation and the (induced)

current and voltage as well as the charge are dependent on the time. With this convention the circuit can be described with:

$$v(t) = R(d)i(t) + \frac{1}{C(d)} q(t). \quad (3.23)$$

Capacitance and the resistance change due to the HV signal are very low as compared to those associated with the LF signal. With this assumption the resistor and the capacitance of the system can be considered to be constant during a time window including a few periods of the HF signal. ($R(d) = R; C(d) = C$). Differentiation equation 3.23 and defining $\frac{d}{dt} q(t) = i(t)$, the DEA equivalent circuit can be described by

$$\frac{d}{dt} v(t) = R \frac{d}{dt} i(t) + \frac{1}{C} i(t) \quad (3.24)$$

The discrete time derivative, considering the small sampling time window T_s , can be approximated with the Euler method, $\frac{d}{dt} y(t) = \frac{y_k - y_{k-1}}{T_s}$ what leads to

$$v_k - v_{k-1} = R(i_k - i_{k-1}) + \frac{T_s}{C} i_k \quad (3.25)$$

In [235], [263] Rizzello et al. proposed an improved algorithm to estimate the resistance and capacitance of a DEA. With the use of a pre-warped Tustin method for the continuous-time derivatives, a stable and accurate estimation is achieved using lower sampling frequencies. The Tustin method is also called bilinear transform or trapezoidal Integral method because it describes the discrete values with a trapezoidal formula compared to the Euler method (rectangular $i(t) = i_k$). This leads to a discretisation which is more exact for the derivative approximation at a discrete point. The derivative is calculated like with the Euler method (just shifted by half of the discretisation window, tangential trapezoidal formula) and the function value is calculated with $y(t) = \frac{y_k + y_{k-1}}{2}$, which considered the trapezoidal function [264].

With the ‘pre-warping’ the nonlinear relationship of the frequency ($\omega_a = \frac{2}{T} \tan(\omega_d \frac{T}{2})$) during the bilinear transformation and discretisation can be eliminated (s-plane to z-plane transformation). Since the electrical system of the DEA is mainly excited with a single high frequency, the pre-warped Tustin method can be tuned for this specific frequency by shifting the frequency with the inverse function of nonlinear relationship [265], [266]. This leads to a factor $K_T = \frac{\tan(\pi f_e T_s)}{2\pi f_e}$ in the equation for the function value of i_k to discretize equation 3.23 like

$$v_k - v_{k-1} = R(i_k - i_{k-1}) + \frac{K_T}{C} (i_k + i_{k-1}) \quad (3.26)$$

It can be shown that the discretization given by equation 3.26 can be robustly used to perform self-sensing also for polychromatic HF input signals, holding spectral content in a broad range around f_e .

In previous works on self-sensing, the procedure described above has been implemented by purposely injecting an additional higher frequency sinusoidal signal on top of the main driving signal. The sensing signal had a fixed frequency, higher than the driving signal frequency, with the aim of generating a readable current. The current generated by the acoustic driving signals, in addition dedicated signals superimposed to the driving signal, which in general holds multiple harmonics (as in the case of soundtracks) can also be used for sensing.

With reference to multi-mode and audio-tactile DEA applications, self-sensing can be realised in different ways and for different application scenarios, as shown in Figure 3.53.

In a first set of applications, the multi-mode DEA can be used with a HF/MF signal superimposed to a LF voltage signal to produce a voltage-induced movement (Figure 3.53 left). The self-induced capacitance change of the DEA can then be estimated by the self-sensing algorithm to calculate the movement of the end-effector. By feeding the DEA with a HF or a MF signal, self-sensing is accomplished either in combination with sound generation or alone.

In a second scenario (Figure 3.53 right) the device can be used as a multi-mode audio-tactile button. In this case the device can produce a vibrotactile stimulation via LF driving, sound through a HF superposed voltage signal and detect a user input by self-sensing. Also in this scenario, using the MF range instead of the HF range, a silent self-sensing mode where no sound is produced can be realized. Measuring the capacitance via self-sensing allows reconstructing the DEA position. This potentially allows generating adjustable multi-mode feedback, which is a function of the measured user input (e.g., touch).

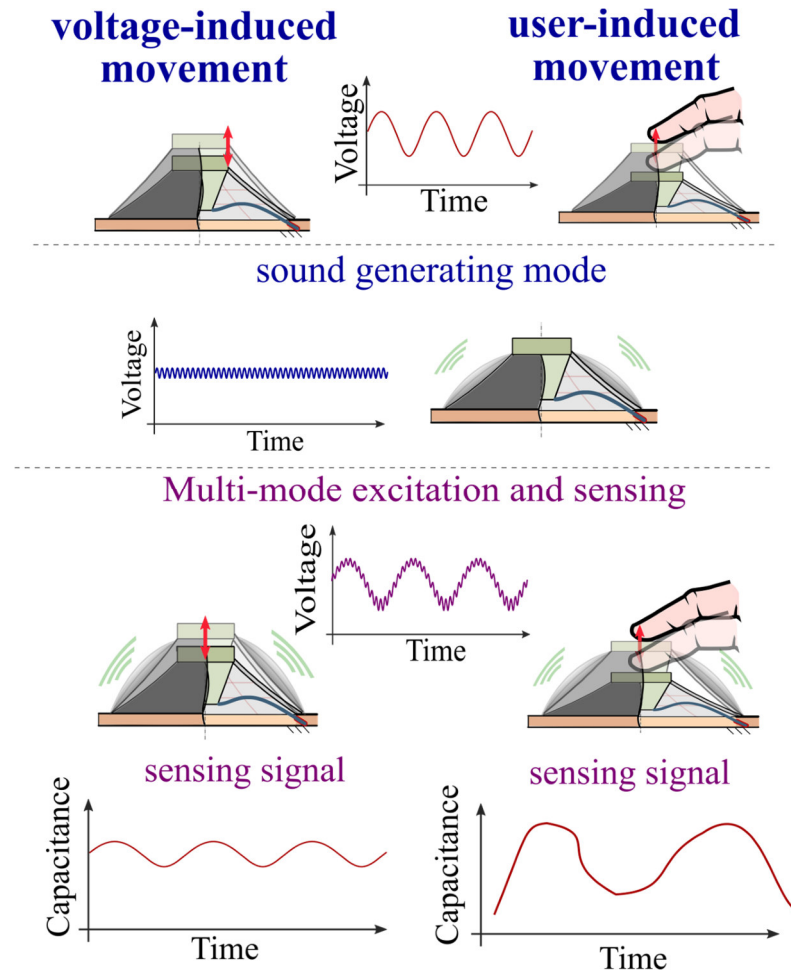


Figure 3.53: Different working modes of the COP-DEA. Left: multi-mode audio-tactile excitation with HF structural vibration and LF linear movement as well as two alternative modes for self-sensing (HF sound-producing working mode and MF silent working mode). Right: user-imposed deformation with two self-sensing modes (HF sound-producing working mode and MF silent working mode) ([261]).

The frequency ranges where the different modes can be achieved depend on the 3 frequency regions of the COP-DEA dynamic responses identified in Figure 3.51. The LF region where a

linear movement of the DEA end-effector appears can be used to provide linear actuation (e.g., haptic feedback to provide to the user). The HF region corresponding to the excitation of the first structural vibrational mode and above can be simultaneously used for self-sensing and sound generation. The MF range between LF and HF is a region where no linear movement appears, and no sound is produced. A silent self-sensing mode can be accomplished through the use of sensing signals within this frequency band.

3.4.1. Characterization of multi-mode DEA self-sensing

Figure 3.54 shows the frequency response of the developed prototype in terms of deformation and SPL, obtained applying a monochromatic excitation at different frequencies (i.e., setting $V_{\max} = V_{\min}$ in equation 3.20), for different amplitudes ($\sqrt{U_2}$) and bias voltages ($V_b = \sqrt{U_0}$) of the driving voltage signal \tilde{v} .

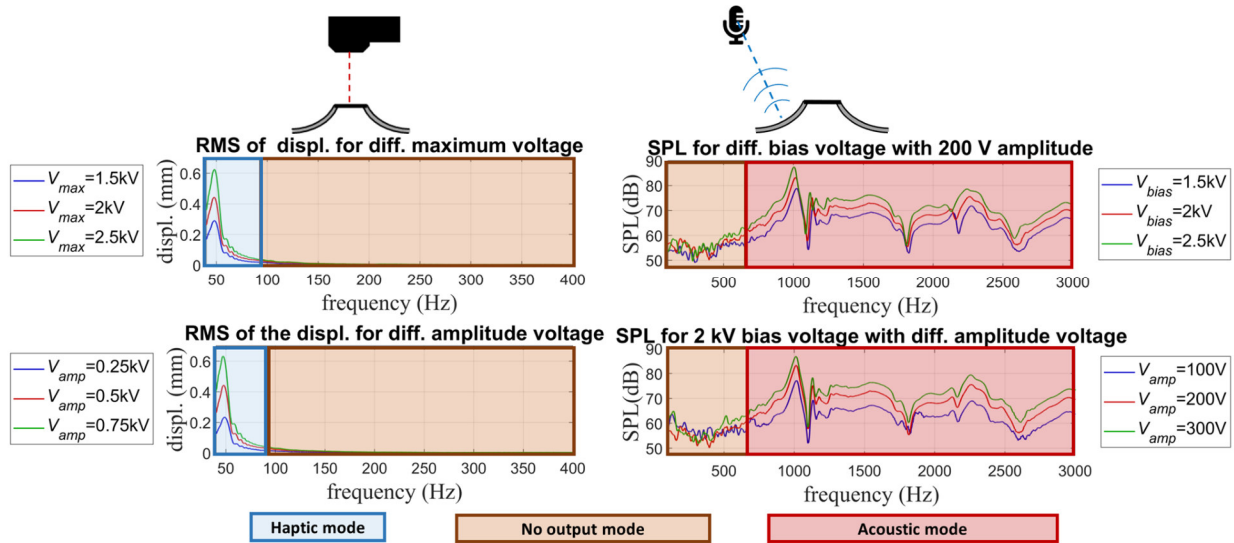


Figure 3.54: COP-DEA frequency response in terms of displacement and sound pressure output, highlighting the LF, MF and HF region of the response ([261]).

In the region from 150 Hz to 700 Hz the deformation and the sound pressure generated by the unit are very low. With that observation, two main regions for the self-sensing can be identified, respectively between 150 Hz and 700 Hz, and above 700 Hz. In the higher-frequency region the unit produces sound and the HF driving signal can be used as self-sensing signal. In the lower-frequency region, the system can perform self-sensing, using a dedicated injected sensing signal while remaining silent.

To validate the self-sensing algorithm against a reference capacitance measurement (obtained with a Rohde & Schwarz Hameg HM 8118 LCR meter), a sinusoidal movement of the end-effector has been impressed through a motor. In Figure 3.55 the capacitance estimated with the self-sensing algorithm (at different applied bias voltages (0.5 kV; 1 kV; 2 kV)) is compared with LCR measurements and the simple geometrical model (compare appendix A.9). LCR meter measurements were obtained with a low-voltage bias applied on the DEA. The HF sensing frequency of the self-sensing algorithm is 1 kHz.

The estimated capacitance of the self-sensing algorithm lies between the LCR meter, which measures a lower capacitance, and the geometric model, which provides a larger capacitance compared to the self-sensing algorithm. The mismatch between LCR measurements and the analytical model is explainable due to the several combined reasons like: necking of the DE membrane;

contact resistance change for different bias voltage; and underestimation of the complex RC-equivalent circuit diagram. The fact that capacitance variations predicted by the algorithm are lower than (and then progressively approach) the expected variations (based on the geometrical model) at low voltages (including the working conditions of the LCR meter) might be due to high resistance of the electrodes (or the contact between electrodes and circuit tracks), which decreases at higher working voltages.

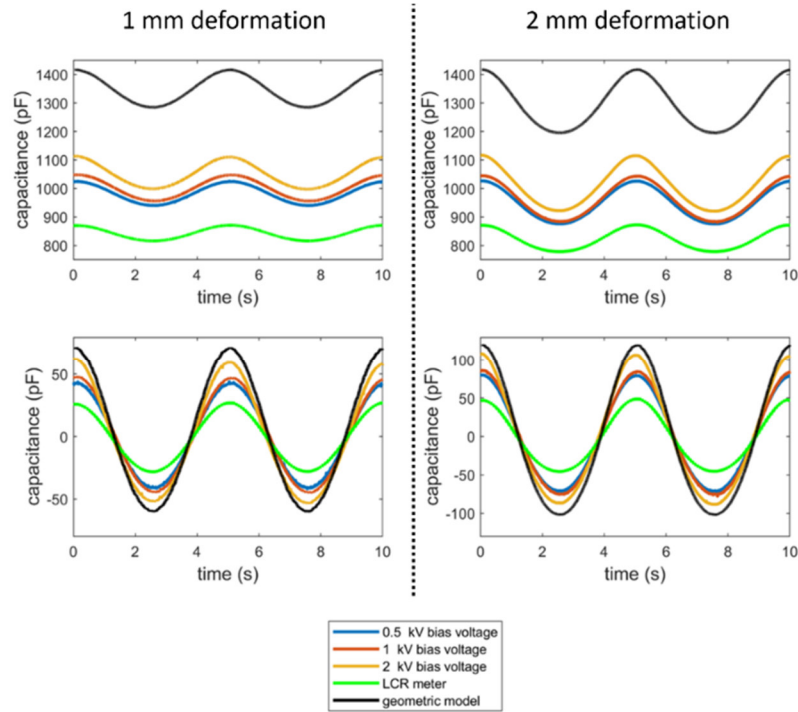


Figure 3.55: Self-sensing algorithm comparison with LCR meter measurement and geometric model (c.f.[261]).

Despite the reported mismatch, the algorithm is found to predict variations in the capacitance variations that can be used in a closed-loop setting to adjust the device output as a function of the estimated deformation.

With the validation of the relative capacitance change, which is the relevant quantity for applications targeting deformation sensing, the self-sensing algorithm results accurate enough to detect even very small movements and the capacitance change is comparable with conventional high accuracy measurements. Consequentially, with the self-sensing procedure it is possible to measure the deformation of the DE element, even with applied high voltage, accurately.

The performance of the self-sensing algorithm in both scenarios illustrated in Figure 3.53, with deformations induced by external stimuli, or by the LF components of the excitation voltage is measured and validated in the following.

Figure 3.56 shows a characterization of the unit performance in the presence of an external input applied by a motor. The unit is driven with a HF signal \tilde{v} (either a sinusoidal signal or a polychromatic audio track) used both to produce a hearable sound and perform self-sensing. For both cases a same deformation of 2 mm is applied by the motor and the audio output is measured with a microphone. The voltage input has a maximum amplitude of 200 V, bias of 2000 V, and maximum sound pressure on the order of 0.15 Pa (78 dB). The test with monochromatic excitation shows

that the sound pressure amplitude changes as a function of the stroke (reaching a maximum when the COP-DEA out-of-plane deformation is maximum). This is a beating distortion, already observed, due to the nonlinear dynamics of the system, whose stiffness (in the structural modes) depends on z .

Correlation between the measured end-effector stroke and the sensed capacitance is quantified in terms of Pearson correlation coefficient (CC) between displacement and capacitance time signals. Such quantity is defined as the ratio between the covariance of the two variables and the product of their standard deviations, and is computed via the Matlab function *corrcoef*. The Pearson CC measures the linear correlation of the two variables with a result between -1 and 1 (± 1 perfect correlation; 0 no correlation) [267].

The CC between the calculated capacitance and the movement of the end-effector is 0.99 in the case of sinusoidal driving signals, and 0.83 in the case of polychromatic driving signals. A comparison of the capacitance calculated by the self-sensing algorithm and the geometric model shows also that the signal shape is like to be expected. The variation of the capacitance ΔC is calculated by subtracting the mean value of the measured capacitance.

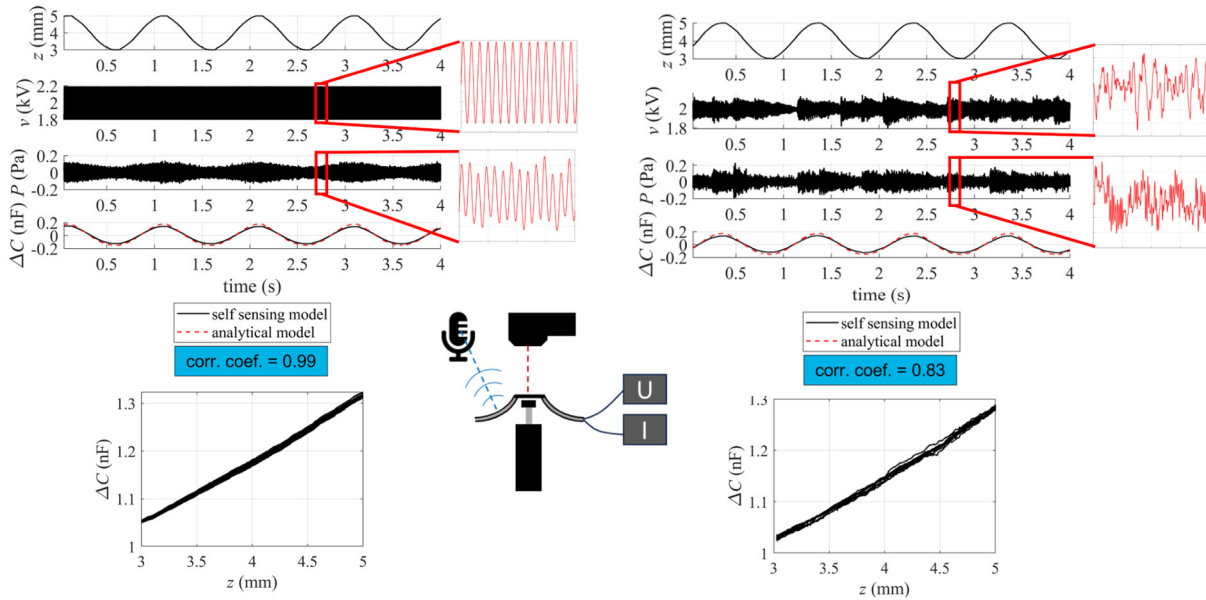


Figure 3.56: Self-sensing performance for motor-induced movement Left: sinusoidal HF signal \tilde{v} . Right: HF signal \tilde{v} rendering a soundtrack ([261]).

In a same manner, self-sensing in the presence of a voltage-induced deformation of the DEA element is characterized in Figure 3.57. For the voltage-induced movement a LF signal with $V_{min} = 500$ and $V_{max} = 2500$ Volt is superimposed to a HF signal with same amplitude and frequency as in the previous motor-induced measurements. The deformation of the end-effector is below 0.5 mm and the maximum sound pressure is on the same order as for motor-induced measurements. Compared to the previous case, fluctuations in sound pressure amplitude are much higher, which can be explained with the variable value of the bias voltage due to the LF signal, which has a much higher influence than the out-of-plane deformation. Increasing the voltage leads to a reduction in the DE membrane stiffness, which in turn leads to larger amplitude vibrations and sound pressure output of the stiffness associated structural modes.

The CC for the sinusoidal HF signal (0.87) is less than that measured in the case of motor induced displacement. This is due to a ripple in the trend of the estimated capacitance, occurring in the

low voltage range. This peak is an artifact due to multiple concurrent causes: 1) in addition to out-of-plane conical deformations, electric activation causes a static lateral deformation of the COP-DEA against the membrane profile necking, which leads to a change in capacitance; 2) the power supply output is subject to distortions in the considered frequency range, due to dynamic effects and the capacitive load created by the DEA. Both above mentioned effects become particularly conspicuous when end-effector displacements are small, as in the example considered here. The mismatch between actual displacement and estimated capacitance in the bottom part of the stroke is also reflected in the capacitance-displacement trend, shown in Figure 3.56 (bottom) for 4 cycles. Whereas the trend shows a monotonic functional behavior over a large portion of the stroke range (similar to Figure 3.55), the univocal correlation between displacement and predicted capacitance is not correctly estimated in the bottom part of the stroke ($z \in [5.0, 5.2]$ mm).

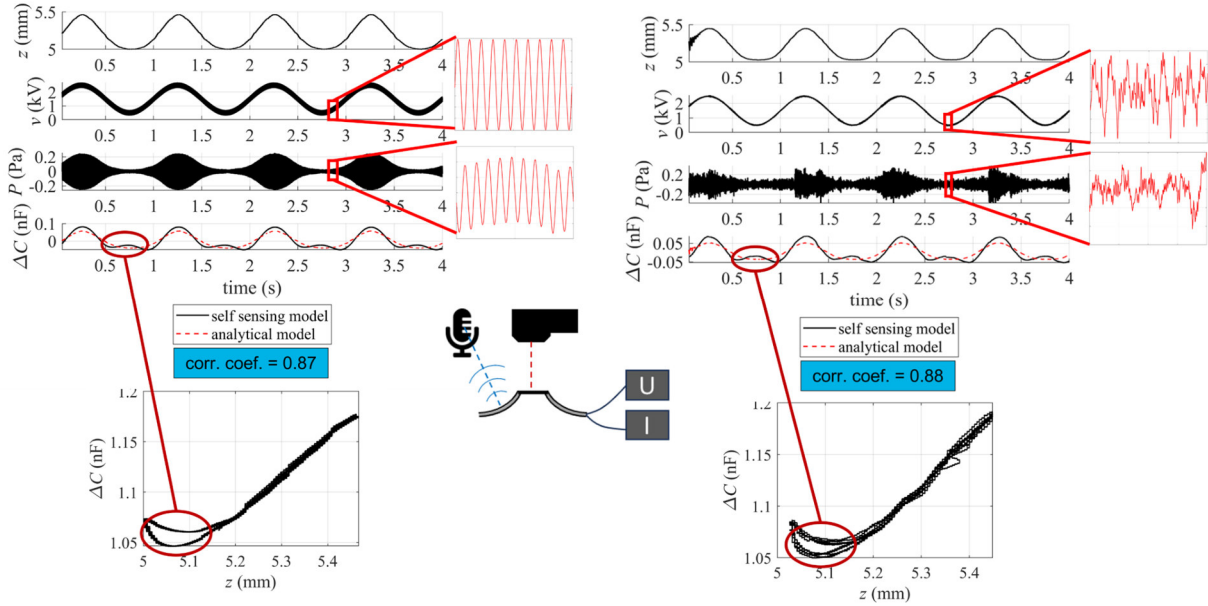


Figure 3.57: Self-sensing performance for voltage-induced movement Left: sinusoidal HF signal \tilde{v} . Right: HF signal \tilde{v} rendering a soundtrack ([261]).

Despite such misestimation of the capacitance over restricted portions of the stroke ranges, the global CC is higher than 0.8 (validation limit for high correlation [268]), and the algorithm is able to capture the general trend of z . In the case of self-measurements performed using a song as the HF signal, the correlation coefficient (0.88) is the same as for sinusoidal HF signals. Comparison of the capacitance trends estimated via self-sensing and with the geometrical model (based on measurements of z) shows a greater deviation compared to that observed in tests with motor-driven deformation (Figure 3.57). This happens because, in this test, capacitance varies in a narrower range, leading to higher relative inaccuracy in the capacitance estimation.

The validation shows that the self-sensing algorithm based on HF driving signals (either monochromatic or broad-banded) in the acoustic range leads to capacitance estimates that retrace the essential features of and have high correlation with the DEA linear displacement.

With this consideration, it is possible to use arbitrarily-complex polychromatic signals (soundtracks) to provide acoustic feedback while simultaneously performing sensing.

A set of measurements with the same procedure as in Figure 3.56 and Figure 3.57 by varying a set of test parameters to test the robustness of the self-sensing capability is performed. For motor-

induced measurements, tests at different frequencies and amplitude of the HF driving signal and with different biasing voltages were performed, while prescribing LF sinusoidal deformations with different deformation frequencies (1 Hz and 3 Hz) and amplitudes by the linear motor.

Tests with different frequencies of signal \tilde{v} were run using an amplitude $\sqrt{U_2} = 200$ V and biasing voltage $V_b = 2$ kV, LF displacements of 2 mm amplitude at 1 Hz. Tests with different values of amplitude $\sqrt{U_2}$ were carried out at constant biasing voltage of 2 kV and same LF deformation as in the previous case. Tests with different bias voltages were run using a HF amplitude of 50 V (which allows to apply different bias voltages, including low bias voltages, while preserving the voltage polarity positive) and same LF deformations as before. Tests with different prescribed deformation amplitude were done using a HF signal of 200 V amplitude, 350 Hz frequency and 2 kV bias voltage.

Results are summarized in Figure 3.58 in terms of SPL and CC between estimated capacitance and measured displacement. The points for the SPL in the plot in Figure 3.58 are the mean values of the SPL over the complete time window of the measurement. The CC is over 0.9 for all parameter combinations, and it decreases under 0.9 just for very low frequencies below 50 Hz.

In the considered region (below the natural frequency of the first structural mode), the SPL increases with higher frequencies and depends on the HF amplitude and the bias voltage, as previously observed. The minimum SPL reached in these tests corresponds to a condition in which the DEA produces no sound, despite minimum values displayed in the plots are on the order of 40-50 dB because of limitations in the microphone and electronics capabilities.

The results provide evidence that, in all configurations, regions can be identified where high SPL can be generated, while concurrently obtaining capacitance measurements with CC close to 1 or, on the other side, regions where the CC is still high but no sound is produced. This allows implementing scenarios where sensing is accomplished either in combination with or independently of sound generation.

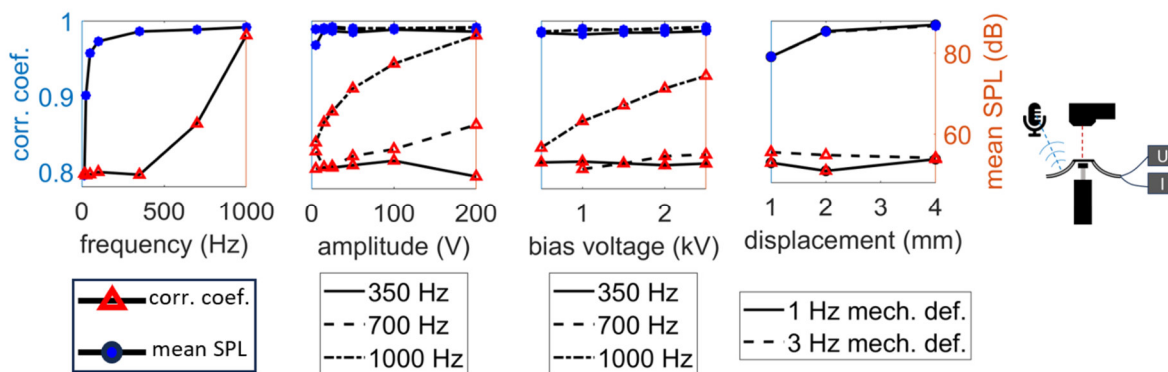


Figure 3.58: Characterization of the CC based on self-sensing (dot markers) and the SPL (triangular markers) for different parameter variations of the DEA system stimulation, with motor induced movement and sinusoidal HF signal ([261]).

The characterization, using a soundtrack as the HF signal, is repeated. Corresponding measurements are shown in Figure 3.59. In this case, the obtained CC is sensibly lower. The bias voltage and the amount of mechanical deformation have the most significant influence on the CC, whereas amplitude V_k has a minor influence on the CC. For bias voltages higher than 1.5 kV and displacements over 2 mm, the CC is higher than 0.8.

It can be concluded that also with a polychromatic signal the self-sensing algorithm is able to provide capacitance estimates that are highly correlated with the device stroke, for a broad range of different parameters of the driving acoustic signal.

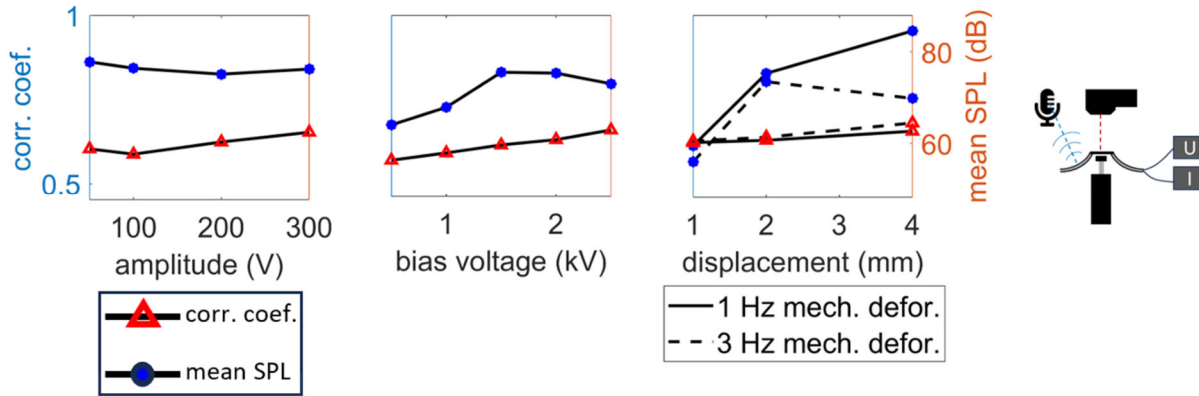


Figure 3.59: Characterization of the CC based on self-sensing (dot markers) and the SPL (triangular markers) for different parameter variations of the DEA system stimulation, with motor induced movement and polychromatic HF signal (soundtrack) ([261]).

The parametric response of the system in the presence of LF voltage-driven deformations is characterized. Results obtained with a monochromatic sinusoidal HF signal are shown in Figure 3.60. For the frequency variation measurements, an amplitude of 200 V and for the amplitude variation 1 kHz HF signal frequency is used. The voltage of the LF driving signal for both cases is a varying sinus from 0.5 - 2.5 kV with a frequency of 1 Hz. For the LF signal variation measurements the amplitude of the HF signal is constant 200 V and the frequency 1 kHz.

The LF voltage is defined as 500 V (minimum voltage) plus a varying crest-to-trough amplitude sinusoidal signal. In the considered tests, the end effector stroke due to LF driving voltage was on the order of 0.45 mm.

In addition to SPL and CC the contribution of the HF signal to the end-effector displacement (magenta x-markers) is isolated and quantified. This was done by applying a low-pass-filter to the displacement measurement and subtracting the LF position signal (orange circular markers) from the initial signal. The values for the HF displacement values are then calculated by using the envelope, calculated by a Hilbert transformation (envelope function in matlab), and the corresponding mean value of this time varying displacement value.

The contribution of HF signal \tilde{v} to the stroke is generally small (on the order of microns), because of the high frequencies and small amplitudes (U_2) involved.

HF driving signals \tilde{v} with frequency close to the DEA's pumping mode natural frequency bring in a greater contribution to the stroke. In this particular condition, the CC drops down because the contribution of the HF component to the stroke becomes non-negligible, and the frequency of the sensing signal is too low to capture it. The HF signal amplitude and LF signal amplitude have an influence on the CC. As expected, low amplitudes of the LF driving voltage \bar{v} (below 1.5 kV variation) lead to small capacitance variations, that the self-sensing algorithm can only resolve with limited accuracy, leading to minimum CC below 0.5 ([268]). These results suggest that a frequency of at least 350 Hz and amplitude $\sqrt{U_2}$ of at least 50 V is requested for \tilde{v} , in order for the self-sensing algorithm to provide CC above 0.8.

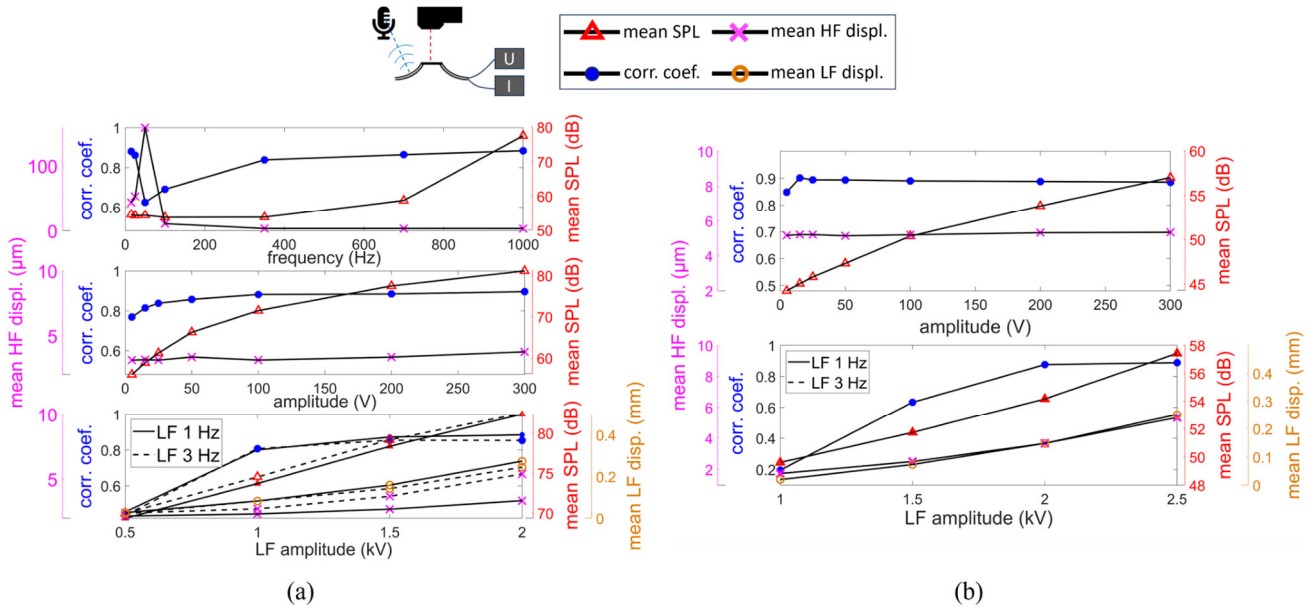


Figure 3.60: Characterization of the CC (dot-markers) based on self-sensing, the SPL (triangular-markers), HF (cross-markers) and LF (circular-markers) mean displacement. Different parameter variations of the DEA system stimulation, with self-induced movement for (a) sinusoidal HF signal and (b) polychromatic HF signal ([261]).

3.4.2. Experimental results

To prove the ability of the self-sensing DEA to concurrently implement 3 working modes (i.e., linear actuation, sound generation, and self-sensing) in practical scenarios, in this section results on measurements performed on a set of structured case study demonstrations are presented. These case studies are meant to provide a practical demonstration of the real-time multi-mode self-sensing capability of the system in combination with HF and LF actuation. The considered case studies refer to both scenarios in which the COP-DEA performs tasks involving externally induced deformations (e.g. smart buttons and audio-tactile interfaces), and scenarios involving voltage-driven linear actuation (e.g. obstacle detection, voltage-driven output adaptation).

3.4.2.1. User-induced movement self-sensing

The first two examples are based on sensing of user-induced deformations, which induce a displacement of the DEA end-effector. The deformation is measured via self-sensing and the output is adjusted (by modifying the HV signal) depending on the intensity of touch, or the number of consecutive detected touches. Here, the HF driving signal is simultaneously used for acoustic feedback and sensing, and an additional LF signal is used to provide an tactile feedback.

Adaptive amplitude adjustment of the HF driving signal

By applying a HF signal with constant amplitude to the demonstrator, the sound pressure decreases when the end-effector is pushed down by the user (Figure 3.61(a)). This is consistent with previously observed dependences of the DEA sound intensity on the out-of-plane deformation ([225] and section 3.2). Leveraging real-time self-sensing, online detection of the out-of-plane deformation of the DEA is possible. Depending on the deformation, the amplitude of the HF signal can be changed to make the sound pressure output of the DEA more constant. Figure 3.61(b) shows the sound pressure output for an amplitude-compensated signal with 1 kHz HF frequency

and an amplitude-range from 100 – 250 V (200 V without compensation). The output amplitude for the compensation is calculated by the maxima and minima of the capacitance (C_0 ; C_1) and amplitude ($U_a \sim \sqrt{U_2}$; U_{a0} ; U_{a1}) $U_a = U_{a0} + \frac{U_{a0} - U_{a1}}{C_0 - C_1} \cdot (C - C_1) = U_{a0} + \frac{\Delta U_a}{\Delta C} \Delta C$. The sound pressure is recognizably smoother as compared to Figure 3.61(a), showing the potential of self-sensing for equalization of the sound output. With the simple control logics used in here, which makes use of a static mapping of the HF signal amplitude as a function of the capacitance, a highly smooth sound output could not be achieved: significant fluctuations in intensity are still present during fast changes in deformations. A route to improve this result consists in combining the proposed closed-loop self-sensing-based approach with a filter (based, e.g., on a dynamic model of the system) accounting for the dynamic evolution of the system (rather than just relying on instantaneous capacitance measurements) to adaptively select the HF signal amplitude.

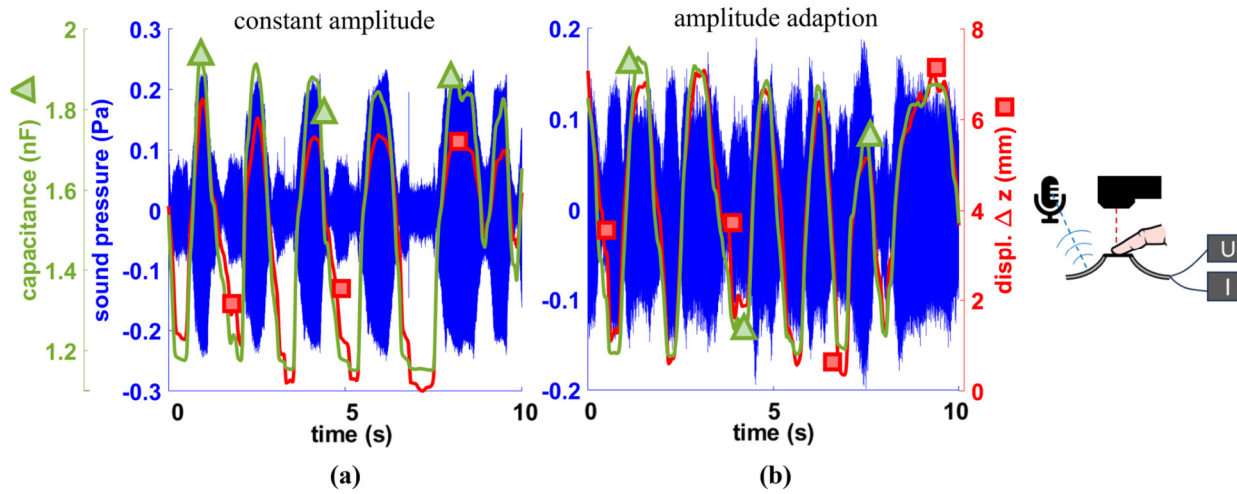


Figure 3.61: User induced deformation and corresponding closed-loop amplitude adaption of the HF signal via self-sensing through the HF driving signal applied to the DE ([261]).

Comparison of Figure 3.61(a) and (b) shows that the peak sound pressure is lower in the test with compensation. Reaching a constant pressure output equal to the maxim pressure in Figure 3.61(a) (~ 0.2 Pa) would indeed require voltages that would lead to an electric field higher than the dielectric strength of the material (80 - 90 V/ μ m).

Adaptive tactile and acoustic feedback adjustment

In audio-tactile interfaces, self-sensing can be used to change the feedback provided to the user. This can be done for both the LF (tactile) and the HF (audio) signal or even for both on the same time.

In Figure 3.62(a), a HF signal is applied to the electrodes with the dual purpose of producing an acoustic output and performing self-sensing. The pitch of the acoustic output is slowly adjusted based on the user's touch intensity. Similar to previously described amplitude adaptation tests, the frequency is continuously updated as a function of the measured capacitance. Depending on the implemented logics, the frequency can be increased with the DEA downward deformation (first two plots in Figure 3.62(a)) or increased (third plot in Figure 3.62(a)). Since the intensity of the DEA acoustic output varies with the frequency and the amount of deformation, the amplitude of

the HF signal might be additionally varied, as in the previous section, to make the SPL more constant.

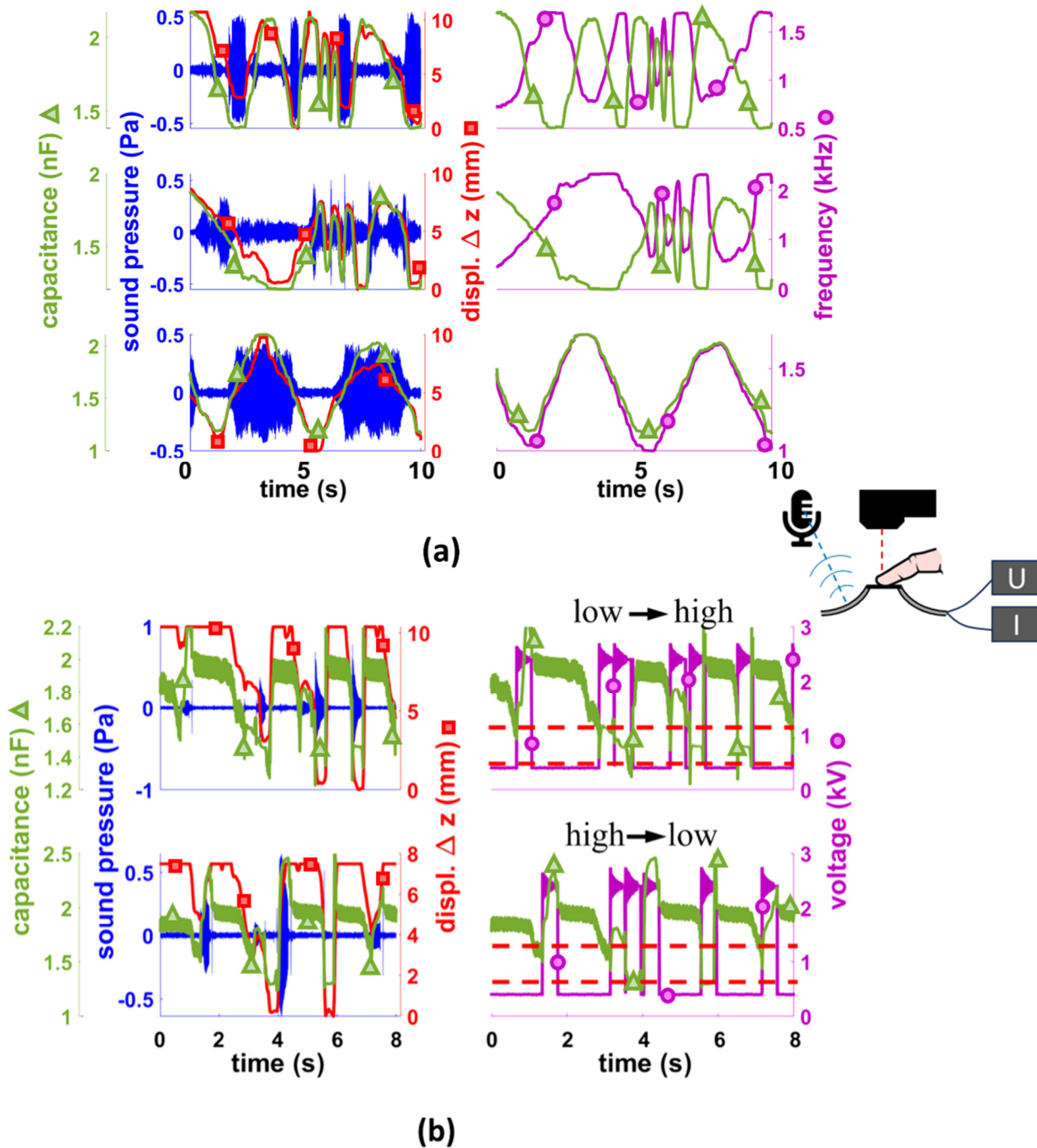


Figure 3.62: User induced deformation and corresponding (a) frequency adaption of the HF signal via through the HF signal applied to the DE; (b) haptic and acoustic feedback adaptation via self-sensing through a MF probing signal ([261]).

In a second test (Figure 3.62(b)), the DEA is used to produce audio-tactile stimuli that are function of the sensed deformation. In this case, a MF signal (350 Hz) is used for sensing, which generates no feedback until a touch is detected. A set of thresholds values for the capacitance (corresponding to different intensity levels of the touch) are defined. If the self-sensing algorithm finds that a certain threshold is overcome, a specific audio-tactile feedback is provided. The

sensing capability with thresholds is comparable with the tests performed in section 3.2.4.3. However, self-sensing allows for additional direct measurements when high voltage is applied. This provides the capability for more complex interactions such as multiple thresholds with different feedbacks. In Figure 3.62(b) two examples of threshold-based feedback with self-sensing are shown. In these tests, two thresholds are implemented: upon reaching the first threshold a haptic click feeling (LF signal) with an overlaid acoustic clicking signal (HF signal) and by reaching the second one another feedback with the same feeling but other acoustic frequency is applied.

In the first example in Figure 3.62(b), a high pitched sound (1500 Hz) is produced upon reaching the first threshold, whereas the pitch of the sound is reduced to 1000 Hz when the second threshold is reached, whereas the logic is swapped in the second example (from 800 Hz to 1800 Hz). While the feedback signal is applied, the self-sensing algorithm still works (relying on currents associated to the HF signal), which makes it possible to detect whether the user is reaching the second threshold before or after the execution of the first feedback signal is completed. In case the second threshold is surpassed the first routine is suppressed and the second feedback routine, with different signal shape, starts. It is therefore an option to give a second feedback directly to the user, without waiting for the first feedback to finish, which would lead to a bad user experience. The magenta signal (round marker) for the right plots in Figure 3.62(b) is showing the supplied feedback voltage signals which is a superimposed rectangular LF signal (resulting in a tactile stimulation) plus a sinusoidal HF signal with an exponentially decreasing amplitude (resulting in a clicking sound). Both stimuli are clearly perceptible by users, as demonstrated by the previous user tests (section 3.2.4.3).

3.4.2.2. Voltage-induced movement self-sensing

Two scenarios, involving self-sensing of voltage-induced end-effector movement, are considered in the following. The first one deals with amplitude adaption of the HF driving signal, whereas in the second one the impact of the moving end-effector with an obstacle is detected, and acoustic feedback is produced accordingly. In both cases, a LF driving signal is superimposed with an HF or MF signal, used for the self-sensing. For the present system, the voltage-induced movement of the DEA is relatively small ($<0.5\text{mm}$), because the button (DEA + biasing element) was specifically designed for haptic feedback applications. Nevertheless, the minor stroke can be accurately measured by the self-sensing algorithm and utilised in a control-loop configuration. Amplitude compensation based on self-sensing

As already seen in section 3.4.1 and 3.2.2 the sound pressure varies strongly with the bias voltage associated to the LF component of the signal. Self-sensing can be used to make the sound intensity steadier by adjusting the HF driving signal amplitude as a function of the sensed deformation.

Figure 3.63 shows the end-effector displacement, sound pressure time-series and capacitance (measured via self-sensing) for a sinusoidal input driving voltage with HF components of 1 kilohertz and 250 V maximum amplitude and LF components with 5 Hz and 750 V amplitude with a bias voltage of 2 kV. In Figure 3.63(a), the HF component of the driving voltage has constant amplitude of 200V, which results in a highly variable sound intensity (the sound pressure is maximum when the LF component of the driving voltage, and, hence, the out-of-plane stroke, are maximum). In Figure 3.63(b), such pressure output is compared with that obtained by continuously varying the HF signal amplitude in a closed-loop fashion, as a function of the measured capacitance (monotonically decreasing the HF signal amplitude with the capacitance) (linear:

$U_a = U_{a0} + \frac{\Delta U_a}{\Delta C_0} \Delta C$; quadratic: $U_a = \sqrt{U_{a0}^2 + \frac{\Delta U_a^2}{\Delta C_0} \Delta C}$). In Figure 3.63(c), in contrast, the HF signal amplitude is adjusted as a function of the instantaneous value of the LF driving voltage component (in an open loop fashion), namely, monotonically decreasing the amplitude with increasing values of $\bar{v}(t)$, as previously suggested in section 3.2.2. In both cases, linear and quadratic dependences of the HF signal amplitude on the capacitance/LF voltage are considered (the quadratic dependence being motivated by the quadratic dependence of Maxwell stresses on the voltage).

Both compensation methods (self-sensing based closed-loop, and input-based open-loop) lead smoother pressure output trends compared to the constant amplitude reference scenario. Quadratic compensations lead to slightly smoother trends as compared to linear adaptation, though their difference is small, given the small displacements to which the DEA is subject. In these tests, the voltage-based compensation (Figure 3.63(c)) is found to provide a smoother sound pressure output than the capacitance-based compensation. This can be explained by the dependence of the sound intensity on the DE membrane tensile stresses, which are influenced by the bias voltage (the higher the bias voltage, the lower the stress on the DE and, hence, its stiffness against structural vibrations). In the conditions of the presented tests, such voltage-induced change in stress has a stronger influence than the DEA configuration (i.e., the out-of-plane stroke) on the sound pressure output and makes the open-loop compensation more effective than the simple capacitance-based compensation presented here.

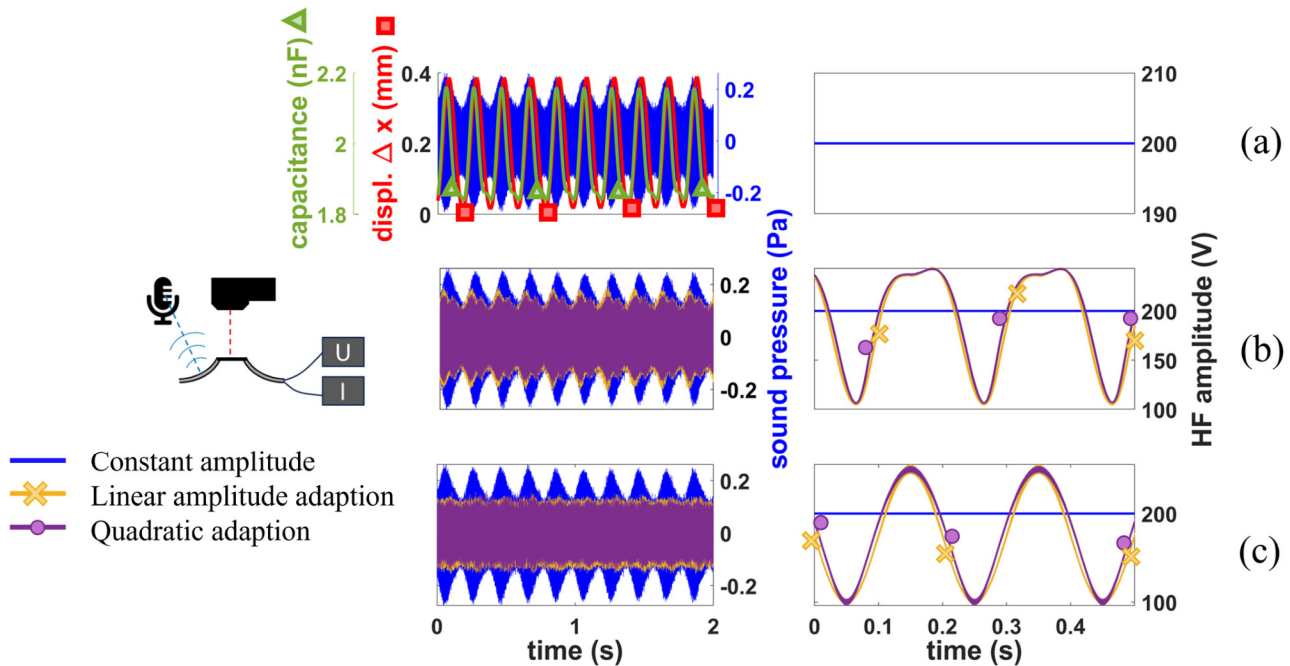


Figure 3.63: Self-induced deformation and corresponding amplitude adaption of the HF signal measured with self-sensing based on the HF signal applied to the DE. (a) Trends of the end-effector displacement, estimated capacitance, and sound pressure time-series in a reference scenario in which the DEA is driven by a constant amplitude HF voltage superposed to a LF driving voltage. (b) Sound pressure obtained by varying the HF signal amplitude as a function of the measured capacitance. (c) Sound pressure obtained by varying the HF signal amplitude as a function of the LF driving signal amplitude ([261]).

In practice, finer compensations, leading to a better rejection of beat distortions than that achieved in here, might be obtained by resorting to more complex logics, which combine open-loop information on the input voltage with real-time measurements of the capacitance, leveraging on

dynamic models of the DEA dynamics. It is also worth remarking that in applications (especially user interaction) the state of the DEA can change because of external factors (impacts, impressed deformations), and such state changes can only be detected through a deformation-based sensing, which necessarily demands for closed-loop logics.

Obstacle detection based on self-sensing

To provide the DEA sample with the ability to detect impact with an obstacle and respond with a sound feedback, self-sensing is used. In situations in which the DEA encounters an obstacle during the execution of a stroke or is subject to loads that are higher than the electrostatic blocking force, the end-effector position will stay constant in spite of input voltage variations. In practice, impact events can be caused by an obstacle located over the DEA end-effector, or a touch by a user. In these situations, the actuator can still generate sound leveraging high-frequency structural modes.

A self-sensing-based obstacle detection is implemented by experimentally mapping the static voltage-free displacement response of the DEA. The map is compared with the actual capacitance measurements obtained via self-sensing during LF actuation. It is possible to identify obstacle impact events by evaluating the difference between expected capacitance and measured capacitance at a given voltage and verifying whether such difference is above a critical threshold.

Two corresponding tests were carried out (Figure 3.64): a first test in which the DEA concurrently produces linear actuation and sound (top row), and a test in which the DEA initially produces silent linear actuation. In both tests, the LF component of the driving voltage initially had lower amplitude, which was then increased, causing the DEA to hit a fixed rigid obstacle located on the end effector trajectory. Obstacle detection was performed via self-sensing, respectively using current measurements associated to the HF driving signal (top) or a MF probing signal (bottom). The error between expected capacitance and measured capacitance for the two tests is shown (magenta line; circular marker) on the right plots. During impact events, the error increases over a predefined threshold, leading to the identification of an impact event. The error is calculated by the following method. The applied LF voltage difference (ΔV) is first calculated and then the capacitance change (ΔC) is computed by the algorithm. The difference of the expected capacitance change (voltage based calculation) and the actually computed capacitance change (based on self-sensing algorithm), are done according to a static map of the device. Upon impacts detection, acoustic feedback is produced, by varying the frequency of the (or introducing a) HF driving voltage component.

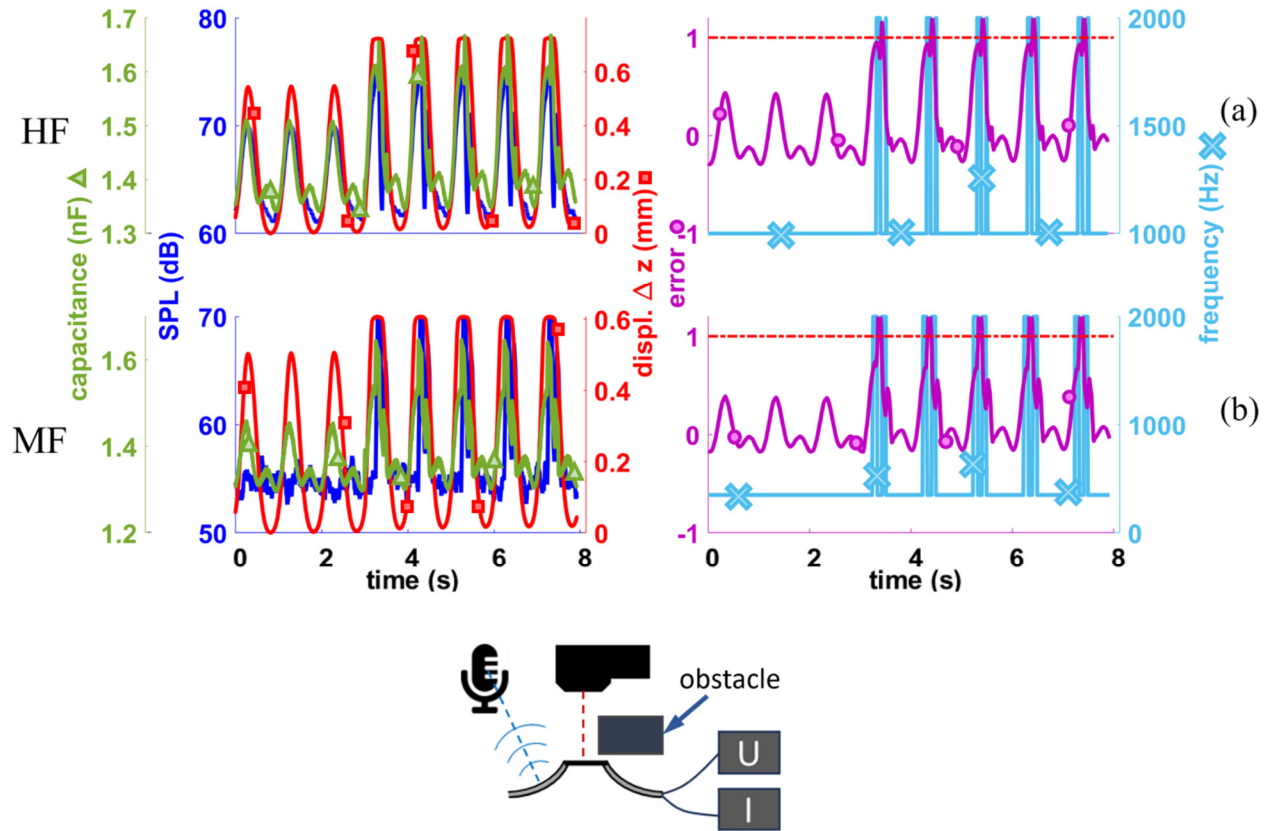


Figure 3.64: Voltage-induced deformation, with obstacle detection performed by comparing the estimated capacitance and the measured self-sensing capacitance. Top row: the DEA is driven with a HF+LF voltage signal, it produces a linear stroke and sound during the entire test, with the pitch of the sound output changing upon obstacle impact. Bottom row: the DEA is driven with a MF+LF voltage signal, it only produces linear actuation during the first part of the test and generates sound upon impact with the obstacle ([261]).

3.5. Textile integrated audio-tactile elements

One important advantage of the presented demonstrators is that the main working layer is based on a μm thin flexible silicone film. This gives to the multi-functional element the natural and inherent capability to work in a mechanically flexible way, which leads to a good usability as textile integrated elements. The integration of the presented functionalities into smart textiles, opens the scope for many application scenarios (compare section 4.1).

Textile integration of the DE can be realized in various ways, in section 2.3.2.1 and 2.3.2.2 manufacturing processes for textile-integrated sensor and actuator elements are exemplary shown. An integration of the DE element into textiles in a compact way is developed in the following section, using the textile itself as pre-load element. For actuator integration, a pre-tensioning element is necessary in nearly all cases for the application of DE elements. This leads to an increase in complexity and size both in production and in application. One approach pursued here is to use the already existing and necessary textile directly as a pre-tensioning element. This has the effect of reducing both the height and the complexity of the structure, thus facilitating its integration into the manufacturing process of the DE element itself. Another approach is to pre-tension the DE element directly on the user's skin (which is also used in [20]). In application, the concept presented and developed here is a hybrid form (skin and textile together form the pre-tensioning element of the DE).

3.5.1. Design of Textile integrated audio-tactile elements

The DEA element of the multi-functional feedback unit needs to be pre-stretched and the output force must be transferred to the skin of the user. One realisation is shown in Figure 3.65, where the DE is pre-stretched by a spacer in static out-of-plane deformation condition. The spacer simultaneously fulfils the task of transferring force to the textile and thus to the user's skin. The DEA is held in place by a silicone frame which can be glued to the textile. A second silicone frame can be used to adjust the distance to the skin and thus adjust the indentation into the skin.

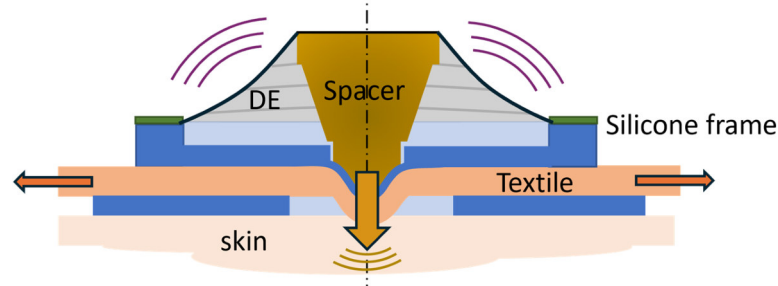


Figure 3.65: Working principle and construction of the DEA based textile integrated audio-tactile feedback element.

The characteristics of the textile and the geometric design of the integrated element have an influence on the behaviour of the haptic feedback of the element. The design of a textile-based pre-tensioning element for the DEA and the estimated stroke and force is shown in Figure 3.66.

The curves in Figure 3.66 are estimated by measurements (tensile tests for textile, DE and skin) and linearized to show the principle qualitative design approach. The stiffness of the textile and the stiffness of the skin can be added together and influence the characteristic of the textile integrated feedback element. With the thickness of the silicone spacer between the skin and the textile the working point of the element can be adjusted, and the actuator behavior can be adapted (Figure 3.66(c)).

A realisation of a textile integrated actuator element based on DEs, is to use only the textile (excluding initial forces from the skin, in the equilibrium configuration) as preload element, which leads to less required components and to a highly integrated solution. The output force of the element is influenced by the pre stretch of the textile and by the geometry of the construction. The geometry basically is influenced by the outer diameter of the spacer and the inner diameter of the free textile part. The force output and deformation of the system can be estimated by intersection of the textile force curve with the DE curve (Figure 3.66).

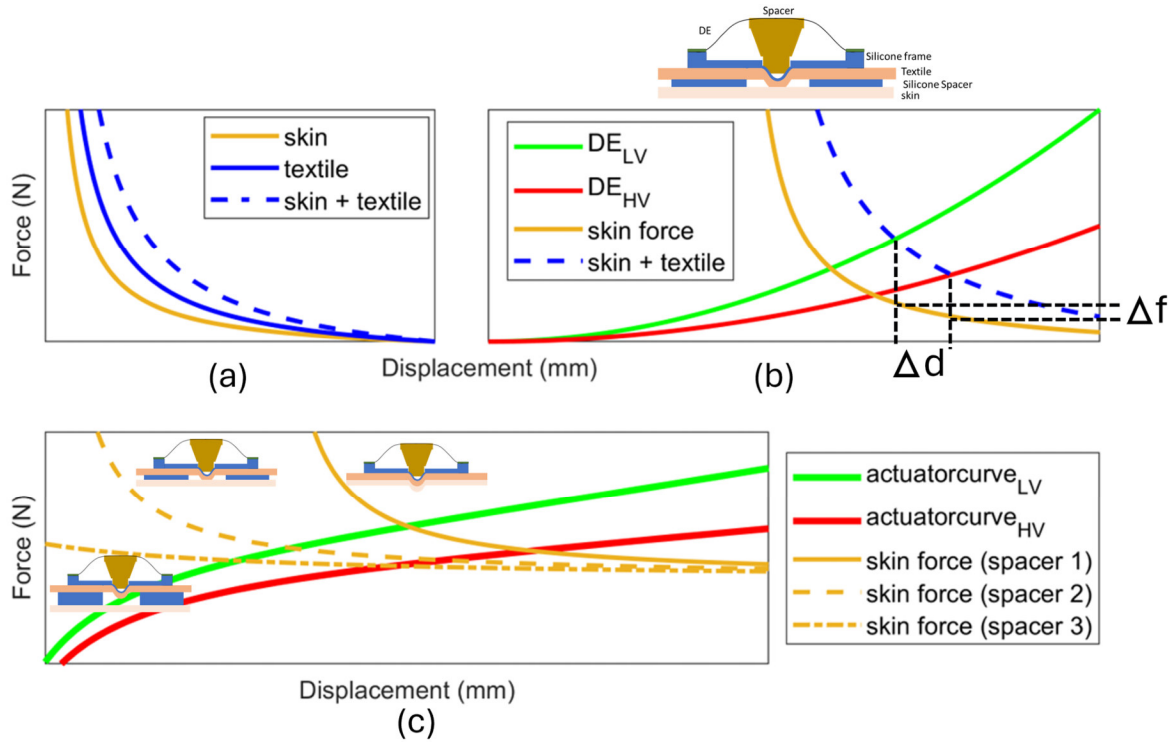


Figure 3.66: Design and influence of the textile pre-tensioning element and spacer. Textile and skin force are combined and work against the DE as a pre-tensioning element. The output performance of the DEA is influenced by the force characteristic of the skin and textile.

Therefore, the used exemplative textile is measured with different pre-stretch and geometry. In order to validate the optimal configuration for the realisation of the textile pre-stretched element, a COMSOL Multiphysics® simulation of the textile force behaviour was conducted (hyper-elastic model). In Figure 3.67 exemplative a comparison of the simulation and measurement of textile tensile tests is shown.

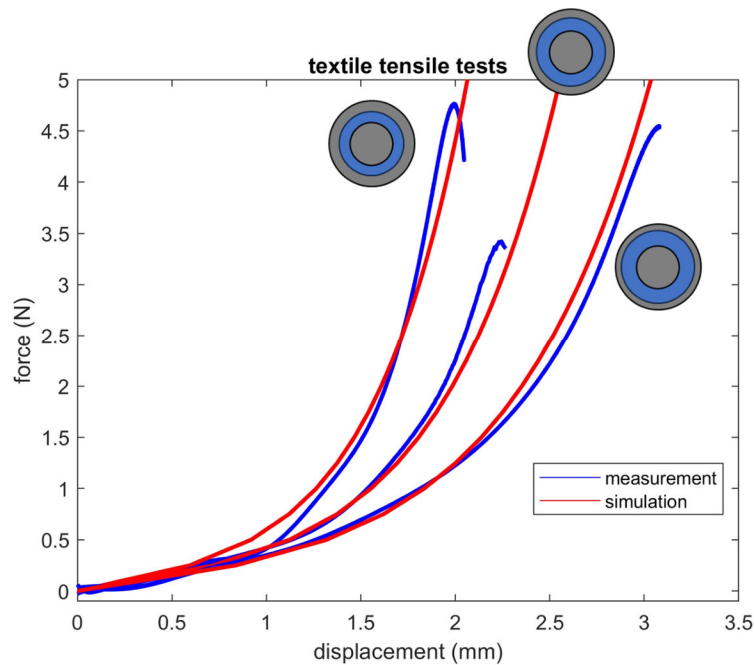


Figure 3.67: Measurement and simulation of pre-stretched textile (20 % biaxial) tensile test for different geometry.

The textile force increases with bigger inner diameter and higher pre-stretch, for bigger outer diameter the force decreases. For the output performance mainly the stiffness of the textile (or the textile force + skin force) is decisive. When the textile is very stiff then the output force is high, but the deformation of the DE-textile composite system is very low and vice versa, if the stiffness is small the deformation can be high but with very low force. With the human JND (Figure 2.23) the force and the displacement should be at least 100 mN and 100 μ m which leads to a certain range of the stiffness for the textile. Additionally, the total out of plane deformation of the system defines a second boundary for the system development, in order not to exceed a certain thickness of the whole system.

The force trend and influence of the geometry can be visualized in Figure 3.68. The output deformation and force depend additionally on the working point of the DE, which can be set by the length of the spacer between textile and DE membrane. It is evident that the behaviour of deformation and force is antithetical with respect to the operating point, inner and outer radius, and pretension of the textile. The product of force and displacement is demonstrated in Figure 3.68 and in the following, which approximately represents the mechanical work performed by the system. The cluster of curves represent the calculated output at different working points (initial equilibrium force of the DE) for different geometries, concerning the inner and outer diameter as shown in Figure 3.67. To take realistic configurations into account, a measured forces of the human skin (lower arm region) is added to the simulated textile force. The magnitude of the skin force is gauged by applying a force to the indenter (12 mm diameter), which is measured using a load cell, and thereby pushing it into the skin.

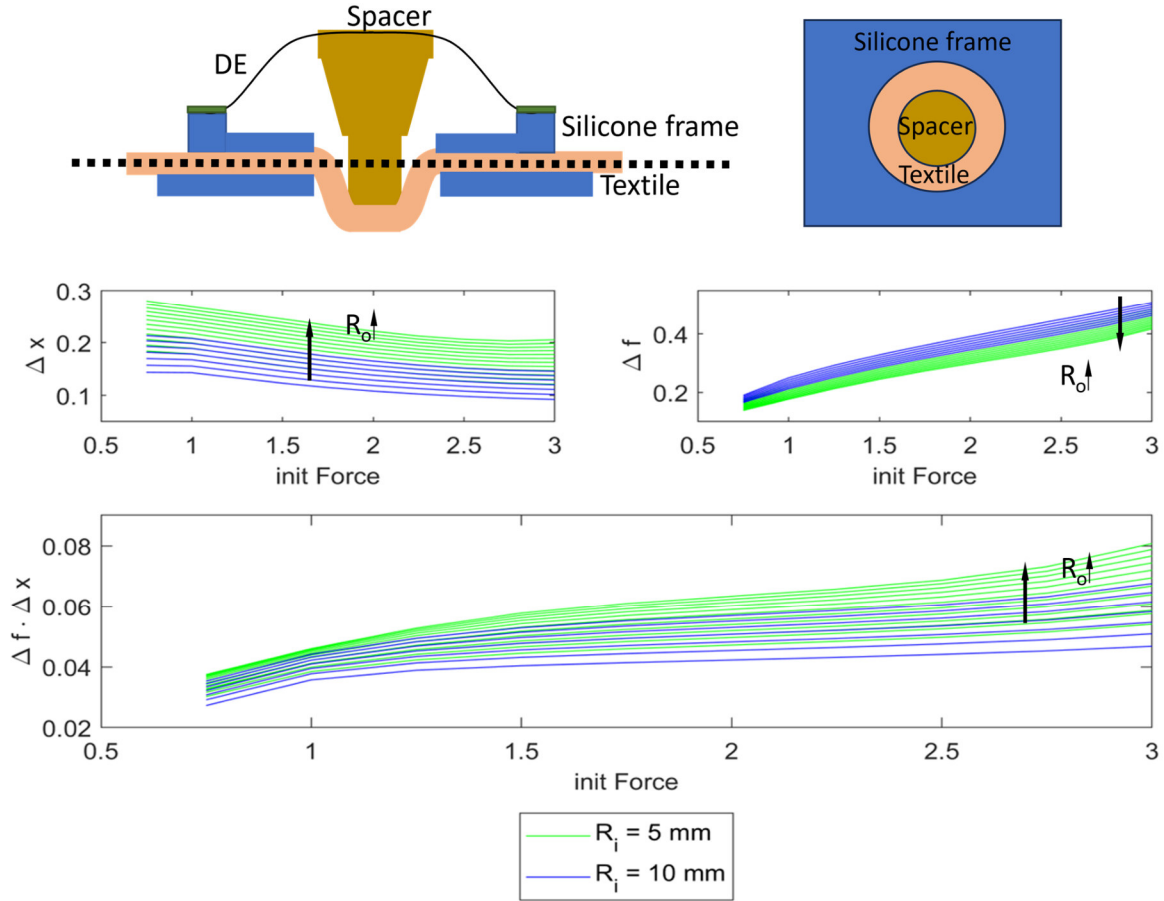


Figure 3.68: Output deformation and force performance for different geometries and different working points of the system.

The output performance (force \cdot deformation) increases by increasing the outer diameter and decreasing the inner diameter of the structure. Based on this, the output performance would theoretically be maximum for lowest inner diameter and highest outer diameter. For the complete system design, the deformation and force separately have to be higher than the thresholds of the JND. Additionally, the system size and thickness has to fit to the application boundaries. Figure 3.69(a) shows the output performance for different geometries ($R_i \in [5\text{mm}, 10\text{mm}]$ and $R_o \in [R_i + 2\text{mm}, 20\text{mm}]$) for 20 % pre-stretch of the textile.

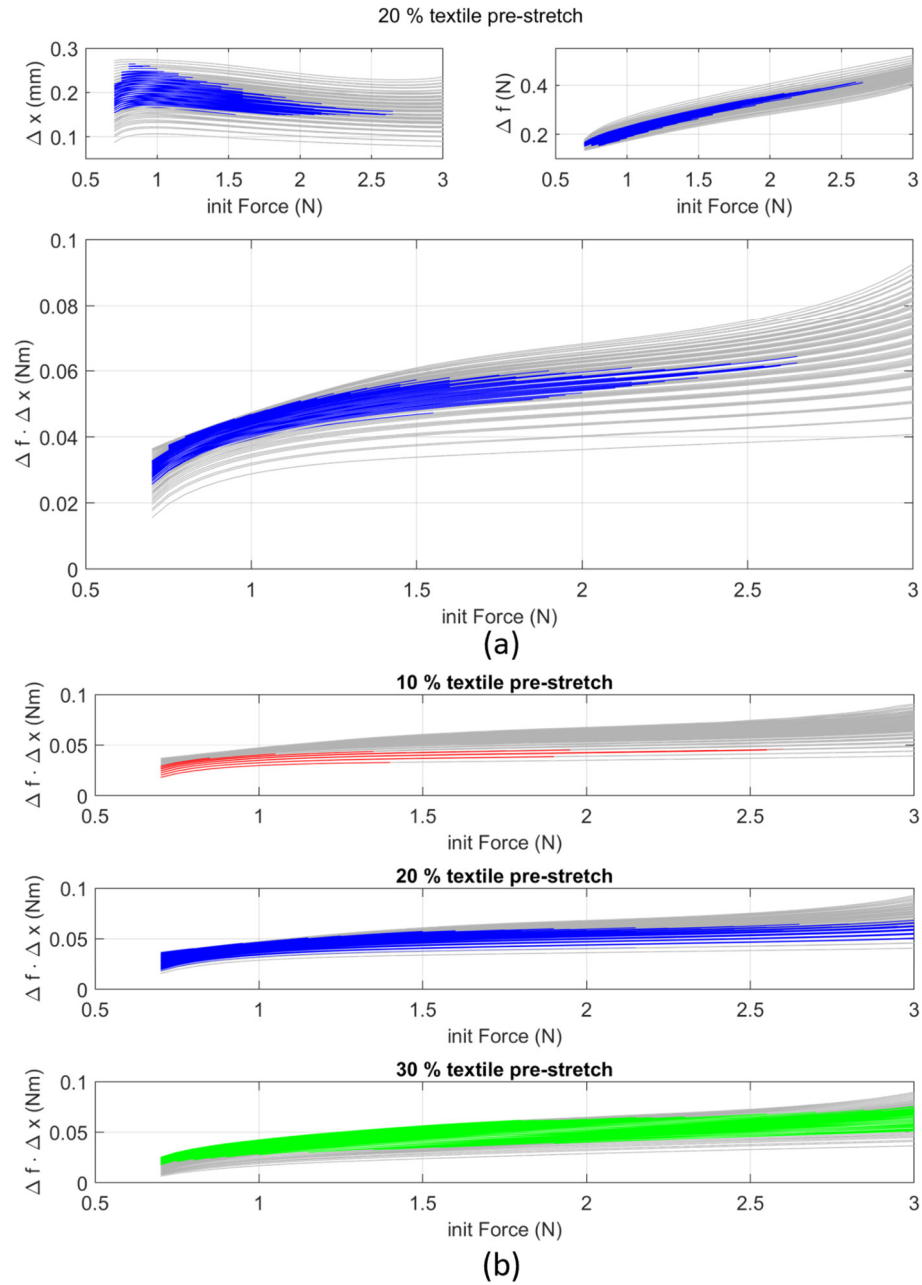


Figure 3.69: Output performance of the system for different geometries (R_i: 5 - 10 mm; R_o up to 20 mm) with (a) output deformation, output force and output work for 20 % textile pre-stretch and (b) for 10%, 20 % and 30% textile pre-stretch. Gray areas identify parameter-region where either the deformation or force is below the JND threshold, or the structure is too big (textile out-of-plane deformation > 3mm).

The grey lines identify the areas where either the JND thresholds are not met or where the thickness of the system is too high (more than 3 mm out-of-plane pre deformation of the system (DEA + textile). In Figure 3.69(b) the output work for different pre-stretch of the textile is shown. The performance of the system increases with the pre-stretches of the textile.

In Figure 3.70 the output performance of the system in dependence of the geometry (inner and outer diameter) is shown.

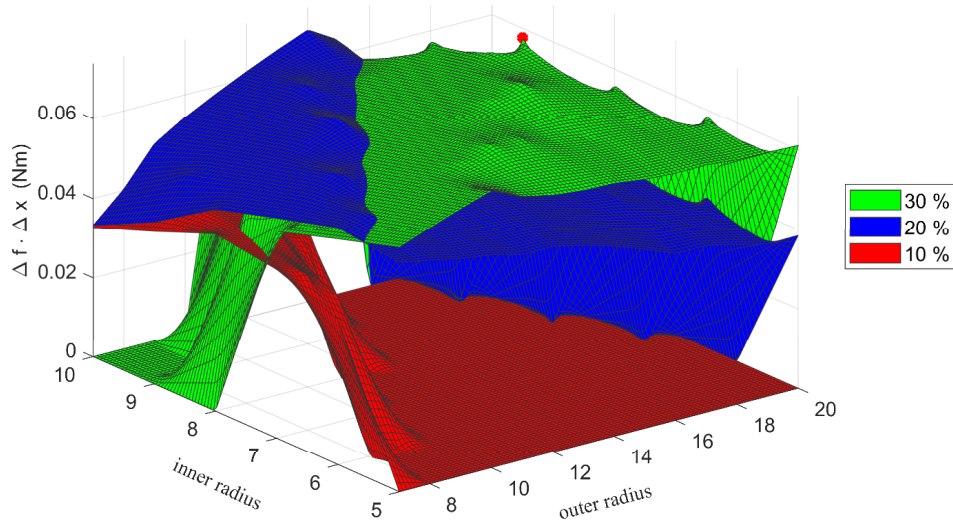


Figure 3.70: Output performance of textile DE system for different textile pre-stretch (maximum output 0.0737 Nm at $R_i = 8$ mm and $R_o = 17$ mm (red dot)).

The maximum output of the system with the used parameters can be reached by a pre-stretch of the textile of 30 %, inner diameter of 8 mm and outer diameter 17 mm. In this configuration the DE is stretched to a working point of 3 N. In Figure 3.70 the complete maximum output for three different pre-stretches of the textile is presented (red dot).

3.5.2. Experimental results

To validate the working principle of the presented textile pre-loaded tactile feedback actuator (see Figure 3.71), different performance measurements are carried out. The measurements are done for different boundary conditions like working point and mechanical deformation of the whole actuator.

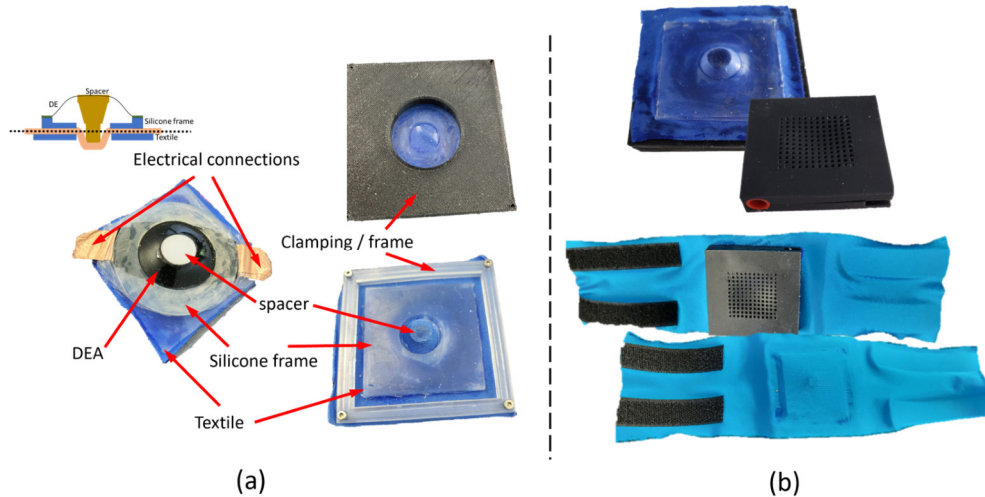


Figure 3.71: Textile integrated DEA prototype with (a) measurement clamps and (b) silicone housing and arm strip integrated prototype.

The silicone frames used to hold the textile pre-stretch have a thickness of 1.5 mm each, the measurement-frames are 3D printed and have an outer diameter of 60 mm. The used textile consists of 80 % polyamide and 20 % elastane (210 g/m²). The textile gets pre-laminated with an adhesive layer and is afterwards glued to the silicone frame. The connection of the centre point of

the DE (compare the end-effector in the sections before) and the textile, is done with a filament printed spacer with a length of 14.5 mm. In Figure 3.72 the electro-mechanical behavior of the textile integrated actuator is shown. To simulate wearing the actuator on a body part, different shapes of the system are compared. As reference the DE-textile composite is measured in the mounting frame, holding the pre-stretch of the textile (30 % biaxial) and pushing with a loadcell (KD40; +/- 10N) onto the textile part of the actuator system.

By applying the high voltage to the DEA, the stiffness of the actuator is reduced, and a differential force can be measured. Three different shaped mechanical elements are used to induce a bending of the DEA element. For this reason, a flat hard-stop element and two round shaped hard stop elements (different radii 2.5 mm and 5mm (curvature of the hard stop profile)) are used for the measurements. The stiffness of the system increases by applying the hard-stop elements compared to the ‘free’ system behavior on the order of 50 %. This can be explained by the clamped textile edge and depends on the geometry of the clamping frame. In the context of utilising pre-tensioning inserts, the clamped textile is already fixed. Consequently, the static pre-stretching of the textile outside the frame exerts no further influence on the force behaviour of the actuator (due to the insert), in comparison to the two other configurations. In Figure 3.72 the actuator system is stretched to 5 mm starting from the equilibrium position.

The change in stiffness of the system is comparatively much smaller for the free-to-move configuration, in relation to the different inserts. Two different actuators are built, based on two different DEA elements (one with 2 layers and one with 5 layers) with the exact same topology of the system (silicone frame shape, textile pre-stretch, spacer length). The stiffness difference of the two configurations is comparably low, which can be explained by the fact that the 2-layer DE is in the reference configuration already much more deformed than the 5-layer DE, which leads to higher initial stiffness of the DEA. The force-variation itself (difference of 0V curve and 2.5 kV) is consequently also comparable for the 2- and 5-layer systems. The main advantage of the 5-layer system is the smaller out-of-plane deformation of the DE and the resulting reduction in the height of the overall superstructure.

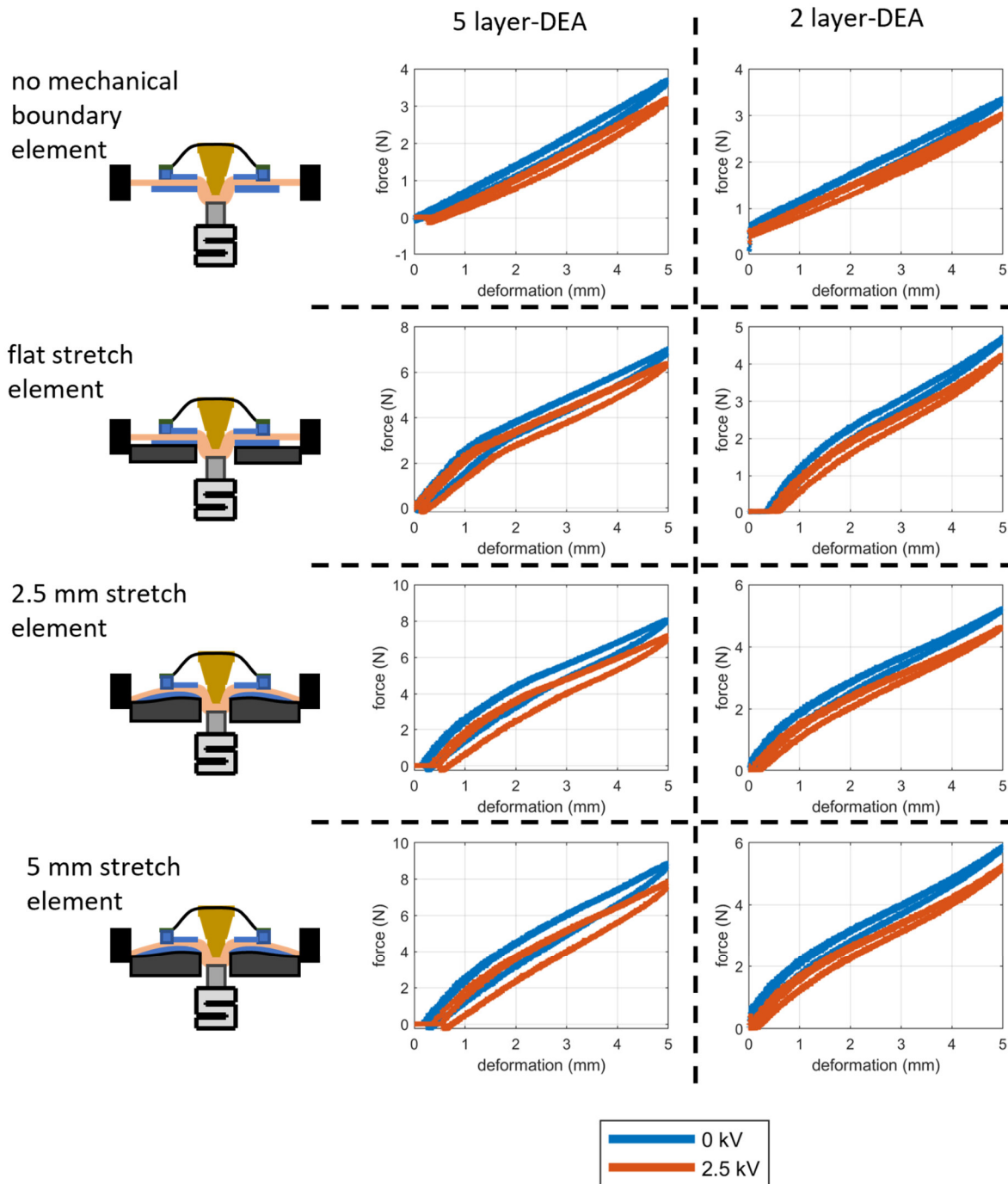


Figure 3.72: Actuator curve (DEA + Textile) for different mechanical configurations, for 2- and 5-layer DEA, with 0V and 2.5 kV electrical actuation.

Audio-tactile Measurements

Tactile measurements

The influence of the boundary conditions and the layers of the DE on the output performance can be validated by measuring the output force and the out-of-plane deformation of the actuator. To show the specific performance of the actuator, the force is measured at a certain working point, by applying a sinusoidal voltage to the DE. Furthermore, the mechanical vibration ('end-effector' motion) is measured with a laser displacement sensor in the reference configuration. In Figure

3.73 the output force of the two elements is shown. For the force measurements the textile actuator is preloaded on the textile side (which is the contact side to the user in the application) with 3 N and the difference force is measured in this working point.

The force increases with the bias-voltage and changes also with the shape of the deforming element. This shows that the output force is depending on the deformation shape of the DE-textile composite, but for an already bent actuator the change of radius has a quiet low influence. In Figure 3.73(c) the output force for the 5-layer actuator is validated over the frequency. For this measurement, it must be taken into account that the whole system (including the loadcell) can have some resonance influence on the measurement. However, the force is in all cases up to 60 Hz much higher than the JND of the human in this frequency range (compare Figure 2.23 in section 2.2.2).

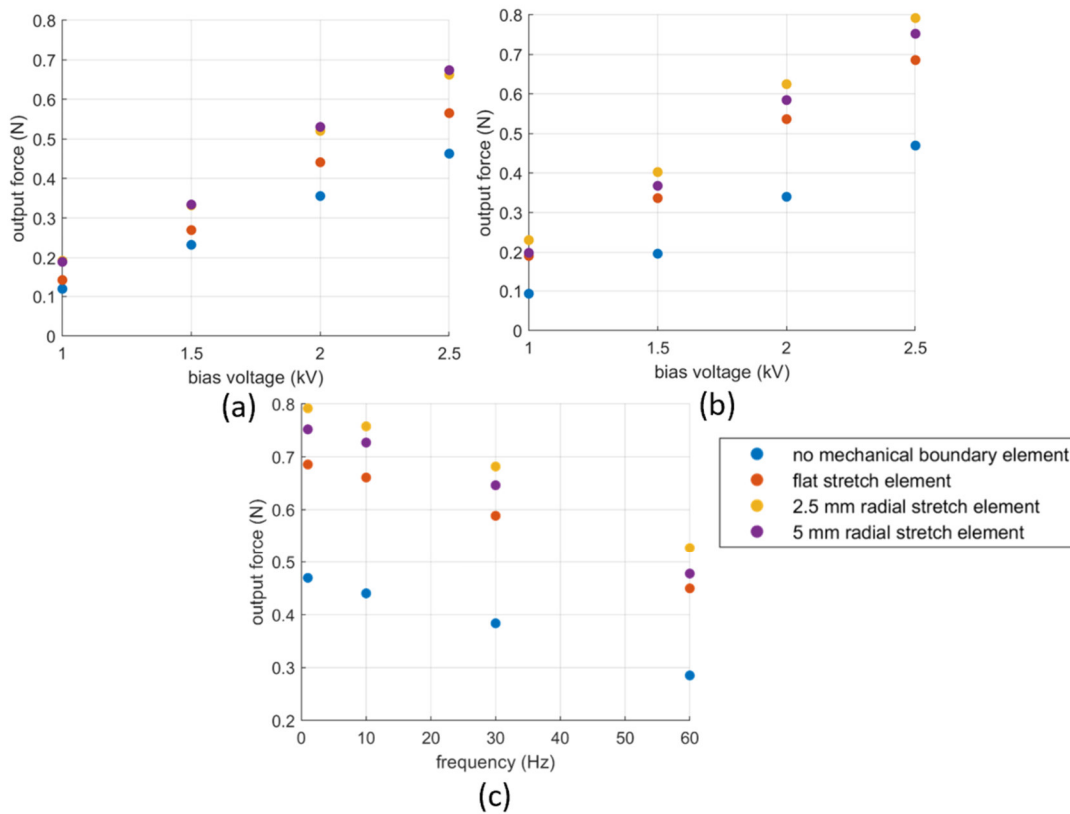


Figure 3.73: Output force of the textile integrated element with 500 V amplitude sinusoidal signal (a) for 2 layer DE with different bias voltages (b) for 5 layer DE with different voltages and (c) 5 layer DE for different signal frequencies.

Additional to the force measurements, in Figure 3.74 the free displacement of the actuator is measured in the reference configuration. For the deformation, the configuration without any mechanical boundary leads to a higher deformation than for the mechanical bended configurations.

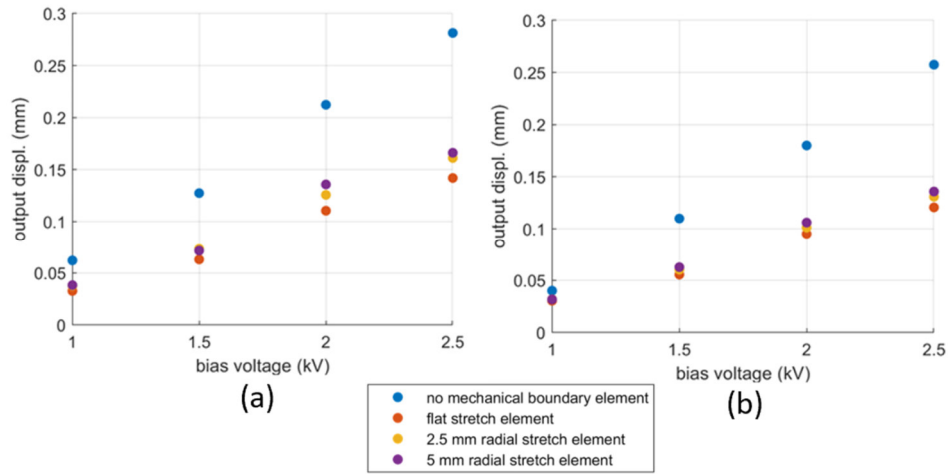


Figure 3.74: Output displacement of the textile integrated element with 500 V amplitude sinusoidal signal (a) for 2-layer DE and (b) 5-layer DE.

The deformation is (opposite to the force) higher for the 2-layer DE element due to the reduced stiffness of the textile. Also, for the deformation, depending on the bias voltage, a deformation higher than the JND can be achieved (Figure 2.23).

The measurements in Figure 3.74 are performed with 1 Hz, in this frequency range the human skin is not very sensitive to vibrations. With higher frequency the sensitivity increases, and the vibration is strongly perceptible. Therefore, in Figure 3.75 the vibrational output for both prototypes over a frequency band from 1 Hz to 60 Hz are shown. The frequency dependent JND for vibrations on the skin can be looked up in Figure 2.23 and included into consideration. For a frequency range higher than approx. 5 Hz the vibration is much higher than the JND of the human (red line). With the shown measurements it is clear that the output performance of the developed textile integrated prototypes is high enough to be good perceptible by the human for tactile applications.

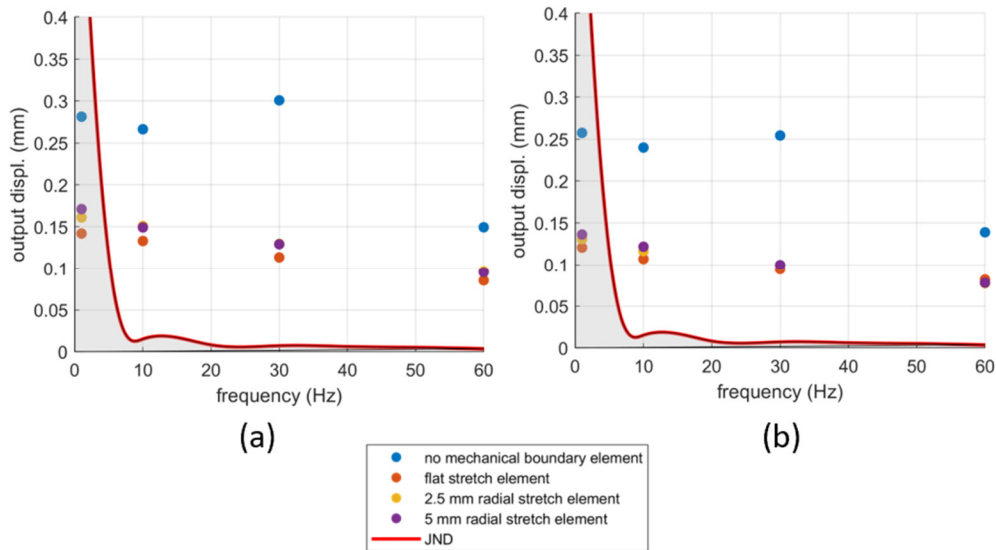


Figure 3.75: Output displacement of the textile integrated element with 500 V amplitude sinusoidal signal with 1 – 60 Hz frequency for (a) for 2-layer DE and (b) 5 layer DE.

As demonstrated in this work, the use of capacitive signals enables the implementation of the self-sensing capabilities. Therefore, a static measurement of the capacitance over deformation for the 4 different configurations is shown in Figure 3.76 (LCR meter).

The cross-influence on the capacitance change depending on the configuration is clearly visible. With that dependency, it is possible to detect the configuration status of the element (e.g. position/bending of the DEA), if the actuator is not touched by the user. If the actuator is fixed in the working point, and the bending dependent capacitance is constant, the interaction with the user (e.g. touch intensity) can be measured. To detect simultaneous touching and changing of the bending (e.g. actuator is not completely fixed to one position) more complex algorithms or multiple DEA elements have to be integrated to realise a reliable measurement.

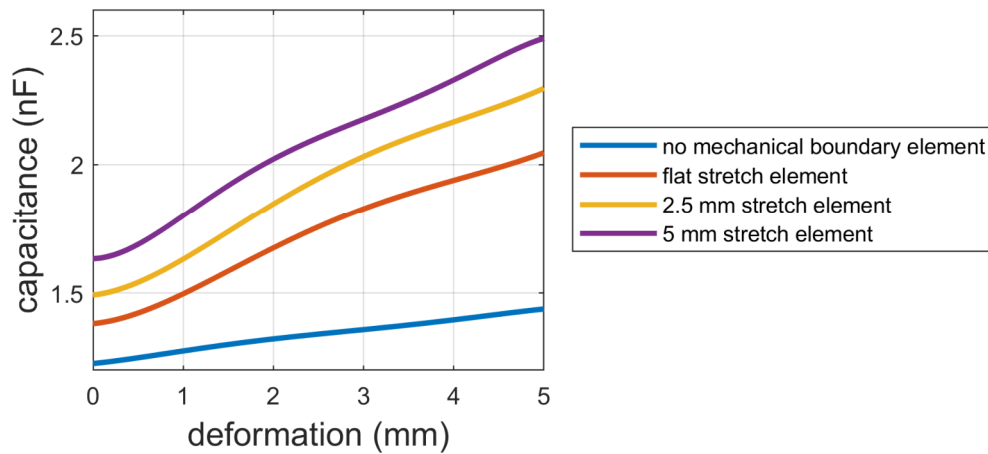


Figure 3.76: Capacitance measurement of demonstrator with 5 DE layers in different configurations.

For the development of textile integrated multi-functional elements also the acoustic response and controllability need to be proven. For that in the following, additional acoustic measurements are performed.

Acoustic measurements

For the acoustic output performance, similar to the previous measurements, the textile-based actuator is clamped in a 3 D printed frame and preloaded with different radii in an out-of-plane shape. The SPL is measured in a same manner as in section 3.2.4.1 and with the same voltage input parameters like in Figure 3.34.

Figure 3.77 shows the SPL for the different configurations (compare Figure 3.72) and for 5- and 2-layer membrane actuators.

As described in section 3.2.1.2, the SPL of the 5-layer prototype is compared to the 2-layer DEA slightly higher, and the first resonance peak appears at a higher frequency. The SPL and the resonant peak of the multi-functional DEA is only weakly dependent on the configuration. Because of the slightly higher pre-stretch of the membrane in the mechanically constrained configurations, the SPL results slightly higher in those cases. The variation in SPL due to preloading is below several dB and can be neglected for practical applications. This means that the DEA can be used as loudspeaker in different deformation configurations, without losing much of the performance, which leads to a flexible usable interface.

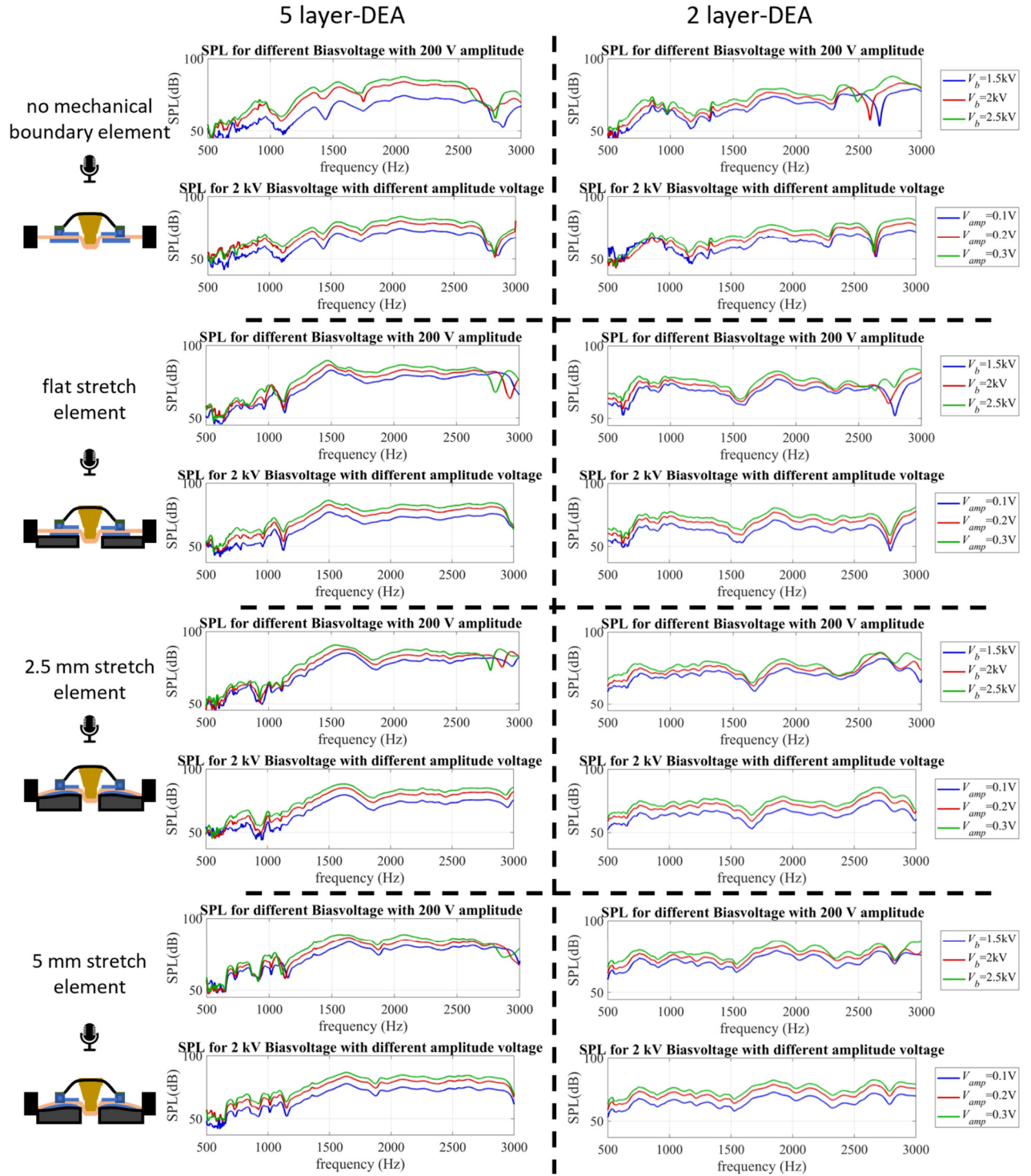


Figure 3.77: SPL of the actuator (DEA + Textile) for different configurations, far 2- and 5-layer DEA, with different bias and amplitude input voltage.

For better comparison of the different configurations, Figure 3.78 presents the SPL in one plot. The only major difference appears for the basic configuration without any mechanical preload where a drop in the SPL appears for a frequency between 2600 Hz and 3000 Hz, which is strongly influenced by the mechanical element and shifts toward higher frequencies by using the stretch elements. The shift in the frequency domain can be additionally influenced by acoustic boundary conditions in the measurement chamber, during the measurement. This behaviour can be explained by the stiffness increase due to the mechanical elements.

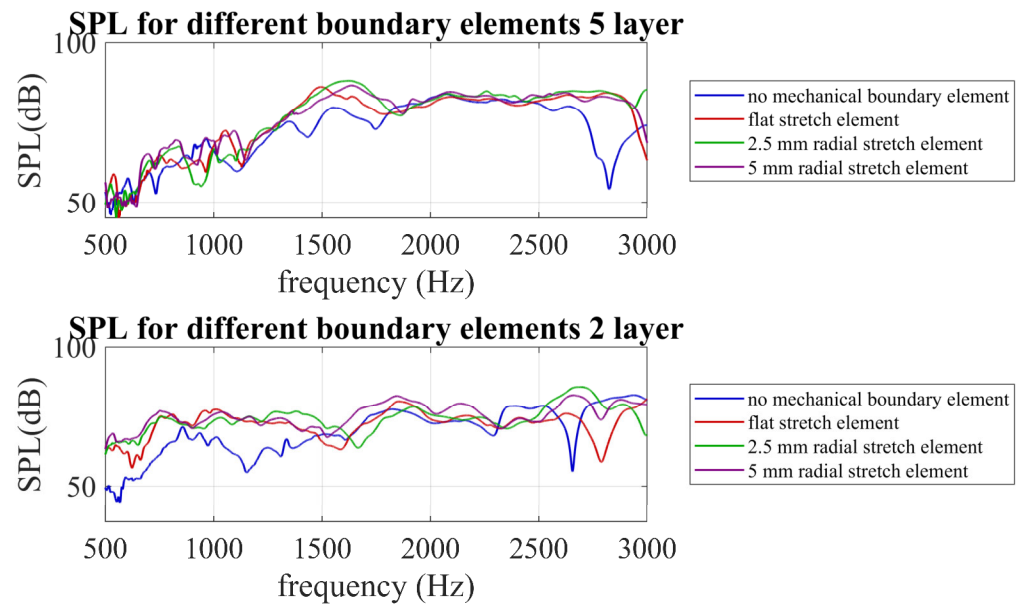


Figure 3.78: SPL for different configurations and different actuator layers.

4. Application examples, Conclusion & Outlook

This chapter closes the thesis by showing some potential application examples and fields, summarizing the main results and providing an outlook for future development and improving of the developed systems and structures.

4.1. Application examples

Multi-functional elements can be used in many different areas and for different applications. In this section a few application examples are shown to validate the benefit of the developed and presented features of multi-functional DETs. In Figure 4.1 a comprehensive approach for distributed connected smart elements is shown. The combination of DE based sensors, actuators and multi-functional elements (as developed in this thesis) with further additional components like smart sensing textiles (e.g. smart vest), generators, electronics, artificial intelligence and brain computer interfaces paves the way for completely new human and user interaction.

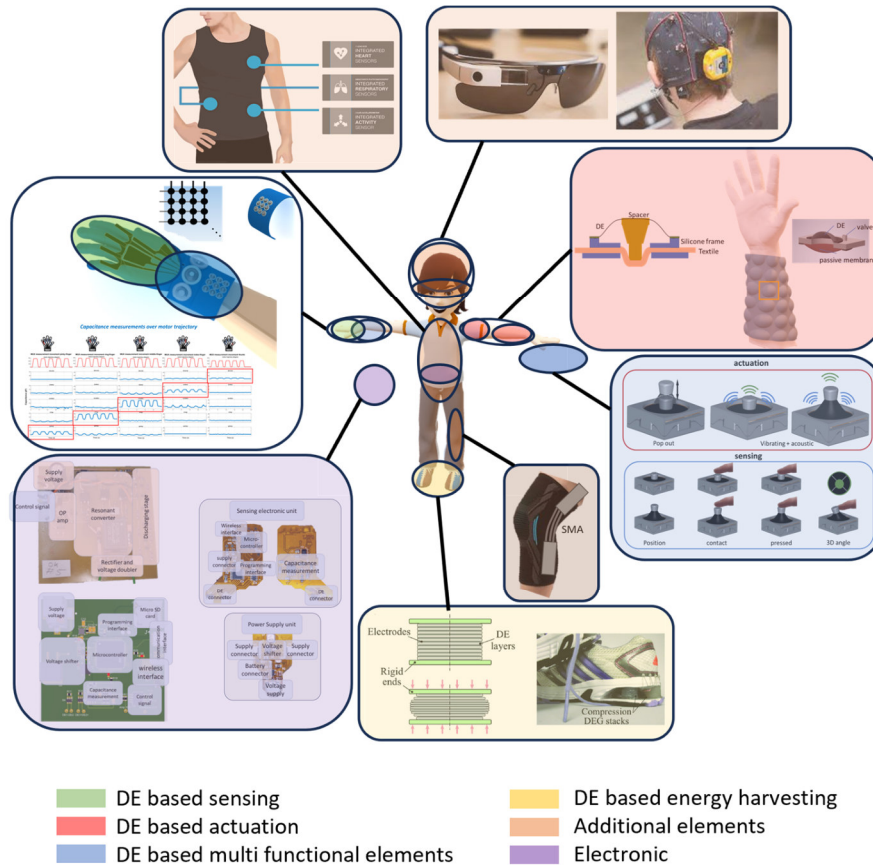


Figure 4.1: Combination of DE based sensor- actuator and multi-functional elements as well as generator with additional conventional elements and electronic to deliver a comprehensive distributed human communication interface.

By integrating the single elements in an unobtrusive and sleek way, the variety of features can be integrated without compromising wearing comfort and ergonomics. Smart materials, like SMAs for example, can additionally be used for force feedback or active support of the user.

The different features of the developed DE based elements of this thesis and their usability and product value enhancement are presented in the following, using individual application examples. The examples show future fields of application and represent only a partial area of implementations. The setups presented have not yet been implemented in practice and are meant to provide a roadmap for future investigation.

Application fields

Industry application

The field of assistance tools for industry applications and production gets more important as a consequence of the digitalisation envisioned by the industry (I 4.0). Many assistance tools and wearables can be used in industry applications. For this field specifically the reliability and robustness of the system is important. One example of assistance tools are smart gloves, potentially combined with tactile and force feedback. Supporting to this work a smart sensing glove is developed, where fine movements of the fingers, with a relatively small design space, can be acquired with sufficient accuracy [215]. If this is combined with multifunctional feedback elements a bi-directional user interaction unit can be designed. The design of the DE elements and the electronic as well as the manufacturing process of the assistance tool are matched to each other. In Figure 4.2 the main potential features of a multi-functional assistive tool, in the form of a sensing and tactile feedback glove are shown.

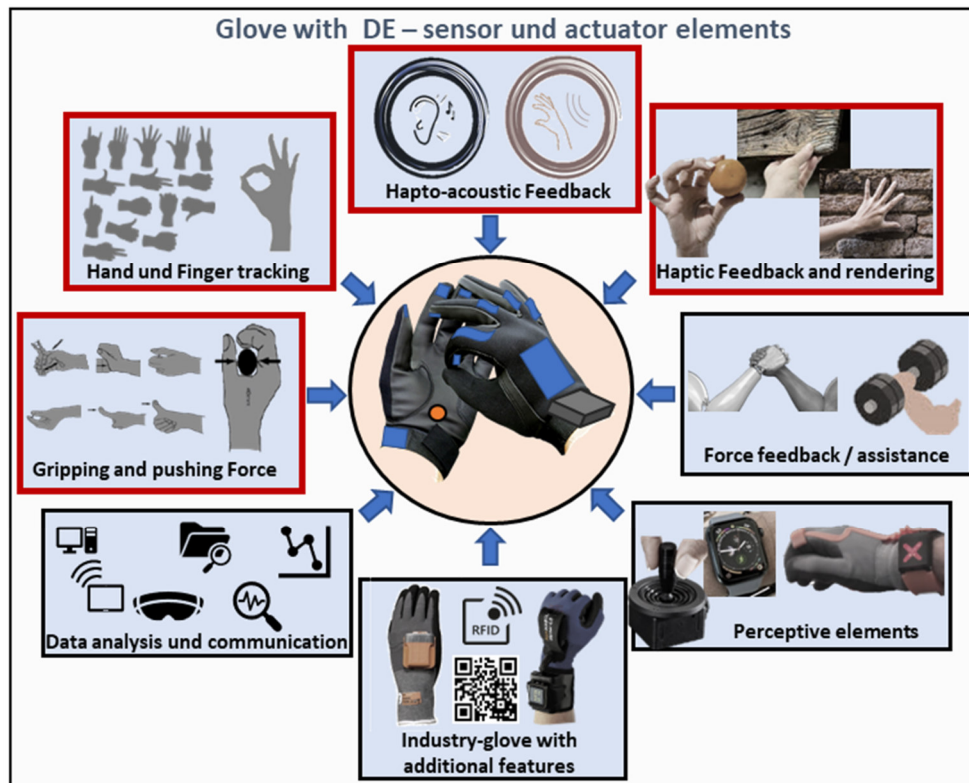


Figure 4.2: Possible features and extensions for a smart glove to provide a fully comprehensive smart assistance tool. DE technology viable features are red marked.

Help for elderly people

In 2018 the total number of people over 65 worldwide outnumber the first time the number of children under 5 [269]. The society is generally getting older and more elderer people need help in the daily life [270]. One potential avenue for assistance is the monitoring of vital signs, with the subsequent application of feedback appropriate to the needs of elderly individuals. . For example, reminding them to take their medicine or practice certain exercises. Another application is in the area of active support of the human, for example stand-up aid or working aid.

Help for handicapped people

Around one billion people of the world population (15%) have some form of disability [271]. Especially for people with physical disabilities wearable assistance tools can help. Similar like for aged people active support and communication are fields of interest for multi-functional assistance tools. But people with intellectual disabilities can also be helped with communication tools, for example by combining brain-computer interaction with physical stimuli generated by feedback-based elements.

Smart surfaces and car interior

A wide range of potential applications for multifunctional elements are smart surfaces. The surfaces can be used in different fields, for communication and control. The interface can be used in all kinds of textile- or non-textile-based surfaces to interact with the surroundings. For example, car interior or smart home control elements can be one use-field. Additionally active smart surfaces, which sense the state of the surface and change the geometry to increase aerodynamic efficiency and attenuate vibrations and noise for example, are a potential field of application.

Virtual / augmented reality and entertainment

VR and AR are highly increasing fields. They can be used in different application scenarios like education and training, industry, navigation, medicine, entertainment, advertising and gaming to just name a few. The ability to recognise human movements or intentions and to convey sensations and hearing through ‘normal’ clothing, for example, enlarges the fields and lowers the threshold for use. In the entertainment area it could be possible to interact with real-like scenarios directly from home.

Human digital twin

Another field of interest is the development of a human digital twin. Especially in the industrial environment digital twins, mainly for products, handling devices and robots for instance are used. The development of a human digital twin is much more difficult to realize. With the use of the sensor characteristics the physical properties of a human can be transferred to a digital image. The model behind the digital twin can not only record the person's current state (e.g. movement, position or vital functions), but also calculate the person's most likely behavior. This can be used to give feedback to the human or to the environment for example to warn the human if a dangerous situation is probable or the concentration level drops down. The efficiency of the digital twin bases mainly on the developed algorithm, but also the sensing data of the human and proper feedback to the human are needed for the potential real use [218].

Sport and medicine

Assistance systems can increase the efficiency of treatment for both doctors and patients. The patient can be supported in a similar way as elder or handicapped people with active assistance and vital value control for instance. On the other side, surgeons can be supported during an operation with tactile and acoustic feedback for example. For sport and competitive sport, the monitoring of the human motion and additionally the real-time feedback to increase the performance can be realised. For example, the movement of an athlete can be sensed in real time and slight adjustments to the movement can be achieved with the help of haptic and/or acoustic feedback. This means that the execution of the movement can be perfected by only repeating it several times. Alternatively, real-time monitoring can be used to detect posture and movement deficits and make the user aware of them (e.g. flat foot, curved back).

Comfort

Another application example can be the comfort of human users. This can be for example an induced pleasant vibration like for massages or temperature stabilisation in garments. The massage effect can be also realised in car seats. Based on DEs a variable higher frequency vibration can be adapted to the user need [272]. The massage function can also be integrated in massage suites. A further application for wearable comfort elements are heating and cooling systems. The heating is often realised by current-carrying conductors that heat up. For wearable cooling systems implementation technologies are not very advance; smart materials with an elastocaloric-cooling effect could help here [273].

4.2. Conclusion

The focus of this thesis is on the development and systematic validation of multifunctional sensing and feedback elements based on dielectric elastomer transducers (DETs). The actuator and sensor properties of DETs have considerable potential for the development of slim, flexible, and high-efficiency textile-integrated smart assistive elements. However, despite the existence of literature proposing certain user interaction and feedback solutions, this thesis is the first to develop and propose a key benefit of DET-based interfaces: the capacity to perform multiple tasks simultaneously using a single interface. The evolved control and methodology extends the functional scope of DETs as a sensor, tactile feedback element and loudspeaker simultaneously, using only one single thin functional membrane.

The structure of a DE based user interface, with multiple capabilities (self-sensing, multi-modal actuation) and needed peripherals, like sensing and high voltage electronics, as well as textile integration concepts are shown. The main development of the simultaneous and efficient use of multi-functionality is investigated and methodically described in full detail. For that the principle of using different frequency regimes (vibration modes) for tactile feedback or movement of the DE and sound generation is shown. With the developed concept the two modes of the DE can be individually and simultaneously controlled. Additionally, the higher frequency regime can be also used for self-sensing, by measuring the voltage and current through the DE. With these investigations it is possible to achieve even three different functionalities with one element and one single control input of the DE simultaneously. In a further step, a concept to integrate the multifunctional elements into textiles is described. All the developments and investigations are validated with measurements and different proof-of-concept tests to demonstrate the practical functionality. The performed validation measurements include acoustic measurements, vibrational measurements, force and displacement measurements as well as electrical measurements, like voltage, current, resistance and capacitance measurements. With this broad and precise validation, the mechanism and the mode of operation can be completely understood and controlled.

Furthermore, several prototypes are built, illustrated and validated by measurements. The prototypes are self-standing units which provide the interaction with a user, to show the practical use of the developed concepts. Altogether, the prototypes also show the broad field of the new development of this investigation, from the theoretical development of a multi-functional actuator over the use of custom made sensing and high voltage electronic to programming of the periphery and the self-sensing algorithm, as well as the integration of the whole system into a functional unit.

Finally, different applications fields and examples are shown to provide a vision of the relevance in industry, medicine, entertainment and further other scope of interest. The different application examples show the potential use of the developed assistive tools in ‘real-world’ applications.

4.3. Future development

The shown concepts and developments of this thesis build the basis for many different further applications and developments. Possible further development areas are miniaturization of the DEA element and the whole structure; the interaction of multiple DEA elements in an array (and the interaction of different vibration modes to the whole structure and the sound output); the use of flexible biasing elements (e.g. silicone or PET based springs), and the use of different materials

(e.g. sputtered electrodes) or manufacturing processes for the DEA. Furthermore, the electronics, for both the sensing and the high voltage electronics, can be improved and self-sensing algorithms can be integrated in a compact microcontroller by reducing the required computing capacity. The high frequency stimulation could be also increased to ultrasonic region in a further step, for example to use a further frequency band for additional sensing and environment interaction capability.

With a further development and adaption of the presented DE models, and integration of controls onto small size microcontrollers, an improvement of the sound quality, the self-sensing accuracy or for example the effective interaction of many different actuator elements can be realised. Additionally, the investigated multi-functionality paradigm, could be also transferred into other systems and smart materials to provide them with different simultaneous application modes. In further research projects, the practical use of the developed systems and their integration into real application cases (e.g. assembly line) will be investigated further [274], [275].

References

- [1] statistisches Bundesamt (state 2024); VCI, “Umsatz der wichtigsten Industriebranchen in Deutschland von 2012 bis 2022 (in Milliarden Euro),” <https://de.statista.com/statistik/daten/studie/203580/umfrage/umsaetze-der-wichtigsten-industriebranchen-in-deutschland/>.
- [2] Statistisches Bundesamt (state 2024); Statista GmbH, “Anzahl der Erwerbstätigen in Deutschland nach Wirtschaftsbereichen im Jahr 2022 (in 1.000),” <https://de.statista.com/statistik/daten/studie/1248/umfrage/anzahl-der-erwerbstaetigen-in-deutschland-nach-wirtschaftsbereichen/>.
- [3] Tzafestas S., “Concerning human-automation symbiosis in the society and the nature.,” *Int. J. Fact. Autom. Robot. Soft Comput* 1.3, pp. 6–24, 2006.
- [4] C. Santos, A. Mehraei, A. C. Barros, M. Araújo, and E. Ares, “Towards Industry 4.0: an overview of European strategic roadmaps,” *Procedia Manuf*, vol. 13, pp. 972–979, Jan. 2017, doi: 10.1016/J.PROMFG.2017.09.093.
- [5] M. Lorenz, “Man and machine in Industry 4.0: how will technology transform the industrial workforce through 2025,” 2015, Boston Consulting Group.
- [6] D. Romero, P. Bernus, O. Noran, J. Stahre, and Å. F. Berglund, “The operator 4.0: Human cyber-physical systems & adaptive automation towards human-automation symbiosis work systems,” *IFIP Adv Inf Commun Technol*, vol. 488, pp. 677–686, 2016, doi: 10.1007/978-3-319-51133-7_80.
- [7] B. G. Mark, E. Rauch, and D. T. Matt, *Industrial Assistance Systems to Enhance Human–Machine Interaction and Operator’s Capabilities in Assembly*. Palgrave Macmillan, Cham, 2021. doi: 10.1007/978-3-030-70516-9_4.
- [8] D. Gorecky, M. Schmitt, and M. Loskyll, “Mensch-Maschine-Interaktion im Industrie 4.0-Zeitalter,” in *Industrie 4.0 in Produktion, Automatisierung und Logistik*, Springer Vieweg, Wiesbaden, 2014, pp. 525–542. doi: 10.1007/978-3-658-04682-8_26.
- [9] T. Bauernhansl, M. ten Hompel, and B. Vogel-Heuser, *Industrie 4.0 in Produktion, Automatisierung und Logistik*. Springer Fachmedien Wiesbaden, 2014. doi: 10.1007/978-3-658-04682-8.
- [10] IIoT World - Connecting the SMASSTs, “Status and trends in the global manufacturing sector,” <https://iiot-world.com/connected-industry/status-and-trends-in-the-global-manufacturing-sector/>.
- [11] A. Botthof and E. A. Hartmann, “Zukunft der Arbeit in Industrie 4.0,” *Autonomik Industrie 4.0*, 2015, doi: 10.1007/978-3-662-45915-7.
- [12] S. Michel, X. Q. Zhang, M. Wissler, C. Löwe, and G. Kovacs, “A comparison between silicone and acrylic elastomers as dielectric materials in electroactive polymer actuators,” *Polym Int*, vol. 59, no. 3, pp. 391–399, Dec. 2009, doi: 10.1002/pi.2751.
- [13] R. Pelrine, R. Kornbluh, Q. Pei, and J. Joseph, “High-speed electrically actuated elastomers with strain greater than 100%,” *Science (1979)*, vol. 287, no. 5454, pp. 836–839, Feb. 2000, doi: 10.1126/SCIENCE.287.5454.836.

- [14] J. J. Kornbluh R., Pelrine R., Eckerle, J., “Electrostrictive polymer artificial muscle actuators,” in *Proceedings. 1998 IEEE International Conference on Robotics and Automation (Cat. No.98CH36146)*, IEEE, pp. 2147–2154. doi: 10.1109/ROBOT.1998.680638.
- [15] R. E. Pelrine, R. D. Kornbluh, and J. P. Joseph, “Electrostriction of polymer dielectrics with compliant electrodes as a means of actuation,” *Sens Actuators A Phys*, vol. 64, no. 1, pp. 77–85, Jan. 1998, doi: 10.1016/S0924-4247(97)01657-9.
- [16] R. D. Kornbluh *et al.*, “Electroelastomers: applications of dielectric elastomer transducers for actuation, generation, and smart structures,” *Smart Structures and Materials 2002: Industrial and Commercial Applications of Smart Structures Technologies*, vol. 4698, pp. 254–270, Jul. 2002, doi: 10.1117/12.475072.
- [17] E. Hajiesmaili and D. R. Clarke, “Dielectric elastomer actuators,” *J Appl Phys*, vol. 129, no. 15, p. 151102, Apr. 2021, doi: 10.1063/5.0043959/1025587.
- [18] F. Carpi, D. De Rossi, R. Kornbluh, R. Pelrine, and P. Sommer-Larsen, *Dielectric elastomers as electromechanical transducers: Fundamentals, Materials, Devices, Models and Applications of an Emerging Electroactive Polymer Technology*. Elsevier Ltd, 2008. doi: 10.1016/B978-0-08-047488-5.X0001-9.
- [19] H. Zhao *et al.*, “A Wearable Soft Haptic Communicator Based on Dielectric Elastomer Actuators,” *Soft Robot*, vol. 7, no. 4, pp. 451–461, Aug. 2020, doi: 10.1089/SORO.2019.0113.
- [20] D. Y. Lee *et al.*, “A Wearable Textile-Embedded Dielectric Elastomer Actuator Haptic Display,” *Soft Robot*, vol. 9, no. 6, pp. 1186–1197, Dec. 2022, doi: 10.1089/SORO.2021.0098.
- [21] J. Yin *et al.*, “Wearable Soft Technologies for Haptic Sensing and Feedback,” *Adv Funct Mater*, vol. 31, no. 39, p. 2007428, Sep. 2020, doi: 10.1002/ADFM.202007428.
- [22] J. Choon Koo, H. Ryeol Choi, K. Jung, J. Nam, Y. kwan Lee, and S. Lee, “A new braille display system design using a polymer-based soft actuator tactile display,” in *Dielectric Elastomers as Electromechanical Transducers*, Elsevier, 2008, pp. 239–248. doi: 10.1016/B978-0-08-047488-5.00023-X.
- [23] E. Leroy, R. Hinchet, E. Leroy, R. Hinchet, and H. Shea, “Multimode Hydraulically Amplified Electrostatic Actuators for Wearable Haptics,” *Advanced Materials*, vol. 32, no. 36, p. 2002564, Sep. 2020, doi: 10.1002/ADMA.202002564.
- [24] G. Frediani, D. Mazzei, D. E. De Rossi, F. Carpi, C. Menon, and P. Varona, “Wearable wireless tactile display for virtual interactions with soft bodies,” *Front Bioeng Biotechnol*, vol. 2, no. 31, 2014, doi: 10.3389/fbioe.2014.00031.
- [25] T. P. Willian *et al.*, “Effects of Solvents on the Material Properties of Screen-Printed Electrodes and a Polydimethylsiloxane Dielectric for Dielectric Elastomer Transducers,” *Adv Eng Mater*, vol. 26, no. 10, p. 2301736, May 2024, doi: 10.1002/ADFM.202301736.
- [26] B. Fasolt, M. Hodgins, G. Rizzello, and S. Seelecke, “Effect of screen printing parameters on sensor and actuator performance of dielectric elastomer (DE) membranes,” *Sens Actuators A Phys*, vol. 265, pp. 10–19, Oct. 2017, doi: 10.1016/J.SNA.2017.08.028.

- [27] B. Fasolt, F. Welsch, M. Jank, and S. Seelecke, "Effect of actuation parameters and environment on the breakdown voltage of silicone dielectric elastomer films," *Smart Mater Struct*, vol. 28, no. 9, 2019, doi: 10.1088/1361-665X/AB2F34.
- [28] B. Fasolt, M. Hodgins, and S. Seelecke, "Characterization of screen-printed electrodes for dielectric elastomer (DE) membranes: influence of screen dimensions and electrode thickness on actuator performance," in *SPIE Smart Structures + Nondestructive Evaluation and Health Monitoring, Electroactive Polymer Actuators and Devices*, 2016, p. 97983E. doi: 10.1117/12.2222095.
- [29] T. P. Willian, B. Fasolt, P. Motzki, G. Rizzello, and S. Seelecke, "Effects of Electrode Materials and Compositions on the Resistance Behavior of Dielectric Elastomer Transducers," *MDPI, polymers*, vol. 15, no. 2, Jan. 2023, doi: 10.3390/polym15020310.
- [30] C. Perri, S. Lenz, G. Rizzello, S. Seelecke, and D. Naso, "Modeling and Validation of a High Voltage Driving Circuit for Dielectric Elastomer Actuators," *IEEE International Symposium on Industrial Electronics*, vol. 2021-June, Jun. 2021, doi: 10.1109/ISIE45552.2021.9576391.
- [31] C. Perri, B. Holz, P. R. Massenio, D. Naso, S. Member, and G. Rizzello, "Design, Modeling, and Experimental Validation of a High Voltage Driving Circuit for Dielectric Elastomer Actuators," 2023, doi: 10.1109/TIE.2023.3288190.
- [32] S. Lenz, B. Holz, S. Hau, and S. Seelecke, "Development of a high voltage source for dielectric elastomer actuators (DEA)," in *Actuators 2018 - 16th International Conference on New Actuators*, 2018.
- [33] P. Loew, G. Rizzello, and S. Seelecke, "Pressure monitoring inside a polymer tube based on a dielectric elastomer membrane sensor," in *SPIE Smart Structures + Nondestructive Evaluation, Electroactive Polymer Actuators and Devices*, 2018, p. 53. doi: 10.1117/12.2296332.
- [34] H. Böse and J. Ehrlich, "Dielectric Elastomer Sensors with Advanced Designs and Their Applications," *Actuators 2023, Vol. 12, Page 115*, vol. 12, no. 3, p. 115, Mar. 2023, doi: 10.3390/ACT12030115.
- [35] A. Meyer *et al.*, "Experimental characterization of a smart dielectric elastomer multi-sensor grid," in *SPIE Smart Structures + Nondestructive Evaluation, Electroactive Polymer Actuators and Devices*, SPIE, 2020, pp. 262–268. doi: 10.1117/12.2558433.
- [36] M. Y. Cheng, X. H. Huang, C. W. Ma, and Y. J. Yang, "A flexible capacitive tactile sensing array with floating electrodes," *Journal of Micromechanics and Microengineering*, vol. 19, no. 11, 2009, doi: 10.1088/0960-1317/19/11/115001.
- [37] Y. Zhu, T. Giffney, and K. Aw, "A Dielectric Elastomer-Based Multimodal Capacitive Sensor," *Sensors 2022, Vol. 22, Page 622*, vol. 22, no. 2, p. 622, Jan. 2022, doi: 10.3390/S22020622.
- [38] Y. Liang, B. Wan, G. Li, Y. Xie, and T. Li, "A novel transparent dielectric elastomer sensor for compressive force measurements," *Electroactive Polymer Actuators and Devices (EAPAD) 2016*, vol. 9798, p. 979830, 2016, doi: 10.1117/12.2219107.

- [39] H. Zhang, M. Y. Wang, J. Li, and J. Zhu, “A soft compressive sensor using dielectric elastomers,” *Smart Mater Struct*, vol. 25, no. 3, Feb. 2016, doi: 10.1088/0964-1726/25/3/035045.
- [40] H. Zhang and M. Y. Wang, “Multi-Axis Soft Sensors Based on Dielectric Elastomer,” *Soft Robot*, vol. 3, no. 1, pp. 3–12, Mar. 2016, doi: 10.1089/SORO.2015.0017.
- [41] B. Y. Lee, J. Kim, H. Kim, C. Kim, and S. D. Lee, “Low-cost flexible pressure sensor based on dielectric elastomer film with micro-pores,” *Sens Actuators A Phys*, vol. 240, pp. 103–109, Apr. 2016, doi: 10.1016/J.SNA.2016.01.037.
- [42] B. Nie *et al.*, “Sensing arbitrary contact forces with a flexible porous dielectric elastomer,” *Mater Horiz*, vol. 8, no. 3, pp. 962–971, Mar. 2021, doi: 10.1039/D0MH01359E.
- [43] Y. Zhu and A. Tairych, “Using a flexible substrate to enhance the sensitivity of dielectric elastomer force sensors,” *Sens Actuators A Phys*, vol. 332, p. 113167, Dec. 2021, doi: 10.1016/J.SNA.2021.113167.
- [44] D. H. Lee, U. Kim, H. Jung, and H. R. Choi, “A capacitive-type novel six-axis force/torque sensor for robotic applications,” *IEEE Sens J*, vol. 16, no. 8, pp. 2290–2299, Apr. 2016, doi: 10.1109/JSEN.2015.2504267.
- [45] A. O’Halloran, F. O’Malley, and P. McHugh, “A review on dielectric elastomer actuators, technology, applications, and challenges,” *J Appl Phys*, vol. 104, no. 7, Oct. 2008, doi: 10.1063/1.2981642/146339.
- [46] R. Pelrine *et al.*, “Applications of dielectric elastomer actuators,” in *Smart Structures and Materials 2001: Electroactive Polymer Actuators and Devices*, SPIE, Jul. 2001, pp. 335–349. doi: 10.1117/12.432665.
- [47] Y. Guo, L. Liu, Y. Liu, and J. Leng, “Review of Dielectric Elastomer Actuators and Their Applications in Soft Robots,” *Advanced Intelligent Systems*, vol. 3, no. 10, p. 2000282, Oct. 2021, doi: 10.1002/AISY.202000282.
- [48] U. Gupta *et al.*, “Soft robots based on dielectric elastomer actuators: a review,” *SMA S*, vol. 28, no. 10, p. 103002, Sep. 2019, doi: 10.1088/1361-665X/AB3A77.
- [49] J. H. Youn *et al.*, “Dielectric Elastomer Actuator for Soft Robotics Applications and Challenges,” *Applied Sciences 2020, Vol. 10, Page 640*, vol. 10, no. 2, p. 640, Jan. 2020, doi: 10.3390/APP10020640.
- [50] G. Y. Gu, J. Zhu, L. M. Zhu, and X. Zhu, “A survey on dielectric elastomer actuators for soft robots,” *Bioinspir Biomim*, vol. 12, no. 1, p. 011003, Jan. 2017, doi: 10.1088/1748-3190/12/1/011003.
- [51] Y. Guo, Q. Qin, Z. Han, R. Plamthottam, M. Possinger, and Q. Pei, “Dielectric elastomer artificial muscle materials advancement and soft robotic applications,” *Smart-Mat*, vol. 4, no. 4, p. e1203, Aug. 2023, doi: 10.1002/SMM2.1203.
- [52] M. Duduta, D. R. Clarke, and R. J. Wood, “A high speed soft robot based on dielectric elastomer actuators,” *Proc IEEE Int Conf Robot Autom*, pp. 4346–4351, Jul. 2017, doi: 10.1109/ICRA.2017.7989501.
- [53] M. Franke, A. Ehrenhofer, S. Lahiri, E. F. M. Henke, T. Wallmersperger, and A. Richter, “Dielectric Elastomer Actuator Driven Soft Robotic Structures With Bioinspired

- Skeletal and Muscular Reinforcement,” *Front Robot AI*, vol. 7, p. 510757, Dec. 2020, doi: 10.3389/FROBT.2020.510757/BIBTEX.
- [54] W. Feng *et al.*, “A large-strain and ultrahigh energy density dielectric elastomer for fast moving soft robot,” *Nature Communications* 2024 15:1, vol. 15, no. 1, pp. 1–10, May 2024, doi: 10.1038/s41467-024-48243-y.
 - [55] Y. Wang *et al.*, “Dielectric elastomer actuators for artificial muscles: A comprehensive review of soft robot explorations,” *Resources Chemicals and Materials*, vol. 1, no. 3–4, pp. 308–324, Sep. 2022, doi: 10.1016/J.RECM.2022.09.001.
 - [56] Y. Yang *et al.*, “Muscle-inspired soft robots based on bilateral dielectric elastomer actuators,” *Microsystems & Nanoengineering* 2023 9:1, vol. 9, no. 1, pp. 1–10, Oct. 2023, doi: 10.1038/s41378-023-00592-2.
 - [57] C. Tang, B. Du, S. Jiang, Z. Wang, X. J. Liu, and H. Zhao, “A Review on High-Frequency Dielectric Elastomer Actuators: Materials, Dynamics, and Applications,” *Advanced Intelligent Systems*, vol. 6, no. 2, p. 2300047, Feb. 2024, doi: 10.1002/AISY.202300047.
 - [58] A. Wiranata *et al.*, “High-Frequency, low-voltage oscillations of dielectric elastomer actuators,” *Applied Physics Express*, vol. 15, no. 1, p. 011002, Dec. 2021, doi: 10.35848/1882-0786/AC3D41.
 - [59] G. Moretti, G. Rizzello, M. Fontana, and S. Seelecke, “High-frequency voltage-driven vibrations in dielectric elastomer membranes,” *Mech Syst Signal Process*, vol. 168, p. 108677, Apr. 2022, doi: 10.1016/J.YMSSP.2021.108677.
 - [60] I. Kajiwarra, S. Kitabatake, N. Hosoya, and S. Maeda, “Design of dielectric elastomer actuators for vibration control at high frequencies,” *Int J Mech Sci*, vol. 157–158, pp. 849–857, Jul. 2019, doi: 10.1016/J.IJMECSCI.2019.05.019.
 - [61] G. Kovacs, L. Düring, S. Michel, and G. Terrasi, “Stacked dielectric elastomer actuator for tensile force transmission,” *Sens Actuators A Phys*, vol. 155, no. 2, pp. 299–307, Oct. 2009, doi: 10.1016/J.SNA.2009.08.027.
 - [62] H. Zhao *et al.*, “Compact Dielectric Elastomer Linear Actuators,” *Adv Funct Mater*, 2018, doi: 10.1002/adfm.201804328.
 - [63] N. Wang, C. Cui, B. Chen, and X. Zhang, “A Soft Gripper Based on Dielectric Elastomer Actuator,” *2017 IEEE 7th Annual International Conference on CYBER Technology in Automation, Control, and Intelligent Systems, CYBER 2017*, pp. 586–591, Aug. 2018, doi: 10.1109/CYBER.2017.8446451.
 - [64] S. Shian, K. Bertoldi, and D. R. Clarke, “Dielectric Elastomer Based ‘grippers’ for Soft Robotics,” *Advanced Materials*, vol. 27, no. 43, pp. 6814–6819, Nov. 2015, doi: 10.1002/ADMA.201503078.
 - [65] S. Pourazadi, H. Bui, and C. Menon, “Investigation on a soft grasping gripper based on dielectric elastomer actuators,” *Smart Mater Struct*, vol. 28, no. 3, Feb. 2019, doi: 10.1088/1361-665X/AAF767.
 - [66] N. Li *et al.*, “A soft gripper driven by conical dielectric elastomer actuator to achieve displacement amplification and compliant grips,” *Intell Serv Robot*, pp. 1–11, Jul. 2024, doi: 10.1007/S11370-024-00553-2/FIGURES/7.

- [67] W. Thongking, A. Wiranata, A. Minaminosono, Z. Mao, and S. Maeda, “Soft Robotic Gripper Based on Multi-Layers of Dielectric Elastomer Actuators”, doi: 10.20965/jrm.2021.p0968.
- [68] M. Follador, F. Tramacere, and B. Mazzolai, “Dielectric elastomer actuators for octopus inspired suction cups,” *Bioinspir Biomim*, vol. 9, no. 4, p. 046002, Sep. 2014, doi: 10.1088/1748-3182/9/4/046002.
- [69] A. Jamali, D. B. Mishra, F. Goldschmidtboeing, and P. Woias, “Soft octopus-inspired suction cups using dielectric elastomer actuators with sensing capabilities,” *Bioinspir Biomim*, vol. 19, no. 3, p. 036009, Apr. 2024, doi: 10.1088/1748-3190/AD3266.
- [70] F. A. Mohd Ghazali, C. K. Mah, A. AbuZaiter, P. S. Chee, and M. S. Mohamed Ali, “Soft dielectric elastomer actuator micropump,” *Sens Actuators A Phys*, vol. 263, pp. 276–284, Aug. 2017, doi: 10.1016/J.SNA.2017.06.018.
- [71] P. S. Chee, C. K. Mah, and M. S. M. Ali, “Soft dielectric elastomer actuator for micropump application,” *Proceedings of the IEEE International Conference on Micro Electro Mechanical Systems (MEMS)*, vol. 2016-February, pp. 561–564, Feb. 2016, doi: 10.1109/MEMSYS.2016.7421687.
- [72] S. Ho *et al.*, “Experimental characterization of a dielectric elastomer fluid pump and optimizing performance via composite materials,” *J Intell Mater Syst Struct*, vol. 28, no. 20, pp. 3054–3065, Apr. 2017, doi: 10.1177/1045389X17704921.
- [73] Z. Li, J. Zhu, C. C. Foo, and C. H. Yap, “A robust dual-membrane dielectric elastomer actuator for large volume fluid pumping via snap-through,” *Appl Phys Lett*, vol. 111, no. 21, Nov. 2017, doi: 10.1063/1.5005982/985973.
- [74] P. Linnebach, G. Rizzello, S. Seelecke, and S. Seelecke, “Design and validation of a dielectric elastomer membrane actuator driven pneumatic pump,” *Smart Mater Struct*, vol. 29, no. 7, p. 075021, Jun. 2020, doi: 10.1088/1361-665X/AB8A01.
- [75] L. Wang, J. Zhuo, J. Peng, H. Dong, S. Jiang, and Y. Shi, “A Stretchable Soft Pump Driven by a Heterogeneous Dielectric Elastomer Actuator,” *Adv Funct Mater*, p. 2411160, 2024, doi: 10.1002/ADFM.202411160.
- [76] C. Christianson, N. N. Goldberg, and M. T. Tolley, “Elastomeric diaphragm pump driven by fluid electrode dielectric elastomer actuators (FEDEAs),” *SPIE Smart Structures and Materials + Nondestructive Evaluation and Health Monitoring*, vol. 10594, pp. 115–121, Mar. 2018, doi: 10.1117/12.2294557.
- [77] C. Cao, X. Gao, and A. T. Conn, “A Magnetically Coupled Dielectric Elastomer Pump for Soft Robotics,” *Adv Mater Technol*, vol. 4, no. 8, p. 1900128, Aug. 2019, doi: 10.1002/ADMT.201900128.
- [78] M. Hill, G. Rizzello, and S. Seelecke, “Development and experimental characterization of a pneumatic valve actuated by a dielectric elastomer membrane,” *Smart Mater Struct*, vol. 26, no. 8, p. 085023, Jul. 2017, doi: 10.1088/1361-665X/AA746D.
- [79] K. Flittner, M. Schlosser, and H. F. Schlaak, “Dielectric elastomer stack actuators for integrated gas valves,” in *SPIE Smart Structures and Materials + Nondestructive Evaluation and Health Monitoring*, SPIE, Mar. 2011, pp. 443–449. doi: 10.1117/12.880050.

- [80] M. Giousouf and G. Kovacs, "Dielectric elastomer actuators used for pneumatic valve technology," *Smart Mater Struct*, vol. 22, no. 10, p. 104010, Sep. 2013, doi: 10.1088/0964-1726/22/10/104010.
- [81] Y.-Y. Jhong, C.-M. Huang, C.-C. Hsieh, and C.-C. Fu, "Improvement of viscoelastic effects of dielectric elastomer actuator and its application for valve devices," in *SPIE Smart Structures and Materials + Nondestructive Evaluation and Health Monitoring*, SPIE, Apr. 2007, pp. 576–584. doi: 10.1117/12.715998.
- [82] P. Linnebach, F. Simone, G. Rizzello, and S. Seelecke, "Development, manufacturing, and validation of a dielectric elastomer membrane actuator-driven contactor," *Original Article Journal of Intelligent Material Systems and Structures*, vol. 30, no. 4, pp. 636–648, 2019, doi: 10.1177/1045389X18818778.
- [83] A. D. Price and A. Ask, "Integrated Design Optimization of Dielectric Elastomer Actuators in High-Performance Switchgear," in *ASME Conference on Smart Materials, Adaptive Structures and Intelligent Systems (SMASIS)*, American Society of Mechanical Engineers Digital Collection, Dec. 2014. doi: 10.1115/SMASIS2014-7574.
- [84] K. Jung, J. Kim, and H. R. Choi, "A self-sensing dielectric elastomer actuator," *Sensors and Actuators A*, vol. 143, pp. 343–351, 2008, doi: 10.1016/j.sna.2007.10.076.
- [85] G. Rizzello, P. Serafino, D. Naso, and S. Seelecke, "Towards Sensorless Soft Robotics: Self-Sensing Stiffness Control of Dielectric Elastomer Actuators," *IEEE Transactions on Robotics*, vol. 36, no. 1, pp. 174–188, Feb. 2020, doi: 10.1109/TRO.2019.2944592.
- [86] Rizzello Gianluca, "Modeling, Control and Self-Sensing of Dielectric Elastomer Actuators," Politecnico di Bari, 2016.
- [87] T. Hoffstadt and J. Maas, "Self-Sensing Control for Soft-Material Actuators Based on Dielectric Elastomers," *Front Robot AI*, vol. 6, p. 496444, Dec. 2019, doi: 10.3389/FROBT.2019.00133/BIBTEX.
- [88] G. Rizzello, D. Naso, A. York, and S. Seelecke, "Closed loop control of dielectric elastomer actuators based on self-sensing displacement feedback," *Smart Mater Struct*, vol. 25, no. 3, p. 035034, Feb. 2016, doi: 10.1088/0964-1726/25/3/035034.
- [89] S. Rosset, B. M. O'Brien, T. Gisby, D. Xu, H. R. Shea, and I. A. Anderson, "Self-sensing dielectric elastomer actuators in closed-loop operation," *Smart Mater Struct*, vol. 22, no. 10, p. 104018, Sep. 2013, doi: 10.1088/0964-1726/22/10/104018.
- [90] T. Hoffstadt and J. Maas, "Model-based self-sensing algorithm for dielectric elastomer transducers based on an extended Kalman filter," *Mechatronics*, vol. 50, pp. 248–258, Apr. 2018, doi: 10.1016/J.MECHATRONICS.2017.09.013.
- [91] G. Rizzello, D. Naso, A. York, and S. Seelecke, "A self-sensing approach for dielectric elastomer actuators based on online estimation algorithms," *IEEE/ASME Transactions on Mechatronics*, vol. 22, no. 2, pp. 728–738, 2017, doi: 10.1109/TMECH.2016.2638638.
- [92] P. Huang, J. Wu, Q. Meng, Y. Wang, and C. Y. Su, "Self-Sensing Motion Control of Dielectric Elastomer Actuator Based on NARX Neural Network and Iterative

- Learning Control Architecture,” *IEEE/ASME Transactions on Mechatronics*, vol. 29, no. 2, pp. 1374–1384, Apr. 2024, doi: 10.1109/TMECH.2023.3300364.
- [93] Z. Ye and Z. Chen, “Self-sensing of dielectric elastomer actuator enhanced by artificial neural network,” *Smart Mater Struct*, vol. 26, no. 9, p. 095056, Aug. 2017, doi: 10.1088/1361-665X/AA7E66.
- [94] R. Heydt, R. Pelrine, J. Joseph, J. Eckerle, and R. Kornbluh, “Acoustical performance of an electrostrictive polymer film loudspeaker,” *J Acoust Soc Am*, vol. 107, no. 2, pp. 833–839, Feb. 2000, doi: 10.1121/1.428266.
- [95] N. Hosoya, S. Baba, and S. Maeda, “Hemispherical breathing mode speaker using a dielectric elastomer actuator,” *J Acoust Soc Am*, vol. 138, no. 4, p. EL424, Oct. 2015, doi: 10.1121/1.4934550.
- [96] M. Gareis and J. Maas, “Acoustical Behaviour of Buckling Dielectric Elastomer Actuators,” *ASME 2019 Conference on Smart Materials, Adaptive Structures and Intelligent Systems, SMASIS 2019*, Dec. 2019, doi: 10.1115/SMASIS2019-5747.
- [97] T. Sugimoto *et al.*, “A lightweight push-pull acoustic transducer composed of a pair of dielectric elastomer films,” *J Acoust Soc Am*, vol. 134, no. 5, pp. EL432–EL437, Nov. 2013, doi: 10.1121/1.4824631.
- [98] C. Graf and J. Maas, “Acoustic transducer based on dielectric elastomers,” in <https://doi.org/10.1117/12.913270>, SPIE, Apr. 2012, pp. 348–358. doi: 10.1117/12.913270.
- [99] P. Bakardjiev, A. Richter, E. Altinsoy, U. Marschner, and J. Troge, “Dielectric elastomer loudspeaker driver,” 2017. doi: 10.24406/PUBLICA-FHG-399728.
- [100] E. Rustighi, W. Kaal, S. Herold, and A. Kubbara, “Experimental Characterisation of a Flat Dielectric Elastomer Loudspeaker,” *Actuators 2018, Vol. 7, Page 28*, vol. 7, no. 2, p. 28, Jun. 2018, doi: 10.3390/ACT7020028.
- [101] D. De Rossi, F. Carpi, N. Carbonaro, A. Tognetti, and E. P. Scilingo, “Electroactive polymer patches for wearable haptic interfaces,” *Proceedings of the Annual International Conference of the IEEE Engineering in Medicine and Biology Society, EMBS*, pp. 8369–8372, 2011, doi: 10.1109/IEMBS.2011.6092064.
- [102] I. Koo, K. Jung, J. Koo, J. Do Nam, Y. Lee, and H. R. Choi, “Wearable fingertip tactile display,” *2006 SICE-ICASE International Joint Conference*, pp. 1911–1916, 2006, doi: 10.1109/SICE.2006.315343.
- [103] I. M. Koo, K. Jung, J. C. Koo, J. Do Nam, Y. K. Lee, and H. R. Choi, “Development of soft-actuator-based wearable tactile display,” *IEEE Transactions on Robotics*, vol. 24, no. 3, pp. 549–558, Jun. 2008, doi: 10.1109/TRO.2008.921561.
- [104] H. Phung, P. T. Hoang, H. Jung, T. D. Nguyen, C. T. Nguyen, and H. R. Choi, “Haptic Display Responsive to Touch Driven by Soft Actuator and Soft Sensor,” *IEEE/ASME Transactions on Mechatronics*, vol. 26, no. 5, pp. 2495–2505, Oct. 2021, doi: 10.1109/TMECH.2020.3041225.
- [105] R. Zhang, P. Lochmatter, A. Kunz, and G. M. Kovacs, “Spring roll dielectric elastomer actuators for a portable force feedback glove,” <https://doi.org/10.1117/12.658524>, vol. 6168, pp. 505–516, Mar. 2006, doi: 10.1117/12.658524.

- [106] R. Zhang, P. Lochmatter, A. Kunz, and G. Kovacs, “Dielectric elastomer spring roll actuators for a portable force feedback device,” *14th Symposium on Haptics Interfaces for Virtual Environment and Teleoperator Systems 2006 - Proceedings*, vol. 2006, pp. 347–353, 2006, doi: 10.1109/HAPTIC.2006.1627137.
- [107] X. Ji *et al.*, “Untethered Feel-Through Haptics Using 18- μ m Thick Dielectric Elastomer Actuators,” *Adv Funct Mater*, vol. 31, no. 39, p. 2006639, Sep. 2021, doi: 10.1002/ADFM.202006639.
- [108] R. Heydt, R. Kornbluh, J. Eckerle, and R. Pelrine, “Sound radiation properties of dielectric elastomer electroactive polymer loudspeakers,” <https://doi.org/10.1117/12.659700>, vol. 6168, pp. 444–451, Mar. 2006, doi: 10.1117/12.659700.
- [109] M. Gareis and J. Maas, “Buckling Dielectric Elastomer Transducers as Loudspeakers,” *Journal of the Audio Engineering Society*, vol. 70, no. 10, pp. 858–870, Oct. 2022, doi: 10.17743/JAES.2022.0032.
- [110] F. Klug, C. Endl, S. Solano-Arana, and H. F. Schlaak, “Design, fabrication, and customized driving of dielectric loudspeaker arrays,” in *Electroactive Polymer Actuators and Devices (EAPAD) XXI*, SPIE-Intl Soc Optical Eng, Mar. 2019, p. 73. doi: 10.1117/12.2515311.
- [111] L. Felicetti, E. Chatelet, A. Latour, P. H. Cornuault, and F. Massi, “Tactile rendering of textures by an Electro-Active Polymer piezoelectric device: mimicking Friction-Induced Vibrations,” *Biotribology*, vol. 31, p. 100211, Sep. 2022, doi: 10.1016/J.BIOTRI.2022.100211.
- [112] W. Kaal and S. Herold, “Electroactive Polymer Actuators in Dynamic Applications,” vol. 16, no. 1, 2011, doi: 10.1109/TMECH.2010.2089529.
- [113] M. Shrestha, Z. Lu, and G.-K. Lau, “Transparent Tunable Acoustic Absorber Membrane Using Inkjet-Printed PEDOT:PSS Thin-Film Compliant Electrodes,” 2018, doi: 10.1021/acsami.8b12368.
- [114] P. Linnebach, G. Rizzello, S. Seelecke, and S. Seelecke, “Design and validation of a dielectric elastomer membrane actuator driven pneumatic pump,” *Smart Mater Struct*, vol. 29, no. 7, p. 075021, Jun. 2020, doi: 10.1088/1361-665X/AB8A01.
- [115] C. Cao, X. Gao, S. Burgess, and A. T. Conn, “Power optimization of a conical dielectric elastomer actuator for resonant robotic systems,” *Extreme Mech Lett*, vol. 35, p. 100619, Feb. 2020, doi: 10.1016/J.EML.2019.100619.
- [116] J. W. Fox and N. C. Goulbourne, “Electric field-induced surface transformations and experimental dynamic characteristics of dielectric elastomer membranes,” *J Mech Phys Solids*, vol. 57, no. 8, pp. 1417–1435, Aug. 2009, doi: 10.1016/J.JMPS.2009.03.008.
- [117] J. W. Fox and N. C. Goulbourne, “On the dynamic electromechanical loading of dielectric elastomer membranes,” *J Mech Phys Solids*, vol. 56, no. 8, pp. 2669–2686, Aug. 2008, doi: 10.1016/J.JMPS.2008.03.007.
- [118] T. Hiruta, N. Hosoya, S. Maeda, and I. Kajiware, “Experimental validation of vibration control in membrane structures using dielectric elastomer actuators in a vacuum

- environment,” *Int J Mech Sci*, vol. 191, p. 106049, 2021, doi: 10.1016/j.ijmecsci.2020.106049.
- [119] S. Nalbach, G. Rizzello, and S. Seelecke, “Experimental Analysis of Continuous Vibrations in Dielectric Elastomer Membrane Actuators via Three-Dimensional Laser Vibrometry,” *Journal of Vibration and Acoustics, Transactions of the ASME*, vol. 141, no. 5, Oct. 2019, doi: 10.1115/1.4043715/725526.
- [120] Moretti G., Gratz-Kelly S., Fontana M., Motzki P., Rizzello G., and Seelecke S., “Audio-tactile transducer device based on dielectric electro-active elastomers,” 20230262396, 2023
- [121] N.-K. Persson, J. G. Martinez, Y. Zhong, A. Maziz, and E. W. H. Jager, “Actuating Textiles: Next Generation of Smart Textiles,” *Advanced Material Technologies*, 2018, doi: 10.1002/admt.201700397.
- [122] V. Sanchez *et al.*, “Textile Technology for Soft Robotic and Autonomous Garments,” *Adv Funct Mater*, vol. 31, no. 6, p. 2008278, Feb. 2021, doi: 10.1002/ADFM.202008278.
- [123] J. Shi *et al.*, “Smart Textile-Integrated Microelectronic Systems for Wearable Applications,” *Advanced Materials*, vol. 32, no. 5, p. 1901958, Feb. 2020, doi: 10.1002/ADMA.201901958.
- [124] T. Agcayazi *et al.*, “Fully-Textile Seam-Line Sensors for Facile Textile Integration and Tunable Multi-Modal Sensing of Pressure, Humidity, and Wetness,” 2020, doi: 10.1002/admt.202000155.
- [125] N. Münzenrieder *et al.*, “Textile integrated sensors and actuators for near-infrared spectroscopy,” *Optics Express, Vol. 21, Issue 3, pp. 3213–3224*, vol. 21, no. 3, pp. 3213–3224, Feb. 2013, doi: 10.1364/OE.21.003213.
- [126] W. Weng, P. eining Chen, S. He, X. uemei Sun, and H. Peng, “Smarte elektronische Textilien,” *Angewandte Chemie*, vol. 128, no. 21, pp. 6248–6277, May 2016, doi: 10.1002/ANGE.201507333.
- [127] D. De Rossi, F. Carpi, and F. Galantini, “Functional materials for wearable sensing, actuating and energy harvesting,” *Advances in Science and Technology*, vol. 57, pp. 247–256, 2008, doi: 10.4028/www.scientific.net/AST.57.247.
- [128] F. Carpi and D. De Rossi, “Electroactive polymer-based devices for e-textiles in biomedicine,” *IEEE Transactions on information Technology in biomedicine*, vol. 9, no. 3, 2005, doi: 10.1109/TITB.2005.854514.
- [129] G. Frediani *et al.*, “Wearable detection of trunk flexions: capacitive elastomeric sensors compared to inertial sensors,” *MDPI - sensors*, 2021, doi: 10.3390/s21165453.
- [130] D. De Rossi^o *et al.*, “electroactive fabrics and wearable biomonitoring devices,” *AUTEX Research Journal*, vol. 3, doi: 10.1515/aut-2003-030404.
- [131] C. R. Walker and I. A. Anderson, “Monitoring diver kinematics with dielectric elastomer sensors,” in *SPIE Smart Structures + Nondestructive Evaluation, Electroactive Polymer Actuators and Devices*, SPIE, 2017, pp. 11–21. doi: 10.1117/12.2260394.
- [132] B. O’Brien, T. Gisby, and I. Anderson, “Stretch sensors for human body motion,” in *SPIE Smart Structures + Nondestructive Evaluation, Electroactive Polymer Actuators and Devices*, Y. Bar-Cohen, Ed., 2014, p. 905618. doi: 10.1117/12.2046143.

- [133] D. Orbaugh, C. Walker, S. Rosset, and I. Anderson, “The challenges of hand gesture recognition using dielectric elastomer sensors,” in *SPIE Smart Structures + Nondestructive Evaluation, Electroactive Polymer Actuators and Devices*, SPIE, 2020, pp. 231–241. doi: 10.1117/12.2558388.
- [134] A. Atalay *et al.*, “Batch fabrication of customizable silicone-textile composite capacitive strain sensors for human motion tracking,” *Adv Mater Technol*, vol. 2, no. 9, p. 1700136, 2017, doi: 10.1002/ADMT.201700136.
- [135] N. Kumar Singh, K. Takashima, T. Shibata Nitin Kumar Singh, and T. Shibata, “Dielectric elastomer based stretchable textile sensor for capturing motion,” in *SPIE Smart Structures + Nondestructive Evaluation, Proceedings Volume 11375, Electroactive Polymer Actuators and Devices (EAPAD) XXII*, SPIE, 2020, pp. 301–308. doi: 10.1117/12.2565743.
- [136] D. Romero, O. Noran, J. Stahre, P. Bernus, and Å. Fast-Berglund, “Towards a human-centred reference architecture for next generation balanced automation systems: Human-automation symbiosis,” *IFIP Adv Inf Commun Technol*, vol. 460, pp. 556–566, 2015, doi: 10.1007/978-3-319-22759-7_64/FIGURES/1.
- [137] B. G. Mark, E. Rauch, and D. T. Matt, “Worker assistance systems in manufacturing: A review of the state of the art and future directions,” 2021. doi: 10.1016/j.jmsy.2021.02.017.
- [138] L. Rodriguez, F. Quint, D. Gorecky, D. Romero, and H. R. Siller, “Developing a Mixed Reality Assistance System Based on Projection Mapping Technology for Manual Operations at Assembly Workstations,” *Procedia Comput Sci*, vol. 75, pp. 327–333, Jan. 2015, doi: 10.1016/J.PROCS.2015.12.254.
- [139] T. du Plessis, K. Djouani, and C. Oosthuizen, “A Review of Active Hand Exoskeletons for Rehabilitation and Assistance,” *Robotics 2021, Vol. 10, Page 40*, vol. 10, no. 1, p. 40, Mar. 2021, doi: 10.3390/ROBOTICS10010040.
- [140] M. Pan *et al.*, “Soft Actuators and Robotic Devices for Rehabilitation and Assistance,” *Advanced Intelligent Systems*, vol. 4, no. 4, p. 2100140, Apr. 2022, doi: 10.1002/AISY.202100140.
- [141] S. Arlati, V. Colombo, G. Ferrigno, R. Sacchetti, and M. Sacco, “Virtual reality-based wheelchair simulators: A scoping review,” *Assistive Technology*, vol. 32, no. 6, pp. 294–305, Nov. 2020, doi: 10.1080/10400435.2018.1553079.
- [142] P. Soltani and A. H. P. Morice, “Augmented reality tools for sports education and training,” *Comput Educ*, vol. 155, p. 103923, Oct. 2020, doi: 10.1016/J.COMPEDU.2020.103923.
- [143] P. Slade, M. J. Kochenderfer, S. L. Delp, and S. H. Collins, “Personalizing exoskeleton assistance while walking in the real world,” *Nature* 2022 610:7931, vol. 610, no. 7931, pp. 277–282, Oct. 2022, doi: 10.1038/s41586-022-05191-1.
- [144] R. W. Nuckols, S. Lee, K. Swaminathan, D. Orzel, R. D. Howe, and C. J. Walsh, “Individualization of exosuit assistance based on measured muscle dynamics during versatile walking,” *Sci Robot*, vol. 6, no. 60, Nov. 2021, doi: 10.1126/SCIROBOTICS.ABJ1362/SUPPL_FILE/SCIROBOTICS.ABJ1362_MOVIE_S1.ZIP.

- [145] A. R. Reddy, G. S. P. Ghantasala, R. Patan, R. Manikandan, and S. Kallam, "Smart Assistance of Elderly Individuals in Emergency Situations at Home," *Internet of Things*, pp. 95–115, 2021, doi: 10.1007/978-3-030-63937-2_6/FIGURES/11.
- [146] F. G. Miskelly, "Assistive technology in elderly care," *Age Ageing*, vol. 30, no. 6, pp. 455–458, Nov. 2001, doi: 10.1093/AGEING/30.6.455.
- [147] J. Cannan and H. Hu, "Human-Machine Interaction (HMI): A Survey," 2012.
- [148] S. W. ; J. ; Kim *et al.*, "Recent Progress in Development and Applications of Ionic Polymer-Metal Composite," *MDPI, micromachines*, p. 13, 2022, doi: 10.3390/mi13081290.
- [149] H. Rahman, H. Werth, A. Goldman, Y. Hida, L. Lane, and P. L. Menezes, "Recent Progress on Electroactive Polymers: Synthesis, Properties and Applications," *MDPI, ceramics*, 2021, doi: 10.3390/ceramics4030038.
- [150] Yoseph. Bar-Cohen, "Electroactive polymer (EAP) actuators as artificial muscles : reality, potential, and challenges," p. 765, 2004.
- [151] R. Pelrine, J. Eckerle, and Seiki Chiba, "Review of artificial muscle approaches," *Third International Symposium on Micro Machine and Human Science, Nagoya, Japan*, 1992.
- [152] R. D. , P. R. E. , and J. J. Kornbluh, "Elastomeric dielectric artificial muscle actuators for small robots," *Proceedings of the Third IASTED International Conference on Robotics and Manufacturing (pp. 14-16)*, 1995.
- [153] R. Pelrine *et al.*, "Applications of dielectric elastomer actuators," *Smart Structures and Materials 2001: Electroactive Polymer Actuator and Devices*, vol. 4329, pp. 335–349, Jul. 2001, doi: 10.1117/12.432665.
- [154] D. J. Korteweg, "Ueber die Veränderung der Form und des Volumens dielectrischer Körper unter Einwirkung electrischer Kräfte," *Ann Phys*, vol. 245, no. 1, pp. 48–61, 1880, doi: 10.1002/ANDP.18792450103.
- [155] W. C. Röntgen, "Ueber die durch Electricität bewirkten Form- und Volumenänderungen von dielectrischen Körpern," *Ann Phys*, vol. 247, no. 13, pp. 771–786, Jan. 1880, doi: 10.1002/ANDP.18802471304.
- [156] axel ritter, *smart materials - in architecture, interior architecture and design*. Birkhäuser-Publishers for Architecture , 2007.
- [157] L. J. Romasanta, M. A. Lopez-Manchado, and R. Verdejo, "Increasing the performance of dielectric elastomer actuators: A review from the materials perspective," *Prog Polym Sci*, vol. 51, pp. 188–211, Mar. 2015, doi: 10.1016/J.PROGPOLYM-SCI.2015.08.002.
- [158] R. Shankar, T. K. Ghosh, and R. J. Spontak, "Dielectric elastomers as next-generation polymeric actuators," *Soft Matter*, vol. 3, no. 9, pp. 1116–1129, Aug. 2007, doi: 10.1039/B705737G.
- [159] D. Xu, A. Tairych, and I. a. Anderson, "Localised strain sensing of dielectric elastomers in a stretchable soft-touch musical keyboard," *SPIE Smart Structures + Nondestructive Evaluation, Electroactive Polymer Actuators and Devices*, vol. 9430, p. 943025, 2015, doi: 10.1117/12.2084770.

- [160] D. Xu, S. Michel, T. McKay, B. O'Brien, T. Gisby, and I. Anderson, "Sensing frequency design for capacitance feedback of dielectric elastomers," *Sens Actuators A Phys*, 2015, doi: 10.1016/j.sna.2015.05.010.
- [161] P. Lotz, "Dielektrische Elastomerstapelaktoren für ein peristaltisches Fluidfördersystem," Dissertation, Technische Universität Darmstadt, 2009. Accessed: Dec. 19, 2022. [Online]. Available: <http://tuprints.ulb.tu-darmstadt.de/2005/>
- [162] F. B. Albuquerque and H. Shea, "Influence of humidity, temperature and prestretch on the dielectric breakdown strength of silicone elastomer membranes for DEAs," *Smart Mater Struct*, vol. 29, no. 10, Oct. 2020, doi: 10.1088/1361-665X/ABA5E3.
- [163] A. Tröls *et al.*, "Stretch dependence of the electrical breakdown strength and dielectric constant of dielectric elastomers," *Smart Mater. Struct*, vol. 22, pp. 104012–104017, 2013, doi: 10.1088/0964-1726/22/10/104012.
- [164] A. J. Nolte, N. D. Treat, R. E. Cohen, and M. F. Rubner, "Effect of relative humidity on the Young's modulus of polyelectrolyte multilayer films and related nonionic polymers," *Macromolecules*, vol. 41, no. 15, pp. 5793–5798, Aug. 2008, doi: 10.1021/MA800732J/SUPPL_FILE/MA800732J-FILE001.PDF.
- [165] C. Johansson and M. Robertsson, "Broadband Dielectric Characterization of a Silicone Elastomer", doi: 10.1007/s11664-007-0124-6.
- [166] D. Koblar, M. Boltě Zar, and C. M. Boltě Zar, "Evaluation of the Frequency-Dependent Young's Modulus and Damping Factor of Rubber from Experiment and Their Implementation in a Finite-Element Analysis," 2013.
- [167] N. Hosoya, H. Masuda, and S. Maeda, "Balloon dielectric elastomer actuator speaker," 2018, doi: 10.1016/j.apacoust.2018.12.032.
- [168] E. Garnell, O. Doaré, C. Rouby, and O. Doar, "Coupled vibro-acoustic modeling of a dielectric elastomer loudspeaker," *J Acoust Soc Am*, vol. 147, no. 3, pp. 1812–1821, Mar. 2020, doi: 10.1121/10.0000930.
- [169] M. Kleiner, *acoustics and audio technology*, 3th ed. J. Ross Publishing, 2012.
- [170] L. F. , Kinsler, A. R. Frey, Coppens Alan B., and J. V. Sanders, *Fundamentals of Acoustics*, 4th ed. John Wiley & Sons, Inc., 2000.
- [171] Everest F. Alton and Pohlmann Ken C., *Master Handbook of Acoustics*, 5th ed. MC Graw Hill, 2009.
- [172] Asmar H. Nakhlé, *Partial Differential Equations and Boundary Value Problems with Fourier Series (2nd Edition) | Enhanced Reader*, 2nd ed. Pearson, 2000.
- [173] G. Moretti, G. Rizzello, M. Fontana, and S. Seelecke, "Finite element modelling of the vibro-acoustic response in dielectric elastomer membranes," in *SPIE Smart Structure + Nondestructive Evaluation, Electroactive Polymer Actuators and Devices (EAPAD) XXIV*, SPIE, Apr. 2022, pp. 102–112. doi: 10.1117/12.2612784.
- [174] G. Moretti and G. Rizzello, "Model-based parameter analysis of dielectric elastomer loudspeakers," *IEEE/ASME International Conference on Advanced Intelligent Mechatronics, AIM*, vol. 2022-July, pp. 1129–1135, 2022, doi: 10.1109/AIM52237.2022.9863404.

- [175] G. Moretti and G. Rizzello, “A linear parameter-varying modelling approach for dielectric elastomer loudspeakers,” *IFAC-PapersOnLine*, vol. 55, no. 20, pp. 534–539, Jan. 2022, doi: 10.1016/J.IFACOL.2022.09.150.
- [176] R. Vertechy, G. Pietro Papini Rosati, and M. Fontana, “Reduced model and application of inflating circular diaphragm dielectric elastomer generators for wave energy harvesting,” *J Vib Acoust*, vol. 137, no. 1, 2015, doi: 10.1115/1.4028508.
- [177] M. Mooney, “A Theory of Large Elastic Deformation,” *J. Appl. Phys*, vol. 11, pp. 582–592, 1940, doi: 10.1063/1.1712836.
- [178] R. S. Rivlin, “Large elastic deformations of isotropic materials IV. further developments of the general theory,” *Philosophical Transactions of the royal society A - mathematical, physical an engineering sciencesd*, vol. 241, no. 835, 1948, doi: 10.1098/rsta.1948.0024.
- [179] G. Moretti, S. Rosset, R. Vertechy, I. Anderson, and M. Fontana, “A Review of Dielectric Elastomer Generator Systems,” *Advanced Intelligent Systems*, vol. 2, no. 10, p. 2000125, Oct. 2020, doi: 10.1002/AISY.202000125.
- [180] R. D. Kornbluh *et al.*, “From boots to buoys: Promises and challenges of dielectric elastomer energy harvesting,” *Electroactivity in Polymeric Materials*, vol. 9781461408789, pp. 67–93, Nov. 2012, doi: 10.1007/978-1-4614-0878-9_3/COVER.
- [181] L. Dorfmann and R. W. Ogden, “Nonlinear theory of electroelastic and magnetoelastic interactions,” *Nonlinear Theory of Electroelastic and Magnetoelastic Interactions*, vol. 9781461495963, pp. 1–313, Nov. 2014, doi: 10.1007/978-1-4614-9596-3/COVER.
- [182] C. Lagomarsini, C. Jean-Mistral, G. Lombardi, and A. Sylvestre, “Hybrid piezoelectric–electrostatic generators for wearable energy harvesting applications,” *Smart Mater Struct*, vol. 28, no. 3, p. 035003, Feb. 2019, doi: 10.1088/1361-665X/AAF34E.
- [183] C. Zhang *et al.*, “Research on spraying process of flexible electrode for dielectric elastomer sensors,” *Journal of Materials Science: Materials in Electronics*, vol. 33, no. 24, pp. 19307–19319, Aug. 2022, doi: 10.1007/S10854-022-08769-7/TABLES/1.
- [184] S. Rosset, O. A. Ararom, S. Schlatter, and H. R. Shea, “Fabrication process of silicone-based dielectric elastomer actuators,” *Journal of Visualized Experiments*, vol. 2016, no. 108, Feb. 2016, doi: 10.3791/53423.
- [185] D. McCoul, S. Rosset, S. Schlatter, and H. Shea, “Inkjet 3D printing of UV and thermal cure silicone elastomers for dielectric elastomer actuators,” *Smart Mater Struct*, vol. 26, no. 12, p. 125022, Nov. 2017, doi: 10.1088/1361-665X/AA9695.
- [186] B. Fasolt, T. Willian, A. Weller, D. Bruch, S. S. Seelecke, and P. Motzki, “Yield increase of DE actuators using novel repair process,” in <https://doi.org/10.1117/12.3010741>, SPIE, May 2024, pp. 97–106. doi: 10.1117/12.3010741.
- [187] E. N. Marieb and K. N. Hoehn, *Human Anatomy & Psysiology*, 12th ed. Pearson Education Limited, 2019.
- [188] N. A. Campbell *et al.*, *Biology*. Pearson Education, Inc., 2017.
- [189] J. G. Betts *et al.*, *Anatomy & Physiology*. OpenStax, Rice University, 2013.
- [190] “haptic,” Merriam-Webster’s Collegiate Dictionary, vol. 11th. 2023.

- [191] “tactile,” Merriam-Webster’s Collegiate Dictionary. 2023.
- [192] Braun Daniel, “Ein System zur Analyse haptischer Eigenschaften von Benutzerschnittstellen,” Dissertation, Karlsruher Institut für Technologie (KIT), 2012.
- [193] M. Grunwald, *Human Haptic Perception: Basics and Applications*. 2008.
- [194] E. B. Goldstein, C. Ryan, and J. Baro, *Sensation and Perception*. 2010.
- [195] E. Kandel, J. D. Koester, S. H. Mack, and S. A. Siegelbaum, “Principles of Neural Science,” 2021.
- [196] S. Standring, *Gray’s Anatomy: The Anatomical Basis of Clinical Practice.*, 42th ed. Elsevier, 2020.
- [197] J. C. Tuthill and E. Azim, “Proprioception,” *Current Biology*, vol. 28, no. 5, pp. R194–R203, Mar. 2018, doi: 10.1016/J.CUB.2018.01.064.
- [198] C. Hatzfeld and R. Werthschützky, “Vibrotactile force perception thresholds at the fingertip,” *Lecture Notes in Computer Science (including subseries Lecture Notes in Artificial Intelligence and Lecture Notes in Bioinformatics)*, vol. 6191 LNCS, no. PART 1, pp. 99–104, 2010, doi: 10.1007/978-3-642-14064-8_15/COVER.
- [199] A. Israr, S. Choi, and H. Z. Tan, “Mechanical impedance of the hand holding a spherical tool at threshold and suprathreshold stimulation levels,” *Proceedings - Second Joint EuroHaptics Conference and Symposium on Haptic Interfaces for Virtual Environment and Teleoperator Systems, World Haptics 2007*, pp. 56–60, 2007, doi: 10.1109/WHC.2007.81.
- [200] G. T. Fechner, *Elements of psychophysics*, vol. 1. Holt, Rinehart and Winston, Inc., 1966.
- [201] C. Becker-Carus and M. Wendt, *Allgemeine Psychologie*. Springer Berlin Heidelberg, 2017. doi: 10.1007/978-3-662-53006-1.
- [202] R. Lundström, “Local vibrations-Mechanical impedance of the human hand’s glabrous skin,” *J Biomech*, vol. 17, no. 2, 1984, doi: 10.1016/0021-9290(84)90131-3.
- [203] C. Hatzfeld, S. Cao, M. Kupnik, and R. Werthschutzky, “Vibrotactile Force Perception - Absolute and Differential Thresholds and External Influences,” *IEEE Trans Haptics*, vol. 9, no. 4, pp. 586–597, Oct. 2016, doi: 10.1109/TOH.2016.2571694.
- [204] R. T. Verrillo, “Comparison of vibrotactile threshold and suprathreshold responses in men and women,” *Perception & Psychophysics 1979 26:1*, vol. 26, no. 1, pp. 20–24, Jan. 1979, doi: 10.3758/BF03199857.
- [205] R. F. Schmidt, “Somato-viscerale Sensibilität: Hautsinne, Tiefensensibilität, Schmerz,” *Physiologie des Menschen*, pp. 206–225, 1977, doi: 10.1007/978-3-662-00222-3_11.
- [206] M. Steinhausen, *Lehrbuch der Animalischen Physiologie : Nach dem Gegenstandskatalog*. Springer-Verlag Berlin Heidelberg, 2013.
- [207] Dipl-Ing Thorsten Alexander Kern, “Haptisches Assistenzsystem für diagnostische und therapeutische Katheterisierungen ‘Mit dem Blindenstock durch Adern tasten!’,” Dissertation, Technische Universität Darmstadt, 2006.

- [208] L. Chittka and A. Brockmann, “Perception Space—The Final Frontier,” *PLoS Biol.*, vol. 3, no. 4, p. e137, Apr. 2005, doi: 10.1371/JOURNAL.PBIO.0030137.
- [209] M. Long, “Human Perception and Reaction to Sound,” *Architectural Acoustics*, pp. 81–127, 2014, doi: 10.1016/B978-0-12-398258-2.00003-9.
- [210] K. Forinash and W. Christian, *Sound: An Interactive Book*. 2022.
- [211] F. Pedrielli, E. Carletti, and C. Casazza, “Just noticeable differences of loudness and sharpness for earth moving machines”.
- [212] D. H. Klatt, “Discrimination of fundamental frequency contours in synthetic speech: Implications for models of pitch perception,” *Journal of the Acoustical Society of America*, vol. 53, no. 1, pp. 8–16, 1973, doi: 10.1121/1.1913333.
- [213] John. Backus, *The acoustical foundations of music*. W.W. Norton, 1969.
- [214] J. Roederer and J. Josephs, “Introduction to Physics and Psychophysics of Music,” *Am J Phys*, vol. 42, no. 8, p. 709, Jul. 2005, doi: 10.1119/1.1987821.
- [215] S. Gratz-Kelly, D. Philippi, B. Fasolt, S. Nalbach, and P. Motzki, “Gesture and force sensing based on dielectric elastomers for intelligent gloves in the digital production,” *tm - Technisches Messen - special Issue in Sensors in fiber-plastic composites*, vol. 91, no. 3–4, pp. 195–207, Mar. 2024, doi: 10.1515/TEME-2024-0003.
- [216] S. Gratz-Kelly, T. F. Krüger, G. Rizzello, S. Seelecke, and G. Moretti, “An audio-tactile interface based on dielectric elastomer actuators,” *Smart Mater Struct*, vol. 32, no. 3, p. 034005, 2023, doi: 10.1088/1361-665X/ACB6DA.
- [217] S. Minocha, D. Stone, C. Jarrett, and M. Woodroffe, *User Interface Design and Evaluation*, 1st ed. Elsevier Science & Technology, 2005.
- [218] T. A. Chowdhury, S. Gratz-Kelly, E. Wagner, P. Motzki, and M. Lehser, “Ensemble Learning Approach for Advanced Predictive Modelling of Biometric Data and Action States with Smart Sensing,” *IEEE Access*, 2024, doi: 10.1109/ACCESS.2024.3466528.
- [219] S. Gratz-Kelly, A. Meyer, P. Motzki, S. Nalbach, G. Rizzello, and S. S. Seelecke, “Force measurement based on dielectric elastomers for an intelligent glove providing worker assessment in the digital production,” in *SPIE Smart Structures + Nondestructive Evaluation, Electroactive Polymer Actuators and Devices*, SPIE, 2020, pp. 242–251. doi: 10.1117/12.2558442.
- [220] T. A. Chowdhury, S. Gratz-Kelly, G. Moretti, E. Wagner, P. Motzki, and M. Lehser, “A novel fusion method for intense heat detection and localization solely based on surface temperature with multimode DEA feedback,” in *SPIE Smart Structures + Nondestructive Evaluation*, SPIE, May 2024, pp. 14–23. doi: 10.1117/12.3009859.
- [221] S. Gratz-Kelly *et al.*, “An Integrated Audio-Tactile Interface Based on Dielectric Elastomer Actuators for User Interaction,” in *ASME 2023 Conference on Smart Materials, Adaptive Structures and Intelligent Systems*, American Society of Mechanical Engineers, Sep. 2023. doi: 10.1115/SMASIS2023-111228.
- [222] G. Berselli, R. Vertechy, G. Vassura, and V. Parenti-Castelli, “Optimal synthesis of conically shaped dielectric elastomer linear actuators: Design methodology and experimental validation,” *IEEE/ASME Transactions on Mechatronics*, vol. 16, no. 1, pp. 67–79, Feb. 2011, doi: 10.1109/TMECH.2010.2090664.

- [223] G. Rizzello, M. Hodgins, D. Naso, A. York, and S. Seelecke, "Modeling of the effects of the electrical dynamics on the electromechanical response of a DEAP circular actuator with a mass–spring load," *Smart Mater Struct*, vol. 24, no. 9, p. 094003, Aug. 2015, doi: 10.1088/0964-1726/24/9/094003.
- [224] Z. Suo, "Theory of dielectric elastomers," *Acta Mechanica Solida Sinica*, vol. 23, no. 6, pp. 549–578, Dec. 2010, doi: 10.1016/S0894-9166(11)60004-9.
- [225] S. Gratz-Kelly, G. Rizzello, M. Fontana, S. Seelecke, and G. Moretti, "A multi-mode, multi-frequency dielectric elastomer actuator," *Adv Funct Mater*, vol. 32, no. 34, 2022, doi: 10.1002/adfm.202201889.
- [226] M. Hodgins, A. York, and S. Seelecke, "Experimental comparison of bias elements for out-of-plane DEAP actuator system," *Smart Mater Struct*, vol. 22, no. 9, p. 094016, Aug. 2013, doi: 10.1088/0964-1726/22/9/094016.
- [227] M. Jabareen and M. Eisenberger, "Free Vibrations of non-homogeneous circular and annular Membranes," *J Sound Vib*, no. 3, pp. 409–429, 2001, doi: 10.1006/jsvi.2000.3249.
- [228] G. Moretti, G. Rizzello, M. Fontana, and S. Seelecke, "High-frequency voltage-driven vibrations in dielectric elastomer membranes," *Mech Syst Signal Process*, vol. 168, p. 108677, Apr. 2022, doi: 10.1016/J.YMSSP.2021.108677.
- [229] E. Garnell, C. Rouby, and O. Doare, "Resistivity-induced coupling between voltage distribution and vibrations in dielectric elastomers," *Smart Mater Struct*, vol. 30, no. 2, p. 025031, Jan. 2021, doi: 10.1088/1361-665X/ABD58F.
- [230] O. Fritzen, "Sensorische Applikationen von dielektrischen Elastomeren," Bachelorthesis, Hochschule für Technik und Wirtschaft, Saarbrücken, 2020.
- [231] D. J. Philippi, "Miniaturisierte und flexible Mess-, Auswerte-und Kommunikations-elektronik für intelligente Handschuhe auf Basis dielektrischer Elastomere," Bachelorthesis, intelligent material systems lab (iMSL), Saarbrücken, 2022.
- [232] C. Perri, S. Lenz, G. Rizzello, S. Seelecke, and D. Naso, "Modeling and Validation of a High Voltage Driving Circuit for Dielectric Elastomer Actuators," in *IEEE International Symposium on Industrial Electronics*, Institute of Electrical and Electronics Engineers Inc., Jun. 2021. doi: 10.1109/ISIE45552.2021.9576391.
- [233] S. Pourazadi, A. Shagerdmootaab, Chan H, Moallem M, and Menon C, "On the electrical safety of dielectric elastomer actuators in proximity to the human body," *Smart Mater Struct*, vol. 26, no. 11, 2017, doi: 10.1088/1361-665X/aa89b1.
- [234] T. A. Gisby, B. M. O'Brien, and I. A. Anderson, "Self sensing feedback for dielectric elastomer actuators," *Appl Phys Lett*, vol. 102, no. 19, May 2013, doi: 10.1063/1.4805352.
- [235] G. Rizzello, F. Fugaro, D. Naso, and S. Seelecke, "Simultaneous Self-Sensing of Displacement and Force for Soft Dielectric Elastomer Actuators," *IEEE Robot Autom Lett*, vol. 3, no. 2, pp. 1230–1236, Apr. 2018, doi: 10.1109/LRA.2018.2795016.
- [236] D. A. Mahns, N. M. Perkins, V. Sahai, L. Robinson, and M. J. Rowe, "Vibrotactile frequency discrimination in human hairy skin," *J Neurophysiol*, vol. 95, pp. 1442–1450, 2006, doi: 10.1152/jn.00483.2005.

- [237] Q. Van Duong, V. Phu Nguyen, A. Tuan Luu, and S. Tae Choi, "Audio-tactile Skinny Buttons for touch User interfaces", doi: 10.1038/s41598-019-49640-w.
- [238] H. Phung, P. T. Hoang, H. Jung, T. D. Nguyen, C. T. Nguyen, and H. R. Choi, "Haptic Display Responsive to Touch Driven by Soft Actuator and Soft Sensor," *IEEE/ASME Transactions on Mechatronics*, vol. 26, no. 5, pp. 2495–2505, Oct. 2021, doi: 10.1109/TMECH.2020.3041225.
- [239] L. Turchet, R. Nordahl, S. Serafin, A. Berrezag, S. Dimitrov, and V. Hayward, "Audio-haptic physically-based simulation of walking on different grounds," *2010 IEEE International Workshop on Multimedia Signal Processing, MMSP2010*, pp. 269–273, Oct. 2010, doi: 10.1109/MMSP.2010.5662031.
- [240] H. Phung, T. Hoang, H. Jung, T. Dat Nguyen, T. Nguyen, and H. R. Choi, "Haptic Display Responsive to Touch Driven by Soft Actuator and Soft Sensor," vol. 26, no. 5, 2021, doi: 10.1109/TMECH.2020.3041225.
- [241] A. Faeth and C. Harding, "Emergent effects in multimodal feedback from virtual buttons," *ACM Trans. Comput.-Hum. Interact.*, vol. 21, no. 3, 2014, doi: 10.1145/2535923.
- [242] T. Mirfakhrai, J. D. W. Madden, and R. H. Baughman, "Polymer artificial muscles," 2007.
- [243] C. Cao, X. Gao, and A. T. Conn, "A Magnetically Coupled Dielectric Elastomer Pump for Soft Robotics," *Adv Mater Technol*, vol. 4, no. 8, Aug. 2019, doi: 10.1002/ADMT.201900128.
- [244] R. Heydt, R. Pelrine, J. Joseph, J. Eckerle, and R. Kornbluh, "Acoustical performance of an electrostrictive polymer film loudspeaker," *J Acoust Soc Am*, vol. 107, no. 2, pp. 833–839, Feb. 2000, doi: 10.1121/1.428266.
- [245] M. E. Altinsoy, "Perceptual features of everyday push button sounds and audiotactile interaction", doi: 10.1250/ast.41.173.
- [246] D. Zanotto, L. Turchet, E. M. Boggs, and S. K. Agrawal, "SoleSound: Towards a novel portable system for audio-tactile underfoot feedback," *5th IEEE RAS/EMBS International Conference on Biomedical Robotics and Biomechatronics*, 2014.
- [247] D. N. Zotkin, R. Duraiswami, and L. S. Davis, "Rendering localized spatial audio in a virtual auditory space," *IEEE Trans Multimedia*, vol. 6, no. 4, pp. 553–564, Aug. 2004, doi: 10.1109/TMM.2004.827516.
- [248] G. Moretti, G. Rizzello, M. Fontana, and S. Seelecke, "A multi-domain dynamical model for cone-shaped dielectric elastomer loudspeakers," <https://doi.org/10.1117/12.2581718>, vol. 11587, pp. 226–239, Mar. 2021, doi: 10.1117/12.2581718.
- [249] S. Addario, S. Gratz-Kelly, D. Naso, G. Rizzello, and G. Moretti, "An experimental parametric analysis of the acoustic response in dielectric elastomer loudspeakers," *Journal of Vibration and Control*, Aug. 2024, doi: 10.1177/10775463241273022.
- [250] G. Rizzello, P. Loew, L. Agostini, M. Fontana, and S. Seelecke, "A lumped parameter model for strip-shaped dielectric elastomer membrane transducers with arbitrary aspect ratio," *Smart Mater Struct*, vol. 29, no. 11, p. 115030, Oct. 2020, doi: 10.1088/1361-665X/ABB09E.

- [251] S. Hau, A. York, and S. Seelecke, "Performance prediction of circular dielectric electro-active polymers membrane actuators with various geometries," *SPIE Smart Structures and Materials + Nondestructive Evaluation and Health Monitoring*, vol. 9430, pp. 76–83, Apr. 2015, doi: 10.1117/12.2082871.
- [252] S. Hau, A. York, G. Rizzello, and S. Seelecke, "Performance Prediction and Scaling Laws of Circular Dielectric Elastomer Membrane Actuators," *Journal of Mechanical Design*, vol. 140, no. 11, Nov. 2018, doi: 10.1115/1.4039104.
- [253] J. Hubertus *et al.*, "Laser Structuring of Thin Metal Films of Compliant Electrodes on Dielectric Elastomers," *Adv Funct Mater*, vol. 33, no. 16, 2023, doi: 10.1002/adfm.202214176.
- [254] J. Hubertus, S. Croce, J. Neu, G. Rizzello, S. Seelecke, and G. Schultes, "Influence of residual stresses of sputtered thin film electrodes for dielectric elastomer applications," in *1st International Electronic Conference on Actuator Technology: Materials, Devices and Applications*, MDPI, 2020.
- [255] H. H. King, R. Donlin, and B. Hannaford, "Perceptual thresholds for single vs. Multi-Finger Haptic interaction," *2010 IEEE Haptics Symposium*, 2010.
- [256] M. E. Altinsoy and S. Merchel, "Audiotactile feedback design for touch screens," in *Lecture Notes in Computer Science*, Springer, Berlin, Heidelberg, 2009, pp. 136–144. doi: 10.1007/978-3-642-04076-4_15.
- [257] M. E. Altinsoy, "Perceptual aspects of auditory-tactile asynchrony," in *Tenth International Congress on sound and vibration*, 2003, pp. 3831–3838.
- [258] M. Im Schloss and C. Kuehn, "Feel the Music! Exploring the Cross-modal Correspondence between Music and Haptic Perceptions of Softness," *Journal of Retailing*, vol. 95, no. 4, pp. 158–169, Dec. 2019, doi: 10.1016/J.JRETAI.2019.10.004.
- [259] K. Collins and B. Kapralos, "Pseudo-haptics: leveraging cross-modal perception in virtual environments," *The Senses and Society*, vol. 14, no. 3, pp. 313–329, Sep. 2019, doi: 10.1080/17458927.2019.1619318.
- [260] I. de Villiers Bosman, K. de Beer, and T. J. Bothma, "Creating pseudo-tactile feedback in virtual reality using shared crossmodal properties of audio and tactile feedback Article history," *SACJ*, vol. 33, no. 1, 2021, doi: 10.18489/sacj.v33i1.883.
- [261] S. Gratz-Kelly, T. F. Krüger, S. Seelecke, G. Rizzello, and G. Moretti, "A tri-modal dielectric elastomer actuator integrating linear actuation, sound generation, and self-sensing capabilities," *Sens Actuators A Phys*, p. 115332, Apr. 2024, doi: 10.1016/J.SNA.2024.115332.
- [262] G. Rizzello, D. Naso, A. York, and S. Seelecke, "A Self-Sensing Approach for Dielectric Elastomer Actuators Based on Online Estimation Algorithms," *IEEE/ASME Transactions on Mechatronics*, vol. 22, no. 2, pp. 728–738, Apr. 2017, doi: 10.1109/TMECH.2016.2638638.
- [263] G. Rizzello, M. Hodgins, S. Seelecke, and D. Naso, "Self-sensing at low sampling-to-signal frequency ratio: An improved algorithm for dielectric elastomer actuators," *MESA 2016 - 12th IEEE/ASME International Conference on Mechatronic and*

- Embedded Systems and Applications - Conference Proceedings*, Oct. 2016, doi: 10.1109/MESA.2016.7587146.
- [264] J. Stoer, *Numerische Mathematik I*, 9th ed. in Springer-Lehrbuch. Berlin, Heidelberg: Springer Berlin Heidelberg, 2005. doi: 10.1007/B138027.
 - [265] A. V Oppenheim and R. W. Schaffer, *Discrete-time signal processing*. 2010. [Online]. Available: www.pearsonhighered.com
 - [266] K. J. (Karl J. Åström and B. Wittenmark, *Computer-controlled systems : theory and design*. Prentice Hall, 1990.
 - [267] J. Cohen, “Statistical Power Analysis for the Behavioral Sciences,” *Statistical Power Analysis for the Behavioral Sciences*, May 2013, doi: 10.4324/9780203771587.
 - [268] J. Cohen, *Statistical Power Analysis for the Behavioral Sciences | Enhanced Reader*, Second edition. 1988.
 - [269] United Nations and Department of Economic and Social Affairs Population Division, “World Population Prospects 2019 Highlights.”
 - [270] United Nations and Department of Economic Social and Affairs Population Division, “World Population Prospects 2022 Summary of Results.”
 - [271] World Health Organization, “Global report on health equity for persons with disabilities,” 2022.
 - [272] S. Nalbach, “Intelligente Antriebssysteme für dynamische Anwendungen auf Basis dielektrischer Elastomere,” *iMSL - intelligent material systems lab*, 2022. doi: 10.22028/D291-39887.
 - [273] M. Schmidt, A. Schütze, and S. Seelecke, “Scientific test setup for investigation of shape memory alloy based elastocaloric cooling processes,” *International Journal of Refrigeration*, vol. 54, pp. 88–97, Jun. 2015, doi: 10.1016/J.IJREFRIG.2015.03.001.
 - [274] “european regional development fund (ERDF),” *Verteilte Produktion für die saarländische Automobilindustrie: Nachhaltig, Vernetzt, Resilient (VproSaar)*.
 - [275] “european regional development fund (ERDF),” *innovative Aktorik und Sensorik für die Produktion von Smarten Materialsystemen (iAS-SMat)*.
 - [276] D. Bruch, S. Hau, P. Loew, G. Rizzello, and S. Seelecke, “Fast model-based design of large stroke dielectric elastomer membrane actuators biased with pre-stressed buckled beams,” in *SPIE Smart Structures and Materials + Nondestructive Evaluation and Health Monitoring*, Denver: SPIE, Mar. 2018, pp. 62–69. doi: 10.1117/12.2296558.
 - [277] S. Hau, D. Bruch, G. Rizzello, P. Motzki, and S. Seelecke, “Silicone based dielectric elastomer strip actuators coupled with nonlinear biasing elements for large actuation strains,” *Smart Mater Struct*, vol. 27, no. 7, p. 074003, Jun. 2018, doi: 10.1088/1361-665X/AAB7D8.
 - [278] M. Hodgins and S. Seelecke, “Mechanical behavior of a bi-stable negative-rate bias spring system,” <https://doi.org/10.1117/12.852373>, vol. 7644, pp. 550–561, Mar. 2010, doi: 10.1117/12.852373.
 - [279] M. Hodgins, A. York, and S. Seelecke, “Experimental Investigation of a Loaded Circular Dielectric Electro-Active Polymer Actuator Coupled to Negative-Rate Bias Spring Mechanism,” *ASME 2012 Conference on Smart Materials, Adaptive*

Structures and Intelligent Systems, SMASIS 2012, vol. 2, pp. 259–264, Jul. 2013, doi: 10.1115/SMASIS2012-8202.

- [280] N. Quaegebeur, A. Chaigne, and G. Lemarquand, “Transient modal radiation of axisymmetric sources: application to loudspeakers,” vol. 71, no. 4, 2010, Accessed: Apr. 21, 2024. [Online]. Available: <https://hal.science/hal-00540287>

List of Appendices

A.1. STATE OF THE ART - EXEMPLATIVE SMART GLOVES	CLXV
A.2. CAPACITANCE MEASUREMENT PRINCIPLES.....	CLXVI
A.3. DE ACTUATOR DESIGN.....	CLXVI
A.4. MODEL OF THE DEA DYNAMIC RESPONSE	CLXVIII
A.5. EFFECT OF THE DEA HOUSING ON THE FREQUENCY RESPONSE	CLXXIII
A.6. DEFINITION OF THE WORKING MODES	CLXXVI
A.7. ADDITIONAL EXPERIMENTAL RESULTS OF THE MULTI-MODE MULTI FREQUENCY DEA	CLXXVII
A.8. CLASSIFICATION OF THE USER TESTS	CLXXVIII
A.9. GEOMETRIC MODEL FOR THE COP-DEA CAPACITANCE	CLXXXI

Appendix

A.1.State of the Art - Exemplative smart gloves

Table A 1: glove realisation state of the art. Subdivided into exoskeleton, gloves with feedback, sensory gloves camera-based systems, industrial applications and scientific research.

	Produkt		Produktart	Aktorprinzip	Sensorprinzip	vorgesehener Einsatzbereich	Sensoren														Produktstatus		
	Firma / Einrichtung	Name					Handpositionstracking	Fingertracking	aktive Injektion	passive Injektion (Pro Hand)	Forcefeedback	Gravitationsrückmeldung	aktive Freiheitsgrade	Drehmoment (Nm)	Winkel	visuelle Rückmeldung	akustische Rückmeldung	taktile Rückmeldung	Vibration	Gewicht (g)		Preis (€)	
Exoskelett	Haption	Hglove	Exoskelett mit Manipulator	konv. Motor	Rotationsensoren	Robotik, Automobilindustrie	x	x	3	9	x	0	3 (6)	0,13	0	0	0	0	750	30.000 €	Einzelanfertigung		
	Exiii	EXOS Wrist EXOS Gripper	Exoskelett	konventioneller Motor	Rotationsensoren	Gaming, Fertigung	x	0	0	2	x	0	2	-	0	+	0	0	0	-	-	in Entwicklung, verfügbar für Firmenkunden	
	BMFB Projekt	PowerGrasp	Soft Exoskelett (mit Arm)	Pneumatisch	IMU, EMG, Drucksensoren	Industrie, Montage	x	x	5	-	0	x	3	-	0	0	0	x	0	-	-	Projektabschluss 12/2018	
	Dexta Robotics	Dexmo	Exoskelett	konv. Motor	Rotationsensoren	Medizin, Ausbildung, Gaming	+	x	5	11 (+6)	x	0	5	0,3	x	+	0	0	0	320	179 \$	Entwicklerkit verfügbar	
	HaptX	HaptX Glove	Exoskelett	mikrofluidisch	Magnetisch	Fertigung, CAD, Entertainment	+	x	5	10 (+6)	x	0	5	0,5	0	+	0	x	0	-	-	release 2018, erste Prototypen	
	Harvard University	Soft robotic glove	roft robotic Exoskelett	mikrofluidisch	elektromagnetisch	Medizin	0	+	5	-	x	x	5	-	0	0	0	0	0	< 500	-	in Entwicklung	
	neofect	NeoMano	Exoskelett, Schnursystem	konv. Motor	-	Medizin	0	0	3	0	x	x	3	-	0	0	0	0	0	-	-	release 2018, erste Prototypen	
	-	Sense Glove	Exoskelett	konv. Motor, Vibrationsmotor	Rotationsensoren	Medizin, Ausbildung, Robotik	+	x	5	20 (+6)	x	0	5	0,7	+	+	0	x	x	300	1.699 €	Vorbestellung möglich	
	-	Sense Glove Nova	Schnursystem	Schnur, Vibrationsmotor	Schnur, optisch	Industrie, Ausbildung	+	x	5	20 (+6)	x	0	5	~1	x	+	0	x	x	-	-	Vorbestellung möglich	
	-	VR gluv	Exoskelett	konv. Motor, Seile	Dehnungssensoren	Gaming, Entertainment	+	x	5	12	x	0	5	0,5	x	+	0	0	0	< 450	597 \$	-	
	YISHENG	C10	Soft Exoskelett	Pneumatisch	-	Schlaganfall Behandlung	-	0	0	0	0	0	x	5	-	0	+	0	0	0	-	-	Kaufbereit
	Xiamen weiyu	stroke recovery glove	Soft Exoskelett	Pneumatisch	-	Schlaganfall Behandlung	-	0	0	5	0	0	x	5	-	0	+	0	0	0	-	-	Kaufbereit
	-	Nuada	Exoskelett, Handschuh	künstliche Sehnen, konv. Motor	IMU, Drucksensor	Medizin, Fertigung, altersunterstützung	x	x	5	-	0	0	5	-	x	0	0	0	0	-	750 \$ 1500 \$	erster Prototyp	
	Cyber Glove Systems	Cyber Glove I,II,III Cyber Grasp	Handschuh Exoskelett	- konv. Motor	Dehnungssensoren -	Fertigung, CAD Fertigung, CAD	+	x	5	18-22	0	0	0	0	x	+	0	0	0	-	-	Kaufbereit	
Handschuh mit Feedback	Contact CI	Maestro	Drahthandschuh	konv. Motor	5 Dehnungssensoren 8 künstliche Sehnen	Fertigung, Ausbildung	+	x	5	13 (+6)	x	0	5	-	x	+	0	x	x	590	-	in Entwicklung	
	cynteract	VR Glove	Drahthandschuh	konv. Motor	künstliche Sehnen, IMU	Medizin, Industrie, Gaming	x	x	5	16	x	0	5	-	0	+	0	0	0	-	-	erste Prototypen, Vorstellung bei Ausstellungen	
	TU Dresden - IS Softwaretechnologie	WEIR	Handschuh + Jacke	Vibrationsmotoren	IMU	Robotik	x	x	2	-	0	0	0	0	x	+	0	x	x	-	-	in Entwicklung	
	neurodigital Technologies	Avarat VR (Glove one)	Handschuh + Bodytracking	10 Vibrationsaktoren	IMU	Gaming	x	x	5	18	0	0	0	0	0	x	+	0	x	x	-	1.100 €	Kaufbereit (2. Prototyp)
	EPFL, ETH Zurich	DextrES	Handschuh	elektrostatische Bremse	Metallstreifen DE	VR	+	x	5	5	x	0	5	ca.0,4	+	0	0	0	0	8 / Finger	-	-	Forschungsprojekt
	Manus VR	Prime II Haptic	Handschuh	Vibrationsmotoren	IMU	VR, Gaming	x	x	5	-	0	0	0	0	x	+	0	x	x	-	2.499 €	Kaufbereit	
	Nolton	HIS VR Glove	Handschuh	Vibrationsmotor	IMU's	Gaming, Ausbildung	+	x	5	17	0	0	0	0	x	+	0	x	x	-	999 \$	Kaufbereit	
	Senso Devices Inc.	Senso Glove (Suit)	Handschuh	5 Vibrationsmotoren	7 IMU's	Gaming, Fertigung	x	x	5	18	0	0	0	0	x	+	0	x	x	-	599 \$	Kaufbereit	
	Tyndall National Institute	-	Handaufsatz	10 Vibrationsaktoren	12 IMU's + 11 IR LEDs für Kameradetektion	Medizin, Ausbildung	x	x	5	27	0	0	0	0	x	x	0	x	x	-	-	Kaufbereit	
	bebop Sensors	Marcel Modular Data Gloves	Handschuh	nicht resonante aktoren	6 IMU's 10 Stoff-Streifensensoren	Gaming, Musik	+	x	5	15	0	0	0	0	x	+	x	x	x	-	-	erste Prototypen, Vorstellung bei Ausstellungen	
	-	Cobra Gloves	-	-	IMUs (7,13,16)	VR, Medizin, Robotik	0	x	5	14-21	0	0	0	0	0	x	+	0	0	0	-	-	Kaufbereit
	Synertrial	Exo Glove	Handschuh	-	IMUs 5	VR, Medizin, Robotik	0	x	5	11	0	0	0	0	0	x	+	0	0	0	-	-	Kaufbereit
	StretchSense	Sensing Gloves	Handschuh	-	DE-Elemente	Gaming, VR	+	x	5	18	0	0	0	0	0	x	+	0	0	0	-	-	in Entwicklung
	Bosch	i Glove	Handschuh	-	MEMS Sensoren	Fertigung, Ausbildung	x	x	5	-	0	0	0	0	0	x	+	0	0	0	-	-	Prototypentests in Fertigung
Sensorhandschuhe	sensoryx	VRFree	Handschuh	-	12 IMU's	Gaming	x	x	5	27	0	0	0	0	0	x	+	0	0	0	-	-	in Entwicklung (bald Verfügbar)
	Manus VR	Prime II Xsense	Handschuh	-	6 IMU's	Gaming	x	x	5	25	0	0	0	0	0	x	+	0	0	0	-	3.990 €	Kaufbereit
	Synergia	Cobra Glove	Handschuh	-	7-17 IMU's	Gaming	x	x	5	18-30	0	0	0	0	0	x	+	0	0	0	-	799 €	Kaufbereit (vers. Ausführungen)
	neofect	Rapael	Handaufsatz	-	Dehnungssensoren	Medizin, Reha	x	x	5	25	0	0	0	0	0	x	+	0	0	0	-	3281 \$	Kaufbereit
	Uni. Of California	-	Handschuh	-	Dehnungssensoren	Zeichensprache	0	x	5	9	0	0	0	0	0	x	+	0	0	0	-	-	Entwicklung
	Global DJ	Tornado A1	Handschuh	-	IMUs	Musik	0	x	0	-	0	0	0	0	0	x	x	+	0	0	-	399 \$	Kaufbereit
	NIT Kerala India	-	Handschuh	-	IR Sensoren + IMU + Hall Sensoren	Unterstützung Hör und Sprachgeschädigte	x	x	4	15	0	0	0	0	-	-	0	0	0	-	-	im Forschungsstatus	
	-	gest	Handschuh zur Befehlseingabe	-	IMU's	PC Bedienung	0	x	4	12	0	0	0	0	0	x	+	0	0	0	-	-	Prototypen
	PPS - Pressure Profile Systems	TactileGlove	Handschuh	-	Drucksensoren (Kapazitiv)	Fertigung, Prozessoptimierung, Sportmedizin	0	0	0	0	0	0	0	0	0	x	+	0	0	0	-	-	Kaufbereit
	Go Touch VR	VR Touch	Fingerhut	konv. Motor	IMU	CAD, Ausbildung	+	x	1-5	2-12	0	0	0	0	0	x	+	0	x	x	20	-	Kaufbereit
	Tactai	Tactai touch	Fingerhut	konv. Motoren	-	Gaming, Schulbildung	0	1	1-5	2-12	0	0	0	0	0	x	+	0	x	x	29	-	-
	Leap Motion	VR Headset North Star	Kamerasystem	-	Kamera	Gaming	x	x	5	bis 27	0	0	0	0	0	x	+	0	0	0	79,99 €	-	Kaufbereit
	Fujitsu	fujitsu intelligent Glove	Einfinger Handschuh	-	3D Brille	Industrie	x	x	1	4	0	0	0	0	+	+	0	0	0	-	-	-	-
	uni saarbrücken mpil	-	Kamerasystem	-	Kamera	Real-time Anwendungen	x	x	5	bis 27	0	0	0	0	0	ox	+	0	0	0	0	-	im Forschungsstatus
Indus-trie	-	ProGlove	Scanhandschuh	-	-	Fertigung, Logistik	x	0	0	6	0	0	0	0	0	x	x	x	0	ca. 50	-	in industrieller Anwendung	
	PANMobil	Werker 4.0	Scanhandschuh	-	-	Fertigung, Logistik	0	0	0	0	0	0	0	0	0	x	x	x	0	0	-	-	in industrieller Anwendung
	Fraunhofer IAO	-	Lasersensoren	Lastenseilzug	Druck, Biege,Lagesensoren	Fertigung, Logistik,Versand	x	x	5	-	0	-	-	-	0	0	0	0	0	-	-	in Entwicklung	
	Sathyabama ItoSaT	-	Gesture recognition	-	resistive Biegesensoren	Braille Blindensprache	0	x	5	-	0	0	0	-	0	+	+	0	0	-	-	in Entwicklung	
Veröffentlichungen / Artikel	Western Sydney University	surgical glove	training glove	-	IMU's	Medizin, Ausbildung	0	x	5	-	0	0	0	0	0	0	0	0	0	0	-	-	-
	Poznan Univ. of techn.	CIE-Data Glove	Handschuh	-	12 IMU's	Real-time Anwendungen	x	x	5	27	0	0	0	0	0	+	0	0	0	-	-	im Forschungsstatus	
	Univ. of california, San Diego	The Language of glove	Handschuh	-	9 Dehnungssensoren	Gestenerkennung, Zeichensprache	x	x	5	9	0	0	0	0	0	+	0	0	0	-	-	im Forschungsstatus	

A.2. Capacitance measurement principles

Classical capacitance measurement methods are shown in Figure A 1. The most commonly used methods are charging and/or discharging time measurement and the LCR meter principle, where the phase shift and amplitude of the current associated to a sinusoidal input voltage are measured. Other methods which are often used are based on a comparison between a known capacitance and the measured capacitance, which can be also realised as a capacitive voltage divider where the measured voltage is proportional to the measured capacitance. This method can be improved by a measuring bridge to have a higher accuracy and reduce environmental influences. A further method to measure the capacitance is the monitoring of the DC charge which can be realised by current measuring. Problems with the charge measuring is mainly the very small amount of charge (and current) in a quasi-static configuration of the DE, which leads to very small accuracy.

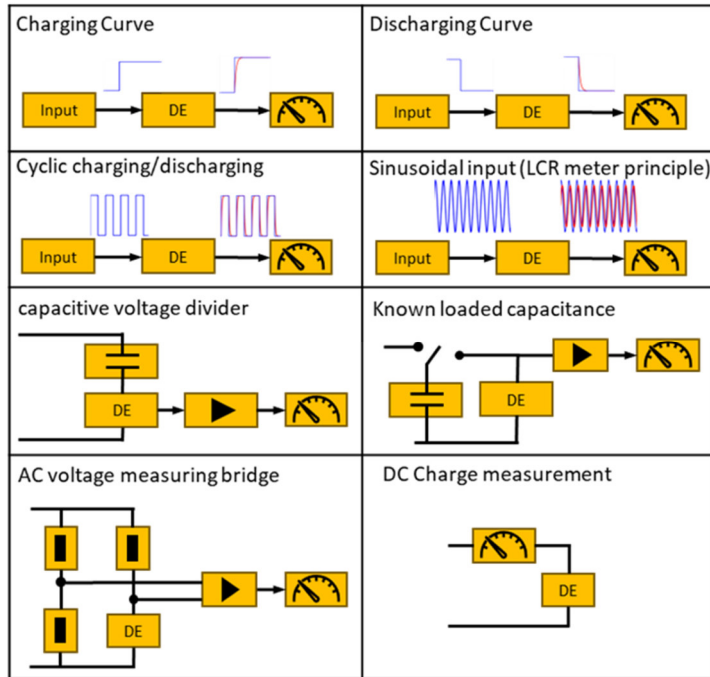


Figure A 1: Different capacitance measurement methods to measure the DE.

A.3. DE actuator design

In Figure A 2 the force characteristics of the different biasing elements and how they influence the output of the DE system is shown.

The mass has only a medium actuator stroke, but the construction is very simple. With a hard stop obviously no stroke can be performed but the output force between high and low voltage applied is maximized and the construction is the simplest. The linear spring is as well simple but offers only a comparable low actuator stroke. The linear spring, or positive rate bias spring (PBS) has the main advantage that the force behavior can be easily adapted by using a different stiffness of the spring and changing the pre-tension of the PBS in the equilibrium state. The magnet-based biasing is a bit more complex to integrate and brings relatively high mass into the system. Depending on the biasing element the maximum stroke of the DEA is very different. Especially for a negative biasing spring (NBS) the displacement of the system can be maximized. The NBS can

be additionally angled in a certain way (with the help of a fixed mechanical setting of the output angle for the beam), which has an impact to the force behaviour of the NBS [276].

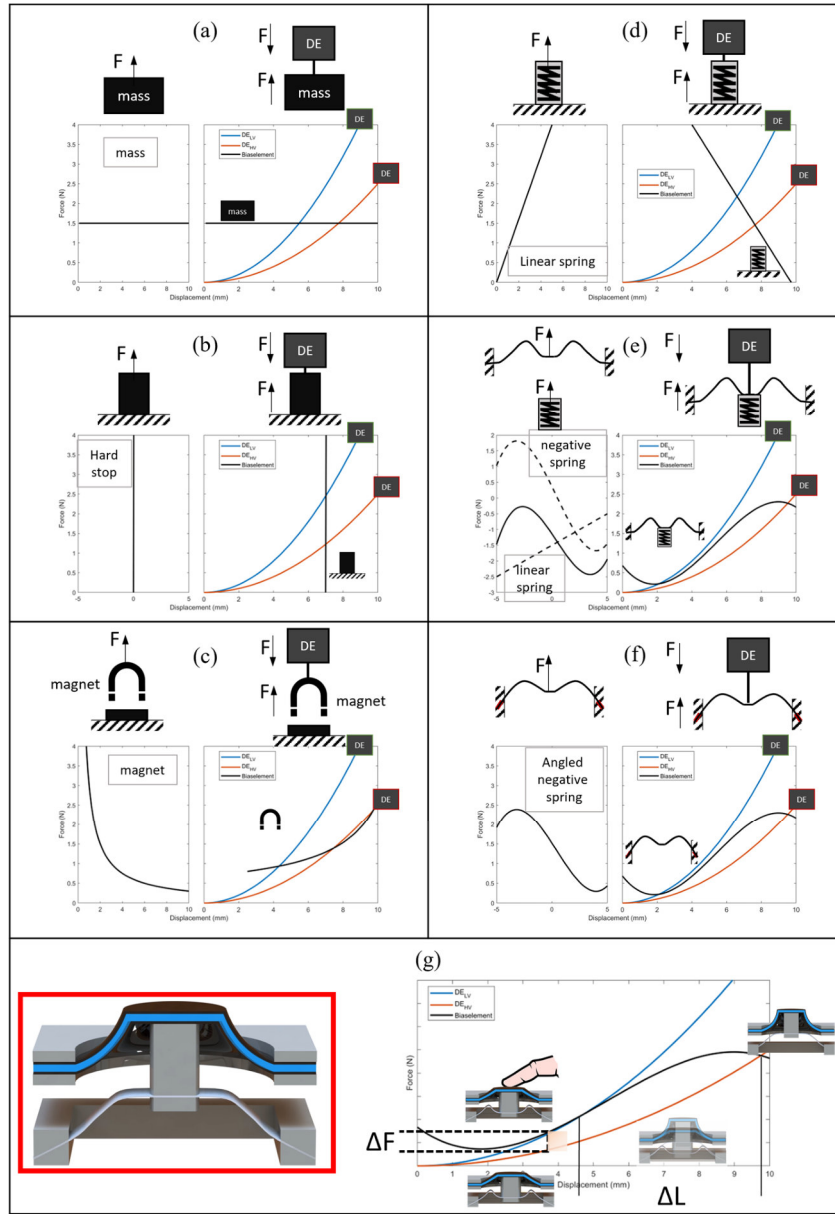


Figure A 2: Biasing elements and influence on the design of the DE System with reaction forces (a) mass (b) hard stop (c) magnet (d) linear spring (e) negative bias spring and (f) angled biasing spring. As well as an example for a circular DE with force and displacement difference (g).

For an angled NBS no additional linear spring is necessary to adjust the force of the biasing element to the DE stiffness. Therefore, the angled NBS is the best method to reach high strokes for a rigid system structure. The NBS force can be influenced by changing the material and the geometry of the leaf spring. The force is linear with the width of the bar and cubic with the thickness of the sheet. The length and the compression of the beam influences the stiffness of the spring and respectively the maxima peaks of the NBS force. With the clamping angle of the NBS force can be shifted from a symmetrical shape (for 0° angle) around the symmetry axis (zero force line) upward, to fit the DE force characteristics (see Figure A 2(g)). By specifically designing the NBS,

fitting to the DE force and the application, it is possible to increase the DEA performance significantly [276], [277], [278], [279].

The shown curves in Figure A 2 are simplified to visualize the principle design process. However, the hysteresis of the DE and the spring have a high impact to the biasing system design in real applications. The hysteresis of the DE is mainly influenced by the electrode material. If the NBS is build out of spring steel the hysteresis is negligible, but by using for example elastomeric pre-load elements, which are much better for flexible integration into textiles, the hysteresis of the bias element material has a much higher influence.

If static conditions are considered, the sum of all forces in the system need to be zero. To calculate (graphically) the force applied to the DEA, the forces F in the moving direction of the DE \hat{e}_{DE} must considered. For one biasing element with the force F_{Bias} the sum of the forces is:

$$\sum F \cdot \hat{e}_{DE} = F_{DE} \cdot \hat{e}_{DE} + F_{Bias} \cdot \hat{e}_{DE} = 0. \quad (5.1)$$

For a biasing element with a unidirectional force in the direction of the DE the equation can be directly written as

$$F_{DE} = -F_{Bias}. \quad (5.2)$$

However, with equation 5.2 the behaviour of the DE system can be explained, by considering the DE force and the biasing force with the specific directions of the corresponding forces. Figure A 2 the graphical determination of the forces and the displacement of the actuator (in correspondence of a given voltage variation) is shown. In the last row (Figure A 2(g)) for example, a system with a COP-DE and an angled NBS is shown. The two colored curves in Figure A 2(g) represent the DE response with (red) and without (blue) voltage, where the black line represents the NBS force behaviour. The movement of the end effector can be read from the x-axis and the force from the y-axis of the resulting displacement-force diagram for the cut-out-forces of the system.

A.4. Model of the DEA dynamic response

Finite element model of the DEA acoustic response

The model described in section 2.1.1.3 and 3.2.1 is implemented in the software Comsol Multiphysics, making use of the in-built Nonlinear Structural Mechanics and Acoustic modules, and implementing user-defined functions to consistently describe the electro-acoustic interactions (i.e., the contribution of the voltage in the energy density function). Consistent coupling between the membrane and the acoustic domain is implemented by means of a moving mesh feature. Further details on the model assumptions and implementation are discussed in [173].

Table A 2: Material parameters used in the simulation ([225]).

Model assumptions		
Hyperelastic params. (3-param. Mooney-Rivlin)	$c_{1,0}$	194 kPa
	$c_{2,0}$	71 kPa
	$c_{0,1}$	-24 kPa
Dielectric permittivity	ε	$2.8 \cdot 8.9 \cdot 10^{-12}$ F/m
Structural damping loss fact.	η_s	0.15
DE density	ρ	1400 kg/m ³

The described model is used to predict the acoustic response of the DEA. Similar to [173], the material parameters listed in Table A 2 were used. In particular, the DE elastic response is described via a generalised Mooney-Rivlin hyperelastic model, the visco-elastic response via a

structural damping (with loss factor η_s). The thickness of the membrane is assumed to be equal to the total thickness of the dielectric layers. A suitable value for the density (higher than the density of the dielectric) of the DE is chosen, to account for the contribution of the screen-printed electrodes on the total DE mass. The geometry of the structure surrounding the DEA was modelled in a simplified way as a thin flat square panel with 80 mm side length. Although this geometry represents a drastic simplification compared to the actual structure, it accounts for sound reflections from the walls around the DE, while still keeping into account acoustic short circuit effects between the front and the back of the membrane (as the box holding the DE is not laterally sealed). The air volume surrounding the sample has been modelled as a spherical 4 volume with a radius of 450 mm, surrounded by a permanently matched layer with thickness equal to the membrane outer radius. Other details on the model and its implementation are provided in [173].

The plots in Figure A 3 compare the experimental trends of the SPL (as a function of the frequency) with the model's predictions. In the simulations, the end-effector of the device is held fixed, and the resulting predictions are compared with the SPL measurements obtained in the two blocking tests presented in Figure 3.2, which feature different bias voltage and out-of-plane deformation, namely: B1: $V_b = 1$ kV, $h_0 = 5.1$ mm; B2: $V_b = 2$ kV, $h_0 = 5.6$ mm. In both tests, the applied voltage has an amplitude $V_\kappa = 100$ V.

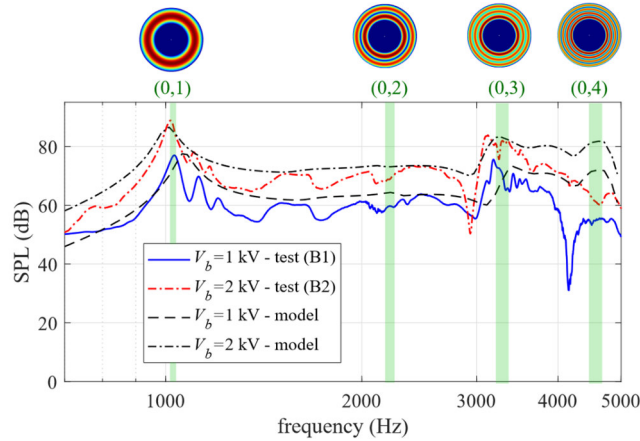


Figure A 3: SPL in blocking conditions (B1 and B2, as defined in Figure 3.2): comparison of experimental data and finite element model predictions. The green bands indicate the range where the natural frequencies of the corresponding modes (whose value is different in the two cases) are comprised ([225]).

The model captures the global qualitative and quantitative trend of the SPL in the considered frequency range. In particular, the model predicts the location and magnitude of the peak associated to the first structural mode (mode (0, 1)), in the neighbourhood of which the SPL rises from 40 dB to 75-85 dB (depending on the biasing voltage). The model shows that, in the considered frequency range, the membrane features at least 4 axial-symmetrical modes (from (0, 1) to (0, 4)). In particular, the acoustic response shows peaks (with an increase in the sound pressure level consistent with the experimental data) in correspondence modes (0, 1) and (0, 3), whereas modes (0, 2) and (0, 4) (with an even number of antinodes) have a minor influence on the acoustic response. In addition to that, the model is able to explain the variation in SPL generated by different electro-mechanical biasing conditions.

As already discussed in [173], because of the drastic simplifications used here to describe the material damping, the model does not entirely capture some features of the acoustic response (e.g., the presence of antiresonances in the acoustic response in the range 4-4.5 kHz), and in particular it tends to overestimate the amount of damping present in the response at the highest frequencies. To improve the model accuracy, one should resort to a more complex damping model (e.g., a rheological visco-elastic model), for which a specific characterization would be required. The model, in the form presented here and in [1], still allows obtaining a reliable estimate of the generated SPL and its dependency on the design parameters.

Nonlinear dynamics

The finite element model presented in Sect. S2 allows solving the linearised continuum dynamics of the DEA in the neighbourhood of a given working configuration and estimate the associated acoustic frequency response. The response of the system to multi-frequency excitations, however, shows trends that can only be explained in terms of nonlinear system's dynamics (namely, the beat distortions shown in Figure 3.26). With the aim of qualitatively explaining the origins of these effects, a lumped-parameter formulation is used, based on a mode described and validated in ([59], [175]), and shortly recalled in the following.

The lumped-parameter model discussed here relies on a modal approach: a set of mode shape functions (namely, the modal eigenfunctions) is used to parameterise the deformed DEA geometry via a finite number of degrees of freedom, and the total DEA deformation is expressed as a finite linear superposition of mode shapes. Each mode shapes describes the DEA displacements associated to a certain free vibration mode. This modal approach is largely used in the analysis of dynamical systems, and it has been applied to DE loudspeakers in the past ([59], [168], [175]).

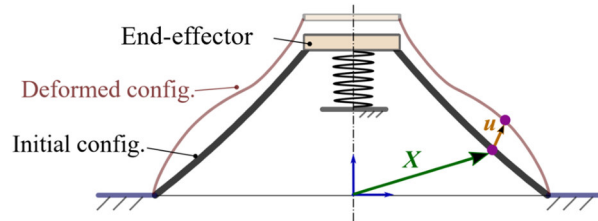


Figure A 4: Cone DEA in the initial (reference) configuration and in a generic deformed configuration ([225]).

Denoting X the position of a generic point over the DE surface (in a reference configuration, e.g., the equilibrium DEA position, prior to voltage application), the displacement field u of a generic point of the DEA (Figure A 4) with respect to the reference configuration can be thus approximated as follows:

$$u(X) = m(X)\alpha \quad (i)$$

where $m = m(X) : \mathbb{R}^3 \rightarrow \mathbb{R}^{3 \times n}$ is a multivariate function whose elements describe the mode shapes of the DEA, and $\alpha \in \mathbb{R}^n$ is a modal coordinate whose dimension, n , equals the number of the considered eigenmodes. α is defined in such a way that $\alpha = 0$ denotes the initial configuration.

The DEA dynamics can be expressed in terms of modal coordinate α leading to the n -dimensional equation 2.19. A formulation for the calculation of the DEA eigenmodes and the single terms in 2.19 is discussed in section 3.2.1 and [59], with reference to the case of purely axial-symmetrical deformations. In particular, the eigenmodes $m(X)$ are calculated by linearising the DEA dynamics in the neighbourhood of a given configuration. Despite this, dynamics 2.19 are

still non-linear, as the eigenmodes here are just used as a mean of parametrising the DEA deformation kinematics in a finite-dimensional fashion (i.e., the eigenmodes, obtained from system linearisation, are here just used to perform a change of coordinates, resulting in reduction of the problem dimension).

As regards the dynamics parameters, it is worth noticing that, in addition to the inertia of the DE membrane and the end effector, the mass matrix M shall include contributions due to the acoustic added mass, i.e., the air of mass put into motion by the membrane vibration. This contribution plays a relevant role in the structural vibrations of thin lightweight membranes. Similarly, damping D accounts for both the viscous stresses in the DE membrane and the acoustic damping (i.e., the energy lost as sound radiation). Based on equation 2.19, the voltage enters the equations of motion through an excitation term (right-hand side of the equation) proportional to U^2 , rendering the contribution of the Maxwell stress. According to Rayleigh theory [280], the acoustic pressure p generated by the DEA at a target point in space is linearly related to the dynamic response by a relationship in the following general form:

$$p = \int_0^t H^T(t - \tau) \ddot{a}(\tau) d\tau, \quad (\text{ii})$$

where $H(t) : \mathbb{R} \rightarrow \mathbb{R}^n$ is a suitably defined kernel vector function, which only depends on the geometry of the membrane and the surrounding environment, and the location of the receptor point.

Multi-frequency input and distortions

Driving the DEA with a multi-frequency input given by the superposition of a LF signal (with frequency f_L) and a HF signal (with frequency f_H) leads to distortions in the acoustic response (see Figure 3.26), namely, the sound level decreases periodically (low-frequency modulation) with a period equal to $1/f_L$. In terms of the sound spectra, this can be interpreted as a beat pattern.

With reference to the experiment discussed in Figure 3.26 (free oscillating DEA driven by a multi-frequency input), Figure A 5a shows the time-series of the generated sound pressure, whereas Figure A 5b shows its spectrum (calculated using the fast Fourier-transform algorithm). In addition to the fundamental component (at frequency f_H), the spectrum includes higher-frequency terms which are multiples of the fundamental ($2f_H, 3f_H, \dots$), which result in harmonic distortions of the output (i.e., distortions within the periodic response at frequency f_H). Most importantly, the spectrum includes harmonic components, which are close to the fundamental frequency and only differ by f_L (or its multiples). As it is well-known, the superposition of the fundamental with such neighbouring harmonics results in a beat pattern, which is ultimately responsible for the time-trend of the sound pressure shown in Figure 3.26 and Figure A 5a

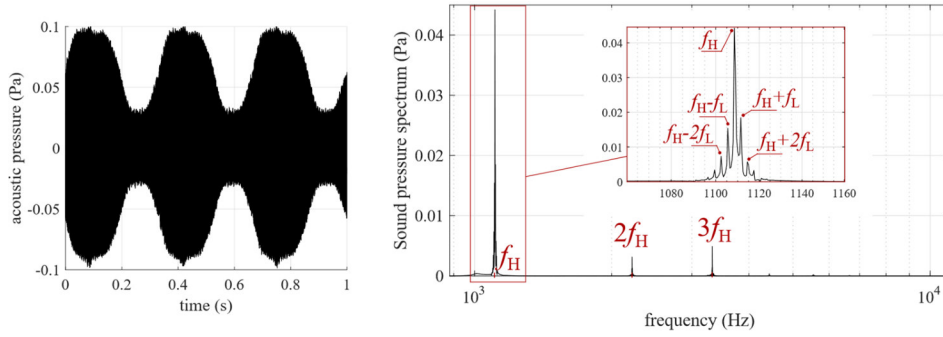


Figure A 5 Time series (a.) and spectrum (b.) of the sound pressure for the test shown in Figure 3.26. In the test, the DEA is subject to a multi frequency input (both the HF and the LF component have sinusoidal waveform and constant amplitude)

The reason why the DEA response includes these higher-order harmonics can be qualitatively explained using model (i)-(ii) and equation 2.19). For the simple purpose of justifying the beat distortion shown in Figure A 5, the following assumptions are introduced:

– The input U^2 is the sum of two terms (a LF term \bar{u} , and a HF term \tilde{u}), assumed sinusoidal for simplicity:

$$U^2 = \bar{u} + \tilde{u}, \text{ where } \bar{u} = v_0 + v_1 \sin(2\pi f_L t), \tilde{u} = v_2 \sin(2\pi f_H t + \phi), \quad (\text{iii})$$

and the amplitude of \tilde{u} is much smaller than that of \bar{u} : $|\tilde{u}(t)| \ll |\bar{u}(t)| \forall t$. As a consequence, the membrane deformation too can be expressed as the sum of two components, as discussed in [59] namely:

$$\alpha(t) = \bar{\alpha}(t) + \tilde{\alpha}(t), \text{ with } |\tilde{\alpha}(t)| \ll |\bar{\alpha}(t)|. \quad (\text{iv})$$

We call $\bar{\alpha}$ the solution to equation 2.19 obtained for $U^2 = \bar{u}$, namely

$$\mathbf{M}\ddot{\bar{\alpha}} + \mathbf{D}\dot{\bar{\alpha}} + \mathbf{K}(\bar{\alpha}) = h(\bar{\alpha})\bar{u}, \quad (\text{v})$$

whereas $\tilde{\alpha}$ is an additional deformation appearing when the DEA is driven by input (iii).

– Multi-frequency input (iii) only excites two vibration modes ($n = 2$): the pumping mode and a structural mode, while the contribution of other modes in the dynamics is neglected. Moreover, since the passband of the pumping mode is well-resolved from those of the structural modes, its assumed that \bar{u} only excites the pumping mode, whereas \tilde{u} only excites the structural mode, namely:

$$\bar{\alpha} = [\bar{\alpha} \ 0]^T, \ \tilde{\alpha} = [0 \ \tilde{\alpha}]^T, \quad (\text{vi})$$

where $\bar{\alpha}$ and $\tilde{\alpha}$ are parameters describing the dynamics of the individual modes.

Equation 2.19 is linearized around trajectory $\bar{\alpha}$, i.e., the pumping mode, and using equation (v) we obtain the following dynamics for $\tilde{\alpha}$, i.e., the excited structural mode:

$$\mathbf{M}\ddot{\tilde{\alpha}} + \left[\frac{\delta \mathbf{K}(\bar{\alpha})}{\delta \alpha} - \bar{u} \frac{\delta \mathbf{h}(\bar{\alpha})}{\delta \alpha} \right] \tilde{\alpha} = h(\bar{\alpha})\tilde{u}. \quad (\text{vii})$$

Equation (vii) is linear with respect to \tilde{u} and $\tilde{\alpha}$, with coefficients (namely, the stiffness and the excitation coefficient) that vary in time in a parametric fashion, as functions of the slow dynamics (namely, of \bar{u} and $\bar{\alpha}$).

The focus lies on the dynamics of $\tilde{\alpha}$ (as this is the main responsible for the sound generation) and thus restricts to consider the second component of equation (vii). For the purpose of exemplification, $\delta K_{22}(\alpha)/\delta \alpha_2$ and $h_2(\alpha)$ (components of $\delta K(\alpha)/\delta \alpha_2$ and $h(\alpha)$) can considered to be

approximated by linear functions, and configuration-induced variations (i.e., dependency on $\bar{\alpha}$) in the stiffness and the excitation are small:

$$\frac{\delta K_{22}(\alpha)}{\delta \alpha_2} = k + k' \bar{\alpha}, \quad h_2(\alpha) = h + h' \bar{\alpha}, \quad \text{for } \alpha = \bar{\alpha} = [\bar{\alpha} \ 0]^T \quad (\text{viii})$$

where k, k', h, h' are constant coefficients with $|k' \bar{\alpha}| \ll |k|, |h' \bar{\alpha}| \ll |h|$.

Replacing (viii) into the second component of (vii) leads to the following dynamics for $\tilde{\alpha}$:

$$M_{22} \ddot{\tilde{\alpha}}(t) + [k + k' \bar{\alpha}(t) - h' \bar{u}(t)] \tilde{\alpha}(t) = [h + h' \bar{\alpha}] \tilde{u}(t). \quad (\text{ix})$$

Because the timescale over which \bar{u} and $\bar{\alpha}$ vary is much longer than the timescale of the variations in \tilde{u} and $\tilde{\alpha}$, we can provide an approximate solution to (ix) by treating the terms into square brackets as constants, and re-introducing the dependency of \bar{u} and $\bar{\alpha}$ on time after the equation has been solved. This leads to the following solution:

$$\tilde{\alpha}(t) \simeq \frac{[h + h' \bar{\alpha}(t)] \tilde{u}(t)}{-M_{22} \omega_H^2 + k + k' \bar{\alpha}(t) - h' \bar{u}(t)} \simeq \left[h + h' \bar{\alpha}(t) + h \frac{h' \bar{u}(t) - k' \bar{\alpha}(t)}{k - M_{22} \omega_H^2} \right] \frac{\tilde{u}(t)}{k - M_{22} \omega_H^2}. \quad (\text{x})$$

In the right-hand side of (x), it is assumed that (viii) holds, and that voltage-induced stiffness variations of the DE are small ($|h' \bar{u}(t)| \ll |k|$), and second order terms are neglected accordingly.

In equation (x), $\bar{u}(t)$ and $\tilde{u}(t)$ are sine waves with frequency of f_L and f_H (equation (iii)) whereas $\bar{\alpha}(t)$ is a periodic signal with fundamental frequency f_L (plus possible additional multiple harmonics). The time trend of $\tilde{\alpha}(t)$ thus contains a fundamental harmonic term proportional to $\tilde{u}(t)$, plus a set of second-order terms which are proportional to the products $\bar{u}(t) \tilde{u}(t)$ and $\tilde{u}(t) \bar{\alpha}(t)$, and they hence lead to additional harmonic terms with frequency $f_H + f_L$ and $f_H - f_L$ (plus similar terms where the integer multiples of f_L appear).

Given that the transfer function between the accelerations and the sound pressure is linear (equation (ii)), this consistently explains the beat harmonics observed in the sound spectrum in Figure A 5b.

It is finally worth noticing that the modelling approach presented here and in [175] provides a possible tool to design advanced control strategies to equalise the DEA acoustic response in the presence of multi-frequency inputs, via model-based filtering.

A.5. Effect of the DEA housing on the frequency response

The active COP-DEA unit (as shown in Figure 3.1 and Figure A 6 a-left) is installed in a 3D-printed housing (see Figure 3.30). In addition to shielding the DEA electrodes' surface from direct contacts with users, such case acts as an acoustic enclosure for the membrane. The internal structure of the housing has the structures shown in Figure A 6a right (compare Figure 3.44 and Figure 3.31), i.e., it includes a slot, where the COP-DEA assembly is located, which eliminates (or significantly reduces) the acoustic short circuit between the front and the back faces of the membrane.

Thanks to such feature, the volume underneath the DE membrane (highlighted in blue in Figure A 6a-right) approximately behaves as a vented enclosure, which is in communication with the atmosphere only through a small-size (mm-scale) gap at the assembly's perimeter. Such enclosure

- Does not affect the low frequency response (e.g., the pumping motion) of the COP-DEA, because of venting

- Works as a bass-reflex at intermediate frequencies, hence preventing acoustic-short circuits between opposite faces of the DE membrane.

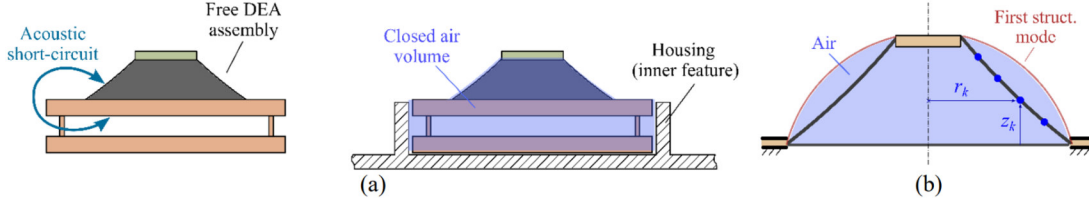


Figure A 6: (a) COP-DEA assembly without housing (left) suffering from acoustic short-circuit and installed inside the box (right). (b) Definition of the first structural vibration mode for the COP-DEA, and surface discretization used to formulate the model [216] (c.f. [59]).

As a result of this, the SPL response of the free DEA at low frequencies in the acoustic spectrum (e.g., in the range 500-900 Hz) differs from that of the boxed DE as shown by the plots in Figure 3.35, with lower-frequency pitches reaching significantly higher levels in the boxed case as a result of bass reflections.

In the frequency ranges where the structural modes are excited, the boxed air volume can be regarded as a closed adiabatic volume, hence contribution additional mechanical stiffness (in addition to the membrane elasticity) to the structural vibrations of the DE membrane. Hereby it is shown that such additional stiffness can be used to explain the shift in the natural frequency of the first peak (i.e., the first structural mode) in the spectra of the boxed DEA in Figure 3.35-left.

The model of vibrating cone DEA discussed by [59] and [175] and section 3.2.1 is used. The model relies on a modal representation of the DEA's dynamics (in the absence of the acoustic enclosure), that can be expressed in the following (linearised) form (equation 2.19):

$$M_\alpha \ddot{\alpha} + D_\alpha \dot{\alpha} + K_\alpha \alpha = d_\alpha(v, \alpha) \quad (\text{xi})$$

where α is a modal coordinate, which allows mapping the position of a set of points on the DE surface via a linear relationship. Denoting $\mathbf{x} = [r_1, z_1, \dots, r_n, z_n]^T$ a vector of radial/axial coordinates of a set of n points on the membrane profile (see Figure A 6b), α allows expressing the position of the points as follows:

$$\mathbf{x} = \mathbf{x}_0 + \mathbf{Q}_\alpha \alpha, \quad (\text{xii})$$

where \mathbf{x}_0 is the equilibrium configuration of the pre-loaded membrane, and \mathbf{Q}_α is a matrix inducing a change of coordinates, whose columns represent mode shape functions that allow parametrising the deformed shape of the membrane. \mathbf{M}_α , \mathbf{D}_α and \mathbf{K}_α are mass, damping and stiffness modal matrices; \mathbf{h}_α is an excitation coefficient, that depends on the applied time-varying voltage $v(t)$ and the membrane deformation kinematics. The detailed calculation of the different dynamic parameters is discussed in the abovementioned reference papers, and it is based on

- Lumped-parameter models of the electro-hyperelastic response of the DE membrane (used to determine \mathbf{K}_α and \mathbf{d}_α)
- Simplified assumptions on the effects of aeroacoustic loads on the membrane, which enter \mathbf{M}_α , \mathbf{D}_α (in the form of acoustic added mass and radiation damping), that in turn can be calibrated based on experimental data.

For the purpose of the present analysis

- The focus is solely on the DE's first structural vibration mode, i.e., it is assumed that the membrane undergoes deformations described by a shape function that leads to bubble-like deformations of the lateral surface (with no axial motion of the end effector) similar to those shown in Figure A 6b (red profile). The membrane deformation is described through

a single parameter (degree of freedom) α , which allows expressing the coordinates of the deformed membrane's point according to equation (xii) (in this case, \mathbf{Q}_α is a column vector expressing the deformation function, and its calculation is detailed in [59]).

- Since we are exclusively interested in evaluating the natural frequency of a particular vibration mode (rather than the forced response), the DE's free dynamics is considered ($\mathbf{d}_\alpha = \mathbf{0}$) and, knowing that the system is significantly underdamped, the damping can be neglected, $\mathbf{D}_\alpha = \mathbf{0}$.
- It is assumed that the volume of air underneath the membrane is closed and evolves adiabatically, and the membrane faces are thus subject to a pressure difference as a result of the compressions/expansions caused by the membrane bubble-like deformation.

With these assumptions, equation (xi) can be recast as a scalar (single-degree-of-freedom) equation, with an additional contribution due to the relative air pressure in the enclosed air volume:

$$M_\alpha \ddot{\alpha} + K_\alpha \alpha = p \Omega'(\alpha) \quad (\text{xiii})$$

Where M_α and K_α are scalars, p is the relative pressure of the air in the closed chamber, $\Omega(\alpha)$ is the volume of the chamber, and $\Omega'(\alpha)$ its first derivative. The term on the right-hand side renders the generalised (Lagrangian) force (projected on coordinate α) due to the air pressure. Pressure p varies with α according to the adiabatic law for ideal gasses:

$$(p + p_0) \Omega(\alpha)^\gamma = p_0 \Omega_0^\gamma, \quad (\text{xiv})$$

where $p_0 = 1$ bar is the atmospheric pressure, $\gamma = 1.4$ is the adiabatic exponent, and $\Omega_0 = \Omega(\alpha)$ is the volume subtended by the pre-loaded membrane in the equilibrium configuration. Linearising Eq. ((xiv) above equilibrium leads to:

$$p = -\gamma p_0 \frac{\Omega'(0)}{\Omega_0} \alpha, \quad (\text{xv})$$

Fitting expression (xv) into equation (xiii) (with the derivative of Ω on the right-hand side evaluated at $\alpha = 0$, i.e., above the equilibrium position), leads to the following equation for the DE membrane undamped free dynamics:

$$M_\alpha \ddot{\alpha} + \left[K_\alpha + \gamma p_0 \frac{(\Omega'(0))^2}{\Omega_0} \right] \alpha = 0 \quad (\text{xvi})$$

where the expression into square brackets expresses the total stiffness of the system, which includes an elastic contribution (K_α) and a contribution due to the air compressibility. The resulting natural frequency for the structural mode described by α is:

$$f_\alpha = \frac{1}{2\pi} \sqrt{\frac{K_\alpha + \gamma p_0 (\Omega'(0))^2 / \Omega_0}{M_\alpha}} \quad (\text{xvii})$$

K_α (and the shape function \mathbf{Q}_α inducing the definition of α) can be calculated using the procedure described by [59], using the hyperelastic parameters described in : and a bias voltage of 2500 V. Using the plot in Figure 3.35(left), a value of 900 Hz for the natural frequency of the first structural mode of the free DEA (without enclosure) can be assumed, and used to compute M_α from equation (xvii), excluding the contribution of the air compressibility (calculating M_α analytically would involve high uncertainty, due to the contribution of the sound radiation added mass).

Table A 3: Parameters used for the calculation discussed.

Model assumptions		
Hyperelast. Params (3-param. Mooney-Rivlin)	$c_{1,0}$	230 kPa
	$c_{2,0}$	8 kPa
	$c_{0,1}$	-29 kPa
Permittivity	ε	$2.4 \cdot 8.85 \cdot 10^{-12}$ F/m
Trapped air volume	Ω_0	30 cm ³

Afterwards, the natural frequency for the assembled DEA (with housing) is calculated using equation (xvii) (including air's stiffness), assuming a volume on the order of 30 cm³ for the air volume (based on the device components' drawings). The estimated natural frequency for the assembled COP-DEA is $f_\alpha = 1030$ Hz, i.e. on the order of 130 Hz higher than the natural frequency of the free DEA. This result is consistent with the position of the peaks in the SPL curve for the assembled device (or slightly higher, since the air volume is treated as tight in the calculations). The variations in the acoustic frequency response for the assembled device (compared to the free DEA) can be consistently explained in terms of the bass-reflex effect generated by the DEA's housing design, which fully explains also the shift (increase) in natural frequency of the first structural mode (i.e., the cut-in acoustic frequency).

A.6. Definition of the working modes

The 5 working modes coded on the user interface demonstrator and discussed in Sect. 3.2.4.2 are implemented through voltage inputs in the form given by 3.20:

$$u(t) = \sqrt{V_0 + V_1 \bar{u}(t) + V_2 \cdot \check{u}(t)},$$

$$\text{with } V_0 = \frac{U_{max}^2 + U_{min}^2}{2}, \quad V_1 = \frac{U_{max}^2 - U_{min}^2}{2}, \quad V_2 = 2U_{max}U_a, \quad U_a \ll U_{max}$$

For Mode 1, $u(t)$ only includes a LF component $\bar{u}(t)$ ($\check{u}(t) = 0$), with $U_a = 0$ V; $U_{max} = 2100$ V; $U_{min} = 200$ V and $\bar{u}(t)$ rendering a square pulse varying between -1 and +1 with time-varying frequency between 3 Hz and 90 Hz.

For Mode 2 a combination of a vibrotactile ($\bar{u}(t)$) and an acoustic ($\check{u}(t)$) signal is applied, which can be described by setting $U_a = 220$ V_{pp}; $U_{max} = 2500$ V; $U_{min} = 700$ V in the equation, with $\bar{u}(t)$ representing a square pulse with frequency of 2 Hz (200 ms 1; 300 ms -1). The high frequency component $\check{u}(t)$ is a sinusoidal signal with a frequency of 850 Hz with an amplitude of 1 when the LF component is U_{max} and 0.3 when the LF component is U_{min} .

For Mode 3 a combination of a vibrotactile ($\bar{u}(t)$) and an acoustic ($\check{u}(t)$) signal is applied with a decreasing and increasing amplitude, which can be described with the equation by setting $U_a = 300$ V_{pp}; $U_{max} = 2300$ V; $U_{min} = 700$ V and $\bar{u}(t)$ is a square pulse with a frequency of 5 Hz (140 ms 1; 60 ms -1) with an exponentially decreasing and increasing amplitude (with the amplitude increasing from 0 to the maximum value, and vice-versa in 2.5 s). The high frequency component $\check{u}(t)$ is a sinusoidal signal with a frequency of 800 Hz with exponentially decreasing and increasing amplitude.

For Mode 4 a haptic and acoustic signal is provided when the user is pushing the button. The LF signal consists in a sequence of two ramps, with a superposed HF sinusoidal signal with a frequency of 1318.5 Hz (E₆), and a third ramp with a sequence of 3 HF pitches (E₆; C₆[#]; A₆). The amplitude of the HF pitches has an exponentially decreasing trend, to emulate the sound of an instrument's key.

The fifth mode only consists of a HF music track with a bias voltage of 2300 V and an amplitude of $300 V_{pp}$, and $\tilde{u}(t)$ replicating a Jingle composed by a sequence of keys (sinusoidal signals with exponentially decreasing amplitude).

A.7. Additional experimental results of the multi-mode multi frequency DEA

In the following, additional measurement results are shown, in order to provide a better understanding of the system response. shows measurements of the SPL at different angles, with and without housing (i.e., free DEA sample vs DEA installed inside the acoustic housing). It can be clearly seen that the DE has directional acoustic response, with the SPL decreasing as the angle approaches 90° . Similar to that, lower bias voltage and amplitude lead to a reduction in SPL. The higher frequency peaks shift to lower frequencies for higher bias voltage, as a result of a decrease in the mechanical stress to which the membrane is subject.

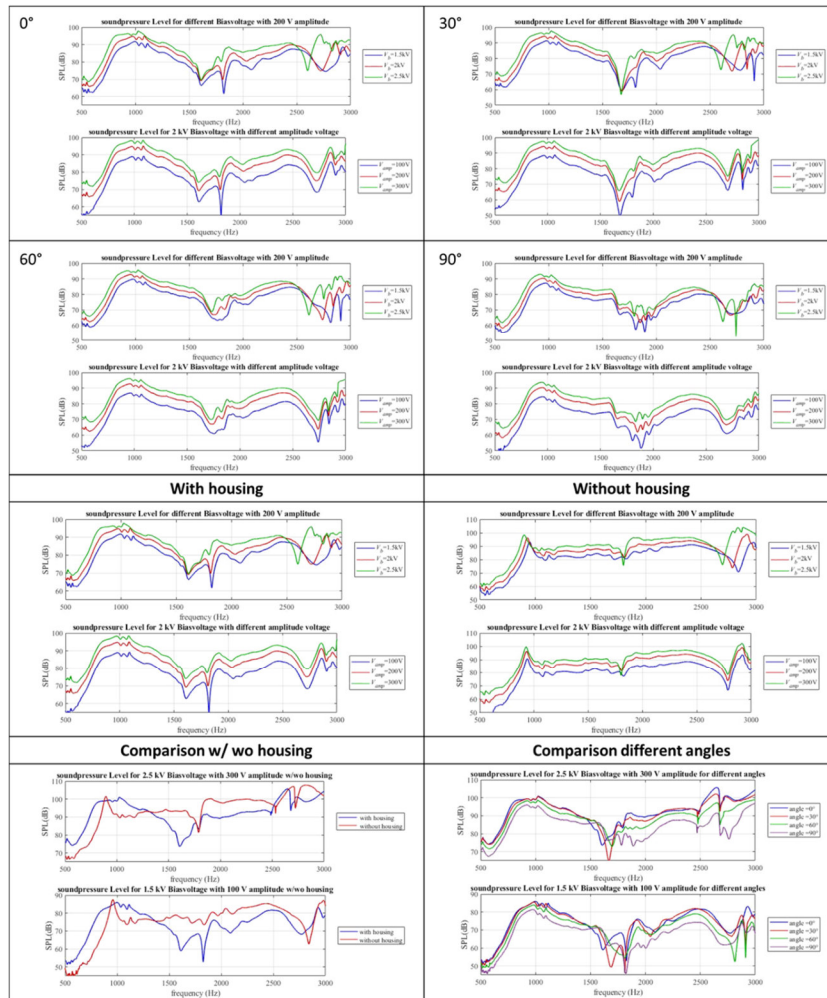


Figure A 7: Further measurements of the DEA performance.

In Figure A 8 measurements of the end effector displacement are shown. The measurements are performed with different signals (bias voltage and amplitude) and for different frequency ranges. Furthermore, measurement results with and without housing are shown. At higher frequencies the end-effector out-of-plane motion falls to zero, as a result of the system dynamics (governed by the inertia of the rigid end-effector). With the housing, the movement in the lower frequency range

is around one half the movement without the housing, due to the increased stiffness owing to the textile layer installed over the end-effector.

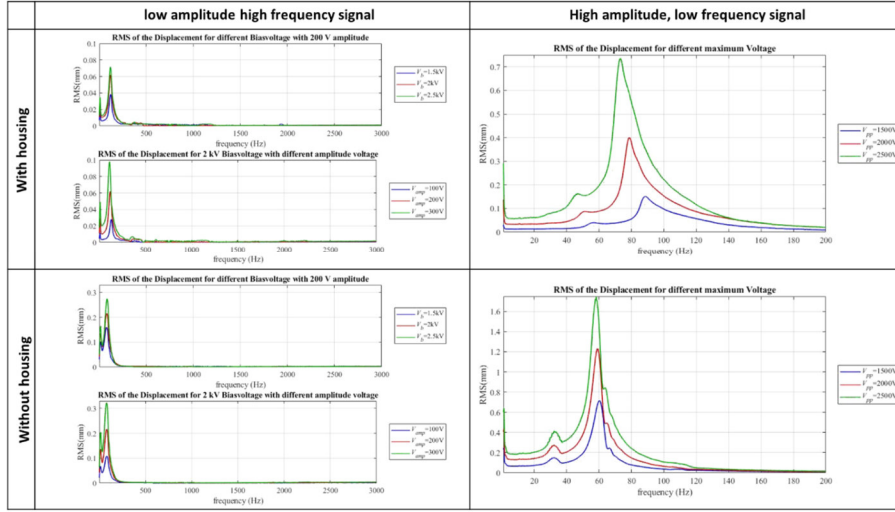


Figure A 8: Displacement of the end effector for different signals with and without housing.

In Figure A 9 force measurements for different preload forces are shown. Also, a comparison of the force measurements at different bias voltages is presented. The force is nearly constant over the frequency and increases with higher bias voltage. For the preload force of 0.1 N and 1 N the output force of the DEA is the same, whereas when the DE is further pushed inward (2N preload) the force decreases, for the DEA moves towards a flat singular configuration.

It is worth remarking that the increase in output force measured at higher frequency is an artifact due to the measurement setup, and it owes to mechanical resonance of the DEA + load-cell assembly.

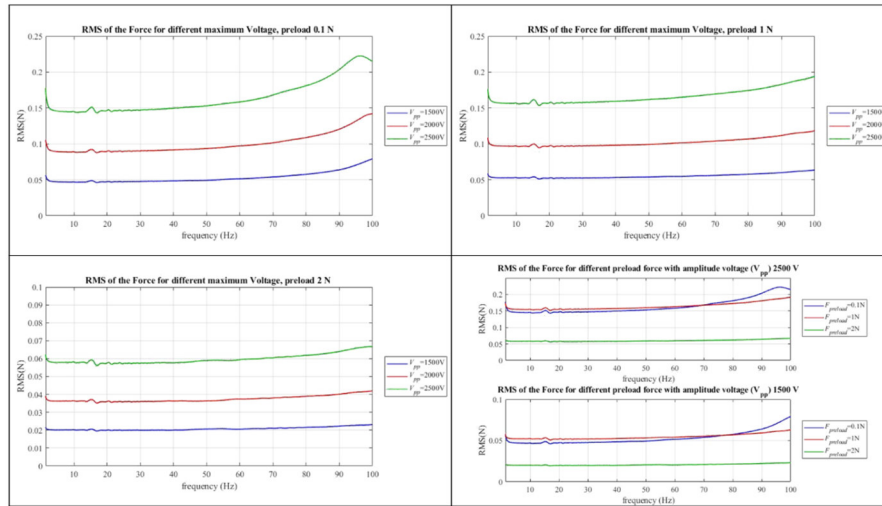


Figure A 9: Force measurement for different pre-load forces and different bias voltage and a comparison (low right side).

A.8. Classification of the user tests

User tests (Figure 3.41 and Figure 3.42) were performed by presenting the users with 8 different combinations of vibrotactile and acoustic feedbacks coming from two distinct user interface units (Figure 3.41). In addition to the confusion matrices in (Figure 3.42), Figure A 10 reports a detailed

overview of the perception results reported by the users for all cases (1-8, as defined in Figure 3.41).

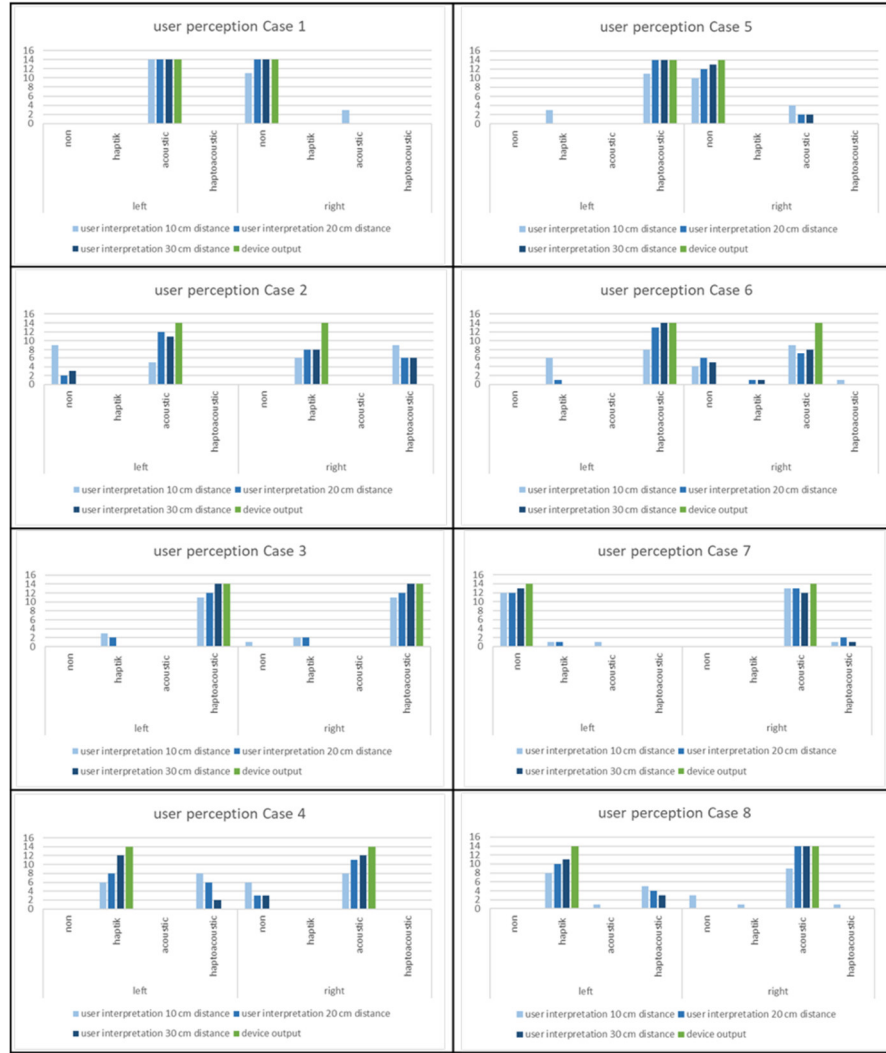


Figure A 10: Statistics of user perception tests with two DEA units (left-right), for 8 different combinations of haptic and acoustic feedback produced by the two units.

Green bars in the histograms represent the actual feedback provided by either of the units (e.g. acoustic on left demonstrator no signal on right demonstrator for case 1 - upper right histogram), whereas blue bars represent user's reported answers (for different experiments with different distances between the units). It can be observed that a better perception of the right signal is possible with a higher distance of the demonstrators. Reducing the distance especially affects the acoustic assignability, as it is more difficult for the user to understand whether sound comes from the left or the right unit. In spite of these natural and expected trends, the results show that the haptic feedback is highly recognisable and highly assignable; acoustic feedbacks are also, in most case, correctly assigned, with misassignments mostly coming from scenarios in which users wrongfully locate the acoustic feedback on the same side from where they receive a haptic stimulation (see, e.g., the histogram on the bottom left corner).

The confusion matrix in Figure 3.42 is generated from the bar diagrams of Figure A 10 by using the classification table shown in Figure A 11. The table allows map wrong (or incomplete) answers produced by the users into off-diagonals entries in the confusion matrices.

assignment for confusion matrix			
actual input	User answer	clasification	Condition
non	haptic	{non_is; hap_is}	-
	acoustic	{non_is; aco_is}	no aco_os
		{aco_os; aco_is}	aco_os
	hapto acoustic	{non_is; hap_is}	-
		{non_is; aco_is}	no aco_os
haptic	non	{hap_is; non_is}	-
	acoustic	{hap_is; non_is} + {non_is; aco_is}	no aco_os
		{hap_is; non_is} + {aco_os; aco_is}	aco_os
		{hap_is; hap_is}	-
	hapto-acoustic	{non_is; aco_is}	no aco_os
acoustic	non	{aco_is; non_is}	no aco_os
	haptic	{aco_is; aco_os}	aco_os
		{aco_is; hap_is}	-
	hapto-acoustic	{aco_is; aco_is}	-
		{non_is; hap_is}	-
hapto-acoustic	non	{aco_is; non_is}	no aco_os
	haptic	{aco_is; aco_os}	aco_os
		{hap_is; non_is}	-
		{aco_is; non_is}	no aco_os
	acoustic	{aco_is; aco_is}	-
		{hap_is; hap_is}	-
	hapto-acoustic	{aco_is; aco_is}	-

Figure A 11: Classification table used for the construction of confusion matrices in Figure 3.42.

Wrong answers can be caused either by a misassignment of the unit form which a certain feedback is produced (e.g., sound being produced by the left unit reported as being produced by the right unit), or a particular stimulation not being perceived at all by the user (e.g., the haptic stimulation or, more unlikely, the acoustic one). The entries in the table in Figure S9 have the following meaning:

- The first column corresponds to the signal actually applied on a certain unit (on either of the sides)
- The second column reports possible (wrong or partial) answers given by the user (for that side)
- The third column reports confusion matrix entries, {row; column}, generated as a result of that particular combination. Subscripts 'is' and 'os' stand for "input side" and "opposite side" respectively (e.g., if the input to which column 1 refers is on the left side, then 'is' means 'left' and 'os' means 'right', and vice versa).
- The 4th column reports conditions under which a certain entry is generated (as a same combination of values on the first and second column can lead to different entries, depending on the scenario). If no condition is specified (-), the corresponding entry is included in the matrix every time that particular input-answer combination occurs.

Note that some incorrect answer combinations lead to multiple entries in the matrix. For example, a DEA (say, the left one) being reported to produce a combined hapto-acoustic feedback (when,

in fact, it was producing only a haptic stimulation, the acoustic one being generated by the right unit) generates two entries: a diagonal term {haptic_l; haptic_l}, accounting for the correct location of the haptic stimulation on the left side; and an off-diagonal {aco_r; aco_l} entry.

If a certain acoustic (or haptoacoustic) signal was applied on either unit, incorrect answers always corresponded to a misassignment of the sound source (left-to-right). For example, in Case 2, sound generated by the left device was interpreted as being generated by the right DEA in 9 cases.

A.9. Geometric model for the COP-DEA capacitance

To compare the measured capacitance change of the COP-DEA with an expected value, a simple geometric model ([222]) is used.

The capacitance of a DE (with n layers) can be calculated from the thickness (L_z) of the films (in a generic deformed configuration) and the corresponding area of the electrodes (A) of the DE (equation 2.1):

$$C = \varepsilon_0 \cdot \varepsilon_r \cdot \frac{A}{L_z} \cdot n = \varepsilon_0 \cdot \varepsilon_r \cdot \frac{A^2}{V_0} \cdot n \quad (\text{xviii})$$

The volume V_0 of the silicone film is considered constant (incompressibility) and the electrode area can be calculated assuming that the deformed DE membrane surface has the shape of a conical frustum with inner radius r_i , outer radius r_o , lateral length and height h (out of plane deformation)

$$A = (r_i + r_o) \cdot \pi \cdot l = (r_i + r_o) \cdot \pi \cdot \sqrt{(r_o - r_i)^2 + h^2} \quad (\text{xix})$$

The capacitance can be thus calculated as a function of the out of plane deformation of the DEA as:

$$C = \varepsilon_0 \cdot \varepsilon_r \cdot \frac{A}{L_z} \cdot n = \varepsilon_0 \cdot \varepsilon_r \cdot \frac{(r_i + r_o)^2 \cdot \pi^2 \cdot ((r_o - r_i)^2 + h^2)}{V_0} \cdot n \quad (\text{xx})$$

The DE volume can be in turn calculated as

$$V_0 = \frac{(r_o^2 - r_i^2)}{\lambda_p^2} \quad (\text{xxi})$$

where λ_p is the pre-stretch in the flat mounting configuration.

List of Tables

TABLE A 1: GLOVE REALISATION STATE OF THE ART. SUBDIVIDED INTO EXOSKELETON, GLOVES WITH FEEDBACK, SENSORY GLOVES CAMERA BASED SYSTEMS, INDUSTRIAL APPLICATIONS AND SCIENTIFIC RESEARCH.....	CLXV
TABLE A 2: MATERIAL PARAMETERS USED IN THE SIMULATION ([225]).....	CLXVIII
TABLE A 3: PARAMETERS USED FOR THE CALCULATION DISCUSSED.	CLXXVI

List of Equations

2.1 ELEMENTARY CAPACITANCE EQUATION	14
2.2 ELEMENTARY CAPACITANCE EQUATION X DIRECTION	14
2.3 ELEMENTARY CAPACITANCE EQUATION X DIRECTION	14
2.4 ELEMENTARY CAPACITANCE EQUATION Z DIRECTION	14
3.26 CHARGE OF A CAPACITOR.....	16
2.6 MECHANICAL ENERGY PLATE CAPACITOR.....	16
2.7 MECHANICAL ENERGY PLATE CAPACITOR.....	17
2.8 FORCE BY ELECTRO- STATIC FIELD.....	17
2.9 MAXWELL STRESS DEA.....	17
2.10 STRAIN IN Z DIRECTION	17
2.11 STRAIN IN X DIRECTION	17
2.12 FORCE PRE TENSIONED MEMBRANE.....	20
2.13MOVEMENT EQUATION PRE TENSIONED MEMBRANE.....	20
2.14 MOVEMENT EQUATION IN POLAR COORDINATES.....	20
2.15 HELMHOLTZ EQUATION	20
2.16 BESSEL EQUATION	20
2.17 MODE SHAPE FUNCTIONS.....	20
2.18 FREQUENCY OF MODE SHAPES.....	20
2.19 MOTION EQUATION OF DE MEMBRANE.....	22
2.20 CHARGE OF A CAPACITOR.....	23
2.21 VOLTAGE DEG	23
2.22 ENERGY OF CAPACITOR.....	23
2.23 ENERGY IN CC CONDITIONS.....	23
2.24 ENERGY IN CV CONDITIONS.....	23
2.25 WEBER-FECHNER-LAW	33
2.26 MECHANICAL IMPEDANCE.....	34
2.27 SOUND PRESSURE LEVEL.....	36
3.1 TIME-VARYING VOLTAGE	52
3.2 QUADRATIC VOLTAGE DEPENDENCY OF DEA THICKNESS.....	52
3.3 QUADRATIC VOLTAGE DEPENDENCY OF DEA THICKNESS WITH BIAS	52
3.4 CHARGING CURRENT	55
3.5 CHARGING CURRENTMAX	55
3.6 CHARGING TIME	55
3.7 DISCHARGING TIME.....	55
3.8 CYCLING TIME SENSING	55
3.9 DYNAMIC OF DE MEMBRANE VIBRATION.....	64

3.10 LINEARIZED MOVEMENT OF DE MEMBRANE POINT	65
3.11 EIGENFREQUENCY OF DE	65
3.12 GEOMETRIC RATIO DE	65
3.13 NATURAL FREQUENCY RELATED TO REFERENCE GEOMETRY.....	68
3.14 FREQUENCY OF THE K-TH VIBRATION-MODE.....	69
3.15 RADIAL STRETCH OF COP-DE MEMBRANE.....	71
3.16 MEMBRANE STRESS OF COP-DE.....	71
3.17 DE THICKNESS BY DEFLECTION.....	71
3.18 MEMBRANE AREA OF COP-DE.....	71
3.19 MEMBRANE STRESS AT DIAMETER D	71
3.20 MULTI-FREQUENCY TIME VARIANT VOLTAGE	78
3.21 HF VOLTAGE COMPONENT	78
3.22 LF AMPLITUDE COMPENSATION	79
3.23 RC CIRCUIT STATE-SPACE-MODEL.....	108
3.24 DERIVED RC CIRCUIT STATE-SPACE-MODEL.....	108
3.25 DISCRETE RC CIRCUIT - EULER.....	108
3.26 DISCRETE RC CIRCUIT - PRE-WARPED TUSTIN METHOD	108
5.1 DE AND BIAS FORCE.....	CLXVIII
5.2 PARALLEL BIASING FORCE	CLXVIII

List of Figures

FIGURE 1.1: EVOLUTION OF INDUSTRY PRODUCTION AND THE DIFFERENT OPERATOR GENERATIONS FROM FIRST INDUSTRY LEVEL TO THE ACTUAL INDUSTRY ENVIRONMENT WITH CYBER PHYSICAL SYSTEMS (CF. [6], [10], [11]).	2
FIGURE 1.2: MAIN PILLARS OF INDUSTRY 4.0. THE DEVELOPED ELEMENTS ARE INTENDED TO IMPROVE THE REALIZATION OF THE HUMAN-MACHINE-INTERACTION AND THE NETWORKING PILLARS (RED MARKED).....	3
FIGURE 1.3: CHALLENGES FOR INDUSTRY OPERATOR (LEFT) AND ELDERLY / DISABLED PEOPLE (RIGHT) AND ADVANTAGES OF INTELLIGENT ASSISTANCE TOOLS. WITH THE MULTIFUNCTIONAL, AUDIO-TACTILE FEEDBACK ELEMENT THE USER CAN BE SUPPORTED BY THE DIRECT INTERACTION WITH THE (DIGITAL) SURROUNDING.	4
FIGURE 1.4: EXEMPLATIVE EAP BASED LOUDSPEAKERS AND HAPTIC TRANSDUCERS ((A) [94]; (B) [103]; (C) [98]; (D) [101]; (E) [97]; (F) [96]; (G) [102]; (H) [104]; (I) ([105], [107]); (J) [106]; (K) ([109], [110]); (L) [111])......	9
FIGURE 1.5: EXEMPLATIVE EAP BASED TEXTILE INTEGRATED ELEMENTS ((A) [19]; (B) [23]; (C) [129]; (D) [131]; (E) [134]; (F) [132]).	11
FIGURE 2.1: FUNCTIONAL PRINCIPLE OF DES AS ACTUATOR (LEFT) AND SENSOR (RIGHT) WITH APPLICATION AND WORKING FIELDS.	14
FIGURE 2.2: QUALITATIVE CAPACITANCE CHANGES DUE TO DIFFERENT KIND OF DEFORMATION FOR A INITIAL CAPACITANCE.	15
FIGURE 2.3: EQUIVALENT CIRCUIT OF DE SENSOR WITH A CASCADE OF RC CIRCUITS. THE PARALLEL RESISTOR IS NEGLIGIBLE (MOHM RANGE); TO REPRODUCE REAL DES, A CASCADE OF SEVERAL SERIES CIRCUITS OF R AND C IS NECESSARY.	16
FIGURE 2.4: ACTUATOR CONFIGURATION PRINCIPLES (A) STACKED ACTUATOR WITH THICKNESS ACTUATION, (B) MEMBRANE ACTUATOR IN PLANE DIRECTION (C) MEMBRANE ACTUATOR OUT OF PLANE DIRECTION (D) ROLLED ACTUATOR (E) TUBE ACTUATOR.	18
FIGURE 2.5: DIFFERENT CONFIGURATIONS AND WORKING PRINCIPLES OF DEA BASED LOUDSPEAKER. (A) CONVENTIONAL LOUDSPEAKER WITH DEA BASED DRIVE, (B) DEA MEMBRANE AS DRIVING UNIT AND DIAPHRAGM AND (C) STRUCTURAL MEMBRANE VIBRATION WITH MECHANICAL OR FLUIDIC BIASING.	19
FIGURE 2.6: ELEMENTARY PART OF A VIBRATIONAL MEMBRANE WITH ACTING AND RESULTING FORCES (C.F. [170]).	19
FIGURE 2.7: NORMAL MODES OF CIRCULAR MEMBRANE WITH 180° OUT OF PHASE VIBRATION (RED -GREEN AREAS) SEPARATED BY NODAL LINES. FREQUENCY DEPENDENCY OF VIBRATION, INCREASING FOR EVERY NODAL LINE (C.F. [170]).	21
FIGURE 2.8: (A) BLOCK-DIAGRAM STRUCTURE OF THE COUPLED MODEL (B) UNDEFORMED AND DEFORMED DE MEMBRANE AND (B) COP-DEA DISCRETISATION FOR MODELLING (C.F. [59]).	22
FIGURE 2.9: WORKING PRINCIPLE OF DEG (A) ENERGY HARVESTING CYCLE (B) DIFFERENT WORKING SCHEMES (CC, CV, OT AND CE CYCLE).	23
FIGURE 2.10: HUMAN MOTION ENERGY HARVESTING WITH DEGS FOR (A) SHOES BASED ON INFLATABLE DEG [180] (B) SHOES BASED ON STACKED DEGS [181] AND (C) KNEE ARTICULATION [182] (C.F. [179]).	24
FIGURE 2.11: MANUFACTURING STEPS FOR DE FABRICATION INCLUDING ELECTRODE MATERIAL AND SILICONE FILM PREPARATION, SCREEN-PRINTING PROCESS, BREAKDOWN TEST, STACKING AND CLAMPING OF THE PRODUCED ACTUATOR.	25
FIGURE 2.12: SCREEN PRINTING PROCESS WITH (A) SIEVE FOR THE DE DESIGN (B) METAL FRAME WITH SILICONE FILM AND (C) EXAMPLES OF POSSIBLE DE DESIGNS. (D) MAXIMUM ELECTRIC FIELD STRENGTH MEASUREMENTS FOR DEAS WITHOUT PRE-STRETCH.	25
FIGURE 2.13: COMPONENTS FOR A DE CHARACTERISATION SETUP. WITH ELEMENTS FOR THE CONTROL OF THE SYSTEM, THE MECHANICAL OR ELECTRICAL STIMULATION OF THE DE SPECIMEN AND VALIDATION/MEASUREMENT UNITS.	26
FIGURE 2.14: (A) COMPONENTS FOR DES CHARACTERISATION AND (B) CAPACITANCE AND RESISTANCE MEASUREMENT OF A REAL DES AND ASSUMED SIMPLIFIED ELECTRICAL MODEL.	27

FIGURE 2.15 COMPONENTS FOR DEA CHARACTERISATION.....	27
FIGURE 2.16: HIGH FREQUENCY MEASUREMENT SETUP FOR DE CHARACTERISATION WITH (A) COMPONENTS OF A LOUDSPEAKER TEST RIG (B) 3D LASER VIBROMETER FOR MEMBRANE MOVEMENT MEASUREMENTS (C) ANECHOIC BOX FOR ACOUSTIC MEASUREMENTS.....	28
FIGURE 2.17: DE SENSOR ELEMENT WITH PERIPHERAL ELEMENTS. THE HUMAN INTERACTION IS SENSED BY THE DES WITH A SUITABLE SENSING ELECTRONIC AND MEASUREMENT BASED DATA ANALYSIS. THE ELECTRICAL AND MECHANICAL CONNECTION REPRESENT THE INTERCONNECTING LEVEL BETWEEN THE DES AND THE SURROUNDING SYSTEM STRUCTURE.	29
FIGURE 2.18 DE ACTUATOR ELEMENT WITH PERIPHERAL ELEMENTS. THE DEA, COMBINED WITH A SUITABLE HIGH VOLTAGE AND CONTROL ELECTRONIC, PROVIDES TACTILE AND ACOUSTIC FEEDBACK TO THE USER. THE ELECTRICAL AND MECHANICAL CONNECTION REPRESENT THE INTERCONNECTING LEVEL BETWEEN THE DEA AND THE SURROUNDING SYSTEM STRUCTURE.....	30
FIGURE 2.19: STRUCTURAL ORGANISATION OF THE NERVOUS SYSTEM (C.F. [187])......	30
FIGURE 2.20: (A) THE NERVOUS SYSTEM OF THE HUMAN BODY AS WELL AS (B) THE STRUCTURE OF NEURONS AND (C) THE PROCESS OF PRECEPTING A SENSORY STIMULUS [189].	31
FIGURE 2.21: THE HUMAN SENSE, INCLUDING MECHANICAL, CHEMICAL, RADIATION AND HAPTIC SENSING, AND THE HAPTIC SUB-GROUP (C.F.[192]). THE HAPTIC SUB-GROUP CONTAINS TACTILE, KINESTHETICS, HEAT AND PAIN FEELING. THE SENSE OF BALANCE IS LOCATED IN THE EAR AND REPRESENTS A HYBRID FORM OF HAPTIC AND HEARING SENSE.	32
FIGURE 2.22: PRINCIPLE OF THE TACTILE AND KINESTHETIC PERCEPTION (C.F. [195], [196], [197], [198], [199]).	32
FIGURE 2.23: JUST NOTICEABLE DIFFERENCE FOR FORCE AND DEFLECTION OF HUMAN SKIN (C.F.[193], [194], [202], [203], [204]).	33
FIGURE 2.24: SIMULTANEOUS AND SUCCESSIVE SPECIAL THRESHOLDS OF DIFFERENT PARTS OF THE HUMAN BODY(C.F.[205], [206].)	34
FIGURE 2.25: QUALITATIVE PROGRESSION OF THE IMPEDANCE AND PHASE OF THE MECHANICAL IMPEDANCE (C.F. [202], [207]).	34
FIGURE 2.26: SINGLE MECHANICAL ELEMENTS (A) AND SIMPLE MODEL FOR THE HUMAN SKIN (B). AS WELL AS A MORE COMPLEX MODEL OF THE HUMAN SKIN (C) ([202], [207]).	35
FIGURE 2.27: ANATOMY OF THE EAR AND THE AUDITORY MEATUS, INCLUDING OUTER, MIDDLE AND INNER EAR [208]......	36
FIGURE 2.28: NORMAL LOUDNESS CONTOURS FOR SOUND PRESSURE LEVEL AND INTENSITY (PURE TONES) ([209], [210]). PHONS LINES REFER TO EQUALLY LOUD PERCEIVED LOUDNESS BY THE HUMAN HEARING.	36
FIGURE 2.29: SPL JND OF THE HUMAN HEARING FOR DIFFERENT FREQUENCIES DEPENDING ON THE INITIAL SPL AND THE FREQUENCY JND DEPENDING ON THE INITIAL FREQUENCY ([213], [214]).	37
FIGURE 2.30: ASSISTANCE TOOL AS USER INTERFACE FOR HMI. THE USER INTERFACE TRANSFERS THE SENSED USER INPUT TO THE UNDERLAYING DIGITAL STRUCTURE AND ENABLES A INTERACTION WITH THE USER BY STIMULATING SPECIFIC PERCEPTIVE RECEPTORS OF THE USER.....	38
FIGURE 2.31: ASSISTANCE TOOL AS A MAIN ELEMENT OF A CYBER-PHYSICAL SYSTEM (CPS) CF.[8]. A MULTI-FUNCTIONAL ASSISTANCE TOOL CAN BE USED AS DIRECT INTERACTION WITH THE VIRTUAL WORLD (VR APPLICATIONS) OR AS INTERACTION WITH REAL PHYSICAL COMPONENTS (AR APPLICATIONS). THE SENSING CAPABILITY OF THE ASSISTANCE TOOL CAN ADDITIONALLY BE USED FOR THE SENSING OF THE ENVIRONMENT (PHYSICAL COMPONENT) AND CONNECT THE VIRTUAL COMPONENT WITH THE PHYSICAL COMPONENT.	39
FIGURE 2.32: STRUCTURE AND COMPONENTS OF INTERACTION INTERFACES. THE SENSOR COMBINED WITH A CERTAIN SENSING ELECTRONICS IS USED TO MEASURE THE USER INPUT. A COMMUNICATION UNIT MANAGES THE INTERACTION TO THE SURROUNDING PERIPHERY AND THE INTERNAL ELECTRONICS (SENSING AND CONTROL ELECTRONICS). THE CONTROL ELECTRONIC DRIVES THE OUTPUT ELEMENTS FOR THE INTERACTION WITH THE USER.	40
FIGURE 2.33 STRUCTURE COMPONENTS OF DE-BASED INTERACTION INTERFACES. THE DE SENSOR COMBINED WITH A CERTAIN SENSING ELECTRONICS (CAPACITANCE MEASUREMENT) IS USED TO MEASURE THE USER INPUT. A COMMUNICATION UNIT MANAGES THE INTERACTION TO THE SURROUNDING PERIPHERY AND THE INTERNAL ELECTRONICS (SENSING AND CONTROL ELECTRONICS). THE CONTROL ELECTRONIC DRIVES THE HIGH VOLT POWER	

AMPLIFIER TO CONTROL THE DE ACTUATOR FOR THE INTERACTION WITH THE USER. ONE DE ELEMENT CAN FULFIL BOTH WORKS OF THE DE (SENSING AND ACTUATION).	41
FIGURE 2.34: EXAMPLES OF DE SENSING ELEMENTS FOR (A) STRIP IN PLANE (SIP) STRETCH SENSING (B) JOINT ANGLE MEASUREMENT AND (C) USER INPUT MEASUREMENT WITH CIRCULAR OUT OF PLANE (COP) DE.....	42
FIGURE 2.35: INFLUENCE OF THE STRUCTURE GEOMETRY AND PRE-STRETCH OF THE DE MEMBRANE TO THE CAPACITANCE-FORCE PERFORMANCE. (A) 30 % BIAxIAL PRE-STRETCH AND (B) 20 BIAxIAL PRE-STRETCH OF THE MEMBRANE. THE DIFFERENT STRUCTURE VALUES CHARACTERIZE THE DISTANCE Δr BETWEEN THE INTERSECTION STRUCTURES ON OPPOSITE SIDE OF THE DE [215].....	43
FIGURE 2.36: MEASURED DEFORMATION OF ONE SEGMENT OF THE FORCE SENSOR WITH (A) FORCE AND DEFORMATION OF THE PRESSED SENSOR SEGMENT AND (B) CAPACITANCE CHANGE FOR THE PRESSED SEGMENT AND COMPARISON WITH THE CAPACITANCE CHANGE OF THE THREE OTHER SEGMENTS.(C) CAPACITANCE VARIATION FOR DIFFERENT GEOMETRIES AND PRE-STRETCH OF THE SILICONE FOIL FOR DIFFERENT SENSORS [215].	44
FIGURE 2.37: MANUFACTURING PROCESS OF THE DE SENSING ELEMENT INCLUDING DE MANUFACTURING, ELECTRICAL CONNECTION, LAMINATION PROCESS, POSSIBLE TEXTILE INTEGRATION AND MECHANICAL CONNECTION [215].	45
FIGURE 2.38: TEXTILE INTEGRATED DE ELEMENT WITH SILICONE FRAME. THE DEA IS ENCAPSULATED BETWEEN TWO SILICONE LAYERS AND CONNECTED TO THE TEXTILE	46
FIGURE 2.39: TEXTILE INTEGRATION AND CONNECTION OF DE ACTUATOR ELEMENTS FORM SINGLE DE MANUFACTURING TO SYSTEM INTEGRATION OF THE WHOLE ACTUATOR.	46
FIGURE 2.40: EXAMPLE FOR A COMMUNICATION MAIN BOARD FOR USER INTERACTION [221].....	47
FIGURE 3.1: CONE DEA SETUP (A) FLAT PRE-STRETCHED AND BIASED MOUNTING CONFIGURATION WITH NBS WITH AND WITHOUT VOLTAGE (B) CONSTRUCTION OF HV AND SENSING LAYER AND (C) CONNECTION TO THE SINGLE DE LAYERS (C.F. [216], [225]).	49
FIGURE 3.2: WORKING PRINCIPLE OF THE AUDIO-TACTILE ELEMENT WITH (A) DEFORMATION MODES OF THE DEA (B) MOTION OF THE DEA ELEMENT FOR LF INPUT, HF INPUT AND COMBINED INPUT VOLTAGES AND (C) SPECTRAL OF AVERAGE AXIAL VELOCITY AND THE RESULTING ACOUSTIC PRESSURE (C.F [225])......	51
FIGURE 3.3: FORCE AND CAPACITANCE MEASUREMENT DEPENDING ON THE END-EFFECTOR DEFORMATION ([216]).54	
FIGURE 3.4: FUNCTIONAL PRINCIPLE OF THE USED DE SENSING ELECTRONIC (A) EQUIVALENT CIRCUIT OF THE CAPACITANCE MEASUREMENT, (B) CHARGING AND DISCHARGING TIME DIAGRAM. ([216])......	55
FIGURE 3.5: MEASUREMENT AND LOGIC ELECTRONIC TO MEASURE THE DEFORMATION OF A DE ON A FLEXIBLE PRINTED CIRCUIT BOARD (FLEX PCB) [221].	56
FIGURE 3.6: SENSING TESTS WITH USERS. PUSHING THE BUTTON CHANGES THE CAPACITANCE AND ALLOWS MEASURING THE NUMBER OF TIMES THE INTERFACE HAS BEEN PUSHED. COUNTS OF THE NUMBER OF TOUCHES PERFORMED BY THE SENSING ALGORITHM FOR EACH THRESHOLD ARE REPRESENTED WITH RED AND BLUE DOTS, AND WRONG/DOUBLE COUNTS ARE REPRESENTED WITH BLACK MARKERS ([216])......	57
FIGURE 3.7: ELECTRONICS ASSEMBLY WITH SILICONE HOLDER, BATTERY, VOLTAGE SUPPLY AND PROGRAMMING UNIT AND SENSING-ELECTRONIC. (A) MEASUREMENT UNIT WITH BATTERY ELEMENT, (B) POWER SUPPLY AND SECOND MEASUREMENT UNIT AND (C) PICTURE OF ASSEMBLED ELECTRONICS WITH SILICONE HOLDER. ([215] C.F. [231]).58	
FIGURE 3.8: OUTPUT FORCE FOR VARIOUS FREQUENCIES AND PRE STRETCH OF DIFFERENT TACTILE FEEDBACK ENERGY	59
FIGURE 3.9: HIGH VOLTAGE CIRCUIT PRINCIPLES AND DIFFERENT REALISATIONS.	60
FIGURE 3.10: REALISED HV CIRCUIT WITH RESONANT CONVERTER, RECTIFIER AND DISCHARGING STAGE ([221]; C.F. [31], [32])......	61
FIGURE 3.11: TEXTILE INTEGRATION PRINCIPLE OF HIGH VOLTAGE ELECTRONICS.	61
FIGURE 3.12: (A) LAYOUT OF A COP DE LOUDSPEAKER WITH INITIAL IN PLANE PRE-STRETCHING AND OUT OF PLANE WORKING CONFIGURATION AND (B) EXEMPLATIVE VIBRATION MODES OF THE DE MEMBRANE (C.F [249])......	66
FIGURE 3.13: BLOCK-DIAGRAM STRUCTURE OF THE (A) ELECTRO-MECHANICAL AND ACOUSTIC COUPLED MODEL AND (B) THE SPLITTING IN A SLOW AND FAST DE DYNAMIC TO REALISE A LPV MODEL [175]	66

FIGURE 3.14: (A) TEST SETUP WITH ANECHOIC SOUND ABSORBING CHAMBER FOR SOUND MEASUREMENTS (B) SCHEMATIC AND PHOTO OF THE EXPERIMENTAL TEST BENCH AND DISTRIBUTION OF THE MEASUREMENT POINT. (C) EXPERIMENTAL CONTOUR PLOTS OF THE DEA MEMBRANE VELOCITY DISTRIBUTION AND MODE NOMENCLATURE (C.F. [59])	67
FIGURE 3.15: COMPARISON OF MODEL (SOLID LINES) AND EXPERIMENTAL (DASHED LINES) OF THE (A) AVERAGE VELOCITY SPECTRA AND (B) SPL OF THE COP DE MEMBRANE. (C.F. [59], [174]).	68
FIGURE 3.16: (A) MEASURED SPL AS A FUNCTION OF THE FREQUENCY, FOR DIFFERENT MEMBRANE THICKNESSES; (B) NATURAL FREQUENCY OF THE FIRST MODE (0,1) AS A FUNCTION OF THE INITIAL THICKNESS. DATA ARE RELATIVE TO A DEA WITH $L_z, 0 = 30$ MM SUBJECT TO BIAS VOLTAGE OF 1 kV AND OUT-OF-PLANE PRE-DEFORMATION $h = 0.25 \cdot d_0$ (C.F. [249]).	70
FIGURE 3.17: (A) MEASURED SPL AS A FUNCTION OF THE FREQUENCY, FOR DIFFERENT MEMBRANE DIAMETERS; (B) NATURAL FREQUENCY OF THE FIRST MODE (0,1) AS A FUNCTION OF THE DIAMETER d_0 . DATA ARE RELATIVE TO DEA WITH $L_z, 0 = 150$ MM (3 LAYERS) SUBJECT TO BIAS VOLTAGE OF 1 kV AND OUT-OF-PLANE PRE-DEFORMATION $h = 0.25 \cdot d_0$	70
FIGURE 3.18: RESULTING PERFORMANCE OF A COP-DE DEPENDING ON THE INNER AND OUTER DIAMETER ((A), (B), (C)) WITH (D) BLOCKING FORCE AND (E) STROKE (C.F. [252]). THE GEOMETRIES OF THE SIX DIFFERENT TEST SPECIMENS USED IN [252] ARE : 1" SMALL (ID: 8.6 MM; OD: 21 MM); 1" MEDIUM (ID: 11.4 MM; OD: 21 MM); 1" SMALL (ID: 13.5 MM; OD: 21 MM); 2" SMALL (ID: 8.6 MM; OD: 41.9 MM) ; 2" MEDIUM (ID: 20.1 MM; OD: 41.9 MM) ; 2" SMALL (ID: 26.8 MM; OD: 41.9 MM).	72
FIGURE 3.19: (A) SPL AS A FUNCTION OF THE FREQUENCY RESPONSE OF THE DE MEMBRANE FOR DIFFERENT VALUES OF HD AND (B) FUNCTION OF THE EIGENFREQUENCY OF MODE (0,1) AS FUNCTION OF HD (C.F. [174]).	72
FIGURE 3.20: SPL AS A FUNCTION OF THE FREQUENCY RESPONSE FOR A DEA WITH $d_0 = 30$ MM AND $t_0 = 150$ MM SUBJECT (A) TO CONSTANT OUT-OF-PLANE DEFORMATION (TOP: $h/d_0 = 25\%$, BOTTOM: $h/d_0 = 33\%$) AND DIFFERENT BIAS VOLTAGES; AND (B) CONSTANT BIAS VOLTAGE (TOP: $V_b = 1.0$ kV, BOTTOM: $V_b = 2.5$ kV) AND DIFFERENT MECHANICAL PRE-LOADS	73
FIGURE 3.21: RANGE OF VARIATION OF NATURAL FREQUENCY OF THE FIRST MODE (0,1) FOR A DEA WITH $d_0 = 30$ MM AND $t_0 = 150$ MM SUBJECT TO DIFFERENT OUT-OF-PLANE PRE-LOADS AND BIAS VOLTAGES	74
FIGURE 3.22: COMPARISON OF THE, (A) MECHANICAL DE BEHAVIOUR AND HYSTERESIS, (B) ELECTRO-MECHANICAL BEHAVIOR AND OUTPUT PERFORMANCE, AND (C) THE SYSTEM BEHAVIOR (DE + NBS) FOR SPUTTERED METAL ELECTRODES AND SCREEN-PRINTED CARBON BLACK ELECTRODE	75
FIGURE 3.23: SPL OF SPUTTERED METAL ELECTRODE MEMBRANE FOR (A) DIFFERENT OUT-OF-PLANE DEFORMATIONS AND (B) DIFFERENT BIAS VOLTAGE	76
FIGURE 3.24: SPL COMPARISON FOR SPUTTERED AND SCREEN-PRINTED ELECTRODE WITH (A) SAME MEMBRANE STRETCH AND (B) SAME DEFORMATION	77
FIGURE 3.25: DIRECT SPL COMPARISON FOR SPUTTERED AND SCREEN-PRINTED ELECTRODE WITH (A) SAME MEMBRANE STRETCH AND (B) SAME DEFORMATION	77
FIGURE 3.26: RESPONSE OF THE DEA TO A MULTI-CHROMATIC INPUT VOLTAGE (A) SINUSOIDAL AND (B) SQUARE WAVE LF INPUT VOLTAGE WITH A HIGH FREQUENCY PITCH (CONSTANT AMPLITUDE BLACK AND VARIABLE AMPLITUDE RED). (C) AXIAL FORCE AND SPL IN TWO DIFFERENT BLOCKING CONDITIONS ([225]).	79
FIGURE 3.27: SPL AND STROKE/FORCE VARIATION FOR MULTI CHROMATIC INPUT VOLTAGE ($V_{max} = 2.4$ kV, $V_{min} = 0.8$ kV AND $V_a = 0.1$ kV). LEFT COLUM ARE FREE DISPLACEMENT TEST, RIGHT COLUMN BLOCKING FORCE TEST AND UPPER ROW REFERS TO CONSTANT LF SINUSOIDAL EXCITATION, WHILE THE LOWER ROW REFERS TO A HF SIGNAL WITH 1180 Hz (C6#) ([225]).	80
FIGURE 3.28: SOUND PRESSURE LEVEL AT 0.35 M IN FRONT OF THE DEA (INPUT: VOLTAGE SWEEP WITH AMPLITUDE $V_a = 100$ V AND DIFFERENT BIAS LEVELS). TWO SCENARIOS ARE CONSIDERED: FREE AND BLOCKED END-EFFECTOR. IN EACH BLOCKING TEST, THE OUT-OF-PLANE DISPLACEMENT OF THE DEA IS SET EQUAL TO THE VALUE MEASURED AT THE SAME BIAS VOLTAGE IN FREE CONDITIONS ([225]).	81
FIGURE 3.29: STRUCTURE COMPONENTS OF DE-BASED INTERACTION INTERFACES BASED ON MULTI-FUNCTIONAL DEA. THE TACTILE AND AUDITIVE FEEDBACK CAN BE SIMULTANEOUSLY REALISED WITH ONE DEA MEMBRANE, THE SENSING IS INTEGRATED IN A ADDITIONALLY SENSING LAYER, STACKED TO THE ACTUATION LAYERS.	82

FIGURE 3.30: HOUSING OF THE DEA INTERFACE. (A) EXPLODED VIEW AND (B) CUT SIDE VIEW OF THE DEVICE AND (C) TOP VIEW WITH CABLES CONNECTED ([216]).	83
FIGURE 3.31: SUBCOMPONENTS OF THE DEA INTERFACE INCLUDING SENSING ELECTRONIC, MICROCONTROLLER, HV ELECTRONIC AND MULTI-FUNCTIONAL DET INTERFACE WITH HOUSING ([216]).	84
FIGURE 3.32: TEST SETUP FOR MULTI-MODE MEASUREMENTS WITH FORCE-, SOUND- AND DISPLACEMENT MEASUREMENT UNITS (C.F. [216]).	85
FIGURE 3.33: LF FREE DISPLACEMENT MEASUREMENT WITH AND WITHOUT HOUSING (LEFT); BLOCKING FORCE FOR DIFFERENT PRELOAD POSITIONS (RIGHT) ([216]).	86
FIGURE 3.34: SPL OF THE PROTOTYPE (WITH HOUSING) FOR DIFFERENT CONTROL INPUT SIGNALS ([216]).	87
FIGURE 3.35: INFLUENCE OF THE HOUSING ON THE SPL (LEFT); AND DIRECTIVITY ANALYSIS OF THE SPL FOR DIFFERENT ANGULAR POSITIONS OF THE MICROPHONE (RIGHT) ([216]).	88
FIGURE 3.36: A) TIME-BEATING LOUDSPEAKER. THE PLOT SHOWS AN EXCERPT (TWO BARS) OF THE TIMESERIES OF THE APPLIED VOLTAGE, THE AXIAL STROKE, AND THE ACOUSTIC PRESSURE. THE DEA IS DRIVEN WITH AN INPUT WHICH IS THE SUM OF A HIGH-FREQUENCY COMPONENT RESPONSIBLE FOR THE TUNE REPRODUCTION, AND A LOW FREQUENCY COMPONENT, CAUSING THE DEA END-EFFECTOR TO MOVE UPWARD IN SYNC WITH THE BEATS OF THE TUNE'S TEMPO. B–D) DEA PLAYING A TUNE UNDER LOAD. B) EXCERPT OF A TIME-SERIES OF VOLTAGE, STROKE AND ACOUSTIC PRESSURE FOR THE FREE DEA (TOP) AND IN THE PRESENCE OF A 20 G MASS APPLIED ON THE DEA'S END-EFFECTOR. C) INCREASING THE VOLTAGE FROM $V_{min} = 0.8$ kV TO $V_{max} = 2.6$ kV CAUSES THE DEA TO LIFT UP THE MASS BY 1.8 MM, WHILE THE TUNE IS HITTING THE TOP NOTES. D) TIME-TREND OF THE SPL (MOVING-AVERAGE) FOR THE TWO CASES WITH FREE AND LOADED DEA ([225]).	91
FIGURE 3.37: AUDIO-TACTILE DEA INTERFACE. A) PICTURE OF A USER PUSHING THE DEA OD, HENCE TRIGGERING AN AUDIO-TACTILE RESPONSE. B) A CONSTANT VOLTAGE OF 1.6 kV IS INITIALLY APPLIED ON THE DEA. PUSHING THE INTERFACE WITH A FINGER CAUSES A PEAK IN THE CURRENT. WHEN THE CURRENT SURPASSES A FIXED THRESHOLD, THE DEA RESPONDS WITH A COMPLEX FEEDBACK CONSISTING OF: A CLICK SOUND (2 kHz FREQUENCY, WITH EXPONENTIALLY DECREASING AMPLITUDE), FOLLOWED BY A LOW-FREQUENCY (4 Hz) AXIAL MOTION OF THE END-EFFECTOR AND A SUPERPOSED PULSATED SOUND (1.5 kHz WITH EXPONENTIALLY DECREASING AMPLITUDE). IN THE PLOTS, THE DEA REPEATS ITS ROUTINE TWICE: IN THE FIRST ITERATION, THE USER PUSHES THE DEA TO TRIGGER IT AND KEEPS IT PRESSED ALL THROUGH THE ROUTINE; IN THE SECOND ITERATION, THE USER PUSHES THE DEA AND THEN REMOVES THE FINGER ([225]).	92
FIGURE 3.38: FEEDBACK CHARACTERISTIC (BLOCKING FORCE, FREE DISPLACEMENT, SPL IN FREE MOTION CONDITION) OF THE DE INTERFACE SUBJECT TO THREE DIFFERENT VOLTAGE EXCITATION WAVEFORMS. TOP: LF EXCITATION SIGNAL (RENDERING A TACTILE STIMULATION); MIDDLE: COMPOSITE LF+HF WAVEFORM (PRODUCING A COMBINED AUDIO-TACTILE STIMULATION). BOTTOM: HF EXCITATION (SOUNDTRACK) ([216]).	94
FIGURE 3.39: TEST SUBJECTS' RATING OF THE TACTILE AND ACOUSTIC OUTPUT INTENSITY FOR THREE DIFFERENT APPLIED EXCITATION SIGNALS (LEFT: LF TACTILE ONLY; MIDDLE: LF+HF AUDIO-TACTILE; RIGHT: HF ACOUSTIC ONLY, AS DEFINED IN FIGURE 3.38). RED CENTRAL LINES INDICATE MEDIAN VALUES, TOP AND BOTTOM EDGES OF THE BLUE BOX INDICATE 25 TH AND 75 TH PERCENTILES, BLACK ERROR BARS INDICATE THE MAXIMA AND MINIMA DATA POINT AND THE RED '+' MARKER INDICATES OUTLIERS (WHEN PRESENT). DATA WERE PROCESSED USING THE IQR COMMAND IN MATLAB. LABELS HA. AND AC. ON THE HORIZONTAL AXIS DENOTE "HAPTIC" AND "ACOUSTIC" FEEDBACKS RESPECTIVELY (C.F [216]).	95
FIGURE 3.40: USER TEST SETUP FOR LOCAL ASSIGNABILITY TESTS WITH TWO UNITS. USER POSITION AND DIFFERENT LOCATIONS OF THE DEMONSTRATORS ([216]).	96
FIGURE 3.41: PERMUTATIONS OF EXCITATION SIGNALS APPLIED ON THE TWO DEAs FOR USER TESTS ([216]).	96
FIGURE 3.42: CONFUSION MATRIX FOR THE USER TESTS WITH 2 REPLICAS OF THE DEA BUTTON, LOCATED AT A DISTANCE OF 10 CM (A), 20 CM (B) AND 30 CM (C) FROM ONE ANOTHER. THE MATRIX ELEMENTS CORRESPOND TO DIFFERENT TYPES OF STIMULI (HAPTIC, ACOUSTIC, NO STIMULUS), ELEMENTS ON THE ROWS STAND FOR THE ACTUAL FEEDBACKS GENERATED BY THE UNITS, WHEREAS ELEMENTS ON THE COLUMNS REPRESENT STIMULI PERCEIVED BY THE USERS. ELEMENTS ON THE DIAGONAL DENOTE A CORRECT ASSOCIATION BETWEEN SUPPLIED STIMULUS AND USER'S ANSWER. ENTRIES IN THE MATRIX CORRESPOND TO THE NUMBER OF TIMES A CERTAIN COMBINATION WAS REPORTED BY USERS. PERCENTAGES ON THE DIFFERENT ROWS QUANTIFY HOW OFTEN A GIVEN STIMULUS WAS	

CORRECTLY IDENTIFIED BY THE USER. PERCENTAGES ON THE COLUMNS INDICATE HOW OFTEN A CERTAIN FEEDBACK CATEGORY REPORTED BY USERS MATCHED THE ACTUAL APPLIED STIMULUS ([216]).	98
FIGURE 3.43: CONTROLLED WORKING MODES OF THE DEA SYSTEM AND CORRESPONDING HIGH VOLTAGE SIGNALS GENERATED BY THE CUSTOM MADE ELECTRONIC [221].	99
FIGURE 3.44: HOUSING AND SETUP OF THE MULTI-MODE DEA DEVICE, INCLUDING HOUSING, DEA-ELEMENT, NBS AND ELECTRONICS [221].	100
FIGURE 3.45: DISPLACEMENT OF THE END-EFFECTOR FOR DIFFERENT VOLTAGE AMPLITUDES [221].	102
FIGURE 3.46: MEASURED ACOUSTIC PRESSURE FOR SINUSOIDAL-SWEEP (0 – 2 KHz) WITH A BIAS VOLTAGE OF 1.5 kV AND AMPLITUDE OF 100 V [221].	102
FIGURE 3.47: SPL OF THE DEA WITH CUSTOM FOR DIFFERENT INPUT SIGNALS OF THE HV SOURCE (TOP). COMPARISON OF THE SPL PERFORMANCE OF THE DEA WITH CUSTOM AND COMMERCIAL HV AMPLIFIERS (BOTTOM) [221].	103
FIGURE 3.48 TOTAL HARMONIC DISTORTION (THD) OF THE SINUSOIDAL SOUND SIGNAL COMPARED WITH COMMERCIAL ELECTRONIC [221].	104
FIGURE 3.49: MULTIMODE LF AND HF COMBINED WORKING MODE OF THE DEA. WITH INPUT VOLTAGE (LF SIN + HF SIN AND LF SIN+ HF SONG), MEASURED SOUND PRESSURE AND DISPLACEMENT OF THE END-EFFECTOR [221].	105
FIGURE 3.50: STRUCTURE COMPONENTS OF DE-BASED INTERACTION INTERFACES WITH MULTI-FUNCTIONAL DEA COMBINED WITH SELF-SENSING.	106
FIGURE 3.51: WORKING REGIONS OF THE AUDIO-TACTILE DEA. WITH LF LINEAR MOVEMENT REGION, MF NO FEEDBACK REGION AND HF ACOUSTIC FEEDBACK REGION. SELF-SENSING REGION CAN BE USED FOR MF AND HF REGIONS AND PARTIALLY LF REGION. THE PLOT IS QUALITATIVE: FREQUENCY RANGES SHOWN ON THE FREQUENCY AXIS ARE AN APPROXIMATE INDICATION THAT HOLDS FOR CENTIMETRE-SCALE DEAS WITH FEATURES/MATERIAL PROPERTIES DISCUSSED ([261]).	107
FIGURE 3.52: DE EQUIVALENT CIRCUIT FOR SELF-SENSING MODEL BY REDUCING THE RC CASCADE TO A SIMPLIFIED SINGLE RC ELEMENT TO ROUGHLY REPRESENT THE DEA ELECTRICALLY (C.F. FIGURE 3.4).	107
FIGURE 3.53: DIFFERENT WORKING MODES OF THE COP-DEA. LEFT: MULTI-MODE AUDIO-TACTILE EXCITATION WITH HF STRUCTURAL VIBRATION AND LF LINEAR MOVEMENT AS WELL AS TWO ALTERNATIVE MODES FOR SELF-SENSING (HF SOUND-PRODUCING WORKING MODE AND MF SILENT WORKING MODE). RIGHT: USER IMPOSED DEFORMATION WITH TWO SELF-SENSING MODES (HF SOUND-PRODUCING WORKING MODE AND MF SILENT WORKING MODE) ([261]).	109
FIGURE 3.54: COP-DEA FREQUENCY RESPONSE IN TERMS OF DISPLACEMENT AND SOUND PRESSURE OUTPUT, HIGHLIGHTING THE LF, MF AND HF REGION OF THE RESPONSE ([261]).	110
FIGURE 3.55: SELF-SENSING ALGORITHM COMPARISON WITH LCR METER MEASUREMENT AND GEOMETRIC MODEL (C.F.[261]).	111
FIGURE 3.56: SELF-SENSING PERFORMANCE FOR MOTOR-INDUCED MOVEMENT LEFT: SINUSOIDAL HF SIGNAL V. RIGHT: HF SIGNAL V RENDERING A SOUND TRACK ([261]).	112
FIGURE 3.57: SELF-SENSING PERFORMANCE FOR VOLTAGE-INDUCED MOVEMENT LEFT: SINUSOIDAL HF SIGNAL V. RIGHT: HF SIGNAL V RENDERING A SOUND TRACK ([261]).	113
FIGURE 3.58: CHARACTERIZATION OF THE CC BASED ON SELF-SENSING (DOT MARKERS) AND THE SPL (TRIANGULAR MARKERS) FOR DIFFERENT PARAMETER VARIATIONS OF THE DEA SYSTEM STIMULATION, WITH MOTOR INDUCED MOVEMENT AND SINUSOIDAL HF SIGNAL ([261]).	114
FIGURE 3.59: CHARACTERIZATION OF THE CC BASED ON SELF-SENSING (DOT MARKERS) AND THE SPL (TRIANGULAR MARKERS) FOR DIFFERENT PARAMETER VARIATIONS OF THE DEA SYSTEM STIMULATION, WITH MOTOR INDUCED MOVEMENT AND POLYCHROMATIC HF SIGNAL (SOUNDTRACK) ([261]).	115
FIGURE 3.60: CHARACTERIZATION OF THE CC (DOT-MARKERS) BASED ON SELF-SENSING, THE SPL (TRIANGULAR-MARKERS), HF (CROSS-MARKERS) AND LF (CIRCULAR-MARKERS) MEAN DISPLACEMENT. DIFFERENT PARAMETER VARIATIONS OF THE DEA SYSTEM STIMULATION, WITH SELF- INDUCED MOVEMENT FOR (A) SINUSOIDAL HF SIGNAL AND (B) POLYCHROMATIC HF SIGNAL ([261]).	116
FIGURE 3.61: USER INDUCED DEFORMATION AND CORRESPONDING CLOSED-LOOP AMPLITUDE ADAPTION OF THE HF SIGNAL VIA SELF-SENSING THROUGH THE HF DRIVING SIGNAL APPLIED TO THE DE ([261]).	117

FIGURE 3.62: USER INDUCED DEFORMATION AND CORRESPONDING (A) FREQUENCY ADAPTION OF THE HF SIGNAL VIA THROUGH THE HF SIGNAL APPLIED TO THE DE; (B) HAPTIC AND ACOUSTIC FEEDBACK ADAPTATION VIA SELF-SENSING THROUGH A MF PROBING SIGNAL ([261]).	118
FIGURE 3.63: SELF-INDUCED DEFORMATION AND CORRESPONDING AMPLITUDE ADAPTION OF THE HF SIGNAL MEASURED WITH SELF-SENSING BASED ON THE HF SIGNAL APPLIED TO THE DE. (A) TRENDS OF THE END EFFECTOR DISPLACEMENT, ESTIMATED CAPACITANCE, AND SOUND PRESSURE TIME-SERIES IN A REFERENCE SCENARIO IN WHICH THE DEA IS DRIVEN BY A CONSTANT AMPLITUDE HF VOLTAGE SUPERPOSED TO A LF DRIVING VOLTAGE. (B) SOUND PRESSURE OBTAINED BY VARYING THE HF SIGNAL AMPLITUDE AS A FUNCTION OF THE MEASURED CAPACITANCE. (C) SOUND PRESSURE OBTAINED BY VARYING THE HF SIGNAL AMPLITUDE AS A FUNCTION OF THE LF DRIVING SIGNAL AMPLITUDE ([261]).	120
FIGURE 3.64: VOLTAGE-INDUCED DEFORMATION, WITH OBSTACLE DETECTION PERFORMED BY COMPARING THE ESTIMATED CAPACITANCE AND THE MEASURED SELF-SENSING CAPACITANCE. TOP ROW: THE DEA IS DRIVEN WITH A HF+LF VOLTAGE SIGNAL, IT PRODUCES A LINEAR STROKE AND SOUND DURING THE ENTIRE TEST, WITH THE PITCH OF THE SOUND OUTPUT CHANGING UPON OBSTACLE IMPACT. BOTTOM ROW: THE DEA IS DRIVEN WITH A MF+LF VOLTAGE SIGNAL, IT ONLY PRODUCES LINEAR ACTUATION DURING THE FIRST PART OF THE TEST, AND GENERATES SOUND UPON IMPACT WITH THE OBSTACLE ([261]).	122
FIGURE 3.65: WORKING PRINCIPLE AND CONSTRUCTION OF THE DEA BASED TEXTILE INTEGRATED AUDIO-TACTILE FEEDBACK ELEMENT.	123
FIGURE 3.66: DESIGN AND INFLUENCE OF THE TEXTILE PRE-TENSIONING ELEMENT AND SPACER. TEXTILE AND SKIN FORCE ARE COMBINED AND WORK AGAINST THE DE AS A PRE-TENSIONING ELEMENT. THE OUTPUT PERFORMANCE OF THE DEA IS INFLUENCED BY THE FORCE CHARACTERISTIC OF THE SKIN AND TEXTILE.	124
FIGURE 3.67: MEASUREMENT AND SIMULATION OF PRE-STRETCHED TEXTILE (20 % BIAXIAL) TENSILE TEST FOR DIFFERENT GEOMETRY.	124
FIGURE 3.68: OUTPUT DEFORMATION AND FORCE PERFORMANCE FOR DIFFERENT GEOMETRIES AND DIFFERENT WORKING POINTS OF THE SYSTEM.	126
FIGURE 3.69: OUTPUT PERFORMANCE OF THE SYSTEM FOR DIFFERENT GEOMETRIES (R_i : 5 -10 MM; R_o UP TO 20 MM) WITH (A) OUTPUT DEFORMATION, OUTPUT FORCE AND OUTPUT WORK FOR 20 % TEXTILE PRE-STRETCH AND (B) FOR 10%, 20 % AND 30% TEXTILE PRE-STRETCH. GRAY AREAS IDENTIFY PARAMETER-REGION WHERE EITHER THE DEFORMATION OR FORCE IS BELOW THE JND THRESHOLD OR THE STRUCTURE IS TOO BIG (TEXTILE OUT-OF-PLANE DEFORMATION > 3MM).	127
FIGURE 3.70: OUTPUT PERFORMANCE OF TEXTILE DE SYSTEM FOR DIFFERENT TEXTILE PRE-STRETCH (MAXIMUM OUTPUT 0.0737 NM AT R_i = 8 MM AND R_o = 17 MM (RED DOT)).	128
FIGURE 3.71: TEXTILE INTEGRATED DEA PROTOTYPE WITH (A) MEASUREMENT CLAMPS AND (B) SILICONE HOUSING AND ARM STRIP INTEGRATED PROTOTYPE.	128
FIGURE 3.72: ACTUATOR CURVE (DEA + TEXTILE) FOR DIFFERENT MECHANICAL CONFIGURATIONS, FOR 2 AND 5 LAYER DEA, WITH 0V AND 2.5 kV ELECTRICAL ACTUATION.	130
FIGURE 3.73: OUTPUT FORCE OF THE TEXTILE INTEGRATED ELEMENT WITH 500 V AMPLITUDE SINUSOIDAL SIGNAL (A) FOR 2 LAYER DE WITH DIFFERENT BIAS VOLTAGES (B) FOR 5 LAYER DE WITH DIFFERENT VOLTAGES AND (C) 5 LAYER DE FOR DIFFERENT SIGNAL FREQUENCIES.	131
FIGURE 3.74: OUTPUT DISPLACEMENT OF THE TEXTILE INTEGRATED ELEMENT WITH 500 V AMPLITUDE SINUSOIDAL SIGNAL (A) FOR 2 LAYER DE AND (B) 5 LAYER DE.	132
FIGURE 3.75: OUTPUT DISPLACEMENT OF THE TEXTILE INTEGRATED ELEMENT WITH 500 V AMPLITUDE SINUSOIDAL SIGNAL WITH 1 – 60 HZ FREQUENCY FOR (A) FOR 2 LAYER DE AND (B) 5 LAYER DE.	132
FIGURE 3.76: CAPACITANCE MEASUREMENT OF DEMONSTRATOR WITH 5 DE LAYERS IN DIFFERENT CONFIGURATIONS.	133
FIGURE 3.77: SPL OF THE ACTUATOR (DEA + TEXTILE) FOR DIFFERENT CONFIGURATIONS, FAR 2- AND 5-LAYER DEA, WITH DIFFERENT BIAS AND AMPLITUDE INPUT VOLTAGE.	134
FIGURE 3.78: SPL FOR DIFFERENT CONFIGURATIONS AND DIFFERENT ACTUATOR LAYERS.	135

FIGURE 4.1: COMBINATION OF DE BASED SENSOR- ACTUATOR AND MULTI-FUNCTIONAL ELEMENTS AS WELL AS GENERATOR WITH ADDITIONAL CONVENTIONAL ELEMENTS AND ELECTRONIC TO DELIVER A COMPREHENSIVE DISTRIBUTED HUMAN COMMUNICATION INTERFACE. 137

FIGURE 4.2: POSSIBLE FEATURES AND EXTENSIONS FOR A SMART GLOVE TO PROVIDE A FULLY COMPREHENSIVE SMART ASSISTANCE TOOL. DE TECHNOLOGY VIABLE FEATURES ARE RED MARKED. 138

FIGURE A 1: DIFFERENT CAPACITANCE MEASUREMENT METHODS TO MEASURE THE DE. CLXVI

FIGURE A 2: BIASING ELEMENTS AND INFLUENCE TO THE DESIGN OF THE DE SYSTEM WITH REACTION FORCES (A) MASS (B) HARD STOP (C) MAGNET (D) LINEAR SPRING (E) NEGATIVE BIAS SPRING AND (F) ANGLED BIASING SPRING. AS WELL AS A EXAMPLE FOR A CIRCULAR DE WITH FORCE AND DISPLACEMENT DIFFERENCE (G). CLXVII

FIGURE A 3: SPL IN BLOCKING CONDITIONS (B1 AND B2, AS DEFINED IN FIGURE 3.2): COMPARISON OF EXPERIMENTAL DATA AND FINITE ELEMENT MODEL PREDICTIONS. THE GREEN BANDS INDICATE THE RANGE WHERE THE NATURAL FREQUENCIES OF THE CORRESPONDING MODES (WHOSE VALUE IS DIFFERENT IN THE TWO CASES) ARE COMPRISED ([225]). CLXIX

FIGURE A 4: CONE DEA IN THE INITIAL (REFERENCE) CONFIGURATION AND IN A GENERIC DEFORMED CONFIGURATION ([225]).CLXX

FIGURE A 5 TIME SERIES (A.) AND SPECTRUM (B.) OF THE SOUND PRESSURE FOR THE TEST SHOWN IN FIGURE 3.26. IN THE TEST, THE DEA IS SUBJECT TO A MULTI FREQUENCY INPUT (BOTH THE HF AND THE LF COMPONENT HAVE SINUSOIDAL WAVEFORM AND CONSTANT AMPLITUDE) CLXXII

FIGURE A 6: (A) COP-DEA ASSEMBLY WITHOUT HOUSING (LEFT) SUFFERING FROM ACOUSTIC SHORT-CIRCUIT, AND INSTALLED INSIDE THE BOX (RIGHT). (B) DEFINITION OF THE FIRST STRUCTURAL VIBRATION MODE FOR THE COP-DEA, AND SURFACE DISCRETIZATION USED TO FORMULATE THE MODEL [216] (C.F. [59]). CLXXIV

FIGURE A 7: FURTHER MEASUREMENTS OF THE DEA PERFORMANCE. CLXXVII

FIGURE A 8: DISPLACEMENT OF THE END EFFECTOR FOR DIFFERENT SIGNALS WITH AND WITHOUT HOUSING.CLXXVIII

FIGURE A 9: FORCE MEASUREMENT FOR DIFFERENT PRE-LOAD FORCES AND DIFFERENT BIAS VOLTAGE AND A COMPARISON (LOW RIGHT SIDE). CLXXVIII

FIGURE A 10: STATISTICS OF USER PERCEPTION TESTS WITH TWO DEA UNITS (LEFT-RIGHT), FOR 8 DIFFERENT COMBINATIONS OF HAPTIC AND ACOUSTIC FEEDBACKS PRODUCED BY THE TWO UNITS. CLXXIX

FIGURE A 11: CLASSIFICATION TABLE USED FOR THE CONSTRUCTION OF CONFUSION MATRICES IN FIGURE 3.42. CLXXX

List of Abbreviations and Acronyms

<i>ADC</i>	<i>analog digital converter</i>	<i>HV</i>	<i>high voltage</i>
<i>AR</i>	<i>augmented reality</i>	<i>IoT</i>	<i>Internet of Things</i>
<i>AT</i>	<i>absolute threshold</i>	<i>IPG</i>	<i>ionic polymer gels</i>
<i>CC</i>	<i>correlation coefficient</i>	<i>IPMC</i>	<i>Ionomeric poly.-metal composites</i>
<i>CCG</i>	<i>constant charge generator</i>	<i>JND</i>	<i>just-noticeable difference</i>
<i>CEG</i>	<i>constant electric field generator</i>	<i>LAN</i>	<i>local area network</i>
<i>CNS</i>	<i>central nervous system</i>	<i>LCE</i>	<i>liquid-crystal elastomer</i>
<i>CNT</i>	<i>carbon nanotubes</i>	<i>LF</i>	<i>lower frequency</i>
<i>COP</i>	<i>circular out of plane</i>	<i>LPV</i>	<i>linear parameter-varying</i>
<i>CP</i>	<i>conductive polymers</i>	<i>MF</i>	<i>middle frequency</i>
<i>CPT</i>	<i>constant position test</i>	<i>NBS</i>	<i>negative rate bias spring</i>
<i>CVG</i>	<i>constant voltage generator</i>	<i>OTG</i>	<i>optimal triangle generator</i>
<i>DAC</i>	<i>digital analog converter</i>	<i>PBS</i>	<i>positive rate bias spring</i>
<i>dB</i>	<i>decibel</i>	<i>PCB</i>	<i>printed circuit board</i>
<i>DEA</i>	<i>dielectric elastomer actuator</i>	<i>PDMS</i>	<i>polydimethylsiloxane</i>
<i>DEG</i>	<i>dielectric elastomer Generator</i>	<i>PET</i>	<i>Polyethyleneterephthalat</i>
<i>DEs</i>	<i>dielectric elastomers</i>	<i>PNS</i>	<i>peripheral nervous system</i>
<i>DES</i>	<i>dielectric elastomer sensor</i>	<i>SIP</i>	<i>strip in plane</i>
<i>DET</i>	<i>dielectric elastomer transducers</i>	<i>SMAs</i>	<i>shape-memory-alloy</i>
<i>EAPs</i>	<i>electro active polymers</i>	<i>SPL</i>	<i>sound pressure level</i>
<i>ERF</i>	<i>electrorheological fluids</i>	<i>THD</i>	<i>total harmonic distortion</i>
<i>FEM</i>	<i>finite-element-methode</i>	<i>UI</i>	<i>user interface</i>
<i>GND</i>	<i>ground connection</i>	<i>VR</i>	<i>virtual reality</i>
<i>HF</i>	<i>higher frequency</i>	<i>WLAN</i>	<i>wireless local area network</i>
<i>HMI</i>	<i>human-machine-interaction</i>		

List of Symbols

Z_m	<i>mechanical impedance</i>	η_d	<i>membrane aspect ratio</i>
∇^2	<i>laplace operator</i>	λ	<i>average radial membrane stretch</i>
ACS	<i>cross-sectional area DE membrane</i>	$\lambda_x, \lambda_y, \lambda_z$	<i>stretch in x, y, z direction</i>
CDE	<i>capacitance of the DE</i>	σ_{Max}	<i>maxwell stress</i>
d_i	<i>inner membrane diameter</i>	A	<i>electrode area</i>
d_o	<i>outer membrane diameter</i>	c	<i>wave speed</i>
$D\alpha$	<i>damping matrice</i>	C	<i>capacitance</i>
E_{el}	<i>electrical energy</i>	f	<i>frequency</i>
E_{gen}	<i>generated energy</i>	h	<i>COP out-of-plane deformation</i>
E_{mech}	<i>mechanical energy</i>	I	<i>current</i>
F	<i>Force</i>	k	<i>angular wavenumber</i>
F_{Bias}	<i>biasing force</i>	P	<i>perception-strength</i>
J_m	<i>Bessel function</i>	P_s	<i>sound pressure</i>
KT.....	<i>pre-warping factor</i>	Q	<i>charge</i>
L_x	<i>length of the dielectric</i>	qt.....	<i>time varying charge</i>
L_y	<i>width of the dielectric</i>	r	<i>polarcoordinates: radius</i>
L_z	<i>thickness of the dielectric</i>	S	<i>stimulus-strength</i>
mk_X	<i>membrane shape functions</i>	U	<i>voltage applied to the DE</i>
$M\alpha$	<i>mass matrice</i>	$u(X)$	<i>target point on DE surface</i>
RDE	<i>resistance of the DE electrode</i>	V	<i>volume of the dielectric</i>
S_0	<i>stimulation threshold</i>	vt.....	<i>time varying voltage</i>
$S_{x,y,z}$	<i>strain in x,y,z direction</i>	Y	<i>young modulus</i>
t_c	<i>charging time</i>	α	<i>modal coordinate</i>
t_d	<i>discharging time</i>	ζ	<i>tension on the DE membrane</i>
t_r	<i>cycle time</i>	θ	<i>polarcoordinates: angular coordinate</i>
T_s	<i>HF sampling time window</i>	κ	<i>amplitude compensation factor</i>
U_{supp}	<i>circuit operating voltage</i>	v	<i>poison`s ratio</i>
v	<i>velocity</i>	ρ	<i>density of DE membrane</i>
vt.....	<i>LF excitation waveform</i>	σ	<i>stress in DE membrane</i>
$v(t)$	<i>HF excitation waveform</i>		
V_b	<i>bias voltage</i>		
V_k	<i>constant excitation amplitude</i>		
W_m	<i>mechanical energy</i>		
ZDE	<i>impedance of the DE</i>		
γ_{mn}	<i>mode shape functions</i>		
ϵ_0	<i>void permittivity</i>		
ϵ_r	<i>relative permittivity</i>		

Curriculum Vitae

Lebenslauf

Studium



Persönliche Daten

Name
Sebastian Gratz-Kelly

Anschrift
Johannstraße 28
66131 Saarbrücken

Telefonnummer
0172 / 8301008

E-Mail Adresse
sebastiangratzkelly
@gmx.net

Bildungsweg

Master of Science –
Mechatronik,
Universität des
Saarlandes, 2017

Bachelor of Science –
Mechatronik,
Universität des
Saarlandes, 2014

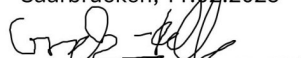
Abitur –
Technisches-
Gymnasium Völklingen,
2010

- Seit 2020 Universität des Saarlandes -
Promotion – Systems Engineering - Lehrstuhl für intelligente
Materialsysteme (Prof. Dr. S. Seelecke)
Themenbereich „Entwicklung intelligenter, multifunktionaler
Nutzeroberflächen auf Basis Dielektrischer Elastomer Wandler zur
Verwendung in der Digitalen Produktion“
- 2014 – 2017 Universität des Saarlandes -
Masterstudium Mechatronik - Vertiefung Mechatronische Systeme und
Elemente
Masterarbeit - Lehrstuhl für Messtechnik (Prof. Dr. A. Schütze)
„Untersuchungen zur Detektion von Verunreinigungen in Wasserstoff bei
hohen Drücken mittels Infrarot-Spektroskopie“
- 2010 – 2014 Universität des Saarlandes -
Bachelorstudium Mechatronik - Vertiefung Mechatronische Systeme und
Elemente
Bachelorarbeit – Lehrstuhl für Elektronik und Schaltungstechnik (Prof. Dr.
M. Möller)
„Echtzeitemulation analoger Bauelemente auf einer digitalen
Rechnerstruktur mithilfe von Wellendigitalfiltern.“

Praxiserfahrung

- Seit 01/2025 ZeMA gGmbH - Wissenschaftlicher Mitarbeiter im Bereich
Transferaktivitäten im Mittelstand Digital Zentrum (MDZ) und European
Digital Innovation HUB (EDIH)
- Seit 03/2022 ZeMA gGmbH - Gruppenleitung Forschungsgruppe Smart Textiles
(Forschungsbereich Smarte Materialsysteme)
- 12/2017 – ZeMA gGmbH - Wissenschaftlicher Mitarbeiter am Lehrstuhl für
12/2024 intelligente Materialsysteme
- 03/2016 – - Hilfwissenschaftler: Arbeitsgruppe Sensorik und Aktorik (ZeMA) /
05/2017 Lehrstuhl für Messtechnik (UdS)
- 01/2015 – -Hilfwissenschaftler: Arbeitsgruppe Montagetechnik (ZeMA) / Lehrstuhl
03/2016 für Montagesysteme (UdS) – in Kooperation mit Daimler AG
- 08/2015 – Hydac Elektronik GmbH
10/2015 Masterpraktikum zum Studium der Mechatronik,
Abteilung Vorentwicklung (Leitung Dr. H. Mannebach)
- 03/2012 – Universität des Saarlandes (UdS)
12/2014 Hilfwissenschaftler: Lehrstuhl für Elektronik und Schaltungstechnik
- 08/2010 – Hydac International GmbH
10/2010 Grundpraktikum zum Studium der Mechatronik

Saarbrücken, 11.07.2025


Sebastian Gratz-Kelly

Publications

Peer-reviewed journal publications

- **S. Gratz-Kelly**, M. Cerino, D. Philippi, D. Göttel, G. Schultes, J. Heppe and P. Motzki, “Optimized sensor-array based on metal sputtered dielectric elastomers for integrated user interaction”, MDPI Materials, 2024, Vol. 17, Issue 23, doi: 10.3390/ma17235993
- T. Chowdhury, **S. Gratz-Kelly**, E. Wagner, P. Motzki and M. Lehser (2024), “Ensemble Learning Approach for Advanced Predictive Modelling of Biometric Data and Action States with Smart Sensing”, IEEE Access, 2024, Vol. 12, doi: 10.1109/ACCESS.2024.3466528
- S. Addario, **S. Gratz-Kelly**, G. Rizzello, D. Naso and G. Moretti (2024), “An experimental parameter analysis of the acoustic response in dielectric elastomer loudspeakers”, Journal of Vibration and Control, Sage Journals, 2024, doi: 10.1177/10775463241273022
- **S. Gratz-Kelly**, T. Krüger, G. Rizzello, S. Seelecke and G. Moretti (2024), “A tri-modal dielectric elastomer actuator integration linear actuation, sound generation, and self-sensing capabilities”, Sensors and Actuator A: Physical, 2024, Vol. 372, Issue 115332, doi: 10.1016/j.sna.2024.115332
- A. Meyer, M. Wagner, **S. Gratz-Kelly**, S. Nalbach and P. Motzki (2024), “Concept studies and application development of textile integrated dielectric elastomer sensors for smart shoe technologies”, tm – Technisches Messen, 2024, Vol. 91, Issue 3-4, doi: 10.1515/teme-2024-0019
- **S. Gratz-Kelly**, D. Philippi, B. Fasolt, S. Nalbach and P. Motzki (2024), “Gesture and force sensing based on dielectric elastomers for intelligent gloves in the digital production”, tm – Technisches Messen, 2024, Vol. 91, Issue 3-4, doi: 10.1515/teme-2024-0003
- **S. Gratz-Kelly**, T. Krüger, G. Rizzello, S. Seelecke and G. Moretti (2023), “An audio-tactile interface based on dielectric elastomer actuators”, Smart Materials and Structures, 2023, Vol. 32, Nr. 3, doi: 10.1088/1361-665X/acb6da
- **S. Gratz-Kelly**, G. Rizzello, M. Fontana, S. Seelecke and G. Moretti (2022), “A Multi-Mode, Multi-Frequency Dielectric Elastomer Actuator”, Advanced Functional Material, 2022, Vol. 32, Issue 34, doi: 10.1002/adfm.202201889

International conference proceedings

- T. A. Chowdhury, **S. Gratz-Kelly**, E. Wagner, P. Motzki and M. Lehser (2024), “A Novel Approach for Optimizing Muscle Activation Level and Localization with Multi-Mode DEA Feedback Capability”, ASME 2024 Conference on Smart Materials, Adaptive Structures and Intelligent Systems (SMASIS), 139090.
- T. A. Chowdhury, **S. Gratz-Kelly**, G. Moretti, E. Wagner, P. Motzki, M. Lehser (2024), “A novel fusion method for intense heat detection and localization solely based on surface temperature with multi-mode DEA feedback”, Proc. SPIE 12948, Soft Mechatronic and Wearable Systemes, 129488
- S. Addario, A. Priuli, J. Hubertus, **S. Gratz-Kelly**, J. Neu, G. Schultes, S. Seelecke, G. Rizzello (2024), “Thermoplastic Polymer Based Negative Stiffness Biasing Mechanism

for High Stroke Dielectric Elastomer Actuator Systems”, Proc. SPIE 12945, Electroactive Polymer Actuators and Devices (EAPAD) XXVI, 1294518

- **S. Gratz-Kelly**, B. Holz, T. Krüger, S. Seelecke, G. Rizzello, P. Motzki, G. Moretti (2023), “An integrated Audio-tactile Interface based on DE Actuators for User Interaction”, ASME 2023 Conference on Smart Materials, Adaptive Structures and Intelligent Systems (SMASIS), 111228.
- **S. Gratz-Kelly**, T. Krüger, S. Seelecke, G. Rizzello, G. Moretti (2023), “A self-sensing approach for multi-mode dielectric elastomer actuator-loudspeaker devices”, Proc. SPIE 12482, Electroactive Polymer Actuators and Devices (EAPAD) XXV, 1248204.
- K. Koshiya, **S. Gratz-Kelly**, P. Motzki, G. Rizzello (2023), “An Embedded Self-Sensing Motion Control System for Strip-Shaped Dielectric Elastomer Actuators”, Proc. SPIE 12482, Electroactive Polymer Actuators and Devices (EAPAD) XXV, 1248201.
- **S. Gratz-Kelly**, S. Nalbach, P. Motzki and S. Seelecke (2021), “Aktor- und Sensorelemente basierend auf Dielektrischen Elastomeren zur Verwendung in tragbaren Assistenztools”, Digitale-Fachtagung Mechatronik.
- **S. Gratz-Kelly**, A. Meyer, P. Motzki, S. Nalbach, G. Rizzello, S. Seelecke (2020), “Force measurement based on dielectric elastomers for intelligent glove providing worker assessment in the digital production”, Proc. SPIE 11375, Electroactive Polymer Actuators and Devices (EAPAD) XXII, 1137525.
- A. Meyer, S. Lenz, **S. Gratz-Kelly**, P. Motzki, S. Nalbach, S. Seelecke, G. Rizzello (2020), “Experimental characterisation of a smart dielectric elastomer multi-sensor grid”, Proc. SPIE 11375, Electroactive Polymer Actuators and Devices (EAPAD) XXII, 1137528.
- **S. Gratz-Kelly**, S. Seelecke (2019), “Intelligente Handschuhe zur Werkerunterstützung in der digitalisierten Produktion”, Industrietag Promotionskolleg Digitalisierung der Produktion
- **S. Gratz-Kelly**, S. Hau, S. Seelecke (2018), “Intelligente Handschuhe zur Werkerunterstützung in der digitalisierten Produktion”, Technische Unterstützungssysteme, die die Menschen wirklich wollen.
- M. Schott, E. Pignanelli, **S. Gratz-Kelly**, A. Schütze (2018), “Modellierung und Simulation eines IR-Messsystems zur Optimierung der Strahlungsintensität für die Wasserstoffqualitätsüberwachung”, Sensoren und Messsysteme -19. ITG/GMA-Fachtagung.
- M. Schott, E. Pignanelli, **S. Gratz-Kelly**, A. Schütze (2017), “Modulares IR-Messsystem zur Überwachung der Wasserstoffqualität für Brennstoffzellenfahrzeuge”, 13. Dresdner Sensor-Symposium 2017 – Association for Sensors and Measurements.

Poster presentations and symposium presentations

- S. Gratz-Kelly, A. Meyer, P. Motzki (2024) “Industrial Developments of Dielectric EAP Sensor Technology”, Industry forum, ASME 20234Conference on Smart Materials, Adaptive Structures and Intelligent Systems (SMASIS).
- **S. Gratz-Kelly**, S. Nalbach, P. Motzki (2023) “integration of smart materials in smart textiles”, Webinar, SmartX Community.

- **S. Gratz-Kelly**, S. Nalbach, P. Motzki (2023) “Integration von smarten Materialien in Textilien – Perspektiven für intelligente Datenauswertung und Ansteuerung”, Symposium Smart Textiles & KI, SmartTEX Netzwerk.
- T. Chowdhury, **S. Gratz-Kelly**, S. Nalbach, P. Motzki (2023) “Textile integrated sensor analysis for biometric data collection and processing – human digital twin in reality”, Symposium Smart Textiles & KI, SmartTEX Netzwerk.
- **S. Gratz-Kelly**, G. Rizzello, M. Fontana, S. Seelecke, G. Moretti (2022), “A multi-mode multi-frequency dielectric elastomer actuator”, EuroEAP international Conference on Soft Transducers and Electromechanically Active Polymers.
- **S. Gratz-Kelly**, B. Fasolt, S. Nalbach, P. Motzki, S. Seelecke G. Rizzello (2021), “actuator and sensor elements based on dielectric elastomers for mobile assistant tool use in industry 4.0 environment”, EuroEAP international Conference on Soft Transducers and Electromechanically Active Polymers.
- **S. Gratz-Kelly**, S. Seelecke (2019), “Tragbare Assistenztools für die Digitale Produktion”, Doktorandentag Graduiertenprogramm GradUS.
- **S. Gratz-Kelly**, S. Seelecke (2019), “Tragbare Assistenztools für die Digitale Produktion”, Industrietag Promotionskolleg Digitalisierung der Produktion.

Demonstrator fair exhibition

- SMASIS 2024
- Hannovermesse 2024
- SMASIS 2023
- SPIE 2023
- Euro EAP 2023
- Hannovermesse 2023
- EuroEAP 2022
- Motek – Internatinal Fachmesse für Produktions- und Montageautomatisierung 2022
- Hannovermesse 2019